Andrés Kecskeméthy · Veljko Potkonjak
Andreas Müller *Editors*

Interdisciplinary Applications of Kinematics

Proceedings of the
International Conference, Lima, Perú,
January 9–11, 2008

Springer

Interdisciplinary Applications of Kinematics

Andrés Kecskeméthy, Veljko Potkonjak,
and Andreas Müller (Eds.)

Interdisciplinary Applications of Kinematics

Proceedings of the International Conference,
Lima, Perú, January 9–11, 2008

Springer

IFToMM

Editors
Andrés Kecskeméthy
University of Duisburg-Essen
Mechanical Engineering
Duisburg
Germany

Andreas Müller
University of Duisburg-Essen
Mechanical Engineering
Duisburg
Germany

Veljko Potkonjak
University of Belgrade
Faculty of Electrical Engineering
Belgrade
Serbia

ISBN 978-94-007-2977-3 e-ISBN 978-94-007-2978-0
DOI 10.1007/978-94-007-2978-0
Springer Dordrecht Heidelberg New York London

Library of Congress Control Number: 2011942889

Printed on acid-free paper

Springer is part of Springer Science+Business Media (www.springer.com)

Preface

The present proceedings collects 14 papers that were selected after a rigorous peer review for the First Conference on Interdisciplinary Applications in Kinematics, held in Lima, Peru, from January 9–11, 2008.

The objective of the conference was to bring together researchers from different fields where kinematics plays a role. This includes not only theoretical fields where kinematics is traditionally established, but in particular applications in which kinematics might contribute new perspectives for practical applications. Examples are the areas of biomechanics, industrial machinery, molecular kinematics, railway vehicles and many others.

The participation of 16 researchers from 10 countries shows the strong interest these topics find in the scientific community. Moreover, the site of the conference in Peru not only proved to be very successful, but also helped to foster the international scientific cooperation in this region, which has outstanding potentials.

We thank the authors for submitting their valuable contributions for this conference as well as the reviewers for performing the reviews in due time. We also thank the publisher Springer for the timely implementation of this book and the valuable advices during the production process. We are very grateful to the Universidad de Piura Campus Lima, the Pontificia Universidad Católica del Perú as well as the University of Duisburg-Essen for sponsoring this conference and contributing to its success. Our special acknowledgements go to the Förderverein Ingenieurwissenschaften Universität Duisburg-Essen (Association of Friends of Engineering Science of the University of Duisburg-Essen) for their valuable contribution to the funding of the present proceedings. Last but not least, we thank the International Federation for the Promotion of Mechanism and Machine Science IFToMM for the ideal support by offering its patronage for this conference.

Andrés Kecskeméthy
Veljko Potkonjak
Andreas Müller

Editors

Organization

Chair

A. Kecskeméthy, University of Duisburg-Essen, Germany

Co-chairs

E. Carrera, Universidad de Piura Campus Lima, Perú
E. Ísmodes, Pontificia Universidad Católica del Perú
R. Callupe, Pontificia Universidad Católica del Perú
R. Hernani, Universidad de Piura Campus Lima, Perú

Conference Organisation and Patronage

University of Duisburg-Essen
Universidad de Piura Campus Lima
Pontificia Universidad Católica del Perú
IFToMM Perú

Programme Committee

J. Ambrósio (Portugal)
J. Angeles (Canada)
M. Ceccarelli (Italy)
B. Corves (Germany)
J. Cuadrado (Spain)
S. Dubowsky (USA)
M. Dutra (Brasil)
B. Heimann (Germany)
M. Hiller (Germany)
T. Huang (China-Beijing)
M. Husty (Austria)
K. Kazerounian (USA)
J. Lenarcic (Slovenia)
C. Lopez-Cajún (Mexico)
J.-P. Merlet (France)
M. Morlock (Germany)
V. Parenti-Castelli (Italy)
B. Roth (USA)
B. Siciliano (Italy)
P. Wenger (France)

Contents

IAK 2008
Conference on Interdisciplinary Applications of Kinematics
A. Kecskeméthy, V. Potkonjak and A. Muller (eds.)
Lima, Peru, 9–11 January 2008

DOUBLE-RING POLYHEDRAL LINKAGES

Karl Wohlhart

Institute for Mechanics
Graz University of Technology
e-mail: wohlhart@tugraz.at, web page: http://www.mechanik.tugraz.at/

Keywords: Deployable over-constrained spatial linkages, double-ring mechanisms, mobilizing an irregular polyhedron.

Abstract. *In this paper we present a new type of over-constrained spatial linkages obtained by inserting planar double-ring mechanisms (modules) into the faces of a polyhedron so that they form closed networks over the polyhedron after being interconnected by appropriate gussets. Such linkages will be called "double-ring polyhedral linkages". Though highly over constrained, these linkages are deformable with one degree of freedom. Recently it was shown that polyhedral linkages can be synthesized with single ring mechanisms as modules. Therefore the question arises: what is the advantage of using double-ring mechanisms as modules instead of single-ring mechanisms? The first answer is: double-ring polyhedral linkages show much greater global stability. This is proved by all manufactured models, and the reason is evident: the single-ring mechanism has twice as many degrees of freedom as there are sides in the polyhedral face into which it is inserted, while the double-ring mechanism is movable with only one degree of freedom. A second answer is: from a double-ring polyhedral linkages a variety of cup-like linkages can be found by simply dividing them into parts.*
In this paper we will first demonstrate on an example that polyhedral linkages can be derived from irregular polyhedra by inserting irregular double-ring mechanism into their faces. However, such bizarre linkages, of which nobody would expect that they are mobile, are only of theoretical interest. Therefore we will then concentrate on the five regular double-ring polyhedral linkages, which are found on the basis of the Platonian polyhedra. For some of the greater linkages we will also show partitions which are linkages in the form of cupolas. An example is also given where a double-ring mechanism is used to design a (non-polyhedral) hall-linkage.

1 INTRODUCTION

If we only know the theoretical structure of a mechanism (number of its links, joints and loops) but nothing about its metric dimensions, we are unfortunately unable to predict its true mobility. If the topological structure formula (Gruebler-Kutzbach) indicates mobility as equal or less than zero, then it can only be concluded that the mechanism in question will be a rigid structure if we change its metric dimensions arbitrarily and get the same result. For the given dimensions, however, it can only be concluded that the mobility of the mechanism cannot be less than the one indicated by the structure formula. Polyhedral linkages belong to the category of over-constrained linkages, which make them scientifically charming and attractive as they are, within certain limits, deployable and therefore practically applicable in engineering in many ways.

In the wake of the pioneering work of H.F. Verheyen on expandable polyhedral structures [1] a great number of papers have appeared on the subject of over-constrained expandable linkages [2-11]. A common feature of the polyhedral linkages synthesized so far is that they are globally closed. All of them have been derived on the basis of closed regular or irregular polyhedra and differ only in the kind of modules (basic components) which are inserted into the polyhedron faces and the kind of multiple rotor joints that interconnect them. It has been shown [5] that for the synthesis of polyhedral linkages essentially three different types of modules are used: streching stars, whirling stars and ring chains. These modules are link groups which are highly mobile mechanisms themselves (their mobility depends on the number of polygon sides of the polyhedral face into which they are inserted). “Closure” is therefore a precondition for the necessary reduction of the mobility of the final over-constrained linkage to only one degree of freedom. Moreover, in the physical sense the global stability of these polyhedral linkages is poor, i.e. all the unavoidable backlashes in the linkage sum up. Recently it was shown [12] that in two cases these elementary very mobile modules can be exchanged for similar modules which are mobile with only one degree of freedom: the stretching star can be exchanged for a double stretching star and the whirling star for a double shield mechanism. This kills two birds with one stone: on the one hand the synthesized polyhedral linkages are globally much more stable, and, on the other hand they offer a variety of possibilities of varied partitioning them into “cupola linkages”. But what about the single-ring modules? Can similar modules with only one degree of freedom also substitute them? Yes, double-ring modules can exchange the single-ring modules.

2. DOUBLE-RINGS MECHANISMS

Planar and spatial double-ring mechanisms (irregular and regular) are treated in [13]. While deforming, these mechanisms retain the similarity of the net from which they are derived.

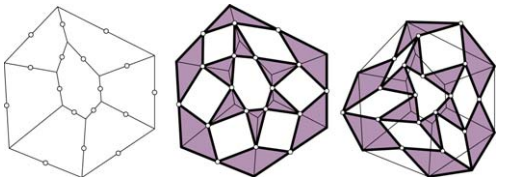

Figure 1: First type of an irregular double-ring mechanism

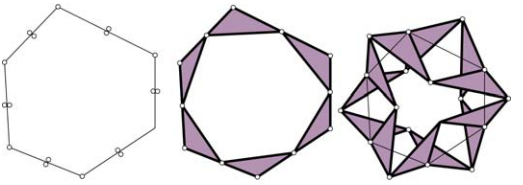

Figure 2: Second type of an irregular double-ring mechanism

We shall distinguish between two types of double ring mechanisms that differ in the generating net. Figure 1 shows the first type: the reference net consists of an outer and an inner line-polygon whose corresponding corner-points are connected by straight lines. Together with the midpoints of the connecting lines the midpoints of the inner polygon determine the triangular links of the inner ring, while the corner-points and the midpoints of the outer polygon, together and the mid-point of the connecting lines determine the quadrangular links of the outer ring. Figure 2 shows the second type of double ring mechanisms: the inner and the outer line-polygons are identified, the inner ring is equal to the outer ring, but the identical links in the rings turn in opposite directions if the double link mechanism deforms.

3. IRREGULAR TETRAHEDRAL LINKAGES

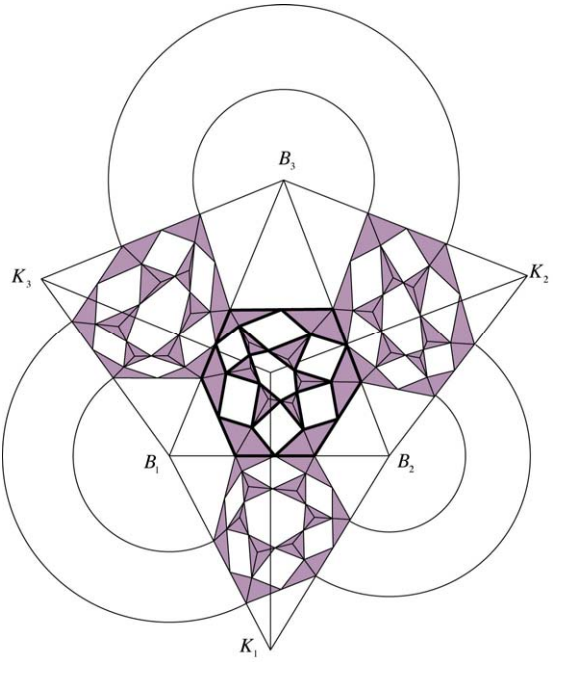

Figure 3: How to synthesize an irregular double-ring tetrahedral linkage

Both types of double rings referred to above, can be used as modules to synthesize irregular polyhedral mechanisms. This will be only show for the cases of the two types of irregular double-ring tetrahedral linkages. The synthesis can start with the net of a given irregular tetrahedron, whose four faces, the basis $B_1B_2B_3$ and the side-faces $K_1B_1B_2$, $K_2B_2B_3$, $K_3B_3B_1$ are displayed in a common plane (Figure 3). In the basis $B_1B_2B_3$ an arbitrary double-ring net can be installed so that every two sides of its outer polygon lie on the sides of the basis. Therewith the double-ring mechanism in the basis is fully given. A second arbitrary double-ring-net may then be inserted into side face $K_2B_2B_3$ so that two sides of its outer polygon coincide with two sides of the outer polygon in the basis. With the net, the second double-ring mechanism is given. Into the side face $K_3B_3B_1$ another double-ring net can be implanted, under the limiting condition that the position of two sides of its outer polygon on the sideline B_3K_3 is already predetermined. With this net, the third double-ring mechanism is given. Into the side face $K_1B_1B_2$ a double-ring-net can finally be installed whose outer polygon is predetermined. Only its inner polygon can be chosen arbitrarily. With this net the fourth double-ring mechanism is fixed.

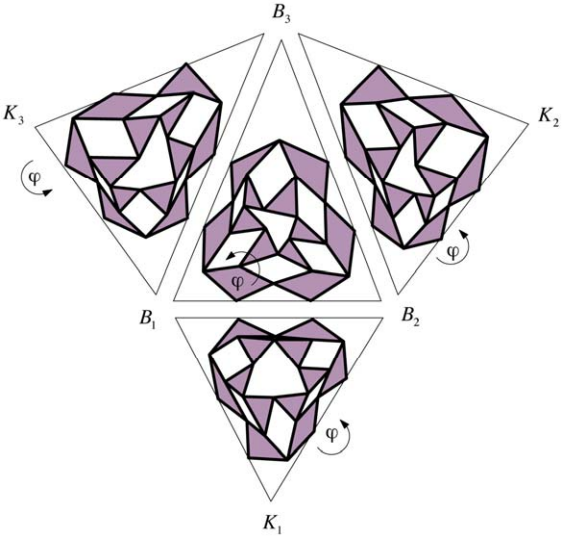

Figure 4: The four double-ring mechanisms activated

The derived planar double-ring mechanisms (Figure 4), consisting of twelve links held together by eighteen rotor joints, are over-constrained but deformable with one degree of freedom. With the number of loops ($L = 7$) and the number of relative degrees of freedom ($\Sigma f_i = 18$) the topological structure formula (Grübler-Kutzbach) yields for their mobility: $m = -3$. The range of their deformability is rather limited by link interference if the two rings are deforming in the same plane. By displacing the inner ring (orthogonally to its plane) the mutual interference between the rings cannot be avoided but reduced, and thus the range of the mobility considerably extended. The four double-rings, all activated by the same angle φ, can be inserted into the faces of tetrahedra whose dimensions are reduced by the factor $\cos\varphi$, and can be interconnected by twelve appropriate rotor bijoints (gussets). Figure 5

shows 3D-pictures of the synthesized double-ring tetrahedral linkage in two phases. As this spatial linkage does not show any symmetry and shows no special dimensions, nobody would expect that it is not a rigid structure but a movable linkage.

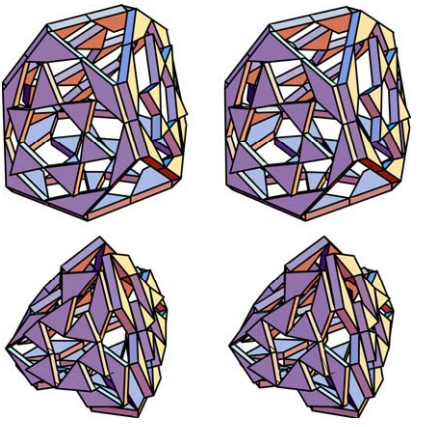

Figure 5: 3D pictures of the irregular double-ring tetrahedral linkage (first type) in two phases

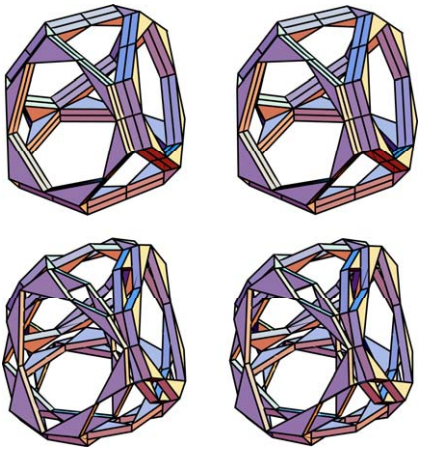

Figure 6: 3D pictures of the irregular double-ring tetrahedral linkage (second type) in two phases

If we start with the second type of double-ring mechanism shown in Figure 2 and proceed in the same manner as before, we find the second irregular double-ring tetrahedral linkage

which is shown in Figure 6. From Figures 5 and 6 it can be seen that the working space of the first linkages is considerably greater than that of the second. As irregular double-ring polyhedral linkages are more of theoretical than practical interest, we do not continue with irregularity but turn our attention to a variety of regular double-ring polyhedral linkages.

4. REGULAR DOUBLE RINGS IN TRIANGULAR-FACED POLYHEDRA

As the faces of a Platonian polyhedron are identical and their perimeters are regular polygons, the double rings used as modules to "mobilize" a Platonian polyhedron must be rotor-symmetric. For the triangular faces of the Platonian tetrahedron, the octahedron and the icosaedrons the following two types of planar double-rings shown in Figure 7 and Figure 8 can be used.

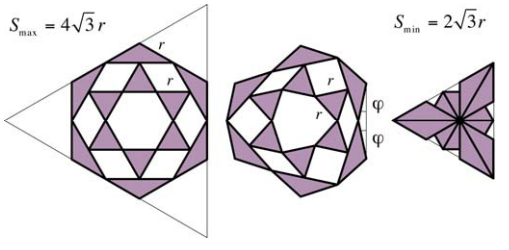

Figure7: First type of a regular double-ring mechanism

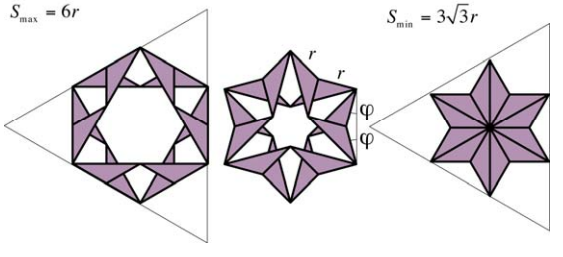

Figure 8: Second type of a regular double-ring mechanism

These double-ring mechanisms are complexes of two homogeneous kinematics chains of an equal number of links connected by rotor-joints. The inner ring of the first type of double-ring consists of six identical links that have the form of equilateral triangles with side length r, and its outer ring consists of identical links in the form of isosceles triangles with the basis length $2r$ and the side-lengths $2r/\sqrt{3}$. The angle φ can be activated between $\varphi = 0$ and $\varphi = 30°$ if the two rings are located in the same plane, but if they can overlap each other, than φ ranges from $\varphi = 0$ to $\varphi = 60°$. The side length S of the triangular faces of the polyhedrons depends on φ:

$$S(\varphi) = 4\sqrt{3}\, r \cos\varphi.$$

In the second double-ring the inner and the outer rings move in different but parallel planes. All links of this double-ring mechanism are identical, they have the form of isosceles triangles with a lateral side length r and a basis length $r\sqrt{3}$. The angle φ goes from zero to $\varphi = 30°$ and the length $S(\varphi)$ of the triangular faces of the polyhedrons into which this double-ring can be inserted as a module is given by:

$$S(\varphi) = 6r \cos\varphi.$$

Polyhedral linkages based on the first type of double-ring shown in Figure 7 reduce their maximal size to their minimum size by the factor $S_{\min} / S_{\max} = 1/2$ if its inner and outer rings, move on different planes. If these rings move in the same plane, the linkage size reduction factor is only $S_{\min} / S_{\max} = \sqrt{3}/2 = 0.866$. For polyhedral linkages based on the first type of double-ring shown in Figure 8 the size reduction factor is also only $S_{\min} / S_{\max} = \sqrt{3}/2 = 0.866$.

5. TETRAHEDRAL, OCTAHEDRAL AND ICOSAHEDRAL LINKAGES

Having prepared three different regular double-ring modules suitable for the insertion into the faces of a tetrahedron, an octahedron or an icosahedron, and being provided with a sufficient number of appropriate gussets (rotor bijoints), we can start with the construction of regular double-ring (triangular-faced) polyhedral linkages.

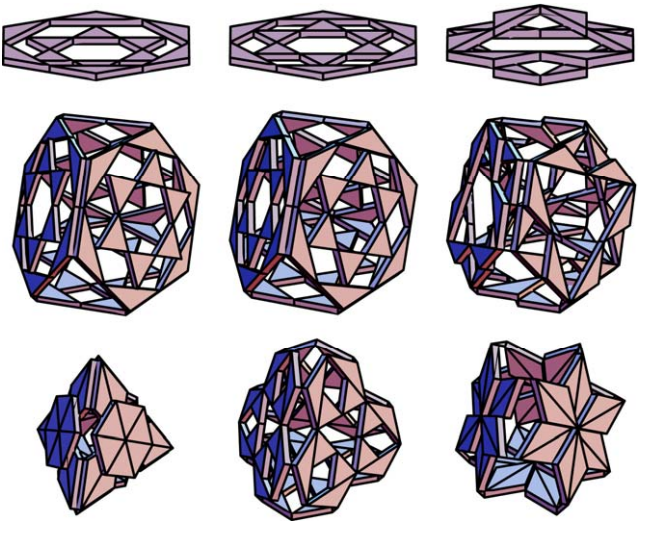

Figure 9: Tetrahedral Linkages with three different modules at their maximal or minimal extension

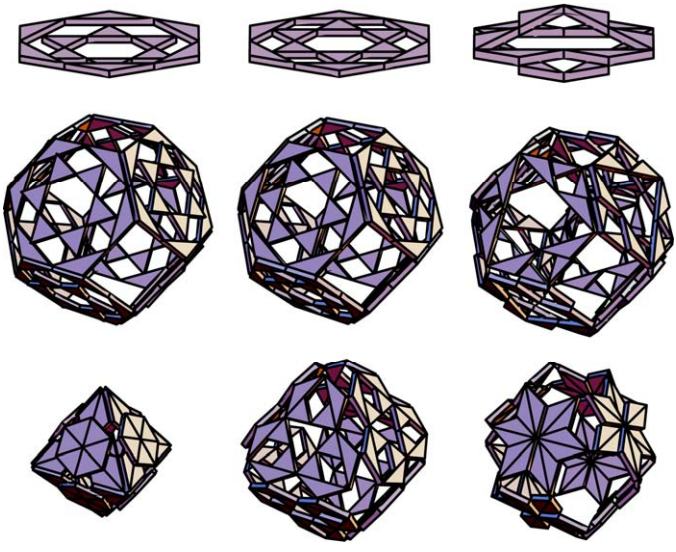

Figure 10: Octahedral linkages with three different modules at theirmaximal or minimal extension

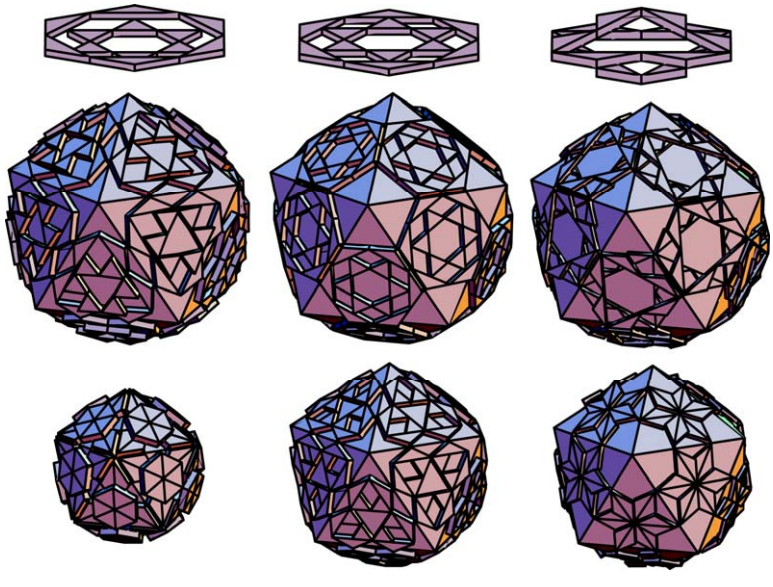

Figure 11: Isotheral linkages with three different modules at their maximal or minimal extension (shown together with the icosahedra)

Figures 8, 9 and 10 show the synthesized linkages in two phases: their maximal or their minimal extension. In Figure 10 the icosahedra (serving as basis in the synthesis process) are included in the presentation to give a clearer view of the complex linkages. By dividing the icosahedral linkage two cupola linkages can be derived which are shown in Figure 12.

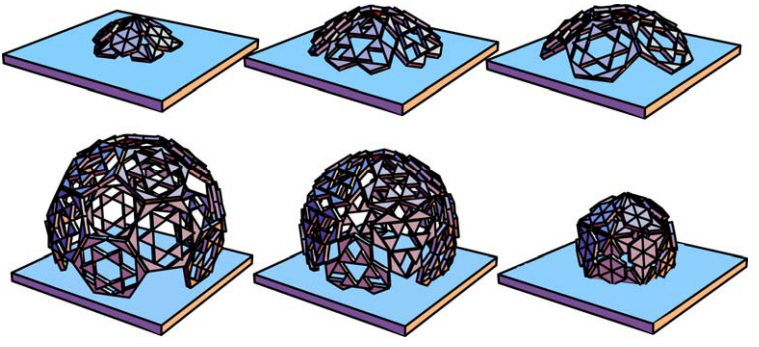

Figure 12: Cupola linkages derived by partitioning one of the icosahedral linkages

6. REGULAR DOUBLE RING IN A HEXAHEDRON

To "mobilize" a regular hexahedron we need double-ring mechanisms that consist of two homogeneous kinematic chains with eight equal links, held together by eight rotor joints. Figure

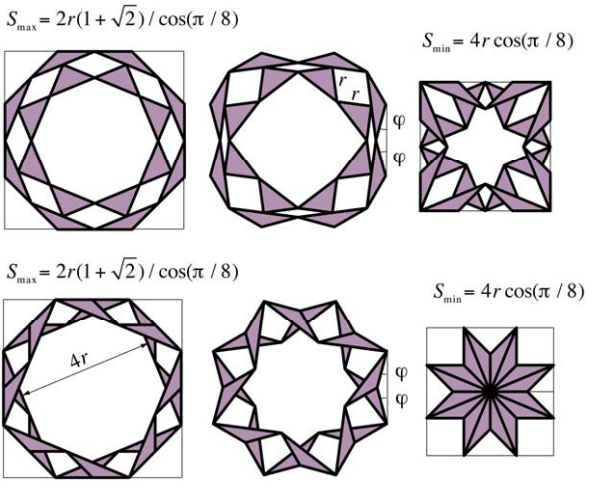

Figure 13: Two equivalent types of regular double-rings for square polyhedron faces

13 presents two equivalent types of such double rings. In both cases the angle φ measuring the deformation runs from $\varphi = 0$ to $\varphi = \pi/4$. The side length of the quadratic faces depends on φ by:

$$S(\varphi) = 2r\,[\frac{\sin\varphi}{\cos\frac{\pi}{8}} + 2\frac{\sin(\frac{3\pi}{8} - \varphi)}{\sin\frac{\pi}{4}}].$$

This formula is valid for both types of double rings. A measure for the extensibility of the linkages, which can be synthesized with these double-rings as modules, is the relation

$$\frac{S_{\min}}{S_{\max}} = \frac{2(\cos\frac{\pi}{8})^2}{(1+\sqrt{2})} = 0.7071.$$

If the two rings in the first case move in the same plane, then the angle φ only goes from $\varphi = 0$ to $\varphi = \pi/8$. The extensibility factor would then be $S_{\min}/S_{\max} = 0.9239$. In the following we will exclude this case because of its poor practical applicability.

7. REGULAR DOUBLE-RING HEXAHEDRAL LINKAGES

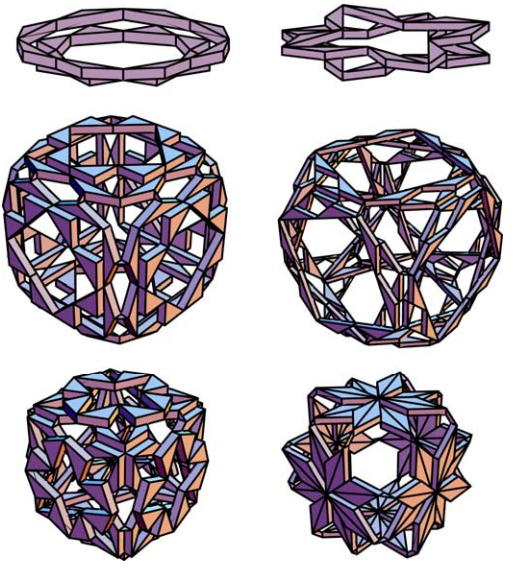

Figure 14: Hexahedral linkages with two different modules at their maximal or minimal extension

The gussets needed for mounting together a double-ring hexahedral linkage with the first type of double ring (Figure 13) are all identical rotor bijoints with orthogonal axes. In the second type of double-ring each needs its proper gussets. Figure 14 shows two synthesized double-ring hexahedral linkages. This linkage can be divided into two parts, each of which is a linkage again (Figure 15). With the square double ring a variety of spatial linkages can be built up, e.g. a linkage hall as shown in Figure 16.

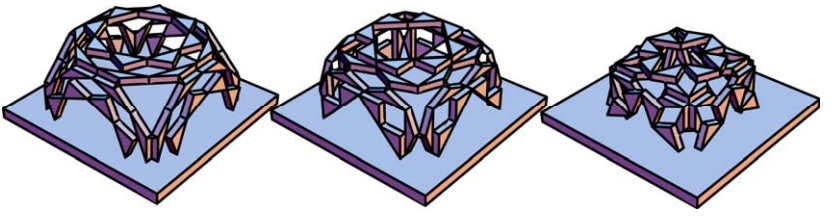

Figure 15: Divided Double-Ring Hexahedral Linkages

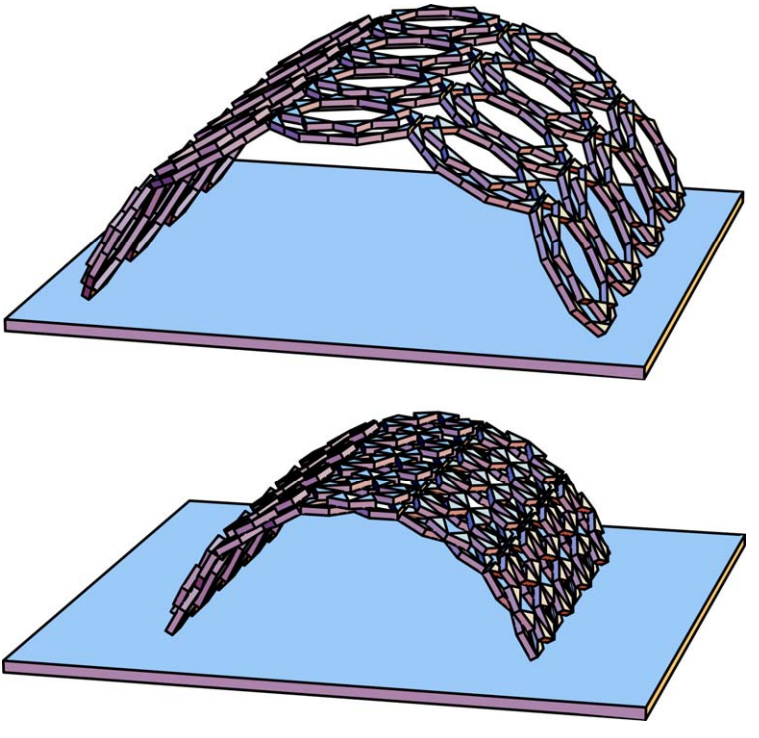

Figure 16: Linkage hall built up by square double rings (two phases)

8. REGULAR DOUBLE-RING IN A DODECAHEDRON

Double-rings mechanisms that can be inserted into the faces of a dodecahedron are shown in Figure17 and Figure18.

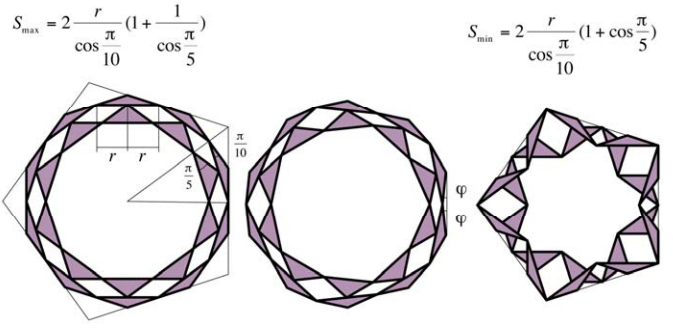

Figure 17: First type of regular double ring for dodecahedral faces

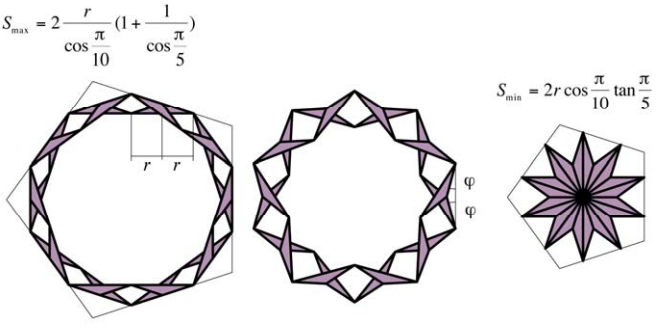

Figure 18: Second type of regular double ring for dodecahedral faces

The side lengths of the faces of dodecahedron depend on the angle φ which measures the deformation of the double ring, For the first type of double ring in Figure 17 the side length S is given by:

$$S(\varphi) = 2r\tan(\pi/5)\left(\frac{\sin\varphi}{\cos(\pi/10)} + 2\frac{\sin[(2\pi/5)-\varphi]}{\sin(\pi/5)}\right), \quad \Rightarrow \frac{S_{\min}}{S_{masx}} = \frac{5+3\sqrt{5}}{10+2\sqrt{5}} = 0.8090.$$

For the second type of double ring in Figure 18 the side length S is given by:

$$S(\varphi) = 2r\cot(\pi/10)\tan(\pi/5)\frac{\cos\varphi}{\cos(\pi/10)}, \quad \Rightarrow \frac{S_{\min}}{S_{\max}} = \frac{5-\sqrt{5}}{2\sqrt{10-2\sqrt{5}}} = 0.5878.$$

9. REGULAR DOUBLE-RING DODEKAHEDRAL LINKAGES

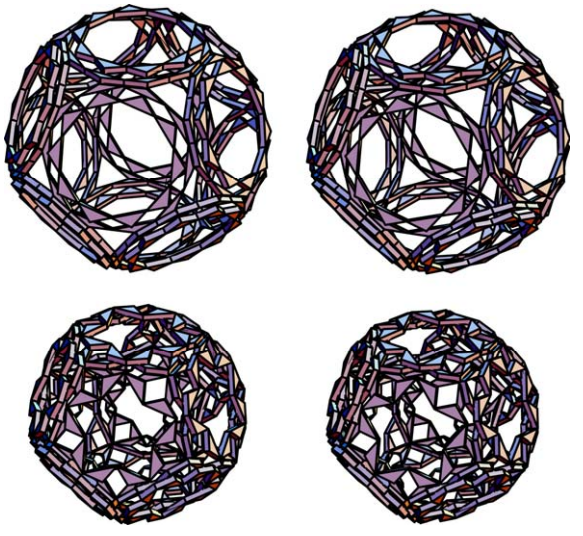

Figure 19: 3D picture of the first type of the double-ring dodecahedral linkage

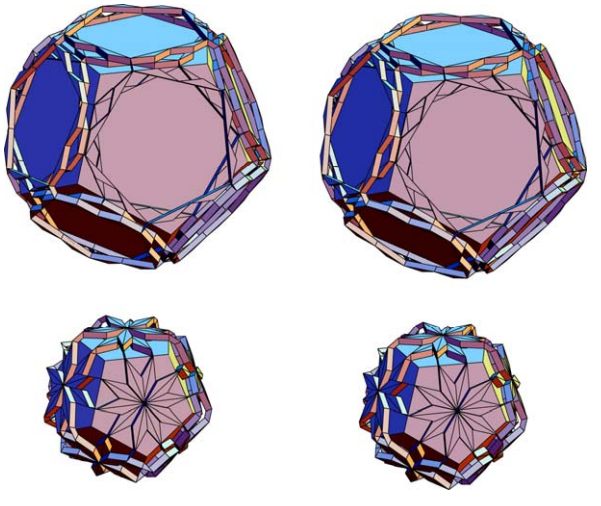

Figure 20: 3D picture of the second type of the double-Ring dodecahedral linkage together with the dodecahedron

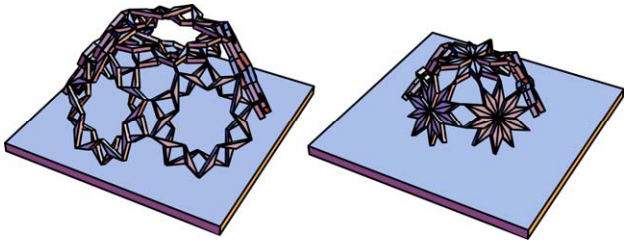

Figure 21: Double-ring dodecahedral cup-linkage in two phases

Figure 19 and 20 show 3D pictures of two double-ring dodecahedral linkages synthesized with the two types of double rings shown in Figure 16 or 17. Such 3D pictures should be looked at in such a way that each eye tries to concentrates on one of the two pictures side by side; a third picture will then appear between the two pictures that looks beautifully three dimensional. A double-ring dodecahedral linkage can be divided into two equal parts, which are linkages in the form of a cup or a cupola (Figure 21).

10. SEMIREGULAR DOUBLE-RING LINKAGES

In section 3 it has been demonstrated that planar double-ring mechanisms can be used to mobilize any irregular polyhedron. Therefore it is clear that all semiregular Archimedean polyhedra also can be enclosed by a polyhedral linkage. Archimedean polyhedra are polyhedra with regular but two different faces. The most popular Archimedean polyhedron is the football polyhedron. Another well-known Archimedean polyhedron is the Miller polyhedron, which consists of triangular and quadrangular, faces (Figure 22).

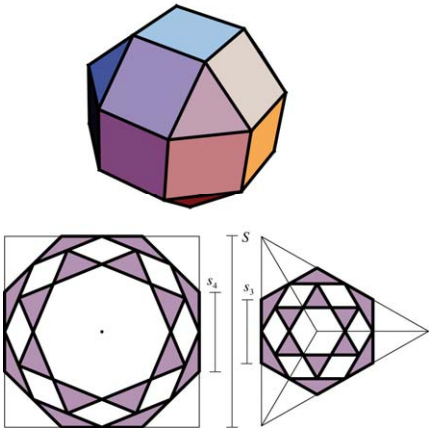

Figure 22: The Miller polyhedron and regular square and triangular double-ring mechanisms

Insertion of regular double-ring mechanisms in all faces would lead to a rigid structure as $s_1 \neq s_2$; at least one of them must be semiregular (Figure 23).

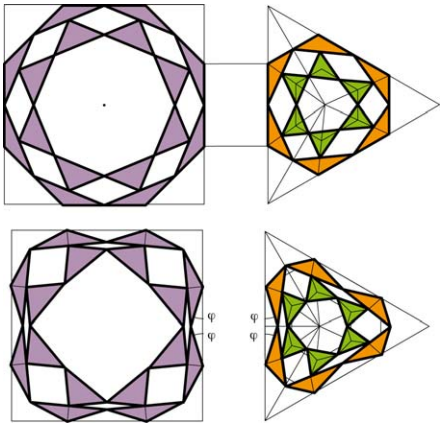

Figure 23 Square and adapted triangular double-ring mechanisms

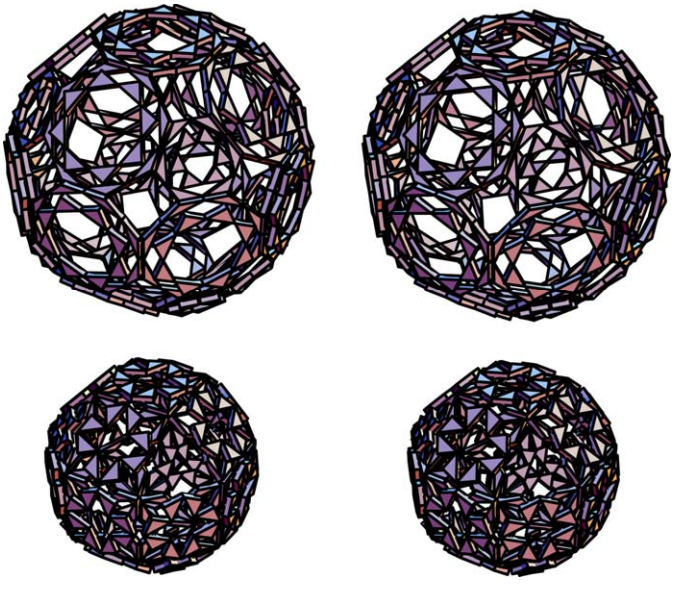

Figure 24 3D picture of a double- ring polyhedral linkage derived from the Miller polyhedron in two phases: maximum and minimum extension

The polyhedral linkage derived from the Miller polyhedron shown in Figure 24 can be divided into two parts, each of them is a linkage (Figure 25 and Figure 26).

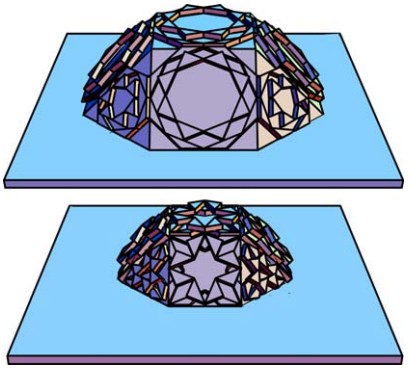

Figure 25: First part of the double-ring (Miller) polyhedral linkage

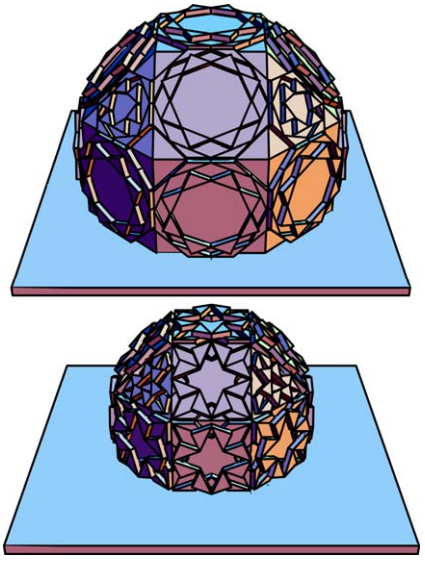

Figure 26 Second part of the double-ring (Miller) polyhedral linkage

11. CONCLUSIONS

It has been demonstrated that it is possible to fill the faces of an irregular polyhedron with irregular double-rings mechanisms which, if interconnected by appropriate gussets yields a robust linkage. Even parts of such double-ring polyhedral linkages are linkages themselves, as the double-ring mechanisms are movable with one degree of freedom. In the cases of Platonian polyhedra, the appropriate double-ring mechanisms are regular and rotor symmetric, which considerably simplifies the synthesis of double-ring polyhedral linkages. These linkages belong to the category of deployable linkages. While deforming from the greatest extension to the minimum extension, their overall size goes back up to fifty percent in some cases.

REFERENCES

[1] H. F. Verheyen. Expandable polyhedral structures based on dipolygonoids. *Proc. Third Conf. on Space Structures*, London, U.K., 88-93, 1984.

[2] C. Hoverman. Reversibly Expandable Double-Curved Truss Structure. *US Patent* 4,942,700, 1990.

[3] K. Wohlhart. New Overconstrained Spheroidal Linkages. *Proc. of the Ninth World Congress on the Theory of Mach. and Mech.,* **1**, 149-154, 1995.

[4] K. Wohlhart. Kinematics and Dynamics of the Fulleroid. *Multibody System Dynamics,* Kluwer Academic Publishers **1**,2, 241-258. 1997.

[5] K. Wohlhart. New Regular Polyhedral Linkages. *Proc. of SYROM,* Bukarest, Rumania, 365-370, 2001.

[6] S.K. Agraval, M. Yim,W. Suh. Polyhedral Single Degree of Freedom Expanding Structures. *Proc. of IEEE,* Seoul, Korea, 3338-3343. 2001.

[7] S. Pelegrino, S.D. Guest. Deployable Structures: Theory and Applications. *Proc. of IUTAM-IASS Symp.* Cambridge, U.K. Kluwer Academic Publishers, London, 1998.

[8] O. Röschel. Möbius Mechanisms. *Proc. of the Symposium Advances in Robot,* ARK 2000, Kluwer Academic Publishers, 375-382.2000.

[9] D. Gagnon-Lachance, C.M. Gosselin. Expandable Polyhedral Mechanisms Based on 1-DOF Faces. *Proceedings of 15^{tth} CISM-IFToMM Symposium on Robot Design, Dynamic and Control* (Romansy), Montreal, Canada,2004.

[10] K. Wohlhart. Polyhedral Zig-Zag Linkages. *Proc. of the Symposium on Advances in Robot Kinematics*, ARK 2004, Kluwer Academic Publishers, 351-360.2004.

[11] F. Kovacs, T. Tarnai, P.D. Fowler, S.D. Guest. A Class of Expandable Polyhedral Structures. *Intern. Journal of Solids and Structures.* **41**,3,4, 1119-1137. 2004.

[12] K. Wohlhart. Cupola Linkages. *Proc. of the 12th World Congress on the Theory of Mach. and Mech.,* Besancon, France, 319-324. 2007.

[13] K. Wohlhart. Double Chain Mechanisms. *Proc. of the IUTAMM-IASS. Symposium on Deployable Structures: Theory and Applications.* Kluwer Academic Publishers, 457-466. 2000.

IAK 2008
Conference on Interdisciplinary Applications of Kinematics
A. Kecskeméthy, V. Potkonjak and A. Müller (eds.)
Lima, Peru, 9–11 January 2008

ROBOTIC HANDWRITING: WHY AND HOW?

Veljko Potkonjak*

*Faculty of Electrical Engineering
University of Belgrade, Bulevar kralja Aleksandra 73, 11000 Belgrade, Serbia
e-mail: potkonjak@yahoo.com

Keywords: Handwriting, Man-machine analogy, Human-like motion, Redundancy resolution, Robot fatigue, Humanoid.

Abstract. *Handwriting has always been considered an important human task, and accordingly it attracted attention of researchers working in biomechanics, physiology, and related fields. There exist a number of studies on this matter. This paper considers human-machine analogy and relates robots with handwriting. The work is twofold: it improves the knowledge in biomechanics of handwriting, and introduces some new concepts in robot control. The idea is to find the biomechanical principles humans apply when resolving kinematic redundancy, express the principles by means of appropriate mathematical models, and then implement them in robots. This is a step forward in generation of human-like motion of robots. Two approaches to redundancy resolution are described: (i) "Distributed Positioning" (DP) which is based on a model appropriate to represent the arm motion in the absence of fatigue, and (ii) "Robot Fatigue" approach, where robot movements similar to the movements of a human arm under muscle fatigue are generated. Both approaches are applied to a redundant anthropomorphic robot arm performing handwriting. The simulation study includes the issues of legibility and inclination of handwriting. The results demonstrate the suitability and effectiveness of both approaches.*

1 INTRODUCTION

It was only recently when humanoid robots were finally recognized as the main direction in the entire work on robotics [1]. One may say that the idea of robots came out from a human desire to create a copy of oneself. This "childish" need was followed by work of craftsmen and engineers who, step by step, starting from toys and dolls, developed anthropomorphic devices (in sixties and seventies) which were technologically sophisticated, scientifically based, and even applicable [2 - 4]. These walking machines represented the true start of robotic science. Industrial potentials of robots turned the focus of research to practical problems of automation. It took researchers and manufacturers a long time to solve so many different problems in industry. The accumulated knowledge and experience, the technology growth, and the saturation in industrial robotics, allowed the robotic community to recognize the service robots and especially humanoid robots as new and profitable directions of work. Recent results show that this was a prospective idea.

Since humanoid robots are expected in services, home works, and other activities that understand close cooperation with humans, it was necessary to supply them with the ability to move in a human-like fashion, to communicate in a human-like manner, and to feature human-like intelligence [1]. The first ability, being the topic of this article, required an extensive study of biomechanics and human-robot analogy. This is how we came to handwriting - a task that seemed to be appropriate only for humans. So, we now pose a crucial question: ***what robots have to do with handwriting***? There are a few answers. Some of them concern just robotics, and we start with them. Handwriting, being a typical human motion, is a highly demanding task regarding kinematics and dynamics. It involves a redundant number of joints (degrees of freedom - DOF). So, handwriting is seen as a "perfect test" for humanoids and even industrial robots. There is also a possibility to improve robot control by learning from humans. Human handwriting engages different levels of motion control: learned patterns (with all associated problems), on-line tracking, etc. By studying biomechanics of handwriting, one can learn about the control concepts, skill acquiring, redundancy resolution, etc. So, perhaps robots will never have to write by hand, but the study of this possibility is still very useful. However, the statement "*never*" should be used conditionally – if humanoids continue to improve their human-likeness, the true robot handwriting might become reality.

The other answer to the dilemma about robots and handwriting concerns biomechanics of human handwriting. The mathematical approaches derived to describe robot kinematics and dynamics could be used to improve models of human handwriting, thus leading to new results. In addition, robotic devices could be developed for diagnostics and rehabilitation of malfunctions in finger-hand-arm coordination.

This article highlights some problems in ***robotic handwriting***, trying to keep a ballance between pure robotics and biomechanics.

2 HANDWRITING: FROM HUMAN TO ROBOT

Handwriting was considered an important human task, and accordingly it attracted attention of researchers working in biomechanics, physiology, and related fields. There exist a number of studies on this matter. Since the majority of them are not of direct interest to our work in robotics, we simply refer to web site *http://www.psychomot.ups-tlse.fr/Ecriture.rtf*, where an extensive listing of such studies may be found, and to paper [5] where relevant biomechanics results have been explained. The work of Potkonjak and his associates [6, 7, 5] was the first to relate the

robot with handwriting. The work was two-fold: it improved the knowledge in biomechanics of handwriting, and introduced some new concepts in robot control. The idea was to find the biomechanical principles humans apply when resolving redundancy, and to implement these principles in robots. Robotic background for this work was found in the concept of micro-macro manipulation [8].

In [9 - 12], the concept of distributed positioning (DP) was proposed to resolve redundancy and improve robot kinematic and dynamic performances. It suggested separation of required motion into a smooth global and fast local motion. These components should be distributed to a redundant number of joints in accordance with their inertial properties: high-inertia joints should take care of smooth global motion while low-inertia redundancy is engaged to solve highly accelerated local motion. The idea was to enable massive industrial robots to perform fast and precise manipulation. Papers [6, 7] introduced handwriting as a test-motion for checking the efficiency of the DP concept. The study [5] was closer to biomechanics. It considered an anthropomorphic arm engaged in handwriting. Due to a higher degree of redundancy, the DP concept could not resolve it completely. The pseudoinverse (optimization) was needed to solve the wrist motion. The obtained results related some important characteristics of handwriting: legibility, inclination of letters, and engagement of fingers (fingers were critical due to relatively quick fatiguing). It was shown that for a given level of legibility, there existed an optimal inclination that minimized the engagement of fingers.

Lately, the human-robot analogy led to the study of the behavior of a "fatigued robot". The reason for this was the fact that humans use their redundancy to avoid, or at least delay, the fatigue problems. When feeling fatigue in some joint, a human reconfigures himself by engaging other joints. So, the exhausted joint is given a chance to rest. This reconfiguration does not compromise the task execution. The idea was to apply the same principle to robots when overloaded. The next benefit from research in fatigue problems is the possibility to achieve some human-like communication. The mentioned reconfiguration, which takes place with a fatigued human, can be observed as it represents a message sent to the surrounding. We wish the robot to behave in the same manner so that we could recognize when it is overloaded. These problems have been elaborated in [13 - 18]. The appropriate mathematical models were derived. The biological background – description of fatigued muscle behavior – was found in [19 – 20].

3 ROBOT ARM KINEMATICS AND DYNAMICS

A robot arm with n DOF is described by means of n joint coordinates (internal or configuration coordinates) forming the configuration vector $\mathbf{q} = [q_1 \dots q_n]^T$. From the task point of view, one is concerned with the end-effector motion described by means of external coordinates $\mathbf{X} = [x\ y\ z\ \theta\ \varphi\ \psi]^T$, where x, y, and z are Cartesian coordinates, and θ, φ, and ψ are orientation angles (yaw, pitch and roll respectively). Another important concept is the operational space. It is a subset of external positions, containing those external coordinates which are responsible for the execution of a given task. Let the operational vector be denoted by $\mathbf{x}$ and has the dimension of $m \le 6$.

Kinematic model understands the relation between configuration and operational space. In its first-order and second-order forms, the model is

$$\dot{\mathbf{x}} = \mathbf{J}(\mathbf{q})\dot{\mathbf{q}}\ ;\ \ddot{\mathbf{x}} = \mathbf{J}(\mathbf{q})\ddot{\mathbf{q}} + \mathbf{K}(\mathbf{q}, \dot{\mathbf{q}})\ , \tag{1}$$

where $\mathbf{J} = \partial \mathbf{x} / \partial \mathbf{q}$ is the Jacobian matrix of dimension $m \times n$ and $\mathbf{K} = \partial^2 \mathbf{x} / \partial \mathbf{q}^2 \, \dot{\mathbf{q}}^2$ is the $m \times 1$ adjoint vector. Redundancy resolution understands the so-called inverse kinematics, i.e., calculation of $\mathbf{q}$ for given $\mathbf{x}$. If $m = n$, the system is nonredundant and the unique solution is possible. If $m < n$, the system is redundant and there exists an infinite number of solutions of the inverse kinematics, meaning that different configuration motions can produce the same operational motion. If one solution is to be selected, then additional requirements, which will "employ" the redundancy, has to be imposed.

A redundant arm usually has a heavy part consisting of *m* joints, which is called the "nonredundant basic configuration". The rest of the arm (*n*-*m* joints) constitutes the redundancy.

Dynamics of the arm – the mechanical part plus second-order actuators – is described by the well-known model

$$\hat{\mathbf{H}}(\mathbf{q})\ddot{\mathbf{q}} + \hat{\mathbf{h}}(\mathbf{q}, \dot{\mathbf{q}}) = \mathbf{u} \tag{2}$$

where $\mathbf{u}$ is the vector of the control inputs, $\hat{\mathbf{H}}$ is the inertial matrix, and $\hat{\mathbf{h}}$ takes care of gravity and velocity-dependent effects. Dynamic model is used to simulate the system behavior.

4 MODELING HANDWRITING SINERGY – DP CONCEPT

4.1 Principles and mathematics

DP is formulated in analogy with human behavior and is intended to model a robot arm involved in fast manipulation. The required robot task, end-effector operational motion $\mathbf{x}(t)$ of dimension *m*, is assumed to have m_a highly accelerated elements. These elements form the subvector $\mathbf{x}_1(t)$. The other elements are smooth (subvector $\mathbf{x}_2(t)$). Now, $\mathbf{x} = [\mathbf{x}_1, \mathbf{x}_2]^T$. We suppose a situation where the massive basic nonredundant configuration (vector $\mathbf{q}_b$ of dimension *m*) cannot solve the task due to the presence of accelerations. DP concept resolves this problem.

Basic nonredundant configuration (*m*-dimensional $\mathbf{q}_b$) is supplemented by a low-inertia redundancy ($\mathbf{q}_r$ of dimension n_r). The entire configuration is now $\mathbf{q} = [\mathbf{q}_b, \mathbf{q}_r]^T$, and has dimension of $n = m + n_r$.

Accelerated motion $\mathbf{x}_1(t)$ is separated in two components: a smooth component $\overline{\mathbf{x}}_1(t)$ and a highly accelerated component $\widetilde{\mathbf{x}}_1(t)$; thus $\mathbf{x}_1 = \overline{\mathbf{x}}_1 + \widetilde{\mathbf{x}}_1$. Some suitable smoothing method is to be applied (a low-pass filter could be used to make this separation). The "basic operational motion" is now defined to be the motion that contains the smoothed component $\overline{\mathbf{x}}_1(t)$ and the subvector $\mathbf{x}_2$ (being already smooth): $\mathbf{x}_b = [\overline{\mathbf{x}}_1, \mathbf{x}_2]^T$. The basic nonredundant configuration $\mathbf{q}_b$ is capable of solving the motion $\mathbf{x}_b$. Mathematically, the solution for $\mathbf{q}_b(t)$ involves the inverse of a nonredundant quadratic ($m \times m$) Jacobian. This represents the *first step* in DP concept.

The redundancy is now forced to solve the high accelerations $\widetilde{\mathbf{x}}_1(t)$. The necessary condition (regarding dimensions) is $n_r \geq m_a$. In the original concept, equality held ($n_r = m_a$) and the unique solution for $\mathbf{q}_r(t)$ was obtained [9 - 12]. This constituted the *second step* in resolving the inverse kinematics. Thus, the entire configura-

tion motion $\mathbf{q}(t)$ was found. Besides the industrial tasks the concepts was checked on the handwriting example [6, 7]. The idea for a handwriting test-task follows the fact that letters require high accelerations and a human solves them by distributing the pencil motion between the massive arm and the low-inertia fingers.

When the focus was moved from industrial robots to humans and humanoids, it was recognized that the wrist joint played an essential role in handwriting. Wrist allows long-term fast writing by reducing the involvement of fingers that are precise but quick fatiguing. The wrist is responsible for inclination of letters, often present with humans. Introduction of the wrist increases the entire degree of redundancy, causing $n_r > m_a$. The *second step* now cannot be performed as described above. The *first step* reduces the redundancy degree from n_r to $n_r - m_a$ but does not eliminate it completely. So, the *second step* needs an additional condition and it is always some optimality criterion. Among different options presented in the literature, we select minimization of finger involvement. This comes out from the fact that fingers can move very precisely but cannot stand long-term fast movement. To measure the finger involvement, an integral criterion was suggested [5]: *IKI* – integral kinematic involvement, being the sum of amplitudes of fingers motions. Some other reasonable criteria (reducing energy or motors temperatures) produced results rather comparable with *IKI* ones [18].

4.2 Example

In a simplified (but still representative) example we consider a planar arm consisting of the shoulder q_1, the elbow q_2, and the wrist q_3 (Fig. 1). In writing, the fingers work together to produce two translations as shown in Fig. 2. Hence, with the robot arm, true fingers are substituted by two linear joints (q_4 and q_5 in Fig. 1). The motion ranges for such "sliding fingers" are $\Delta_4 = q_{4\max} - q_{4\min} = 0.05m$ and $\Delta_5 = q_{5\max} - q_{5\min} = 0.05m$. The complete set of numerical parameters used in the example is not seen important to understand the method and the key results.

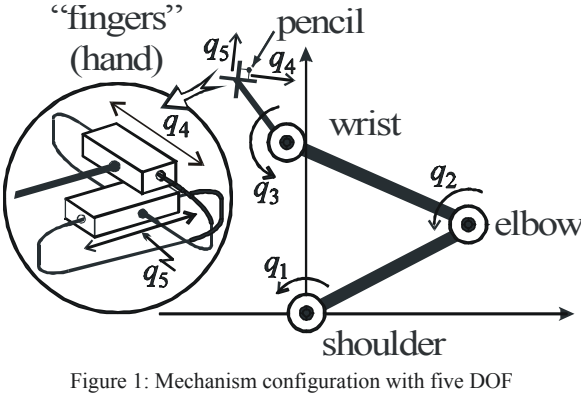

Figure 1: Mechanism configuration with five DOF

The task consists in writing a prescribed sequence of letters shown by solid lines in Fig. 3. Under (a), an *x*-*y* representation is presented (*x* and *y* being operational coordinates), while (b) and (c) show the time histories $x(t)$ and $y(t)$. This reference sequence is set so as to be close to real letters and, at the same time, to be easy to describe mathematically (cycloids, circles, and straight lines have been used).

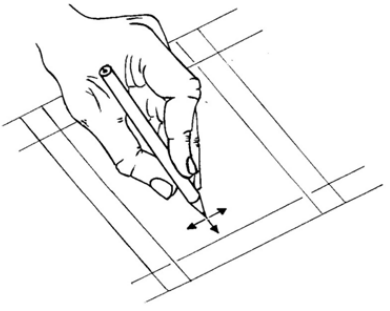

Figure 2: Coordinated motion of fingers produces two translations

For this example, it holds that $\mathbf{x} = \mathbf{x}_1 = [x, y]^T$, $m = m_a = 2$, and $\mathbf{x}_2$ does not exist. Smoothing understands separation: $x = \bar{x} + \tilde{x}$, $y = \bar{y} + \tilde{y}$. The results, smooth components $\bar{x}(t)$ and $\bar{y}(t)$, are shown in Fig. 3 by dashed lines. The basic operational motion contains these smooth components: $\mathbf{x}_b = \bar{\mathbf{x}}_1 = [\bar{x}, \bar{y}]^T$.

Mechanism configuration is separated in two functional parts. Shoulder and elbow constitute the nonredundant basic configuration: $\mathbf{q}_b = [q_1, q_2]^T$, $m = 2$. The wrist and the two linear "fingers" represent the redundancy: $\mathbf{q}_r = [q_3, q_4, q_5]^T$, $n_r = 3$.

The basic configuration $\mathbf{q}_b$ cannot handle the original task $\mathbf{x}(t) = [x(t), y(t)]^T$ due to the presence of high accelerations. The *first step* of DP concept is to force the basic configuration to solve the smooth motion $\mathbf{x}_b = [\bar{x}, \bar{y}]^T$. In order to get the maximum from the configuration, minimum smoothing (by using the "sliding window" method) is performed, i.e., just to the level that configuration can handle.

Once the motion $\mathbf{q}_b(t)$ is found, we start the *second step* in order to solve for the redundancy $\mathbf{q}_r$. Since $n_r = 3 > m_a = 2$, *step two* still faces the problem of redundant DOF: two operational motions, $\tilde{\mathbf{x}}_1 = [\tilde{x}, \tilde{y}]^T$, are to be solved by using three configuration coordinates, $\mathbf{q}_r = [q_3, q_4, q_5]^T$. In order to get a unique solution of the inverse kinematics, we introduce an optimality criterion by trying to minimize the involvement of fingers. The criterion *IKI* is applied. Solid lines in Fig. 4 shows the results, time histories $\mathbf{q}_r(t)$. One can observe that motions of fingers (q_4 and q_5) violate the ranges Δ_4 and Δ_5 (during writing letters *d* and *j*), meaning that the found solution is not possible to realize. Any attempt to do this would lead to incorrect shape of letters and reduced legibility. This is the consequence of the fact that wrist is not of great help when letters are strictly vertical, and accordingly, too much is required from the fingers (they are not long enough). In order to allow the wrist to help more efficiently, we modify the task (i.e., the reference) by inclining the letters. Example of inclined writing (for the angle $\alpha = 30^0$) is shown in Fig. 5. With the inclination, the engagement of the wrist (q_3) increases and the engagement of the fingers (q_4 and q_5) reduces. This is obvious from Fig. 4 (different kinds of line are used for different inclination). After an inclination of 24^0, translation q_4 falls into the allowable region Δ_4, while, after 34^0, the other translation q_5 falls into Δ_5. This means that any sequence, inclined for 34^0 or more, can be written "ideally".

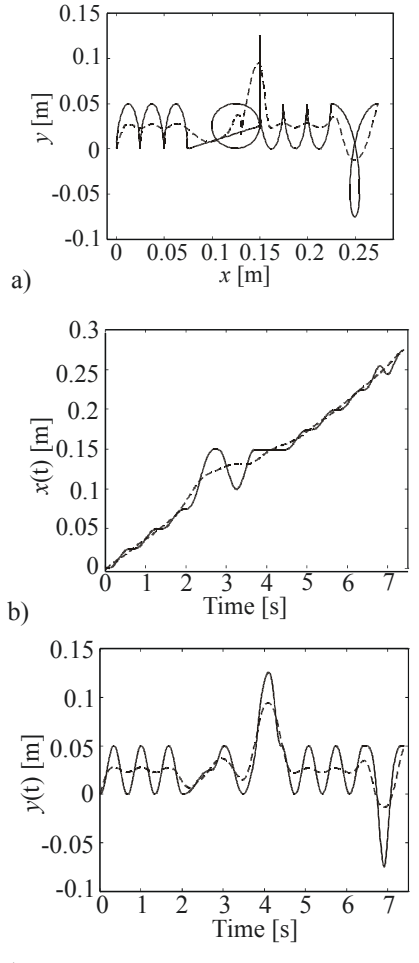

Figure 3: Definition of the task: (a) sequence of letters; (b), (c) time histories of operational coordinates. The solid lines show the prescribed motion, and the dashed lines show the smooth components

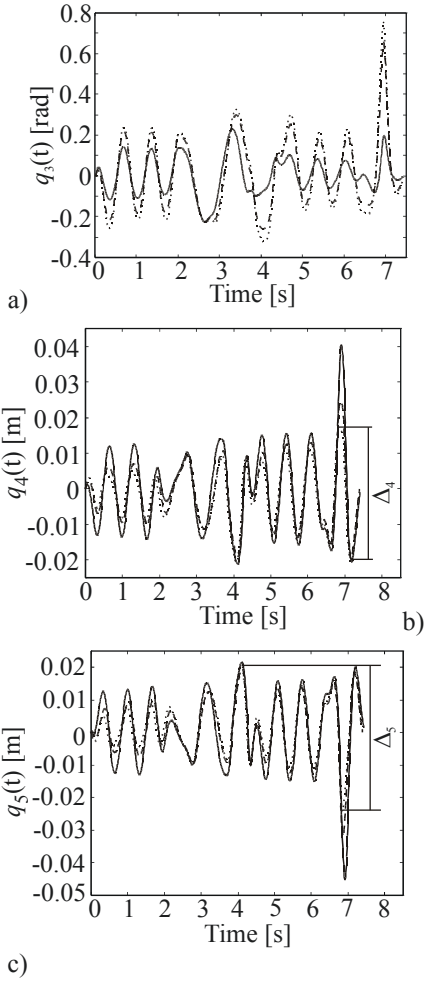

Figure 4: Solution to the motion of the redundancy (the solid lines stand for strictly vertical letters, the dashed lines for the inclined writing $\alpha=24^0$, and the dotted lines for the inclination of $\alpha=34^0$

After introducing inclination, we make a step forward and note a general fact that humans often do not insist on ideal execution of a given task. In the topical example, handwriting, this means that some deformed shape of letters is acceptable provided they are legible. This relaxed condition opens the possibility for some additional optimization. Here, we prescribe some level of legibility and try to further reduce the involvement of fingers (*IKI* criterion). Legibility of a sequence of letters is defined on the basis of the mean square deviation from the ideal sequence. If e is the mean square error, then legibility is its normalized value, $L_e = (e_{\max} - e)/(e_{\max} - e_{\min})$, being in the interval $L_e \in [0,1]$. For the ideal sequence (i.e., the reference), it holds $e = e_{\min} = 0$ and $L_e = 1$. The values $e = e_{\max} = 0.0163$ and $L_e = 0$ stand for the thresh-

old – the lowest legibility still worth considering. Let us note that [5] used a modified definition based on a function that introduced subjective feeling of legibility.

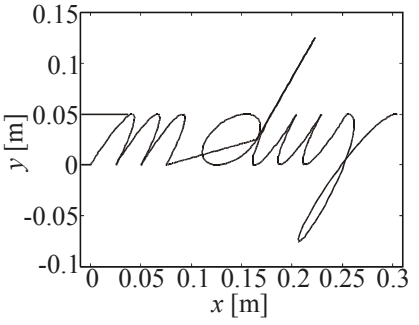

Figure 5: Inclined letters ($\alpha = 30^0$)

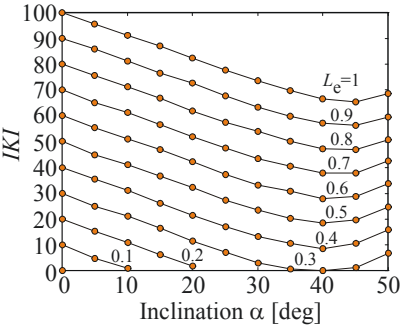

Figure 6: Relation of finger involvement (IKI), inclination of writing (α), and legibility (L_e)

Fig. 6 presents the results; it relates involvement of fingers (*IKI*), inclination (α), and legibility (L_e). Each curve corresponds to some level of legibility L_e and shows how *IKI* depends on inclination angle α. Each curve features a clear minimum. Reducing the legibility, the point of minimum moves slightly to the left (towards smaller inclinations). Observing the diagram, one can conclude that, for any selected level of legibility, there exists an optimal inclination that minimizes the involvement (*IKI*) of fingers (for instance, if legibility is prescribed to be 0.6, the optimal inclination is 40^0, and the corresponding *IKI* is about 28). For other criteria (*IKI* replaced by energy consumption or by motor heating) the diagrams feature similar behavior [18].

4.3 Discussion on application

DP concept shows to be a good model to describe human motion in handwriting. Humans really distribute the prescribed motion to a redundant number of joints in accordance with their inertial characteristics and the muscles potentials. On the other hand, the method is very suitable to be implemented in robots. An interesting issue, left for discussion, is the way of smoothing the accelerated motion. With humans, this is the question of learning. The same principle may be introduced for robots but it opens a complex problem of machine learning. It is expected that smoothing may be successfully solved by using some appropriate low-pass filter (as it was done above). One, however, notes that for on-line applications, the adaptation of the cut-off frequency is a problem that deserves separate discussion.

5 ROBOT FATIGUE

5.1 Principles

If the human arm is submitted to a long-term or heavy work, fatigue will appear. Until the symptoms of fatigue appear, we talk about the REGULAR MOTION. When fatigue in some muscles of the human arm exceeds the threshold level, the arm tends to reconfigure itself and thus disturbs the steady state imposed by the DP concept. On-line RECONFIGURATION is needed since it must be based on the current level of fatigue. Reconfiguration means depressed involvement of the exhausted joint and higher engagement of the others. In this way, the exhausted joint (or joints) is given a

chance to rest. This reconfiguration is an "inner" process, meaning that it does not effect the correct execution of the task. Mathematically speaking, a redundant system has an infinite number of configuration motions for one operational motion, and reconfiguration means the selection of a new configuration from this set.

When a fatigued human changes posture, this can be observed, and thus, reconfiguration represents a message about his state. Surrounding people may react to the message although the task execution is not compromised.

If the heavy-duty task lasts too long, then arm joints, one by one, will become fatigued. After a few reconfigurations, there will be no joint able to help. From this moment, the task execution will not be correct any more. Deviations will appear and we then talk about the DEGENERATION phase. This could be considered as a new message to the surrounding environment.

We try to find models of the described behavior and apply it to both human and robot arms. The biological background – description of fatigued muscle behavior – was found in [19 - 20]. With robots, the motor temperature represents the measure of joint fatigue. The threshold is the temperature that exceeds the allowable level, meaning that the arm is overloaded.

5.2 Mathematics

REGULAR MOTION. Redundancy resolution is based upon the DP concept, along with the request for the maximal comfort. The later follows from the observed behavior of humans [21]. Instead of a low-pass filter used for DP in Section 4, here we directly apply the method of pseudoinverse. To achieve this, the appropriate criterion is introduced:

$$\Omega(\dot{\mathbf{q}}) = 0.5 \cdot \dot{\mathbf{q}}^T \mathbf{W}' \dot{\mathbf{q}} + 0.5 \cdot (\dot{\mathbf{q}} - \dot{\mathbf{q}}_\alpha)^T \mathbf{W}''(\dot{\mathbf{q}} - \dot{\mathbf{q}}_\alpha) \tag{3}$$

where $\mathbf{W}'$ and $\mathbf{W}''$ are $n \times n$ positive-definite symmetric weighing matrices. The first term enables penalization of the motion of some joints relative to others and is used to distribute the joint motions in accordance to DP concept (i.e., to stimulate the motion of low-inertia joints and penalize the motion of high-inertia joints). By changing the weighing matrix $\mathbf{W}'$, this term enables a proper reconfiguration of the robot in accordance with the actual progress of fatigue. The second term is used to maximize the comfort. Comfortable motion of a joint is seen as the motion being near the middle position of the joint range. According to [22], $\dot{\mathbf{q}}_\alpha = -k_\alpha(\partial G(\mathbf{q}) / \partial \mathbf{q})^T$, and to maximize the comfort we define $G(\mathbf{q})$ as a measure of deviation from the middle values [21, 23].

The minimization of the criterion (3) is performed via the method of Lagrange multipliers. The Lagrangean corresponds to the functional (3) and the kinematic constraint (1). The calculation of the configuration velocities $\dot{\mathbf{q}}$ involves the weighed pseudoinverse of the Jacobian matrix (according to [24]):

$$\dot{\mathbf{q}}^* = \mathbf{J}_{\mathbf{W}}^{\#} \dot{\mathbf{X}}^* + (\mathbf{I} - \mathbf{J}_{\mathbf{W}}^{\#} \mathbf{J}) \mathbf{W}^{-1} \mathbf{W}'' \dot{\mathbf{q}}_\alpha , \tag{4}$$

where $\mathbf{W} = \mathbf{W}' + \mathbf{W}''$, and $\mathbf{J}_{\mathbf{W}}^{\#} = \mathbf{W}^{-1}\mathbf{J}^T(\mathbf{J}\mathbf{W}^{-1}\mathbf{J}^T)^{-1}$ is the weighted pseudoinverse of the Jacobian matrix. The sign * is used to indicate that reference motion is in question.

Regarding the control, a PD regulator could be adopted: $u_j = K_{Pj}(q_j^* - q_j) + K_{Vj}(\dot{q}_j^* - \dot{q}_j)$, $j = 1,\ldots,n$, where q_j^* is the reference position, q_j is the

actual position, K_{Pj} and K_{Vj} are position and velocity feedback gains. Applying this control law, the motion $q_j(t), j=1,...,n$ will result, which is expected to track closely the reference $q_j^*(t)$.

RECONFIGURATION. We now look for a mathematical method to force the reconfiguration in accordance with the actual progress of fatigue. With robots, motor temperature Θ_j is the measure of fatigue in joint j. The critical value $\Theta_{j,cr}$ is defined for each motor, limiting the desired motor working mode. It is not a final limit but rather a bound of a desirable region. Above the critical value, the robot joint "feels fatigue". Some appropriate algorithm should force redistribution of engagement in order to relax the exhausted joint. The algorithm introduces the penalty functions into the weighing matrix:

$$\mathbf{W} = \mathrm{diag}[\varphi_1(\Theta_1), \ldots, \varphi_n(\Theta_n)]. \tag{5}$$

"Penalty functions" $\varphi_j(\Theta_j)$ should penalize the exhausted joints and stimulate those that are still "fresh". Mathematically speaking, $\varphi_j(\Theta_j)$ should be constant until Θ_j reaches $\Theta_{j,cr}$, and monotonically increasing above $\Theta_{j,cr}$. In this way, the penalty functions $\varphi_j(\Theta_j)$ will contribute to reduced movement of each joint in which the actual value of fatigue exceeds an assigned critical limit. The choice of a particular penalty function is task dependent. One possibility, used in the simulation study of this article, is a quadratic function:

$$\varphi_j(\Theta_j) = \begin{cases} w_j, & \Theta_j < \Theta_{j,cr} \\ w_j + k_{\varphi,j}(\Theta_j - \Theta_{j,cr})^2, & \Theta_j \geq \Theta_{j,cr} \end{cases}, \tag{6}$$

where the initial weighting factor w_j is a scalar constant, and the coefficient $k_{\varphi,j} > 0$ determines the desired slope of the penalty function.

When feeling fatigue in some joints, the robot will reconfigure itself in the above way. This is done while keeping the required operational trajectory (thus, reconfiguration does not effect the execution of the task). It is expected that the reduced engagement of exhausted joints will give them a chance to rest and go out of the critical working mode. Several reconfigurations may happen, one after the other, as different joints are reaching the critical levels. If the task is not too tough, the robot will finally find a steady state in which it can operate for a longer time (some results that support this expectation are reported in [13 - 15]). To control the robot we still use the PD regulator.

DEGENERATION. If the task imposed on the robot is too demanding, it may happen that, in spite of reconfiguration, the motor temperatures continue to rise. This means that the reconfiguration will delay the fatigue problem but will not eliminate it. To handle this situation, some upper limits for the temperatures (fatigue) are adopted, i.e. $\Theta_{j,\max}$, $j = 1,...n$. These limits indicate the point of entering a dangerous motor working mode. In this situation, further rise of temperature must be prevented regardless of the quality of the output work. This is done by activating a "current limiter". Limiting the motor current, being the source of heating, should stop the rise of tem-

perature. The limiter will allow the current that is smaller than the required value by the factor D, and thus, for joint j it will be:

$$i_j = D_j(\Theta_j) i_j^{req}, \tag{7}$$

where i_j is the actual current and i_j^{req} is the value required by the dynamics of the given task. $D_j(\Theta_j)$ is called the "current-damping factor". It depends on the actual level of temperature (fatigue). In order to efficiently relax the joint in accordance with its fatigue, a decreasing function is adopted:

$$D_j(\Theta_j) = \begin{cases} 1, & \Theta_j \le \Theta_{j,\max} \\ e^{-(\Theta_j - \Theta_{j,\max})}, & \Theta_j > \Theta_{j,\max} \end{cases}. \tag{8}$$

Damping the current will result in insufficient joint torques and accordingly in the degeneration of the actual trajectory. The reference configuration motion $\mathbf{q}^*(t)$ will still come out from the imposed (reference) task trajectory $\mathbf{x}^*(t)$, but the limited joint torques will result in actual motion $\mathbf{q}(t)$ that might be far away from the reference. As a result, the actual task trajectory $\mathbf{x}(t)$ will be considerably degenerated.

Thus, in the third phase, the robot will still “try to do the job”, but since “it is tired”, the results will be unsatisfactory.

For simulation purposes we need a mathematical model that relates the source of thermal energy (i.e. rotor winding current) and the temperatures of the rotor and the housing [13 - 14]. The thermal dynamics model involves the thermal capacities of the rotor and the housing and the transfer of energy, rotor-to-housing and housing-to-ambient. The second-order model (for the j^{th} joint motor) is:

$$T_{rj}\dot{\Theta}_{rj} = Z_{rj} \cdot R_j i_j^2 - (\Theta_{rj} - \Theta_{hj}), \quad T_{hj}\dot{\Theta}_{hj} = \frac{Z_{hj}}{Z_{rj}}(\Theta_{rj} - \Theta_{hj}) - (\Theta_{hj} - \Theta_a), \tag{9}$$

where Θ_{rj} and Θ_{hj} are the rotor and housing temperatures, T_{rj} and T_{hj} are the thermal time constants, Z_{rj} and Z_{hj} are the energy-transfer resistances rotor-to-housing and housing-to-ambient, Θ_a is the ambient temperature, and $R_j i_j^2$ represents the Joule power loss. The time constants influence the slope of the temperature progress while the resistances define the steady state levels. The thermal dynamic model can be reduced to a first-order if appropriate choice of parameters is made. All the relevant effects will be preserved [15 - 17]. The first-order model is:

$$T_j\Theta_j = Z_j R_j i_j^2 - (\Theta_j - \Theta_a). \tag{10}$$

The thermal model, along with the dynamic model of the arm (eq. (2)), enables simulation.

5.3 Example

We consider the robotic arm shown in Fig. 1 in Sec. 4. The task (i.e., the reference) in that example was defined flexible, allowing different inclination of letters. For the present analysis, we set inclination to $\alpha = 20^0$ (as it will be seen in Fig. 10(a)).

Simulation in this work is performed to prove the feasibility of the concept. Thus, the system parameters need not be realistic but rather chosen so as to stress the relevant effects. In addition, a too long simulation should be avoided. Starting from this, we adopted the appropriate values for system parameters.

To show the most interesting simulation effects, we will explore the behavior of joints 4 and 5 ("fingers"), and the overall execution of the task.

Figure 7 shows the behavior of the joint No. 4. Fig. 7(a) presents the progress of motor temperature (joint fatigue Θ_4). Fig. 7(b) presents the variation of joint involvement. As a measure showing how much a particular joint (e.g. the j^{th} one) is involved in the task execution, a variable called "kinematic involvement" – KI_j is introduced. It is calculated for each repetition of the sequence of letters: $KI_j = \int_{T=9s} |\dot{q}_j| dt$, where $T = 9s$ is the time needed to accomplish one sequence. Fig. 7(c) shows the reference motion of the joint, $q_4^*(t)$, and Fig. 7(d) shows its real motion ($q_4(t)$). Figure 8 presents the behavior of the joint No. 5.

Figure 9 shows the error in the task execution. This is the deviation (*DEV*) from the ideal sequence of letters, i.e. from the reference trajectory (x^*, y^*). The error is calculated for each repetition of the sequence and represents the normalized mean square error over the sequence.

Let us discuss the simulation results.

Phase 1 – REGULAR MOTION – lasts for $t \in [0\ ,\ t_1 \approx 80s]$. Phase 1 starts immediately and lasts until the fatigue in some joint (motor temperature Θ_j) exceeds the assigned critical level $\Theta_{j,cr}$. In this phase the continuous progress of fatigue in both joints (4 and 5) is monitored (diagrams 7(a) and 8(a)). The joint involvements are at a constant level (Figs. 7(b) and 8(b)) meaning a steady situation in the distribution of the task to robot joints. This steady distribution is supported by the diagrams 7(c),(d) and 8(c),(d), where the oscillations with constant magnitudes can be observed. In this phase, the error of writing (*DEV* in Fig.9) is rather small. Phase 1 ends at about $t_1 = 80s$ when joint 5 feels fatigue, i.e. the motor temperature exceeds the critical level: $\Theta_5 \geq \Theta_{5,cr}$ (see Fig. 8(a)).

Phase 2 – RECONFIGURATION – lasts for $t \in [t_1 \approx 80s\ ,\ t_2 \approx 190s]$. When joint 5 feels fatigue**,** phase 2 begins. Reconfiguration starts since the penalty function in joint 5 forces its reduced engagement. This reduction appears as a drop in the involvement KI_5 at $t_1 = 80s$ (Fig. 8(b)). This is also obvious in the diagrams of Fig. 8(c),(d) where the magnitudes of oscillations decrease. Since the other joints have to help, one may observe the increased involvement KI_4 (Fig. 7(b)). This higher engagement of joint 4 can be recognized in Figs. 7(c),(d) as increased density of oscillation diagrams. The joint 4 is not the only one to help. So, if behavior of joint 3 was depicted, it would feature increased involvement as well.

During the phase 2, at about $t' = 160s$, the temperature in joint 4 reaches the critical level: $\Theta_4 \geq \Theta_{4,cr}$ (see Fig. 7(a)). At that moment, the penalty function starts to depress the engagement of joint 4, thus causing the drop of involvement KI_4, as it is obvious from Fig. 7(b).

In spite of reconfiguration, the temperatures Θ_4 and Θ_5 continue to progress. This is due to a highly demanding task (relative to system parameters).

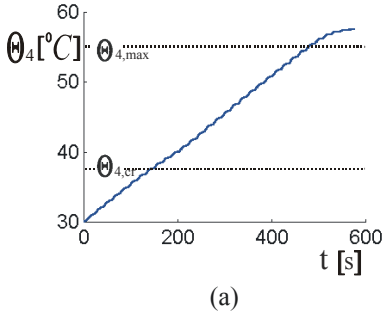

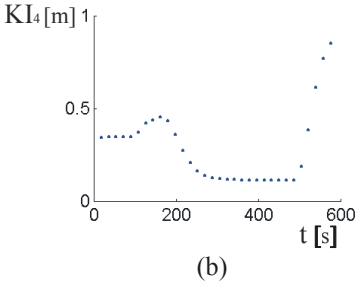

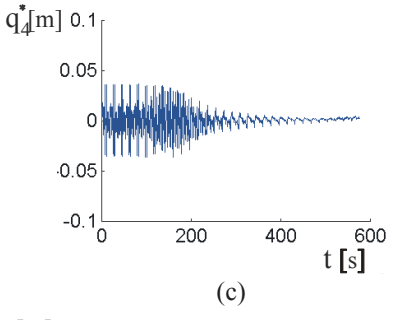

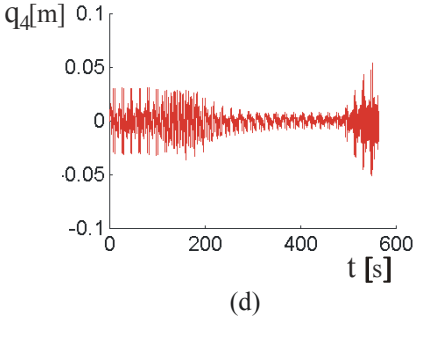

Figure 7: Behavior of joint No. 4: (a) joint fatigue $\Theta_4(t)$, (b) joint involvement $KI_4(t)$, (c) reference motion $q_4^*(t)$, and (d) realized motion $q_4(t)$

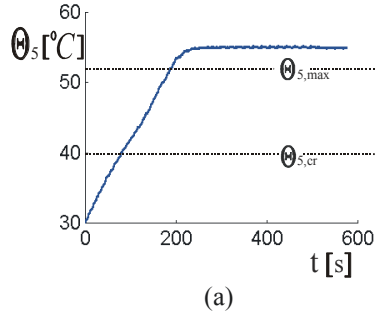

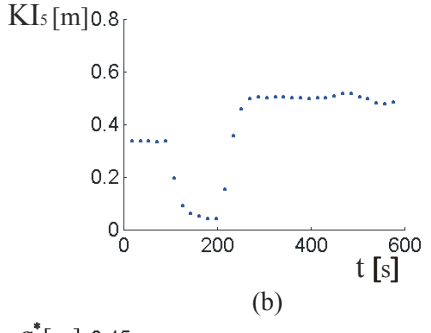

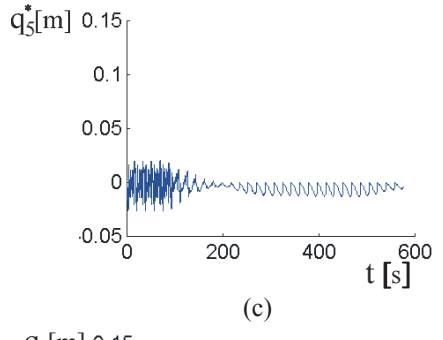

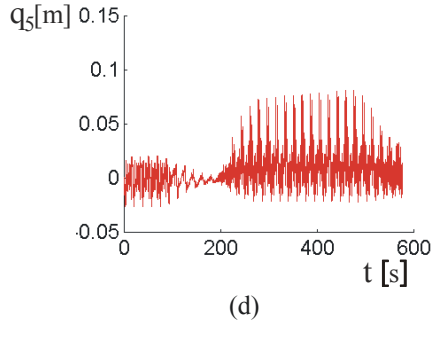

Figure 8: Behavior of joint No. 5: (a) joint fatigue $\Theta_5(t)$, (b) joint involvement $KI_5(t)$, (c) reference motion $q_5^*(t)$, and (d) realized motion $q_5(t)$

During the phase 2, the task error *DEV* is slightly increased (Fig. 9). The small rise od writing error means that the tracking of the reference sequence is still good.

Phase 2 ends at about $t_2 = 190s$, when the fatigue in joint 5 exceeds the next limit (upper level): $\Theta_5 \geq \Theta_{5,\max}$.

Phase 3 – DEGENERATION – lasts for $t > t_2 \approx 190s$**.** When joint 5 excedes $\Theta_{5,\max}$, phase 3 begins. The current limiter in the joint activates, reducing the joint drive. The reference joint motion (shown in Fig. 8(c)) still comes out from inverse-kinematics calculation, expressing what the robot intends to do. The slightly increased magnitudes in the reference express the attempt of joint 5 to help joint 4 a bit (according to the simultaneous action of the two penalty functions, 4 and 5). This means that the robot still intends to follow reconfiguration procedure and do the job well, i.e. to write perfectly. However, the reduced joint drive will make the joint 5 less controllable, and hence, the magnitude of realized motion in the joint will rise considerably (as seen in Fig. 8(d)). So, tracking is not good any more. The kinematic involvement of joint 5 (KI_5 in Fig. 8(b)) will rise rapidly. However, one should note that this rise is not forced by a strong drive, but contrary, caused by insufficient motor current and joint drive. The fatigue Θ_5 will stop rising and will reach the steady state (see Fig. 8(a)).

The joint 4, still strongly driven, will continue to track the reference motion (obvious from comparing the diagrams of Fig. 7(c),(d)), and consequently, joint fatigue will continue to rise (Fig. 7(a)). At about $t'' = 480s$, joint fatigue exceeds the upper level: $\Theta_4 \geq \Theta_{4,\max}$. The current limiter in the joint activates and the drive reduction causes lower controllability. So, the joint will no more track the reference, and oscillations will rise (compare diagrams of Fig. 7(c),(d)). This increased kinematic involvement (obvious in Fig. 7(b) as well), caused by insufficient drive, will not contribute to motor heating. The reduced current will allow the temperature Θ_4 to reach the steady state (as shown in Fig. 7(a)).

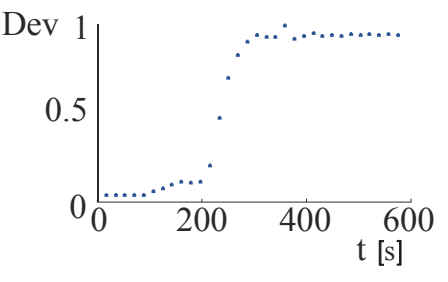

Figure 9: Error in task execution: deviation (*DEV*) of realized letters from the reference (ideal) sequence.

During phase 3, the error in writing rapidly increases (see Fig.9), which means that the quality of task execution is becoming very low (that is why we talk about degeneration).

The deviation of actual letters from the reference pattern deserves more attention. Fig. 10 shows how the realized letters gradually degenerate from the reference sequence. As mentioned above, during the phases 1 and 2, the writing error was rather small. However, in phase 3 the trajectory rapidly degenerates. Figure 10(b)-(d) presents several realized sequences, all belonging to phase 3. Compared with the reference (ideal) sequence shown in Fig. 10(a), gradual degeneration is obvious. This is handwriting of a tired robot.

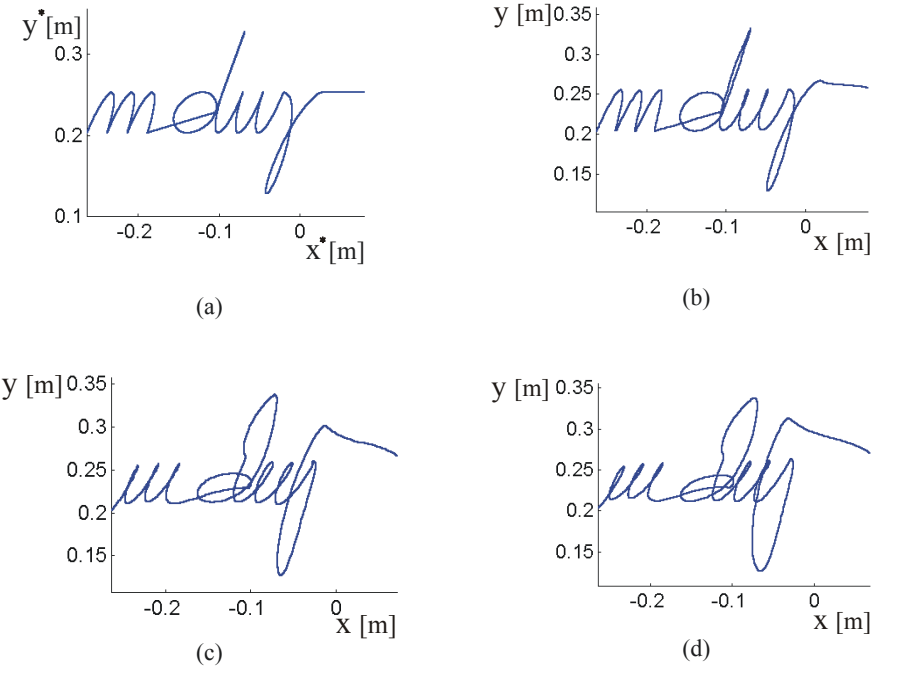

Figure: 10 Gradual degeneration of writing. (a) Reference sequence. (b)-(d) Degenerated sequences are recorded for the following repetitions: (b) 12th forward sequence, time: $198 \le t \le 207$, (c) 14th forward sequence, time: $234 \le t \le 243$, (d) 22nd forward sequence, time: $378 \le t \le 387$.

6 CONCLUSIONS

A robotic arm engaged in handwriting was considered. The work was two-fold: to improve the knowledge in biomechanics of handwriting, and to introduce some new concepts in robot control. The biomechanical principles humans apply when resolving kinematic redundancy were found and mathematically modeled in order to be applicable to robot control. This contributed to the human-like motion of robots. The other aspect concerns humans and opens the possibility to apply robots in diagnostics and rehabilitation of malfunctions in finger-hand-arm coordination.

Two approaches were proposed to model and control a human-like motion of the robot arm in a writing task.

The first approach, based on the concept of distributed positioning (DP), was suggested as a good model of arm motion in the phase where fatigue does not appear. The prescribed motion of the end-effector was distributed to a redundant number of arm joints in accordance to their acceleration capabilities. The justification of the usual inclination of letters was presented and the relation between the inclination, legibility, and the fingers' involvement was discussed. It was found that for some prescribed level of legibility, the optimal inclination existed.

For the phase where fatigue appears, the concept of robot fatigue was proposed. It emulated the progress of biological fatigue. Penalty functions were utilized to ensure redistribu-

tion of the joint involvement when some of them "felt" fatigue. The arm automatically adapted to the situation, taking a new posture giving the exhausted joint the chance to rest while engaging more the other joints. The three phases of task execution, namely:

- *regular motion*, before the symptoms of fatigue;
- *reconfiguration,* after some joints feel fatigue; and
- *degeneration,* caused by the long and hard work that makes all joints tired,

were discussed. The human-like reaction of a fatigued robot could be observed (thus being a kind of a message), giving a chance to prevent undesired consequences.

REFERENCES

[1] T. Fukuda, R. Michelini, V. Potkonjak, S. Tzafestas, K. Valavanis, M. Vukobratovic, *How Far Away is 'Artificial Man',* IEEE Robotics and Automation Magazine*, March 2001, 66-73, 2001.*

[2] M. Vukobratovic, D. Juricic, Contribution to the Synthesis of Biped Gait, *IEEE Trans. on Biomedical Engineering*, Vol. 16, No. 2, 1969.

[3] D. Juricic, M. Vukobratovic, Mathematical Modelling of a Bipedal Walking System, *ASME Publ. 72-WA/BHF-13*, 1972.

[4] M. Vukobratovic, D. Hristic, Z. Stojiljkovic, Development of Active Anthropomorphic Exoskeleton, *Medical and Biological Engineering*, Vol. 12, No. 1, 1974.

[5] V. Potkonjak, M. Popovic, M. Lazarevic, J. Sinanovic, Redundancy Problem in Writing: From Human to Anthropomorphic Robot Arm, *IEEE Transactions on SMC*, Part B: Cybernetics, Vol. 28, No. 6, 790-805, Dec. 1998.

[6] V. Potkonjak, A. Krstulovic, Mathematical Modelling of a Redundant Antropomorphic Arm, *Robotics and Autonomous Systems* (Elsevier) 9, 165-170, 1992.

[7] V. Potkonjak, A. Krstulovic, A., Simulation of a Redundant Antropomorphic Arm, *Robotics and Autonomous Systems* (Elsevier) 9, 171-179, 1992.

[8] J.K. Salisbury, J.D. Abramowitz, Design and Control of a Redundant Mechanisam for Small Motion, Proc. IEEE Intl. Conf. Robotics and Automation, 323-328, St. Louis, MO, March 1985.

[9] V. Potkonjak, Distributed Positioning for Redundant Robotic Systems, *Robotica*, Vol.8, No.1, 61-67, (1990).

[10] V. Potkonjak, A. Krstulovic, Contribution to the Kinematics and Dynamics of Redundant Robots Via Distributed Positioning, *Journal of Intelligent and Robotic Systems* (Kluwer Academic Publishers) 5, 229-239, 1992.

[11] V. Potkonjak, G. Djordjevic, C. Milosavljevic, D. Antic, D. Popovic, Kinematic Redundancy and Sensor Redundancy for Enhancement of Robot Tracking Performances, *Journal of Intelligent and Robotic Systems*, 15, 263-289, 1996.

[12] V. Potkonjak, G. Djordjevic, C. Milosavljevic, D. Antic., Design of Tactical and Executive Level of Redundant Robot Control Via Distributed Positioning, *International Jornal of Robotics & Automation* (IASTED), Vol. 11, Issue 3, 102-110, 1996.

[13] V. Potkonjak, S. Tzafestas, D. Kostic, G. Djordjevic, Human-Like Behavior of Robot Arms: General Considerations and the Handwriting Task, Part I: Mathematical De-

scription of Human-Like Motion: Distributed Positioning and Virtual Fatigue, *Robotics and CIM* (Elsevier) 17, 305-315, 2001.

[14] V. Potkonjak, D. Kostic, S. Tzafestas, M. Popovic, M. Lazarevic, G. Djordjevic, Human-Like Behavior of Robot Arms: General Considerations and the Handwriting Task, Part II: The Robot Arm in Handwriting, *Robotics and CIM* 17, 317-327, 2001.

[15] V. Potkonjak, D. Kostic, M. Rasic, G. Djordjevic, Motion in Human and Machine: A Virtual Fatigue Approach, *IEEE Trans. SMC* Part A: Systems and Humans , Vol. 32, No. 5, 582-595, September 2002.

[16] V. Potkonjak, S. Tzafestas, J. Radojicic, Modeling Robot "Psycho-Physical" State and Reactions – A New Option in Human-Robot Communication, Part 1: Concept and Background, *Journal of Intelligent and Robotic Systems*, Vol. 35, No. 4, 339-352, Oct. 2002.

[17] V. Potkonjak, S. Tzafestas, J. Radojicic, D. Kostic, Modeling Robot "Psycho-Physical" State and Reactions – A New Option in Human-Robot Communication, Part 2: Modeling and Simulation, *Journal of Intelligent and Robotic Systems*, Vol. 35, No. 4, 353-364, Oct. 2002.

[18] V. Potkonjak, S. Tzafestas, D. Kostic, G. Djordjevic, M. Rasic, Illustrating man-machine motion analogy in robotics - The handwriting problem, *IEEE Robotics & Automation Magazine*, Vol. 10, No. 1, 35-46, March 2003.

[19] L. Vodovnik, S. Rebersek, *Improvements in Voluntary Control of Paretic Muscles Due to Electrical Stimulatio; Electrical Stimulation as a Rehabilitation Method to Improve Abnormal Locomotion and Manipulation*, Final Report, pp. 64-78, Ljubljana 1975.

[20] Y. Giat, J. Mizrahi, M. Levy, A Model of Fatigue and Recovery in Paraplegic's Quadriceps Muscle Subjected to Intermittent FES, *Journal of Biomechanical Engineering*, Vol. 118, August 1996.

[21] H. Cruse, E. Wischmeyer, M. Bruwer, P. Brockfield, A. Dress, On the Cost Functions for the Control of the Human Arm Movement, *Biological Cybernetics*, No. 62, 519-528, 1990.

[22] A. Liégeois, Automatic Supervisory Control of the Configuration and Behavior of Multibody Mechanisms, *IEEE Transactions on Systems, Men, and Cybernetics*, Vol. 7, No. 12, 868-871, December 1977.

[23] T.F. Chan, R.V. Dubey, A Weighted Least-Norm Solution Based Scheme for Avoiding Joint Limits for Redundant Joint Manipulators, *IEEE Transactions on Robotics and Automation*, Vol. 11, No. 2, 286-292, April 1995.

[24] D.E. Whitney, The Mathematics of Coordinated Control of Prosthetic Arms and Manipulators, *Transactions of the ASME, Journal of Dyn. Syst., Meas. and Control*, Vol. 94, No. 4, December 1972.

IAK 2008
Conference on Interdisciplinary Applications of Kinematics
A. Kecskeméthy, V. Potkonjak and A. Müller (eds.)
Lima, Peru, 9–11 January 2008

A KINEMATICS BASED METHODOLOGY FOR THE DESIGN OF GANGWAYS AND COUPLER HOUSINGS OF RAILWAY VEHICLES

Jorge Ambrósio

IDMEC, Instituto Superior Técnico, Universidade Técnica de Lisboa
Av. Rovisco Pais 1, 1049-001 Lisboa, Portugal
e-mail: Jorge@dem.ist.utl.pt, web page: http://www.dem.ist.utl.pt/IDMEC/

Keywords: gangway design, train working space, railway geometry, guiding constraints.

Abstract. *Generally most of the railway analysis that involves motion is dealt with railway dynamics tools and not with purely kinematic analysis tools. That is derived from the treatment of the railway vehicles by using the optics of the stability and comfort analysis, which ultimately deal with the problem of the rail-wheel contact. However, there are important problems in railway vehicle and infrastructure design for which purely kinematic analysis tools can be used with gains in computational efficiency and usability by technical experts. Actual construction of light rail vehicles requires that the interface between successive cars in the train is fully open being the articulation between them made of gangways. Couplers connect different vehicles allowing for them to be articulated while ensuring that the traction efforts are transmitted along the train. Also, at the level of the infrastructures the knowledge of the workspace of the train vehicles is of fundamental importance to design passenger platforms or to define the feasible locations of railway equipment avoiding interference with the train operation. These equipments exemplify the type of features for which the relative motion between the train vehicles needs to be evaluated, in particular, the relative angles and distances between the fixation points of the features are of fundamental interest. A kinematics methodology based on Cartesian coordinates for the kinematic analysis of multibody systems and specialized to the railway analysis is summarized here and used to develop the planar models of the trainsets. Besides the standard kinematic joints used in multibody systems the trajectory following constraint, which guides the vehicles over the railroad, is essential part of the procedure. The methodology is applied to the study of a complex trainset in which the objectives are to evaluate the relative orientation and positions between the carbodies and to appraise the feasibility of insertion of the trainset in the geometry of the railroad geometry. The methodology and the models developed are validated with respect to the classical procedures used in industry to obtain the results necessary to design the vehicle components. The insertion of track and vehicle perturbations in kinematics analysis deserves a particular and detailed treatment in this work. For the use of the computational tool in an industrial environment, supported by the methods described, suitable graphical interfaces are also presented here.*

1 INTRODUCTION

The study of the relative motion between the vehicles of a train is traditionally achieved through the use of multibody dynamics tools only [1,2]. In these, the dynamics of the train resulting from the complex interaction between wheels and rail [3] or from the aerodynamic forces is obtained for particular running conditions [4]. The study of the motion envelops of the train, also known as gabarits, or of the extremes of the relative orientations between the vehicles is done by running successive simulations in perturbed situations. Not only the computational time to run each simulation, for relatively short tracks may be unreasonably long but also the amount of data required to setup predictable models may not be feasible in early phases of design. Due to these limitations the study of the relative motion between vehicles, for the design of gangways, shown in Fig. (1), or coupler housings, depicted by Fig. (2), has relied in the drawing instruments of CADD rather than in design tools of CAD. In this work it is shown how a purely kinematic approach can be used to respond to some of the design needs in railway vehicles and infrastructures.

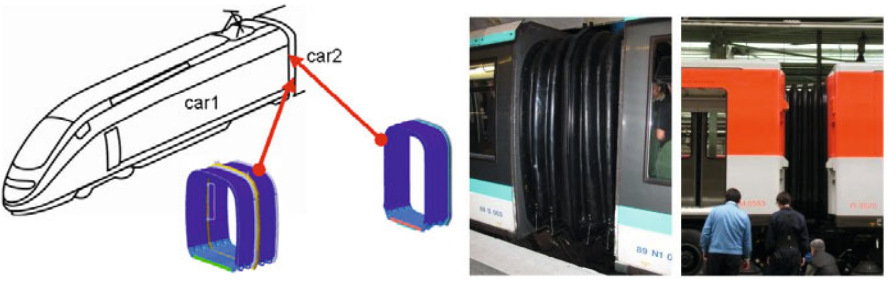

Figure 1: Gangways between cars of railway vehicles

Figure 2: Coupler housings for railway vehicles

The movement of the wheelsets over the railway is characterized by a complex interaction between wheels and rails with nonlinear and time variable contact forces [5,6]. The rail-wheel contact modeling involves, among other topics, the contact mechanics, friction and rigid body dynamics [7,8]. The result of all contributions to the final motion of the wheelsets is a highly nonlinear behavior, although contained inside displacement limits during normal operating conditions. In fact, when the wheelsets travel along the railway in the longitudinal direction there are also appreciable transversal translations and yaw and roll rotations of the wheelsets. For the developments that follow it is assumed that the motion of the wheelsets follows exactly the geometry of the railway. Two types of railway geometries are defined here: the reference geometry, which would be followed in a perfect rail/wheel contact in a perfect railway

by a train without any clearance or deviation from its nominal design; deviated geometries, which account for all clearances, imperfections and wear of the train and railroad components. The deviated railway geometry is such that all normal operating conditions for a particular train are included inside the limits of the railway geometry. All deviations of the position and all flexibility of the mechanical systems lead to operation conditions that are well within the perturbed geometry of the railway geometry considered.

The wheelsets are connected to the chassis of the bogies by a set of joints that control the relative motion between wheels and chassis and by a set of springs and dampers. This subsystem is designated by primary suspension [5]. In turn, the bogie chassis is connected to a support beam to which one of the carshell connecting shaft is attached. The connection between chassis and support beam is also done by a set of kinematic joints, springs and dampers, designated by secondary suspension [5]. Each train carbody is generally mounted in the top of two bogies. The attachment between the carbody and each bogie is done by a shaft rigidly connected to the carbody that is inserted in a bushing joint located in the support beam of the bogie. This joint allows for a free yaw rotation of the bogie with respect to the carbody. However, the relative roll rotation is penalized by a moment that results from the deformation of the bushing joint. All these mechanical arrangements have maximum excursions for angles and displacements between mechanical components that are used if and only if the dynamics of the vehicles requires, which would lead that jounce stops, bounce stops and other limiters would be reached. In this work the performance of the vehicles is studied in the limits of the relative displacement of each mechanical component, if compatible with the railway geometry.

Figure 3: Gaps between the vehicle exit and the station platforms

The objective of this work is to present a general methodology that allows modeling trainsets and simulating the relative motion between carbodies of the trainset when the wheelsets follow a given reference motion. In order for the kinematic tools described in this work to be used in the framework of industrial design a mapping between the mechanical clearances and uncertainties and the deviation between the nominal track geometry and its deviated configuration is proposed. Also, a graphical interface that uses the quantities familiar to the railway analyst is presented. In the process, the numerical tool is applied to the definition of working envelopes of the train, which is ultimately used in the design of the passenger platforms exemplified in Fig. (3). Being the kinematic procedure described and applied here purely bidimensional, each model has a single degree of freedom that needs to be guided. For the purpose a driver for the driving wheelset is used.

The methodologies used are applied to the study of a trainset model of a surface metro vehicle as a form of demonstrating the use of the kinematic tool in an industrial environment. During the design of the vehicle considered in this work particular attention is paid to the possibility of the towing of a non-operational vehicle by another and to the feasibility of the operation of the rolling stock in the track with small radius curves in a historical European city.

2 KINEMATIC ANALYSIS METHODOLOGY

Kinematic analysis is the study of the motion of a system independently of the forces that cause it. For this purpose, a set of coordinates to describe the system components is chosen, eventual relations among those coordinates representing physical joints between system components are defined as well as a set of drivers. The kinematic analysis is carried on by solving the set of equations resulting from the kinematic and driver constraints [9].

2.1 Kinematic analysis

Let a set of coordinates, described by vector **q**, be defined to represent the position and orientation of each rigid component of multibody system, and represented in Fig. (4). Depending on the choice of coordinates used to describe the multibody system a larger or smaller set of constraint equations relating these coordinates are defined [9].

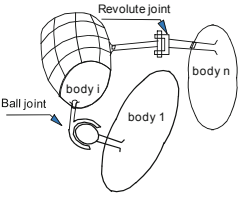

Figure 4: Multibody System

The number of degrees-of-freedom of the system is equal to the number of coordinates minus the number of independent constraint equations. In kinematics, each degree-of-freedom of the system must be driven being the equation that describes each motor referred to as driving constraint. Let all equations representing the different constraints be grouped together as

$$\boldsymbol{\Phi}(\mathbf{q}, t) = \mathbf{0} \tag{1}$$

The set of Eq. (1) is nonlinear in the coordinates **q** and eventually with respect to *t*. Its solution is obtained using the Newton-Raphson method [5].

The time derivative of Eq. (1) provides the velocity equations for the system, given by

$$\dot{\boldsymbol{\Phi}} = \mathbf{0} \quad \equiv \quad \boldsymbol{\Phi}_{\mathbf{q}}\dot{\mathbf{q}} = \boldsymbol{\nu} \tag{2}$$

where $\dot{\mathbf{q}}$ is the vector of the velocities and $\boldsymbol{\nu}$ contains the partial derivatives of the position equations with respect to time. Note that $\dot{\mathbf{q}}$ is the time derivative of **q** in the planar case.

The time derivative of Eq. (2) leads to the acceleration equations of the system, written as

$$\ddot{\boldsymbol{\Phi}} = \mathbf{0} \quad \equiv \quad \boldsymbol{\Phi}_{\mathbf{q}}\ddot{\mathbf{q}} = \boldsymbol{\gamma} \tag{3}$$

where $\ddot{\mathbf{q}}$ is the time derivative of $\dot{\mathbf{q}}$ and $\boldsymbol{\gamma}$ contains the equations terms that are acceleration independent. The solution of Eqs. (2) and (3) are obtained using a linear equations solver.

2.2 Rigid body definition

Let Fig. (5) represent a rigid body to which a body fixed reference frame $\xi\eta$ is attached. The position and orientation of the rigid body is described by a vector $\mathbf{r}_i$, and an orientation θ_i. For each rigid body the body coordinates are $\mathbf{q}_i = \left[x, y, \theta\right]_i^T$. The complete system with *nb* bodies is described by the set of coordinates **q** given by:

$$\mathbf{q} = \left[\mathbf{q}_1^T \quad \mathbf{q}_2^T \quad \cdots \quad \mathbf{q}_{nb}^T\right]^T \tag{4}$$

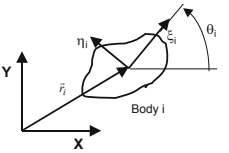

Figure 5: Body fixed reference frame

In the multibody models, developed using the methodologies described hereafter, the train carbodies are represented as rigid bodies. The couplers and other devices are not represented as rigid bodies but simply as joints. Because the complete models are analyzed in the context of a kinematic analysis no force elements or contact elements are considered.

2.3 Couplers: Revolute – Revolute Joints

The couplers are components of the train responsible for the connection between two successive carbodies. They work by maintaining the two points, one in each carbody, at a fixed distance. They are modeled here as composite revolute-revolute joints, which connect two bodies *i* and *j*, as depicted by Fig. (6). There is one constraint equation defining the condition for point *P* of body *i* to remain at a fixed distance of point *P* of body *j*, i.e.,

$$\mathbf{\Phi}^{(r-r,1)} = 0 \equiv \mathbf{d}^T \mathbf{d} - d_0^2 = 0 \tag{5}$$

where d_0 is the initial length of the coupler joint and vector $\mathbf{d}$ is written as

$$\mathbf{d} = \mathbf{r}_j - \mathbf{A}_j \mathbf{s}'_j - \mathbf{r}_i - \mathbf{A}_i \mathbf{s}'_i \tag{6}$$

In Eq. (6) the transformation matrix from the body *i* fixed coordinates to the inertia frame *xy* is denoted by $\mathbf{A}_i$, all other quantities are represented in Fig.(3). The notation (.)' indicates that the quantity (.) is expressed in the body-fixed coordinate system.

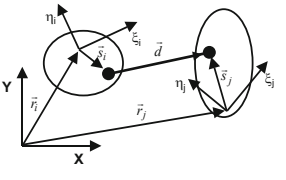

Figure 6: Revolute-Revolute joint representing the coupler

The contribution of the revolute-revolute joint to the Jacobian matrix $\mathbf{\Phi_q}$ is given by

$$\mathbf{\Phi}_{\mathbf{q}}^{(r-r,1)} = \begin{bmatrix} a & b & c & d & e & f \end{bmatrix} \tag{7}$$

where

$$a = 2\left(x_i^P - x_j^P\right) \tag{8a}$$

$$b = 2\left(y_i^P - y_j^P\right) \tag{8b}$$

$$c = 2\left(x_i^P - x_j^P\right)\left(y_i^P - y_j\right) + 2\left(y_i^P - y_j^P\right)\left(x_i^P - x_j\right) \tag{8c}$$

$$d = -2\left(x_i^P - x_j^P\right) \tag{8d}$$

$$e = -2\left(y_i^P - y_j^P\right) \tag{8e}$$

$$f = 2\left(x_i^P - x_j^P\right)\left(y_i^P - y_j\right) - 2\left(y_i^P - y_j^P\right)\left(x_i^P - x_j\right) \tag{8f}$$

where x_i^P and y_i^P are the coordinates of point P belonging to body i. These coordinates are the components of vector $\boldsymbol{r}_i^P$ given by

$$\boldsymbol{r}_i^P = \boldsymbol{r}_i + \mathbf{A}_i \mathbf{s}_I' \tag{9}$$

The contribution of the constraint for the right-hand-side of the acceleration equation is

$$\begin{aligned}\boldsymbol{\gamma} = -2\Big\{&\left(\dot{x}_i - \dot{x}_j\right)^2 + \left(\dot{y}_i - \dot{y}_j\right)^2 + \left[\left(x_i^P - x_i\right)\left(x_j^P - x_i\right) + \left(y_i^P - y_i\right)\left(y_j^P - y_i\right)\right]\dot{\theta}_i^2 + \\ &+\left[\left(x_j^P - x_j\right)\left(x_i^P - x_j\right) + \left(y_j^P - y_j\right)\left(y_i^P - y_j\right)\right]\dot{\theta}_j^2 - \\ &-\left[\left(x_i^P - x_i\right)\left(x_j^P - x_i\right) + \left(y_i^P - y_i\right)\left(y_j^P - y_i\right)\right]\dot{\theta}_i\,\dot{\theta}_j + \\ &+\left[\left(x_j^P - x_i\right)\left(\dot{y}_i - \dot{y}_j\right) + \left(y_i^P - y_i\right)\left(\dot{x}_i - \dot{x}_j\right)\right]\dot{\theta}_i - \\ &-\left[\left(x_j^P - x_j\right)\left(\dot{y}_i - \dot{y}_j\right) + \left(y_j^P - y_j\right)\left(\dot{x}_i - \dot{x}_j\right)\right]\dot{\theta}_j\Big\}\end{aligned} \tag{10}$$

2.4 Ball Attachments: Revolute Joints

In some cases of the trainset modeling different carbodies are connected to each other by ball joints and not by couplers. Let two bodies i and j be connected by a revolute joint, as depicted by Fig. (7). This means that the position of point P in body i is coincident all the time with the position of point P in body j. This condition is described by

$$\boldsymbol{\Phi}^{(r,2)} = \mathbf{0} \equiv \mathbf{r}_i + \mathbf{A}_i \mathbf{s}_i' - \mathbf{r}_j - \mathbf{A}_j \mathbf{s}_j' = \mathbf{0} \tag{11}$$

The conditions of the revolute joint to the Jacobian matrix is given by

$$\boldsymbol{\Phi}_{\mathbf{q}}^{(\mathrm{r},2)} = \begin{bmatrix} 1 & 0 & -\left(y_i^P - y_i\right) & -1 & 0 & \left(y_j^P - y_j\right) \\ 0 & 1 & \left(x_i^P - x_i\right) & 0 & -1 & -\left(x_i^P - x_j\right) \end{bmatrix} \tag{12}$$

where the meaning of x_i^P and y_i^P is the same as in Eq. (8). The contribution of the revolute joint to the right-hand-side of the acceleration equations is given by:

$$\boldsymbol{\gamma} = \begin{Bmatrix} \left(x_i^P - x_i\right)\dot{\theta}_i^2 - \left(x_j^P - x_j\right)\dot{\theta}_j^2 \\ \left(y_i^P - y_i\right)\dot{\theta}_i^2 - \left(y_j^P - y_j\right)\dot{\theta}_j^2 \end{Bmatrix} \tag{13}$$

2.5 Railway Geometry

The railway geometry is described by a cubic spline curve that interpolate a set of points given by the user [10,11]. The advantage of these curves is that the continuity of their first and second derivatives is guaranteed. Furthermore, the position of any point over the curve is defined in terms of a local parameter that is associated with the length traveled over the curve. In this form, the information on the length traveled each wheelset of the train is available.

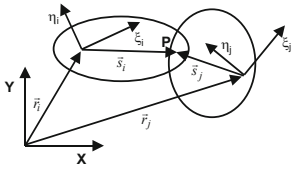

Figure 7: Revolute joint representing a ball joint

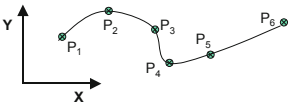

Figure 8: Points interpolated by cubic spline segments

Let a set of points, representing the railway, be defined in the plane *XY*, as represented in Fig. (8). Each point P_i is described by its coordinates $(xy)_i$. Let cubic spline segments be used to represent the interpolation curves being each spline segments given by [11]

$$P(s_l)=\begin{bmatrix} s_l^3 & s_l^2 & s_l & 1 \end{bmatrix}\begin{bmatrix} 2 & -2 & 1 & 1 \\ -3 & 3 & -2 & -1 \\ 0 & 3 & 1 & 0 \\ 1 & 0 & 0 & 0 \end{bmatrix}\begin{bmatrix} P(0) \\ P(1) \\ P'(0) \\ P'(1) \end{bmatrix} \tag{14}$$

where the parameter $s_l \in [0,1]$, $P(0)$ and $P(1)$ represent the coordinates of the end points of each spline segment. The spline derivatives at the end points are calculated in order to ensure C^2 continuity between spline segments. Assuming that the second derivatives of the first and last point of the set of points defining the railway to be interpolated are null, the first parameter derivatives at all other points are obtained as

$$\begin{bmatrix} 2 & 1 & & & & & \\ 1 & 4 & 1 & & & & \\ & & \ddots & & & & \\ & & & 1 & 4 & 1 & \\ & & & & 1 & 2 & \end{bmatrix}\begin{Bmatrix} P'_0 \\ P'_1 \\ \vdots \\ P'_{n-2} \\ P'_{n-1} \end{Bmatrix}=\begin{Bmatrix} 3\,(P_1 - P_0) \\ 3\,(P_2 - P_0) \\ \vdots \\ 3\,(P_{n-1} - P_{n-3}) \\ 3\,(P_{n-1} - P_{n-2}) \end{Bmatrix} \tag{15}$$

The position of each point over the railway is described by a global parameter that accounts for the length of the spline segments measured from the first given point up to the actual position of the referred parameter. This global parameter is related for each spline segment with a local parameter, bounded to be a number between zero and one.

2.6 Pivot Reference Motion

The motion of each wheelset of the train must be constrained to remain in the railway, as illustrated in Fig. (9). Then a new coordinate, corresponding to the global parameter locating the constrained point to be over the curve represented by the spline, must be defined.

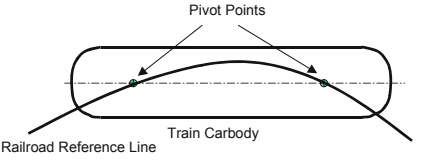

Figure 9: Point of a rigid body constrained to be coincident with a curve

Let a point *P* located on a rigid body *i* be on a curve, controlled by a parameter s^g. This condition is described by [12,13]

$$\boldsymbol{\Phi}^{(sp,2)}=\mathbf{0} \;\equiv\; \boldsymbol{r}_i^{\,P}-\mathbf{P}\left(s^g\right)=\mathbf{0} \tag{16}$$

where $\boldsymbol{r}_i^P = \boldsymbol{r}_i + \mathbf{A}_i \mathbf{s}_i'^P$ and the parameter s_l, local to the spline segment where point P is constrained to move, is a function of the global parameter s^g. The relation between the parameters is

$$s^g = \sum_{n=1}^{k-1} l_n + s_l l_k \tag{17}$$

where k is the number of the spline segment where points P is actually located and l_k is its length. Note also that the local parameter $s^l \in [0,1]$. The contribution of the constraint of each pivot to the Jacobian matrix is then given by:

$$\mathbf{\Phi}_{\boldsymbol{q}}^{(sp,2)} = \begin{bmatrix} -1 & 0 & \xi_i^P \sin\theta + \eta_i^P \cos\theta_i & \dfrac{d\,x(s_l)}{ds_l}\dfrac{1}{l_k} \\ 0 & -1 & \xi_i^P \cos\theta_i - \eta_i^P \sin\theta_i & \dfrac{dy(s_l)}{ds_l} \end{bmatrix} \tag{18}$$

where the first 3 columns refer to the x, y and θ coordinates of body i and the 4th column refers to the global parameter locating point P in the curve.

The contribution of the constraint to the right-hand-side of the acceleration equations is:

$$\gamma = -\begin{Bmatrix} \left(\xi_i^P \cos\theta_i - \eta_i^P \sin\theta_i\right)\omega_i^2 + \dfrac{d^2x(s_l)}{ds_l^2}\left(\dfrac{\dot{s}^g}{l_k}\right)^2 \\ \left(\xi_i^P \sin\theta_i - \eta_i^P \cos\theta_i\right)\omega_i^2 + \dfrac{d^2y(s_l)}{ds_l^2}\left(\dfrac{\dot{s}^g}{l_k}\right)^2 \end{Bmatrix} \tag{19}$$

In eqs. (17) and (18) the quantities $x(s_l)$ and $y(s_l)$ are the components of the spline P(s^g).

2.7 Driving Constraint

For the train to move on the railway it is necessary that one of the pivot points, which corresponds to the locomotive wheelset, in driven. This corresponds to set up the kinematics of the driven pivot. Let point i be the driven pivot and the system coordinate associated with this pivots be denoted by s_i^g. The constraint equation for the driven constraint is written as:

$$\mathbf{\Phi}^{(d,1)} = \mathbf{0} \equiv s_i^g - s_0^g - v_0 t - \tfrac{1}{2} a_0 t^2 = 0 \tag{20}$$

where s_0^g, v_0 and a_0 are the position, velocity and acceleration of the driven point and t is time.

The contribution of the constraint to the Jacobian matrix is given by:

$$\mathbf{\Phi}_{\boldsymbol{q}}^{(d,1)} = [1] \tag{21}$$

while the right-hand-sides of the velocity and acceleration equations are respectively

$$\nu^{(d,1)} = -v_0 - a_0 t \tag{22}$$

$$\gamma^{(d,1)} = -a_0 \tag{23}$$

Note that in kinematic analysis of a trainset only one driving constraint is set. Assuming that the trainset is all mounted together, only one degree of freedom has to be driven.

2.8 Numerical Methods

For any trainset system the constraint equations are set up taking into account the system's topology. The set of equations obtained in this form is a system of nonlinear equations, which are in number equal to the number of coordinates used to describe the system, and that are solved using the Newton-Raphson method [9]. Starting from initial estimates for the system coordinates, the iterative procedure to correct the positions is started by solving:

$$\mathbf{q}^{l+1} = \mathbf{q}^l - \mathbf{\Delta q}^l \tag{24}$$

where

$$\mathbf{\Phi}_{\mathbf{q}}\left(q^{l}\right)\Delta\mathbf{q}^{P}=\mathbf{\Phi}\left(\mathrm{q}^{1},t\right) \tag{25}$$

The index l represents the iteration step for which Eq. (25) is being evaluated. The iterative procedure described by Eq. (24) ends when the following condition is met

$$\left\|\mathbf{q}^{l+1}=\mathbf{q}^{l}\right\|\leq\varepsilon \tag{26}$$

The kinematic analysis is carried on by performing the following steps:

1. Setup the initial conditions for the positions and initialize the time counter
2. Construct the position Eq. (1) and solve them to obtain $\mathbf{q}$
3. Construct the velocity Eq. (2) and solve them to obtain $\dot{\mathbf{q}}$
4. Construct the acceleration Eq. (3) and solve them to obtain $\ddot{\mathbf{q}}$
5. Increment the time counter and
6. If time is smaller than final time go to step 2)
7. If time exceeds the final time stop the analysis.

When the condition described by Eq. (26) is not achieved in a limited number of iterations the iterative procedure is assumed as being stalled and a non-convergence situation is reported. Situations where a solution for Eq. (25) cannot be found correspond to cases for which the motion of the system locks. For example, if the trainset dimensions are such that it cannot negotiate a curve without derailing, the situation arising from the numerical solution process will indicate that no solution is possible for Eq. (26). In the resolution of nonlinear equations multiple solutions are available. When the initial estimates are close to one of the solutions it is expected that the iteration procedure converges to that solution.

3 TRAINSET KINEMATICS ANALYSIS PROGRAM

Based on the methodology described in section a general purpose computer program, designated by *Gangway Analysis Program* (GAP), is implemented. This program, with the flowchart represented in Fig. (10), enables the user to supply different information related with the railway geometry and the train topology and to simulate its motion.

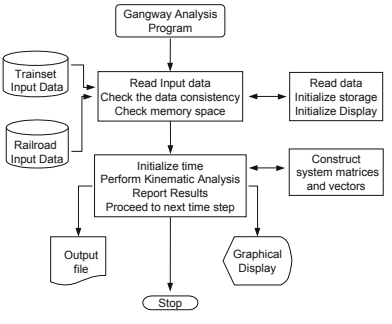

Figure 10: Flowchart of the Gangway Analysis Program

The construction of the input to build or edit the train model or the railway representation is guided through a graphical interface that has the first window represented in Fig. (11a). The general dimensions of the model are the first part of the input required to build the train model and they are summarizes in Fig. (11b). Note that although most of the train models develop their motion of interest in the horizontal plane (*XY*) there are cases for which vertical curves (*XZ*) are of interest, especially for the study of gangway attachments and couplers housings.

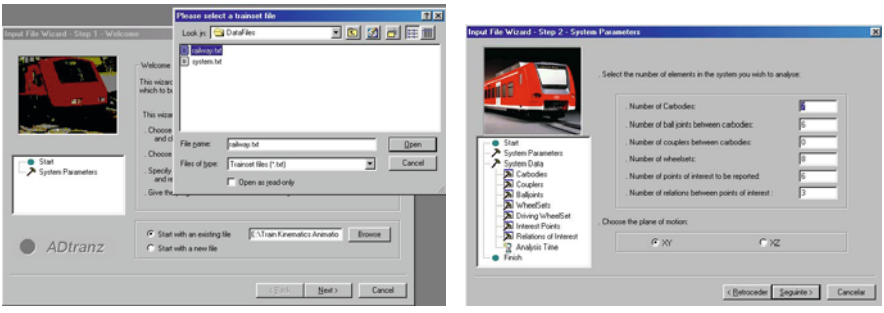

(a) (b)

Figure 11: Graphical interface for the Gangway Analysis Program: (a) opening window; (b) general dimensions for the train model.

The kinematic and geometric information required to setup the bodies of the vehicle system and the coupler joints is illustrated by the graphic interface depicted in Fig. (12). Similar graphical input is available for all remaining information to build the vehicle input, not being shown here for the sake of conciseness. A similar graphical interface is defined to enter the data to build the railway while guiding the analyst on its construction.

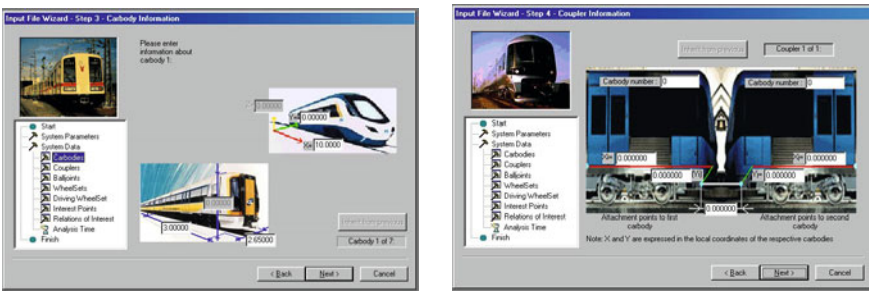

(a) (b)

Figure 12: Graphical interface for the Gangway Analysis Program: (a) Initial carbody information; (b) Information required to set a coupler between adjacent vehicles.

Having all input defined, the program starts evaluating the train kinematics and the results are displayed in a graphical environment represented in Fig. (13). The output graphical interface of GAP includes 3 windows containing alphanumeric and graphical information concerning the actual status of the program. This graphical information includes all numerical information being generated by the program at every step, the geometry of the railway with the actual position of the train and the configuration of the trainset relative to the train carbody number 1, which allows the user to observe the relative motion. Other information displayed in this window is the actual value of three special relations between points defined in each carbody. These relations may be the distance between two given points of interest or an angle between vectors defined by two pairs of points. The maximum and minimum values of these relations are always updated and displayed in this window. Note that most of the design decisions made during the construction, or fitting, of gangways and housings on a train concern the extreme values for the type of geometric relations referred.

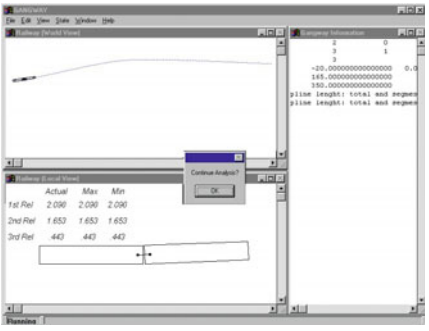

Figure 13: Graphical environment of the trainset kinematic analysis program GAP

When an increment of the time counter is finished a warning box appears in the center of the screen. When finally the program is over, either because the end of the analysis time was reached or because an error condition occurred, a new window is displayed stating that the program stopped. This tool computes also the working envelope of a given trainset system and represents it as shown in Fig. (14). This envelope is the smallest possible three-dimensional surface that includes in its interior all the trajectories of any possible point defined on the train surface.

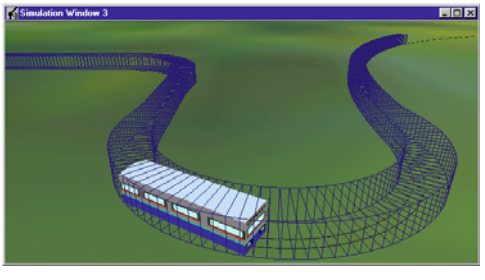

Figure 14: Working space of the trainset vehicle defined as a succession of cross-sections represented by convex hulls of the trajectories of all points of the vehicle surface.

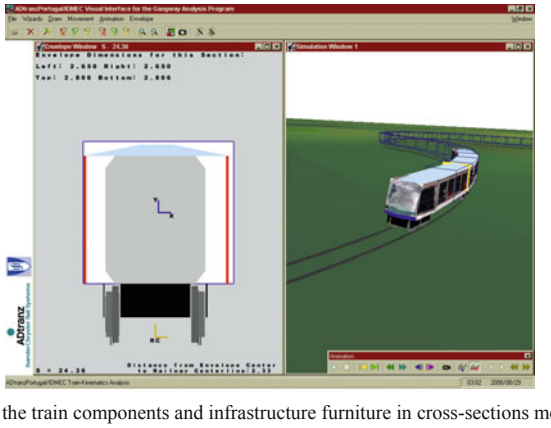

Figure 15: Position of the train components and infrastructure furniture in cross-sections moving on the trainset.

This work space of the trainset during its motion, looking like a tube of generalized shape, is obtained by interpolation of the convex polygons points which result from the intersection of the points trajectories of the convex hull of points within its motion along the railway. Knowing the location and orientation of each carbody at each time step, the location of the outermost points of each carbody is computed for every step. The points furthest away from the railway define the resulting convex hull. By moving a plane, perpendicular to the tangent vector to the railway, the different cross-sections of the train and of the railroad furniture are displayed, as shown in Fig. (15). In this window it is possible to obtain any dimension of the clearance or interference between any feature of the railway. This is the feature of the Gangway Analysis Program used to support the design of the passenger platforms and railroad equipment location.

4 APPLICATION TO THE STUDY OF A SURFACE METRO TRAINSET

The methodology proposed for the kinematic analysis of the kinematics of trainsets is applied in the design of a surface metro vehicle. The purpose of the study is twofold. Firstly it is required that the angles between the different vehicles and the distances between selected points are evaluated for different railroad geometries, in which the vehicles are supposed to operate. This data is used in the design of the gangway connections between the vehicles, which allow passengers to travel in between consecutive vehicles. The second purpose of the study is to verify the feasibility for the trainsets to negotiate the railroads in which they are supposed to operate, even when to trainsets are connected through a coupler to form a longer train.

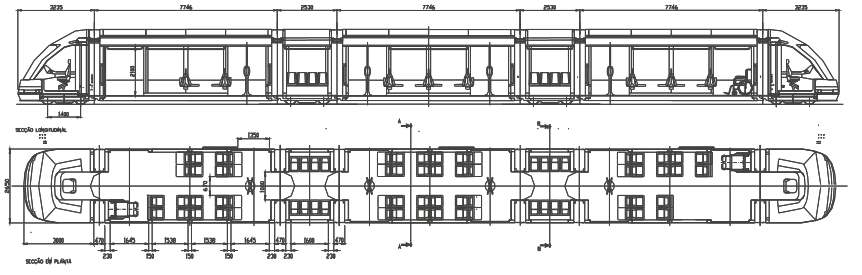

Figure 16: Geometry and dimensions of a single surface metro trainset.

Each trainset model, of the surface metro system shown in Fig. (16), is made of 7 vehicles, represented by rigid bodies, 6 revolute joints, 8 guiding constraints and 1 driving constraint [14]. In the study presented in this work two of such trainsets are used connected by a coupler, which is modeled by a composite revolute-revolute joint, as shown in Fig. (17). The complete system is described by 42 coordinates and its motion is constrained by 30 joints, of the types described, which account for 42 independent kinematic constraints.

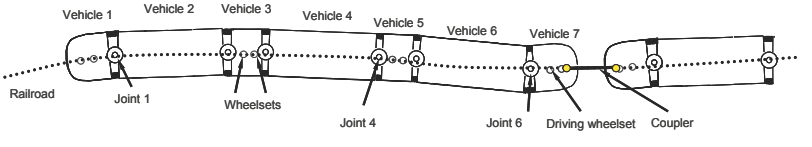

Figure 17: Representation of the multibody model of the two trainsets connected by a coupler.

The generic geometry of railroads, represented in Fig. (18), include tangent tracks, constant radius curves and spiral curves. In between tangent and curve segments or between curves with different radius a spiral curve is generally used to ensure a smooth transition between the railroad segments [15]. By smooth transition it is meant that the radius of the railroad does not change abruptly between two segments but instead changes smoothly. Ultimately, the design of the spiral curves are responsible for increasing the comfort when the train is operated at nominal speeds for which the tracks have been designed. Due to the implementation of the railroad in an old part of the city, in which the surface metro is operated, the geometry of the track does not include the spiral curves.

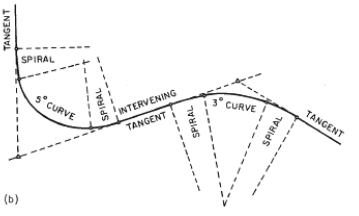

Figure 18: General geometry for a standard railroad includes spiral segments in between track segments with different curvatures. The spiral segments are curves represented by cubic polynomials.

In the case studied to demonstrated the methodology proposed here the railroad geometry starts by a tangent track with 100 m, followed by a 90º curve with a constant radius of 25 m which is followed by another 90º curve, also with a 25 m radius but with the concavity on the opposite direction of the first. The railroad is finalized with a 100 m tangent track. The vehicles are simulated until the complete track is covered being the relative motion between the trainset vehicles and vehicle 1 depicted by Fig. (19).

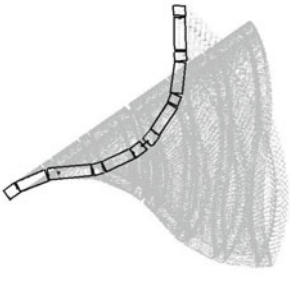

Figure 19: Positions of the different vehicles of the trainset (in grey) with respect to the first vehicle. In black, the actual position of the trainset.

In order to represent some more realistic operating conditions the coordinates of the points that define the railroad are perturbed, in the perpendicular direction to the tangent to the track, by displacements of 6 cm. The results of 4 simulations, defined as R1_1 through R1_4, are presented in Figs. (20) and (21) in terms of the angle between vehicle 1 and 2 and the distance between two of the attachment points of the gangways on the same vehicles, respectively. Fig. (20) shows that the angle between the vehicles changes in the range of [-6º,+5.5º] for all track conditions.

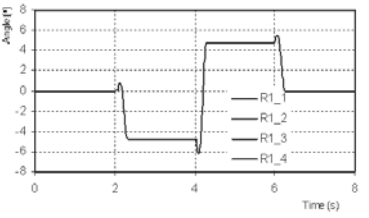

Figure 20: Variation of the angle between vehicle 1 and 2 while negotiating the railroad.

The distance of the attachment points of the gangway between vehicles 1 and 2 is in fact more sensitive to the track perturbations than the alignment angles, as perceived by Fig. (21). It is observed that the vehicles come as close as 0.20 m and as far apart as 0.75 m, which means that the folded thickness of the gangway cannot exceed 0.20 m and its stretched length must be larger than 0.75 m, in what the attachment points used to draw Fig. (21) are concerned.

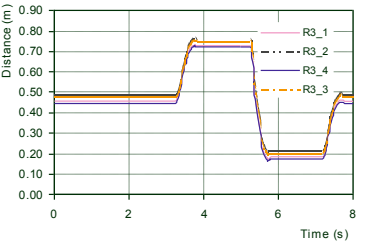

Figure 21: Distance between the attachment points of the gangway on vehicle 1 and 2 for the tracks.

The results obtained in the simulations are much than those described in this work. In fact, besides the distance between every pair of attachment points of all gangways and the angles between the vehicles it is also of importance to evaluate the angle between the coupler and each one of the vehicles. Such angle allows for the designer to include an opening for the coupler in the vehicle front that is wide enough for its operation but not so large that it would jeopardize the strength of the vehicle front.

5 OPERATIONAL PERTURBATIONS

The displacements of the train vehicles on the railroad is subjected to a large number of perturbations due to the irregularities and wear of the vehicle components and of the track and due to the dynamics of the vehicles. The wheelsets have lateral motion and inplane rotations, with respect to the railroad, during their normal operation. Also the mechanical joints of the suspensions or the attachment between the vehicle box and the bogies have clearances, misadjustments and elastic deformations that lead to a deviation bogies center with respect to the nominal position of the centerline of the track. All these factors lead to variations on the angles and distances between the attachment points of gangways and couplers and to the increase of clearances or interferences between vehicles and infrastructure features. In the limit, when the train is negotiating a very small curve, the ability to proceed with its motion without derailment may be inexistent. Therefore, the treatment of the track and vehicle irregularities, or the dynamic effects disregarded during the kinematic analysis, is of utmost importance.

The different contributions for the operational perturbations are designated as perturbation parameters and are represented in Fig. (22). The list of the perturbation parameters for the horizontal kinematics of the train set includes wheel and rail wear and irregularities, suspension clearances and flexibilities and mounting tolerances. The vertical kinematics may be affected by a different set of perturbations, but with the origin in the same mechanical sub-systems of the train vehicle and track.

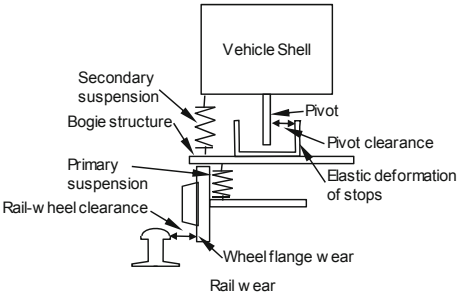

Figura 22: Parâmetros de Perturbação

The perturbations existing in a particular vehicle of the train are not necessarily equal to those of other cars. Therefore, instead of considering the particular conditions of each railway vehicle type it is preferred to use, in this work, the maximum values that can be considered for each one of the perturbation parameters identified. The values of such parameters, for the horizontal and vertical kinematics, are listed in Tables 1 and 2.

Perturbation parameters	(mm)
Rail-wheel contact:	
Lateral wear of rail	10
Lateral wear of rail flange	8
Gauge variation	15
Lateral wheel-rail clearance	5
Bogie :	
Lateral displ. of primary suspension	8
Lateral displ. of secondary suspension	30
Bogie-car box connection (Pivot):	
Lateral clearance of pivot connection	5
Elastic deformation of pivot stops	5

Table 1: Perturbation parameters for the horizontal kinematics of the railroad

Perturbation parameters	(mm)
Railway vertical irregularities	15
Wheel regular wear	10
Wheel irregular wear	5
Vertical displ. of primary suspension	30
Vertical displ. of secondary suspension	30

Table 2: Perturbation parameters for the vertical kinematics of the railroad

The cumulative effect of the perturbation parameters is represented in the kinematic analysis tool as perturbed paths for the reference motion of the bogies pivots. Through a series of kinematic analysis, in which all possible combinations of perturbations applied in all pivots of all vehicles in the train, the maximum and minimum values for the angles and distances between points are obtained. The cumulative effects of the perturbation parameters, depicted as clearances from hereafter, require the representation of two tracks parallel to the nominal track. The distance between those perturbed tracks is equal to the clearance. The perturbed tracks are automatically generated by the kinematic analysis code based on the nominal track. The position of the control points of the perturbed tracks is calculated by using half of the clearance as the distance between each of the control points of the nominal track and the control of the perturbed track in a direction normal to the nominal track. The position of the perturbed control points is given by

$$P_i^{(+)} = P_i + C_l \left\{ \begin{array}{c} +\left.\dfrac{dy}{ds^g}\right|_{P_i} \\ -\left.\dfrac{dx}{ds^g}\right|_{P_i} \end{array} \right\} \left(\sqrt{\left(\left.\frac{dy}{ds^g}\right|_{P_i} \right)^2 + \left(\left.\frac{dx}{ds^g}\right|_{P_i} \right)^2} \right)^{-1} \tag{27}$$

$$P_i^{(-)} = P_i - C_l \left\{ \begin{array}{c} +\left.\dfrac{dy}{ds^g}\right|_{P_i} \\ -\left.\dfrac{dx}{ds^g}\right|_{P_i} \end{array} \right\} \left(\sqrt{\left(\left.\frac{dy}{ds^g}\right|_{P_i} \right)^2 + \left(\left.\frac{dx}{ds^g}\right|_{P_i} \right)^2} \right)^{-1} \tag{28}$$

where C_l is the clearance and $P^{(+)}$ and $P^{(-)}$ are the positions of the control points for the perturbed tracks in both sides of the nominal track.

The kinematic analysis with a perturbed motion is defined by forcing the pivots of the vehicle to follows the perturbed track, as shown in Fig. (23). For two pivots in a car the number of combinations, i.e., the number of kinematic analysis to be carried on, is four, as depicted by Fig. (24). In general, for a train with n pivots the number of kinematic analysis is 2^n, and they must all be evaluated.

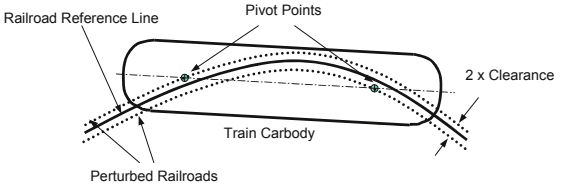

Figure 23: Motion of a railroad vehicle in a perturbed track

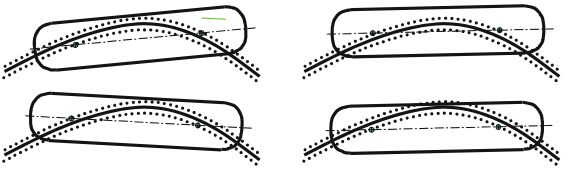

Figure 24: Combinations for the perturbed track kinematic simulations for a vehicle with four pivots

6 CONCLUSIONS

A general purpose methodology for the kinematic analysis of trainsets has been presented in this work. Using Cartesian coordinates, standard mechanical joints between the system components and trajectory following constraints a complete train set is modeled and simulated in rail tracks with any general geometry. The methodology presented here can be used in the design of train components such as gangways and couplers, in the design of the geometrical features of the railroad infrastructures such as station platforms and railroad furniture or even to evaluate the ability of any given trainset to negotiate any particular railroad geometry. The methodology developed, and the computer program in which it has been implemented, has been demonstrated in the analysis of a light rail vehicle in use in a traditional European city. It has been shown how the perturbations of different nature can be introduced in the kinematic analysis and how doing so the use of a dynamic analysis for the railway vehicle is avoided.

REFERENCES

[1] G.A. Scott, Multibody Simulation Software – VAMPIRE, *Vehicle System Dynamics*, **22**(Sup), 127-129, 1993.

[2] W. Rulka, A. Eichberger, SIMPACK – An Analysis and Design Tool for Mechanical Systems*, Vehicle System Dynamics*, **22**(Sup), 122-126, 1993.

[3] J. Pombo and J. Ambrósio, Application of a Wheel–Rail Contact Model to Railway Dynamics in Small Radius Curved Tracks, *Multibody Systems Dynamics*, **19**(1), 91-114, 2008.

[4] J. Pombo, J. Ambrósio, M. Pereira, F. Rauter, A. Collina, A. Facchinetti, Influence of the Aerodynamic Forces on the Pantograph-Catenary System for High Speed Trains, *Vehicle Systems Dynamics*, accepted in 2008.

[5] R.V. Dukkipati, J.R. Amyot. *Computer-aided simulation in railway dynamics*, M. Dekker Inc., New York, New York, 1988.

[6] V.K. Garg, R.V. Dukkipati. *Dynamics of railway vehicle systems*, Academic Press, New York, New York, 1984.

[7] X.Quost, M.Sebes, A.Eddhahak, J.-B.Ayasse, H.Chollet, P.-E.Gautier. F.Thouverez. Assessment of Semi-Hertzian Method for Determination of Wheel-Rail Contact Patch, *Vehicle System Dynamics*, **43**(8), 539-559, 2005.

[8] E.Kassa, C.Andersson, J.Nielsen. Simulation of Dynamic Interaction Between Train and Rail-way Turnout, *Vehicle System Dynamics*, **44**(3), 247-258, 2006.

[9] P. Nikravesh. *Computer-aided analysis of mechanical systems*. Prentice-Hall, Englewood Cliffs, New Jersey, 1988.

[10] F. Yamaguchi. *Curves and surfaces in computer aided geometric design*. Springer-Verlag, Berlin, Germany, 1988.

[11] V.B. Anand. *Computer graphics and geometric modelling for engineering*, J. Wiley, New York, New York, 1994.

[12] J. Pombo, J. Ambrósio. Modelling Tracks for Roller Coaster Dynamics. *International Journal of Vehicle Design*, **45**(4), 470-500, 2007.

[13] J. Pombo, J. Ambrósio. General Spatial Curve Joint for Rail Guided Vehicles: Kinematics and Dynamics. *Multibody Systems Dynamics*, **9**, 237-264, 2003.

[14] J.Ambrósio. *Trainset Kinematic: A Planar Analysis Program for the Study of the Gangway Insertion Points*, Technical Report IDMEC/CPM/97/005, Institute of Mechanical Engineering, Instituto Superior Técnico, Lisbon, Portugal, 1997.

[15] A.R.V. Pinto, Bases *Técnicas dos Traçados do Metroplitano de Lisboa (Technical foundations for the design of tracks of the Lisbon metro system)*, Revista da Ordem dos Engenheiros, Lisboa, Portugal, 1978.

IAK 2008
Conference on Interdisciplinary Applications of Kinematics
A. Kecskeméthy, V. Potkonjak and A. Müller (eds.)
Lima, Peru, 9–11 January 2008

INVESTIGATION OF SELF RESONANCE IN VIBRATION EXCITATION SYSTEMS

Kazimieras Ragulskis[a], Ramutis Palevicius[*b], Arvydas Palevicius[c], Arvydas Barila [b]

[a]Lithuanian Academy of Science, Gedimino pr. 3, LT-01103, Vilnius, Lithuania
e-mail:kazimieras.ragulskis@ktu.lt, web page: http://lma.lt

[b]Department of Multimedia Engineering, Kaunas University of Technology,
Studentu st. 50, LT-51368, Kaunas, Lithuania
e-mail: Ramutis.Palevicius@ktu.lt, web page: http://if.ktu.lt/en/

[c]International Studies Centre, Kaunas University of Technology,
A. Mickeviciaus 37, LT-44244, Kaunas, Lithuania
e-mail: Arvydas.Palevicius@ktu.lt, web page: http://www.ktu.lt

Keywords: Vibroexciter, Non-linear vibrations, Mathematical modeling, System simulation.

Abstract. *Eccentric angular motion transfer mechanisms are analyzed in the paper. The debalancing mass has an additional degree of freedom in these mechanisms. It was found that certain types of such mechanisms posses interesting nonlinear dynamical features when a self-resonance motion mode occurs. Such self-resonance motion mode takes place when the main driving element rotates with relatively high angular velocity, but low frequency vibrations are generated in the range of fundamental frequency of the system. Numerical and experimental investigations of nonlinear vibration excitation systems were performed. Such vibration excitation systems have high practical value as there is no necessity for complex vibration control equipment – the stability of operation is guaranteed by non-linear dynamical interactions. Digital holographic system was used for experimental investigations of the dynamical properties of the system. The results of the investigations validated the results of the theoretical analysis and provide a background for developing new type of dynamical mechanisms.*

1 INTRODUCTION

Various types and modifications of vibration excitation systems are widely applied in different areas of engineering and technology. Every technological process has its own optimal regimes of vibration characterized by range of frequencies and amplitudes. Moreover, every vibration excitation system possesses individual characteristics describing the relationship between the transferred vibration power and frequency - amplitude characteristics. Naturally, different types of vibration excitation systems based on various principles of excitation have special and dedicated areas of application. One of the widely applied types of vibration excitation systems are based on the principle of dis-balance of the driving eccentric inertia element. It can be noted that such systems have small dimensions, their construction is relatively simple and durable; variation of generating frequency is rather simple. Such kinds of systems are exploited in construction and road engineering, mining and agricultural engineering.

The operation of vibration excitation systems is most effective in the regime of resonance. Such regimes are usually supported by automatic control systems. The stability of the systems without control usually is poor; on the other hand the close loop control systems are rather expensive. Another possibility for generating stable resonance vibrations without close loop control systems was found and investigated in number of research reports on nonlinear dynamics [1], [2], [3]. In this study it is shown that resonance vibrations can be excited without adaptation of frequency of forced oscillations – effect of self resonance can be applied for this purpose. The main driving shaft in such vibroexciters in fact can rotate with any angular velocity. The eccentric non-linear forces generate stable vibrations which frequency corresponds to the natural fundamental frequency of the non-linear system.

Eccentric dis-balance vibroexciter with an additional degree of freedom is presented in Fig. (1) [4]. Such vibroexciters when de-balancing mass has an additional degree of freedom are used for the development of self-resonating systems.

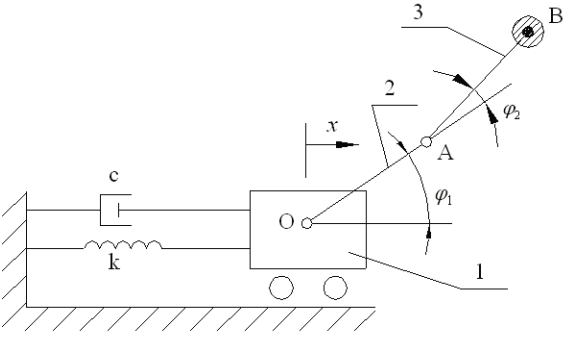

Figure 1: Eccentric vibroexciter: 1 – casing with vibroexciter; 2 and 3 – double pendulum joints.

Kinetic energy of the system takes the following form:

$$T = 0{,}5m_0\dot{x}^2 + 0{,}5m[\dot{x}^2 + r^2\dot{\varphi}_1^{\,2} + R^2(\dot{\varphi}_1 + \dot{\varphi}_2)^2 + 2Rr\dot{\varphi}_1(\dot{\varphi}_1 + \dot{\varphi}_2)\cos\varphi_2 - 2r\dot{x}\dot{\varphi}_1\sin\varphi_1 - \\ - 2R\dot{x}(\dot{\varphi}_1 + \dot{\varphi}_2)\sin(\varphi_1 + \varphi_2)] \quad (1)$$

where φ_1 ir φ_2 rotational angles; m_0 – mass of link 3 concentrated in point B; m – the mass of the casing; x – displacement of the vibration exciter; $R = AB$; $r = OA$.

Differential equations of motion, taking into account Eq. (1), takes the form:

$$\begin{cases} \ddot{\alpha} + 2\nu\dot{\alpha} + \omega_n^2\alpha = \mu\lambda\ddot{\varphi}_1 \sin\varphi_1 + \mu\ddot{\varphi}_1 \sin(\varphi_1+\varphi_2) + \mu\ddot{\varphi}_2 \sin(\varphi_1+\varphi_2) + \mu\lambda\dot{\varphi}_1^2 \cos\varphi_1 + \\ + \mu(\dot{\varphi}_1+\dot{\varphi}_2)^2 \cos(\varphi_1+\varphi_2), \\ (1+\lambda^2)\ddot{\varphi}_1 = \dfrac{A_1}{mR^2} - \dfrac{B_1}{mR^2}\dot{\varphi}_1 + \lambda\ddot{\alpha}\sin\varphi_1 + \ddot{\alpha}\sin(\varphi_1+\varphi_2) + 2\lambda\dot{\varphi}_1\dot{\varphi}_2 \sin\varphi_2 - 2\lambda\ddot{\varphi}_1\cos\varphi_2 + \\ + \lambda\dot{\varphi}_2^2 \sin\varphi_2 - \ddot{\varphi}_2 - \lambda\ddot{\varphi}_2\cos\varphi_2 , \\ \ddot{\varphi}_2 = -\dfrac{B_2}{mR^2}\dot{\varphi}_2 - \ddot{\varphi}_1 - \lambda\ddot{\varphi}_1\cos\varphi_2 + \ddot{\alpha}\sin(\varphi_1+\varphi_2) - \lambda\dot{\varphi}_1^2\sin\varphi_2 , \end{cases} \tag{2}$$

where $\alpha = \dfrac{x}{R}, \mu = \dfrac{m}{m+M}, \lambda = \dfrac{r}{R}$, x – displacement of the vibration exciter, $2\nu = \dfrac{c}{m+M}$, c – coefficient of viscous friction, $\varpi_n^2 = \sqrt{\dfrac{k}{m+M}}$, k –stiffness, ϖ_n^2 – the natural frequency of the vibration excitation system, $A_1 - B_1\dot{\varphi}_1$ and $-B_2\dot{\varphi}_2$ generalized moments according to the coordinates φ_1 ir φ_2 (driving and resistance forces) and these moments are linear functions.

2 NUMERICAL INVESTIGATION OF THE EFFECT OF SELF-RESONANCE

The system of equations Eq. (2) has been solved using approximate analytical techniques applying the method of small parameter. System of differential equations Eq. (2) was also solved using numerical techniques in order to investigate transient and steady state system behavior.

In order to solve Eq. (2) numerically, when $\varphi_1 = \omega_1 t$, it is necessary to replace Eq. (2) with the equivalent first order system. First, we have to solve Eq. (2) for $\ddot{\alpha}$ and $\ddot{\varphi}_2$ and to introduce new variables for $\alpha, \dot{\alpha}, \varphi_2$ and $\dot{\varphi}_2$:

$$\begin{cases} x_1 = \alpha \\ x_2 = \dot{\alpha} \\ x_3 = \varphi_2 \\ x_4 = \dot{\varphi}_2 \end{cases} \tag{3}$$

Then from Eq. (2) and Eq. (3) we have first order system:

$$\begin{cases} \dot{x}_1 = x_2 \\ \dot{x}_2 = \dfrac{F_\alpha + \mu F_\varphi \sin(\varphi_1+\varphi_2)}{1-\mu\sin^2(\varphi_1+\varphi_2)} \\ \dot{x}_3 = x_4 \\ \dot{x}_4 = \dfrac{F_\varphi + F_\alpha \sin(\varphi_1+\varphi_2)}{1-\mu\sin^2(\varphi_1+\varphi_2)} \end{cases} \tag{4}$$

where

$$F_\alpha = -2\nu x_2 - \omega_n^2 x_1 + \mu\lambda\ddot{\varphi}_1 \sin\varphi_1 + \mu\ddot{\varphi}_1 \sin(\varphi_1+x_3) + \mu\lambda\varphi_1^2 \cos\varphi_1 + \mu(\dot{\varphi}_1+x_4)^2\cos(\varphi_1+x_3)$$

$$F_\varphi = -b_2 x_4 - \ddot{\varphi}_1 - \lambda\ddot{\varphi}_1\cos x_3 - \lambda\dot{\varphi}_1 \sin x_3$$

It is assumed that ω_1 at the initial time moment varies by exponential law and it reaches its maximal value during a predefined time interval, i.e. the variation law of ω_1 can be described by:

$$\varpi_1 = \varpi_{1\max}(1 - e^{-ct}) \text{ , where c is a constant.} \tag{5}$$

Keeping in mind Eq. (5), φ_1 will be calculated using formula:

$$\varphi_1 = \varpi_{1\max}[t + \frac{1}{c}(e^{-ct} - 1)] \tag{6}$$

The variation of ω_1 is presented in Fig. (2).

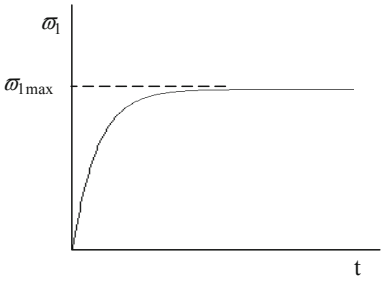

Figure 2: Plot of ω_1.

MATLAB (Mathworks Co.) specialized numerical routines were used for solving a system of ODEs in Eq. (4). A family of curves shown in Fig. (3) – Fig. (4) represent solution of Eq. (4) in various regimes (self resonance and non self resonance).

Fig. (3) shows the solution of system of equations when the vibration exciter is operating in usual mode (not self resonance mode). The following parameters were used for calculations: $\omega_{1\max} = 35$, $\omega_n = 15$, $\lambda = 0.1$, $\mu = 0.01$, $\nu = 10$, $b_2 = 0.15$. The produced solution show that the vibration excitation system operates like ordinary eccentric vibration exciter, the velocities of both dis-balances are approximately equal (both dis-balances form one dis-balance). The second pendulum slightly oscillates in respect to the first one.

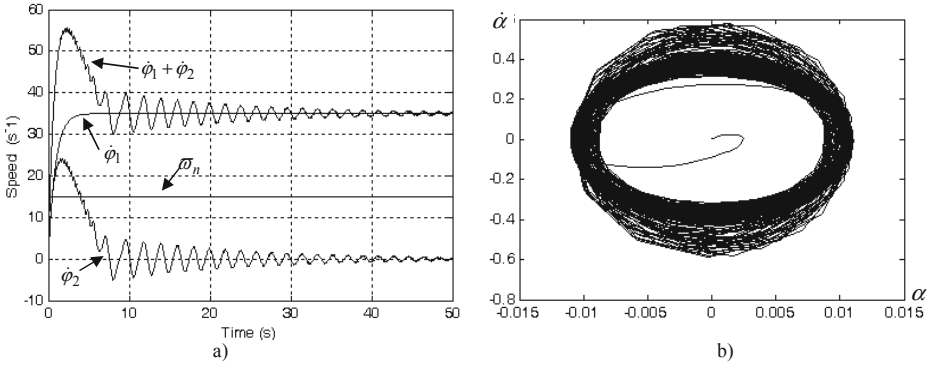

Figure 3: Solution of the system Eq. (4): a) - angular velocities of the double pendulum joints; b) – phase plane.

Fig. (4) presents the solution of the system of equations when the vibration exciter operates in self-resonance mode. The following parameters were used for simulations: $\omega_{1\max} = 35$, $\omega_n = 15$, $\lambda = 0.1$, $\mu = 0.02$, $\nu = 10$, $b_2 = 0.05$. In this regime of motion the angular velocities of the dis-balances are different. The angular frequency of the shaft is much higher than the natural frequency; the angular frequency of link 4 and the frequency of the generated vibrations are similar but still little lower that the natural frequency of the system. Though the angular frequency of the driving shaft is higher than the natural frequency, the system operates in the regime of self resonance.

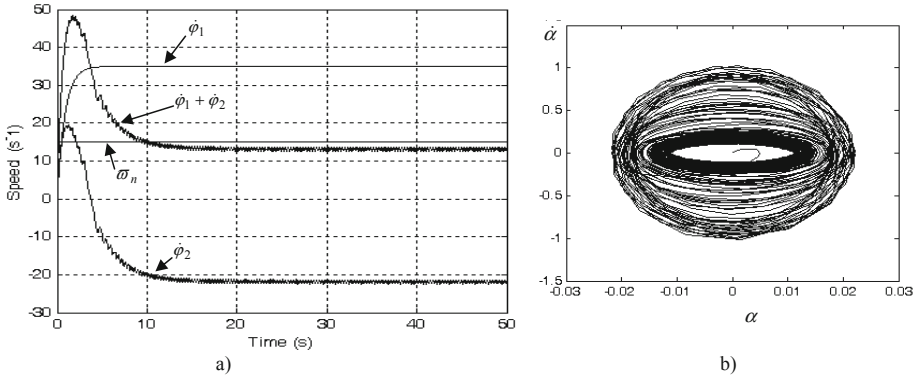

Figure 4: Solution of the system Eq. (4) (self resonance regime): a) - angular velocities of the double pendulum joints; b) – phase plane

Thus numerical simulations confirm conclusions produced by analytic investigations. It is determined that self resonance mode can coexist with usual vibration modes at certain parameter values when the vibration exciter operates in automatic resonance mode.

3 EXPERIMENTAL INVESTIGATION OF THE EFFECT OF SELF-RESONANCE

The goal of the experimental investigations was to analyze the steady state regimes of motion of vibroexciters with embedded dis-balance and to determine the frequences of self-resonance. Eccentric vibroexciter was designed for experimental investigations; its construction is presented in Fig. (5).

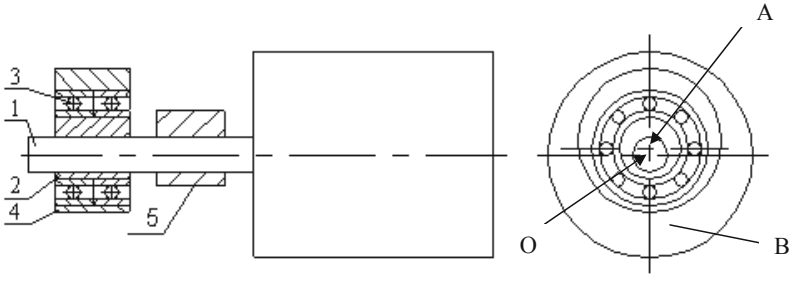

Figure 5: The construction of eccentric vibroexciter: 1 – axis of electric motor; 2,4,5 – dis-balances; 3 – bearing.

Complex dis-balance consisting from two dis-balances 2 and 4 is mounted on the axis of variable AC electric motor. The dis-balances are jointed by bearing 3. It can be noted that the axes of rotation of dis-balances 2 and 4 do not coincide. The additional dis-balance 5 is used for balancing the shaft of electric motor. Different kinds of viscous materials were used to fill the spacing between dis-balances 2 and 4 thus varying the damping moment. The vibroexciter was mounted on the springs with variable stiffness.

The eccentric vibroexciter Fig. (5) was placed and fixed firmly by four bolts on a hollow steal cube. The digital holography PRISMA system is used for the investigation vibration modes of the cheek of the hollow steal cube which is excited by the fixed eccentric vibroexciter.

3.1 Experimental optical setup

The tests used the PRISMA system layout [5] shown in Fig. (6). The PRISMA system shown in Figure 6 is a two beam speckle pattern interferometer. The laser beam directed at the object. is the object beam; the other beam. which goes directly to the camera, is the reference beam. Laser light is scattered from the object and collected by the camera lens, which also images the object onto the CCD camera sensors. The reference beam goes directly to the camera, usually in an optical fiber, where it overlaps the image of the object Shape changes that occur between a reference and a stressed state of the object produce fringes on top of the image of the object. which is displayed on the TV monitor.

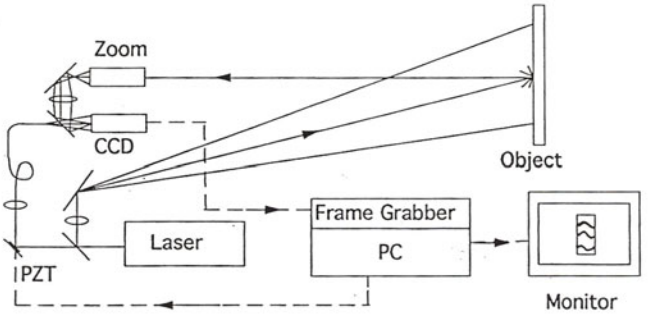

Figure 6. Optical setup for PRISMA system.

Phase shifting is required for TV holography. Phase shifting is usually accomplished by applying a voltage to a piezoelectric (PZT) crystal behind one of the mirrors in the reference beam. This changes the optical path length of the reference beam by a quarter wave length of light between each frame. A common test procedure is to collect eight TV frames of phase shifted data. The first four frames are collected and stored in computer memory as the reference state of the object The object is then stressed for the test, and another four frames of data are collected and stored. The eight frames of data, four frames from the object reference state and four frames from the object stressed state, are then processed in the PC. The result is displayed as fringes on top of the image of the object on the TV monitor [5] tokios nėra nuorodos. The fringes show a contour map of the shape change between the object reference and the stressed state. Data collection and processing can be done at the TV frame rate, so object shape changes that are slow compared to 30 Hz are displayed on the TV monitor as they happen, which is called "real time".

Because the TVH system is an optical interferometer, a fraction of a wave length of light path length change between the reference beam and the object beam shifts the fringe pattern. and random path length changes caused by unwanted vibration completely wipe out the fringes and destroy the data; consequently, TV holography is done in an optical laboratory, on an optical table that is supported on an air suspension system, to isolate the optical system and test part from mechanically vibrations caused by rotating machinery or people walking around the work area.

TVH also imposes special conditions on the laser light source. If the laser has many longitudinal modes, then the reference and the object beam path lengths must be carefully matched. This is of course possible on a large optical table, but inconvenient for building a small TVH system. Single frequency lasers are convenient for TVH. They have a long enough coherence length that object and reference beam path lengths do not need to be the same; consequently, with single frequency lasers it is possible to configure a convenient TVH interferometer package. The disadvantage, of course, is that high power, single frequency lasers are expensive.

PRISM combines all the necessary equipment for deformation and vibration measurement of most materials in a small lightweight system. A standard system includes holography and computer systems integrated with proprietary state of the art software. The main parts of the PRISMA system setup are presented in Fig. (7).

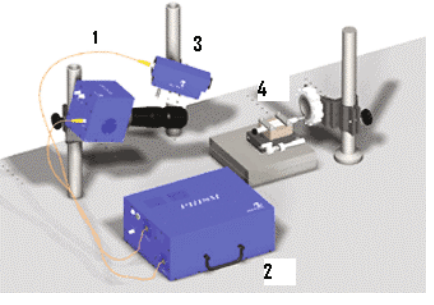

Figure 7. PRISMA system setup: 1- videohead; 2 – control block; 3 – illumination head of the object; 4- eccentric vibroexiter

Success in deformation and vibration measurement requires a fast affordable solution. PRISM offers a high-speed holographic technique for production measurement of vibration and deformation without surface contact and minimal sample preparation. PRISM can access complex geometries (deep recesses or curves) difficult or impossible for other techniques and can be configured for specific needs in experimental investigation of mechanical and mechatronics systems.

3.2 Experimental results

The hollow steal cube was excited by the fixed eccentric vibroexciter and by changing rotational frequencies the various working regimes of vibroexciter were achieved. At the same time the cheek of the hollow steal cube because of vibroexciter was forced to vibrate and the vibrating modes were recorded in real time by the PRISMA holographic system. The recorded holographic interferograms are presented in the Fig. (8). It is clearly seen that only holographic interferogram which is recorded in the self-resonance mode illustrate about the steady state regime while other because of the noise they are not seen and illustrate the transient re-

gimes of vibroexciter. The holographic PRISMA system allows recording the time-average vibration only.

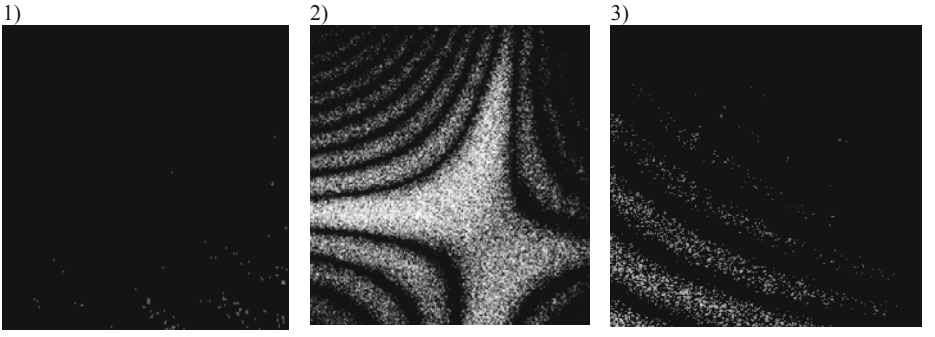

Figure 8. Holographic interferogram of the cheek of the hollow steal cube: 1- before self-resonance mode; 2- self-resonance mode; 3 – after self resonance mode

4 CONCLUSIONS

The dynamics of eccentric vibroexciter with complex disbalance is investigated. It is determined what kind of exciters with high speed motors can generate low frequency vibrations in steady state regimes of operation.

The effect of self-resonance is experimentally investigated. This effect can be effectively applied for securing the functionality of different mechanisms in the regime of resonance.

The recorded holographic interferograms illustrates the existing the steady state regime in eccentric vibroexciter which corresponds to self resonance mode of vibroexciter

REFERENCES

1. Ehrich, F. E. Indenfication and Avoidance of Instabilities and Self-Excited Vibrations Rotating Machinery. ASME Paper 72-DE-21, May 1972.
2. I.V.Andrianov, V.V.Danishevskyy. Asimptotic approach for non-linear periodical vibrations of continuous structures. *Journal of sounds and vibrations,* **249(3),** 465-481, 2002.
3. A.J.Mcmillan. A non-linear friction model for self-excited vibrations. *Journal of Sound and Vibration,* **205(3)**, 323-335, 1997.
4. K. Ragulskis, R. Palevicius, M. Ragulskis, A. Palevicius, D. Rubliauskas. Investigation of the effect of self-resonance of vibration excitation systems. Proceedings of SPIE, Ancona, Italy, June 22-25, 2004.
5. Palevičius, Arvydas, Hayman, G.; Steinzig, M.. Holographic PRISMA system for investigation of mechatronic systems. Vibroengineering 2006 Proceedings of the 6th International Conference, Kaunas, Lithuania, October 12-14, 2006.

*Ramutis.Palevicius@ktu.lt, tel. 370 37 310347

IAK 2008
Conference on Interdisciplinary Applications of Kinematics
A. Kecskeméthy, V. Potkonjak and A. Müller (eds.)
Lima, Peru, 9–11 January 2008

KINEMATIC CRITERIA FOR STRUCTURAL SYNTHESIS OF MAXIMALLY REGULAR PARALLEL ROBOTS WITH PLANAR MOTION OF THE MOVING PLATFORM

Grigore Gogu

Mechanical Engineering Research Group
French Institute of Advanced Mechanics and Blaise Pascal University,
Campus de Clermont-Ferrand / les Cézeaux, BP 265, 63175 Aubière, France
e-mail: Grigore.Gogu@ifma.fr

Keywords: Kinematic criteria, Structural synthesis, Parallel robots, Maximally regular.

Abstract. *This paper presents an application of kinematics in the structural synthesis of maximally regular parallel robots with planar motion of the moving platform. The moving platform has three planar degrees of freedom, which are two planar translations and one rotation around an axis perpendicular to the plane of translations. A method is proposed for structural synthesis of maximally regular parallel robots with planar motion of the moving platform based on new kinematic criteria. A one-to-one correspondence exists between the actuated joint velocity space and the external velocity space of the moving platform. The Jacobian matrix mapping the two vector spaces of the maximally regular parallel robots is a 3×3 identity matrix throughout the entire workspace. The condition number and the determinant of the Jacobian matrix being equal to one, the maximally regular parallel robots perform very well with regard to force and motion transmission capabilities. The new kinematic criteria, used for structural synthesis, are based on the recent formulae proposed by the author for mobility, connectivity, redundancy and overconstraint of parallel robots. These kinematic criteria allow us to get new families of over constrained and non overconstrained maximally regular parallel robots with planar motion of the moving platform. The solutions, obtained by this systematic approach of structural synthesis, are presented for the first time in the literature.*

1 INTRODUCTION

Parallel manipulation has been the subject of study of much robotic research during the last two decades. Parallel robotic manipulators (PMs) are composed of an end effector (moving platform) connected to the base (fixed platform) by at least two kinematic chains called legs or limbs. The moving platform of a *TaRb*-type parallel robot can complete $0 \leq a \leq 3$ independent translational motions (*T*) and $0 \leq b \leq 3$ rotational motions (*R*).

Rigidity, accuracy, high speed, and high load-to-weight ratio are the main merits of PMs. With respect to serial manipulators, disadvantages include a smaller workspace, complex command and a lower dexterity due to a high motion coupling and multiple singularities inside their workspace. Maximally regular and fully-isotropic parallel manipulators overcome these disadvantages. They have a very simple command and realize important energy-saving due to the fact that for a unidirectional motion only one motor works as in serial manipulators.

We know that the Jacobian matrix of a robotic manipulator is the matrix mapping (i) the actuated joint velocity space and the end-effector velocity space, and (ii) the static load on the end-effector and the actuated joint forces or torques. Isotropy of a robotic manipulator is related to the condition number of its Jacobian matrix, which can be calculated as the ratio of the largest and the smallest singular values. A robotic manipulator is fully-isotropic if its Jacobian matrix is isotropic throughout the entire workspace, i.e., the condition number of the Jacobian matrix is one. Thus, the condition number of the Jacobian matrix is an interesting performance index characterizing the distortion of a unit sphere under this linear mapping. The condition number of the Jacobian matrix was first used by Salisbury and Craig [1] to design mechanical fingers and developed by Angeles [2] as a kinetostatic performance index of the robotic mechanical systems. The isotropic design aims at ideal kinematic and dynamic performance of the manipulator [3]. In an isotropic configuration, the sensitivity of a manipulator is minimal with regard to both velocity and force errors and the manipulator can be controlled equally well in all directions. The concept of kinematic isotropy has been used as a criterion in the design of various parallel manipulators [4], [5].

Five types of PMs are identified in [6]: (i) maximally regular PMs, if the Jacobian *J* is an identity matrix throughout the entire workspace, (ii) fully-isotropic PMs, if the *J* is a diagonal matrix with identical diagonal elements throughout the entire workspace, (iii) PMs with uncoupled motions if *J* is a diagonal matrix with different diagonal elements, (iv) PMs with decoupled motions, if *J* is a triangular matrix and (v) PMs with coupled motions if *J* is neither a triangular nor a diagonal matrix. Fully-isotropic PMs give a one-to-one mapping between the actuated joint velocity space and the external velocity space. The condition number and the determinant of the Jacobian matrix being equal to one, the manipulator performs very well with regard to force and motion transmission.

The term maximally regular parallel robot was recently coined by Merlet [7] to define isotropic robots. We use this term to define just the particular case of fully-isotropic PMs, when the Jacobian matrix is an identity matrix throughout the entire workspace. Various solutions of maximally regular and fully-isotropic PMs have been very recently presented in the literature [8]-[15].

Parallel manipulators with planar motion of the moving platform are used in applications that require positioning and orienting a body in a plane. They enable two independent translations in the plane and one rotation on an axis perpendicular to the plane of translations. Planar and/or spatial mechanisms can be used to obtain the planar motion of the moving platform.

Various architectures are used in the literature to obtain three-legged PMs based on planar mechanisms [7]. The possible combinations of revolute, R, and prismatic, P, joints which connect the moving platform to the fixed base in a three-legged planar PM are: RRR, PRR, RPR,

RPR, RRP, PPR, RPP and PRP. The successions of the three joints start from the fixed base to the mobile platform. Since any one of the three joints in any of the seven kinematic chains may be actuated there are 21 possible limb architectures. The various combinations of these limb architectures give 1653 possible planar PMs with only lower pairs possessing three DoFs [16]. These architectures were extensively studied in [16-32]. We note that they are not fully-isotropic.

The first solutions of fully-isotropic PMs with planar motion of the moving platform have been presented in [13]. These solutions are based on four families of planar and spatial over-constrained mechanisms. This paper represents a development of the approach presented in [13] by presenting new families of overconstrained and non-overconstrained PMs in a unified approach of structural synthesis. These solutions are presented for the first time in the literature.

The classical methods used for structural synthesis of PMs can be divided into four approaches: (i) the methods based on displacement group theory [33]-[34], (ii) the methods based on screw algebra [35]-[38], (iii) the method based on constraint and direct singularity investigation [8] and (iv) the method based on the theory of linear transformations [11]-[15].

The approach presented in this paper is founded on the theory of linear transformations and integrates the new formulae of mobility, connectivity, redundancy and overconstraints of parallel manipulators proposed in [39]-[42].

The main aims of this paper are to present the new kinematic criteria for structural synthesis along with new families of maximally regular PMs with planar motion of the moving platform based on planar and spatial mechanisms.

2 KINEMATIC CRITERIA FOR STRUCTURAL SYNTHESIS

The main kinematic criteria used for structural synthesis are associated with mobility, connectivity, redundancy and overconstraint of parallel mechanisms.

Mobility is the main structural parameter of a mechanism and also one of the most fundamental concepts in the kinematic and the dynamic modelling of mechanisms [39]. IFToMM terminology defines the mobility or the degree of freedom as the number of independent coordinates required to define the configuration of a kinematic chain or mechanism [43].

Mobility M is used to verify the existence of a mechanism $(M>0)$, to indicate the number of independent parameters in robot modelling and to determine the number of inputs needed to drive the mechanism.

Earlier works on the mobility of mechanisms go back to the second half of the nineteenth century. During the twentieth century, sustained efforts were made to find general methods for the determination of the mobility of any rigid body mechanism. Various formulae and approaches were derived and presented in the literature. Contributions have continued to emerge in the last years. Mobility calculation still remains a central subject in the theory of mechanisms.

The various methods proposed in the literature for mobility calculation of the closed loop mechanisms fall into two basic categories:

a) approaches for mobility calculation based on setting up the kinematic constraint equations and calculating their rank for a given position of the mechanism with specific joint locations,

b) formulae for a quick calculation of mobility without the need to develop the set of constraint equations.

The approaches used for mobility calculation based on setting up the kinematic constraint equations and their rank calculation are valid without exception. The major drawback of these approaches is that the mobility cannot be determined quickly without setting up the kinematic

model of the mechanism. Usually this model is expressed by the closure equations that must be analyzed for dependency. There is no way to derive information about mechanism mobility without performing position, velocity or static analysis by using analytical tools (screw theory, linear algebra, affine geometry, Lie algebra, etc). For this reason, the real and practical value of these approaches is very limited in spite of their valuable theoretical foundations. Moreover, the rank of the constraint equations is calculated in a given position of the mechanism with specific joint locations. The mobility calculated in relation to a given configuration of the mechanism is an instantaneous mobility which can be different from the general mobility (global mobility or gross mobility). Global mobility has a single value for a given mechanism; it is a global parameter characterizing the mechanism in all its configurations except its singular ones. Instantaneous mobility is a local parameter characterizing the mechanism in a given configuration including singular ones. In a singular configuration the instantaneous mobility could be different from the global mobility.

A formula for quick calculation of mobility is an explicit relationship between the following structural parameters: the number of links and joints, the motion/constraint parameters of joints and of the mechanism. Usually, these structural parameters are easily determined by inspection without any need to develop the set of kinematic constraint equations.

We note that the classical formulae for a quick calculation of mobility, known as Chebychev-Grübler-Kutzbach formulae do not fit many classical mechanisms and recent parallel robots. These formulae have been recently reviewed in [39] and their limits have been set up in [40]. New formulae for quick calculation of the mobility have been proposed in [41] and demonstrated via the theory of linear transformations. A development of these contributions can be found in [6].

The connectivity between two links of a mechanism represents the number of independent finite and/or infinitesimal displacements allowed by the mechanism between the two links.

The number of overconstraints of a mechanism is given by the difference between the maximum number of joint kinematic parameters that could lose their independence in the closed loops, and the number of joint kinematic parameters that actually lose their independence in the closed loops.

Let us consider the case of a parallel mechanism $F \leftarrow G_1\text{-}G_2\text{-}\ldots G_k$ in which the end-effector $n \equiv n_{Gi}$ is connected to the reference link $1 \equiv 1_{Gi}$ by k simple or complex kinematic chains G_i ($1_{Gi}\text{-}2_{Gi}\text{-}\ldots n_{Gi}$). The mechanism $F \leftarrow G_1\text{-}G_2\text{-}\ldots G_k$ is characterized by:

R_{Gi} - the vector space of relative velocities between the extreme links n_{Gi} and 1_{Gi} in the kinematic chain G_i disconnected from the mechanism F,

R_F - the vector space of relative velocities between the extreme links $n \equiv n_{Gi}$ and $1 \equiv 1_{Gi}$ in the mechanism $F \leftarrow G_1\text{-}G_2\text{-}\ldots G_k$,

$S_{Gi}=dim(R_{Gi})$ –the connectivity between extreme the links n_{Gi} and 1_{Gi} in the kinematic chain G_i disconnected from the mechanism F,

$S_F=dim(R_F)$ - the connectivity between the extreme links $n \equiv n_{Gi}$ and $1 \equiv 1_{Gi}$ in the mechanism $F \leftarrow G_1\text{-}G_2\text{-}\ldots G_k$.

The formulae demonstrated in [6] for mobility M, connectivity S_F, overconstraint N and redundancy T of the parallel mechanism $F \leftarrow G_1\text{-}G_2\text{-}\ldots G_k$ represent the kinematic criteria for structural synthesis of parallel robotic manipulators:

$$M = \sum_{i=1}^{p} f_i - r \tag{1}$$

$$N = 6q - r \tag{2}$$

$$T = M - S_F \tag{3}$$

where

$$S_F = dim(R_F) = dim(R_{G1} \cap R_{G2} \cap ... \cap R_{Gk}) \tag{4}$$

$$r = \sum_{i=1}^{k} S_{Gi} - S_F + r_l \tag{5}$$

and

$$r_l = \sum_{i=1}^{k} r_l^{Gi} . \tag{6}$$

where p represents the total number of joints, q is the total number of independent closed loops in the sense of graph theory, f_i is the mobility of the ith joint, r - the number of joint parameters that lose their independence in the mechanism F, r_l^{Gi} - the number of joint parameters that lose their independence in the closed loops of limb G_i, r_l - the total number of joint parameters that lose their independence in the closed loops that may exist in the limbs of the mechanism F.

We note that the intersection in Eq. (4) is consistent if the operational velocity spaces R_{Gi} are defined by the velocities of the same point situated on the end-effector. This point is called the characteristic point, and is denoted in this paper by H. It is the point with the most restrictive motion of the end-effector.

The connectivity S_F of the end-effector $n \equiv n_{Gi}$ in the mechanism $F \leftarrow G_1\text{-}G_2\text{-}...G_k$ is less than or equal to the mobility M of the mechanism F.

The basis of the vector space R_F of relative velocities between the end-effector $n \equiv n_{Gi}$ and the reference link $1 \equiv 1_{Gi} \equiv 0$ in the mechanism $F \leftarrow G_1\text{-}G_2\text{-}...G_k$ dos not vary with the position of the characteristic point on $n \equiv n_{Gi}$.

When there are various ways to choose the basis of the operational spaces, the bases of R_{Gi} in Eq. (4) are selected such as the minimum value of S_F is obtained. By this choice, the result of Eq. (4) fits in with general mobility definition as the minimum value of the instantaneous mobility.

We consider the translations along the x- and y-axes and the rotation about the z-axis that is perpendicular to the Oxy plane. We denote by q_1, q_2, q_3 and $\dot{q}_1$, $\dot{q}_2$, $\dot{q}_3$ the finite displacements and the velocities in the actuated joints and by v_x, v_y and ω_z the translational and angular velocities of a characteristic point H situated on the moving platform. With these notations, the linear mapping between the actuated joint velocity space and the end-effector velocity space is defined by:

$$\begin{bmatrix} v_x \\ v_y \\ \omega_z \end{bmatrix} = [J] \begin{bmatrix} \dot{q}_1 \\ \dot{q}_2 \\ \dot{q}_3 \end{bmatrix} \tag{7}$$

where J is the Jacobian matrix.

If the following conditions for mobility, connectivity between the mobile and the fixed platform and for the base (R_F) of the vector space of relative velocities of the mobile platform are fulfilled, than the parallel mechanism F has uncoupled motions.

a) General conditions for any position of the mechanism when $\dot{q}_1 \neq 0$, $\dot{q}_2 \neq 0$, and $\dot{q}_3 \neq 0$

$$3 \leq M_{Gi} = S_{Gi} \leq 6 \quad (i=1,2,3) \tag{8}$$

$$M = 3 \tag{9}$$

$$S_F = 3 \tag{10}$$

$$(R_F)=(v_x, v_y, \omega_z). \tag{11}$$

b) Particular conditions when $\dot{q}_1=0$

$$S_F=2 \tag{12}$$

$$(R_F)=(v_y, \omega_z). \tag{13}$$

c) Particular conditions when $\dot{q}_2=0$

$$S_F=2 \tag{14}$$

$$(R_F)=(v_x, \omega_z). \tag{15}$$

c) Particular conditions when $\dot{q}_3=0$

$$S_F=2 \tag{16}$$

$$(R_F)=(v_x, v_y). \tag{17}$$

Condition $M_{Gi}=S_{Gi}$ indicates the fact that each limb is non-redundant and $M=S_F$ the fact that the parallel mechanism is also non redundant.

If the Jacobian J is a diagonal matrix the parallel manipulator has uncoupled motions and the singular values are equal to the diagonal elements. The Jacobian J of a fully isotropic mechanism has non zero identical singular values and unit condition number. Consequently, if all diagonal elements of a diagonal Jacobian matrix are identical, than the PM is fully isotropic. The existence of this mechanism involves:

$$v_x=\lambda\ \dot{q}_1 \tag{18}$$

$$v_y=\lambda\ \dot{q}_2 \tag{19}$$

$$\omega_z=\lambda\ \dot{q}_3 \tag{20}$$

where λ is the value of the diagonal elements. The parallel mechanism respecting the conditions (18)-(20) is fully-isotropic and implicitly it has uncoupled motions. This mechanism realizes a homothetic transformation of coefficient λ between the velocity of the actuated joints and the velocity of the moving platform. When $\lambda=1$ the Jacobian matrix becomes the 3×3 identity matrix and the PM is maximally regular. In this paper, we focus on the structural synthesis of this type of parallel robots with planar motion of the moving platform based on spatial mechanisms.

3 MAXIMALLY REGULAR PARALLEL ROBOTS WITH PLANAR MOTION OF THE MOVING PLATFORM

The basic kinematic structure of a PM with planar motion of the moving platform is obtained by concatenating three limbs G_1 ($1_{G1}\equiv0$-...-$n_{G1}\equiv n$), G_2 ($1_{G2}\equiv0$-...-$n_{G2}\equiv n$), and G_3 ($1_{G3}\equiv0$-...-$n_{G3}\equiv n$). The first link 1_{Gi} of each limb is the fixed platform denoted by *0* and the final link is the moving platform denoted by *n*. We consider $v_x=\dot{x}$, $v_y=\dot{y}$ and $\omega_\alpha=\dot{\alpha}$ the translational and angular velocities of a characteristic point *H* situated on the mobile platform. We note that α is the rotation angle of the moving platform around z-axis ($\omega_\alpha\equiv\omega_z$).

We used an evolutionary morphology (EM) approach [6] for structural synthesis of each limb G_i ($i=1,2,3$). EM is formalized by a 6-tuple of design objectives, protoelements (initial components), morphological operators, evolution criteria, morphologies and a termination criterion. The final objectives are expressed by (8-17) and (18)-(20) where $\lambda=1$. The protoelements are the revolute and prismatic joints. The morphological operators are:

(re)combination, mutation, migration and selection. These operators are deterministic and are applied at each generation of EM. Evolutionary morphology is a complementary method with respect to evolutionary algorithms that starts from a given initial population to obtain an optimum solution with respect to a fitness function. EM creates this initial population to enhance the chance of obtaining a "more global optimum" by non-quantified diversification of the initial population. Evolutionary algorithms are optimization oriented methods; EM is a conceptual design oriented method. More details on evolutionary morphology could by find in [6].

The simplest kinematic structure of a maximally regular PM with planar motion of the moving platform (Fig. 1) has the limbs G_1 and G_2 of type $\underline{P}PR$ ($\underline{P} \perp P \perp^{\perp} R$) and the limb G_3 is a homokinetic double universal joint with telescopic shaft of type $\underline{R}UPU$. We have denoted by U a universal joint of type $R \perp R$. We consider that the first joint of each limb G_i ($i=1,...,3$) is actuated (the underlined joint). The direction of the actuated prismatic joint is parallel to the x-axis in limb G_1 and the y-axis in limb G_2. The input and the output shaft of the homokinetic double universal joint in limb G_3 are parallel to the z-axis.

The limbs G_i ($i=1$ and 2) have $M_{Gi}=S_{Gi}=3$ and $(R_{Gi})=(v_x, v_y, \omega_z)$. The limb G_3 has $M_{G3}=S_{G3}=6$ and $(R_{G3})=(v_x, v_y, v_z, \omega_x, \omega_y, \omega_z)$. The notation $\perp$ between two joints indicates that the joints have orthogonal axes/directions. In $\underline{P} \perp P \perp^{\perp} R$, the notation $\perp^{\perp}$ indicates that the axis of the revolute joint is perpendicular to the direction of the both prismatic joints.

The basic kinematic structure of a maximally regular parallel robot of type $2\underline{P}PR\text{-}1\underline{R}UPU$ with planar motion of the moving platform $n=7$ presented in Fig. 1 has three limbs ($k=3$), two independent closed loops ($q=2$), twelve revolute and prismatic joints ($p=12$) with $\sum_{i=1}^{p} f_i = 12$ and three simple limbs with $S_1=S_2=3$, $S_3=6$ and $r_l^{Gi}=0$ ($i=1,2,3$). We note that in a simple limb no closed loops exist [6]. Equations (4-6) give $S_F=3$, $r=9$ and $r_l=0$. Equations (1)-(3) indicate that this solution is non-redundant ($T=0$) with three degrees of mobility ($M=3$) and three degrees of overconstraint ($N=3$).

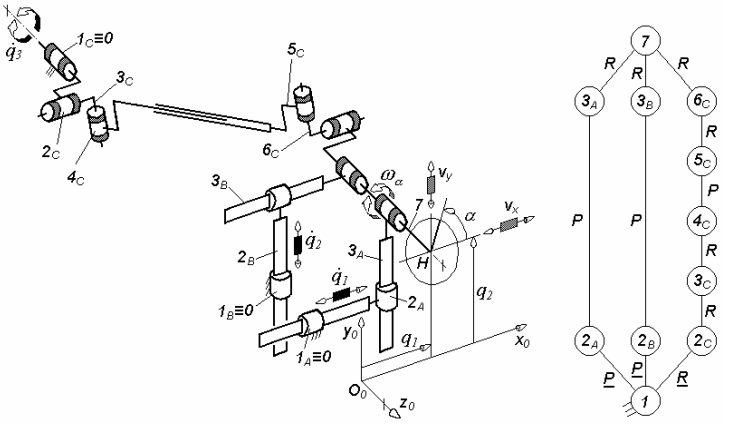

Figure 1: Basic kinematic structure of maximally regular PM with planar motion of the moving platform and three degrees of overconstraint.

a) *PC*R-PPR-RUPU*-type

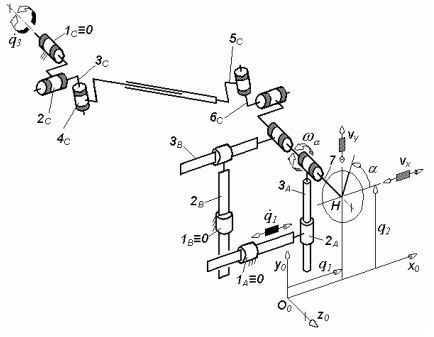

b) *PPC*-PPR-RUPU*-type

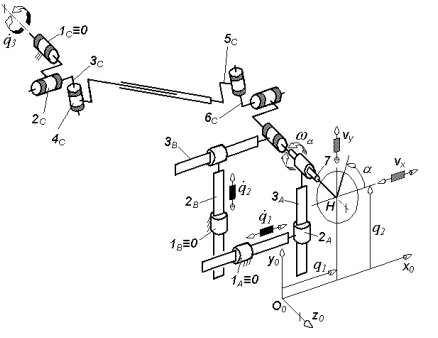

c) *PR*PR-PPR-RUPU*-type

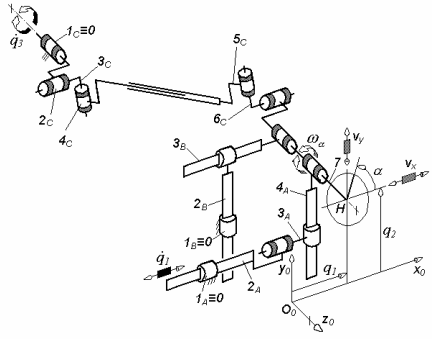

d) *PPR-PC*R-RUPU*-type

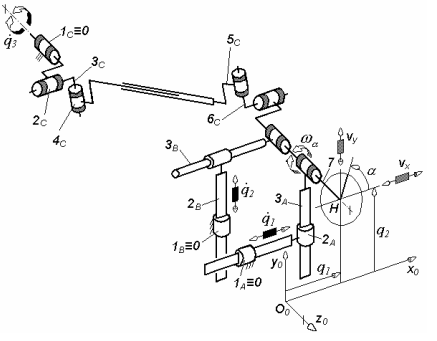

e) *PPR-PPC*-RUPU*-type

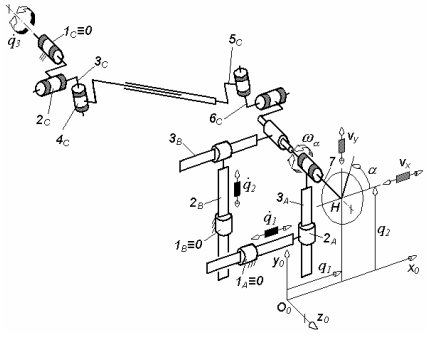

f) *PPR-PR*PR-RUPU*-type

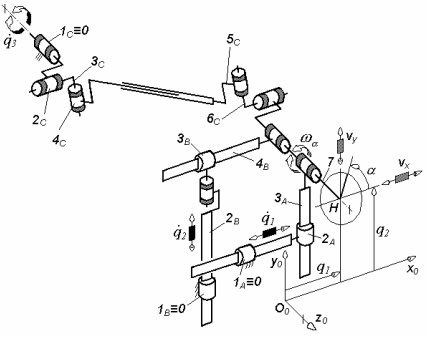

Table 1: Basic kinematic structures of maximally regular PMs with planar motion of the moving platform and two degrees of overconstraint.

a) *PC*C*-PPR-RUPU*-type

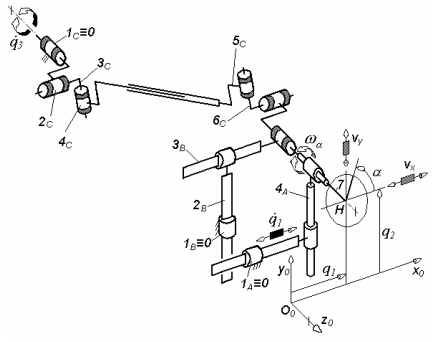

b) *PR*C*R-PPR-RUPU*-type

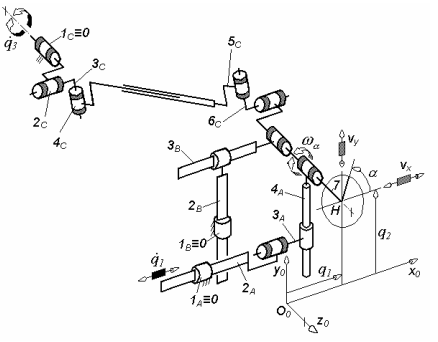

c) *PR*PC*-PPR-RUPU*-type

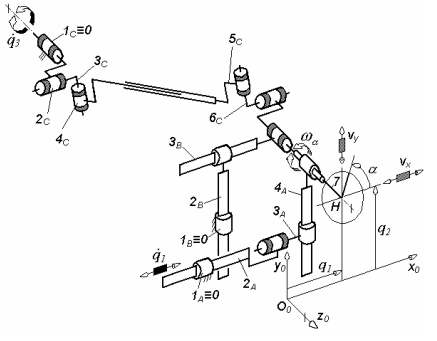

d) *PPR-PC*C*-RUPU*-type

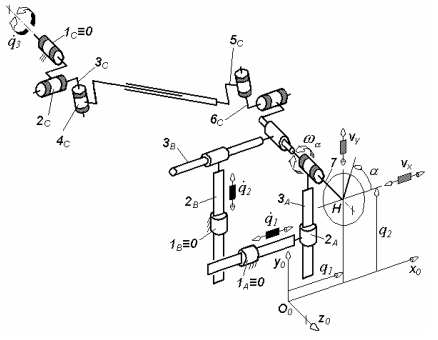

e) *PPR-PR*C*R-RUPU*-type

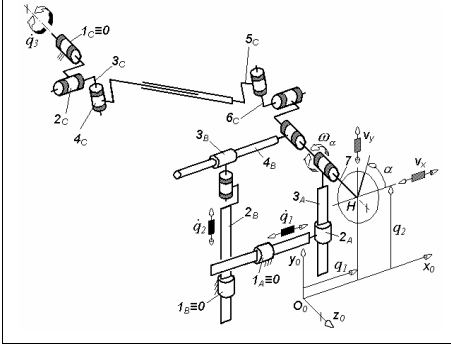

f) *PPR-PR*PC*-RUPU*-type

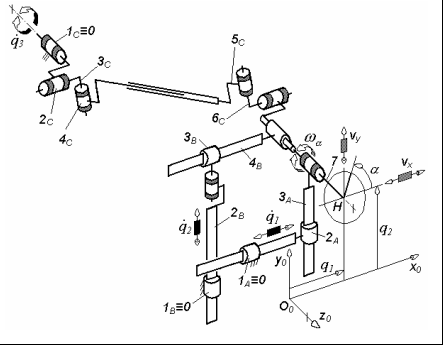

Table 2: Basic kinematic structures of maximally regular PMs with planar motion of the moving platform and one degree of overconstraint.

g) <u>P</u>C*R-<u>P</u>C*R-<u>R</u>UPU-type	h) <u>P</u>C*R-<u>P</u>PC*-<u>R</u>UPU-type
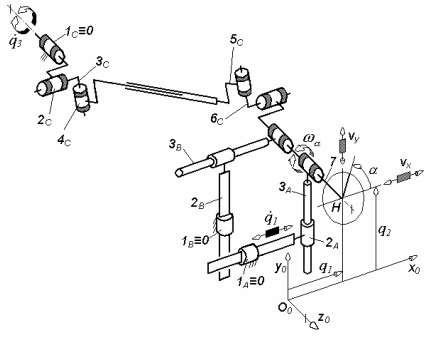	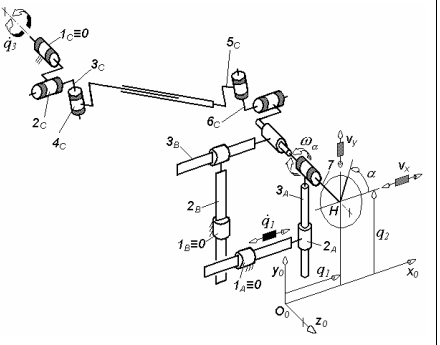
i) <u>P</u>PC*-<u>P</u>C*R-<u>R</u>UPU-type	j) <u>P</u>PC*-<u>P</u>R*PR-<u>R</u>UPU-type
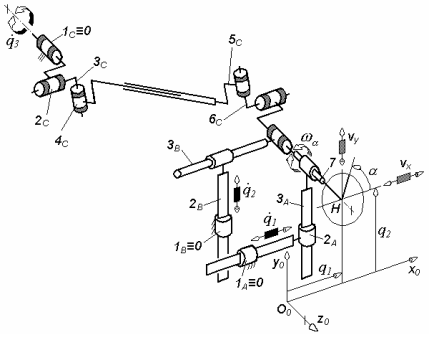	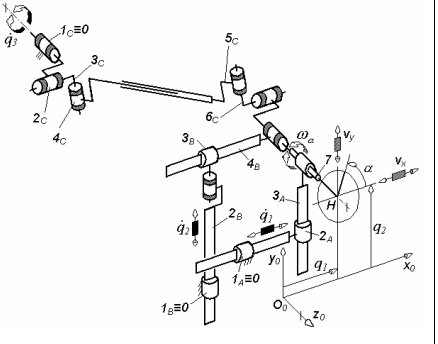
k) <u>P</u>RPR-<u>P</u>PC*-<u>R</u>UPU-type	l) <u>P</u>R*PR-<u>P</u>R*PR-<u>R</u>UPU-type
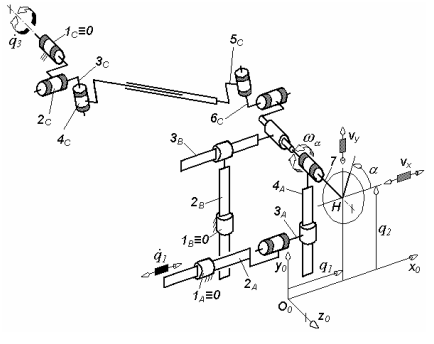	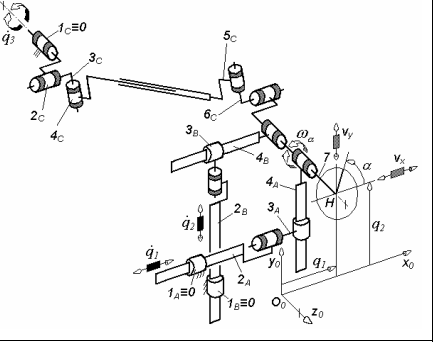

Table 2: (continued).

a) *PR*C*C*-PPR-RUPU*-type

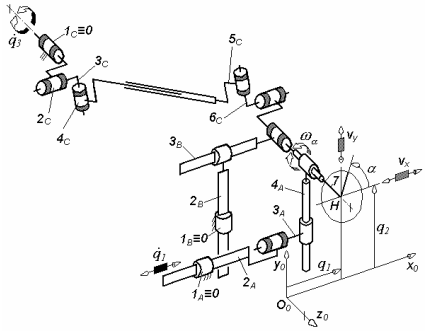

b) *PPR-PR*C*C*-RUPU*-type

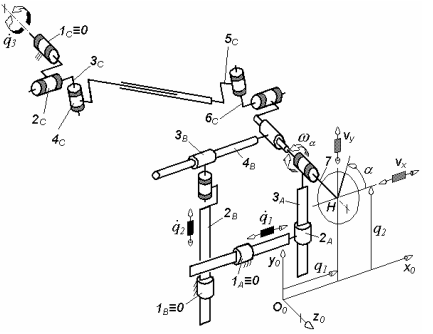

c) *PC*C*-PC*R-RUPU*-type

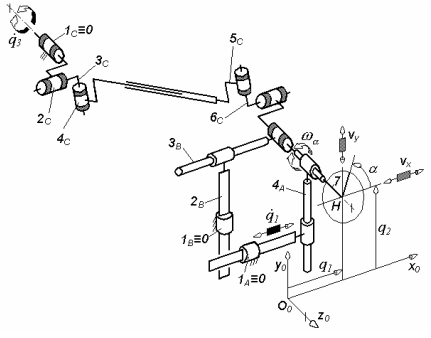

d) *PR*PC*-PR*PR-RUPU*-type

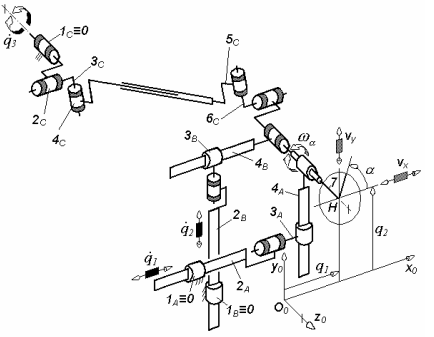

e) *PR*C*R-PPC*-RUPU*-type

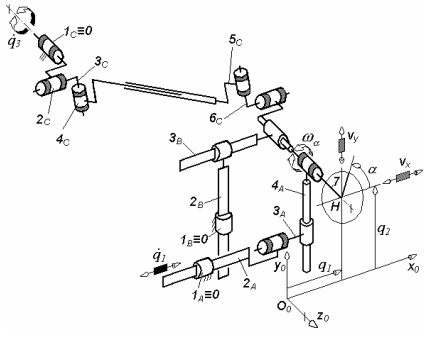

Table 3: Basic kinematic structures of non overconstrained maximally regular PMs with planar motion of the moving platform.

Kinematic structure	Table	Bases of the vector spaces R_{Gi}	
		(R_{G1})	(R_{G2})
*PC*R-PPR-RUPU*	1a	$(v_x, v_y, \omega_y, \omega_z)$	(v_x, v_y, ω_z)
PPC-PPR-RUPU*	1b	$(v_x, v_y, v_z, \omega_z)$	(v_x, v_y, ω_z)
*PR*PR-PPR-RUPU*	1c	$(v_x, v_y, \omega_x, \omega_z)$	(v_x, v_y, ω_z)
*PPR-PC*R-RUPU*	1d	(v_x, v_y, ω_z)	$(v_x, v_y, \omega_x, \omega_z)$
PPR-PPC-RUPU*	1e	(v_x, v_y, ω_z)	$(v_x, v_y, v_z, \omega_z)$
*PPR-PR*PR-RUPU*	1f	(v_x, v_y, ω_z)	$(v_x, v_y, \omega_y, \omega_z)$
*PC*C*-PPR-RUPU*	2a	$(v_x, v_y, v_z, \omega_y, \omega_z)$	(v_x, v_y, ω_z)
*PR*C*R-PPR-RUPU*	2b	$(v_x, v_y, \omega_x, \omega_y, \omega_z)$	(v_x, v_y, ω_z)
*PR*PC*-PPR-RUPU*	2c	$(v_x, v_y, v_z, \omega_x, \omega_z)$	(v_x, v_y, ω_z)
*PPR-PC*C*-RUPU*	2d	(v_x, v_y, ω_z)	$(v_x, v_y, v_z, \omega_x, \omega_z)$
*PPR-PR*C*R-RUPU*	2e	(v_x, v_y, ω_z)	$(v_x, v_y, \omega_x, \omega_y, \omega_z)$
*PPR-PR*PC*-RUPU*	2f	(v_x, v_y, ω_z)	$(v_x, v_y, v_z, \omega_y, \omega_z)$
*PC*R-PC*R-RUPU*	2g	$(v_x, v_y, \omega_y, \omega_z)$	$(v_x, v_y, \omega_x, \omega_z)$
*PC*R-PPC*-RUPU*	2h	$(v_x, v_y, \omega_y, \omega_z)$	$(v_x, v_y, v_z, \omega_z)$
PPC-PC*R-RUPU*	2i	$(v_x, v_y, v_z, \omega_z)$	$(v_x, v_y, \omega_x, \omega_z)$
PPC-PR*PR-RUPU*	2j	$(v_x, v_y, v_z, \omega_z)$	$(v_x, v_y, \omega_y, \omega_z)$
*P*RPR-PPC*-RUPU*	2k	$(v_x, v_y, \omega_x, \omega_z)$	$(v_x, v_y, v_z, \omega_z)$
*PR*PR-PR*PR-RUPU*	2l	$(v_x, v_y, \omega_x, \omega_z)$	$(v_x, v_y, \omega_y, \omega_z)$
*PR*C*C*-PPR-RUPU*	3a	$(v_x, v_y, v_z, \omega_x, \omega_y, \omega_z)$	(v_x, v_y, ω_z)
*PPR-PR*C*C*-RUPU*	3b	(v_x, v_y, ω_z)	$(v_x, v_y, v_z, \omega_x, \omega_y, \omega_z)$
*PC*C*-PC*R-RUPU*	3c	$(v_x, v_y, v_z, \omega_y, \omega_z)$	$(v_x, v_y, \omega_x, \omega_z)$
*PR*PC*-PR*PR-RUPU*	3d	$(v_x, v_y, v_z, \omega_x, \omega_z)$	$(v_x, v_y, \omega_y, \omega_z)$
*PR*C*R-PPC*-RUPU*	3e	$(v_x, v_y, \omega_x, \omega_y, \omega_z)$	$(v_x, v_y, v_z, \omega_z)$

Table 4: Bases of the vector spaces R_{Gi} ($i=1,2$) of the maximally regular PMs with planar motion of the moving platform presented in Tables 1-3.

To simplify the notations of the links e_{Gi} of limbs Gi ($i=1,...,3$ and $e=1,...,n$), by avoiding the double index in Fig. 1 and the following figures, we have denoted by e_A the links belonging to the limb G_1 ($e_A \equiv e_{G1}$) and by e_B and e_C the links of the limbs G_2 ($e_B \equiv e_{G2}$) and G_3 ($e_C \equiv e_{G3}$).

The solutions presented in Tables 1-3 have $k=3$, $q=2$, $M=S_F=3$, and $r_l=0$. Equations (2) and (5) give the following values: $\sum_{i=1}^{k} S_{Gi} = 13$ for the solutions with two degrees of overconstraint, $\sum_{i=1}^{k} S_{Gi} = 14$ for the solutions with one degree of overconstraint, and $\sum_{i=1}^{k} S_{Gi} = 15$ for the non overconstrained solutions. Solutions with two and one degree of overconstraint can be obtained from the basic solution in Fig. 1 by introducing idle mobilities in the joints of the limbs G_1 and/or G_2 (see Tables 1 and 2). No overconstrained solutions can be obtained by introducing three idle mobilities in the limbs G_1 and/or G_2 as we can see in Table 3. The joints in which the idle mobilities are introduced are denoted by *.The basis of the vector space of relative velocities between the mobile platform 7 and the fixed base in the kinematic chain associated with the limb G_3 disconnected from the parallel mechanism is $(R_{G3}) = (v_x, v_y, v_z, \omega_x, \omega_y, \omega_z)$ for all solutions in Tables 1-3. The bases (R_{G1}) and (R_{G2}) are systematized in Table 4. In Tables 1-4, C stands for the cylindrical joint.

Figure 2 presents a derived structural solution of maximally regular PM with planar motion of the moving platform obtained from the basic solution in Fig. 1 by superposing the last revolute joints of the limbs G_1 and G_2. In this case, moving platform 7 is connected by just two revolute joints to a complex and a simple limb ($k=2$). The complex limb is obtained by interconnecting G_1 and G_2 and the simple limb is the former G_3-limb of type $\underline{R}UPU$.

The complex limb of type ($\underline{P}PP\underline{P}$)$R$ combines a closed loop ($\underline{P}PP\underline{P}$) with a revolute joint. Two joint parameters lose their independence in the closed loop $\underline{P}PP\underline{P}$-type and $r_l=2$. The basis of the vector space of the relative velocities between the mobile platform 7 and the fixed base in the kinematic chain ($\underline{P}PP\underline{P}$)$R$ disconnected from the parallel mechanism is (v_x, v_y, ω_z).

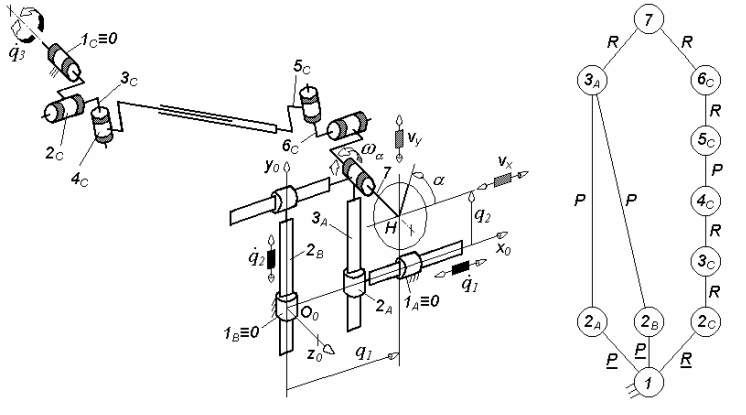

Figure 2: Derived kinematic structure of maximally regular PM with planar motion of the moving platform and four degrees of overconstraint.

The derived kinematic structure of the maximally regular parallel robot of type (*PPPP*)*R*-*RUPU* with planar motion of moving platform $n=7$ presented in Fig. 2 has four degrees of overconstraint (N=4). Equations (2) and (5) give the following values**:** $r_f=3$ for the solutions with three degrees of overconstraint, $r_f=4$ for the solutions with two degree of overconstraint, $r_f=5$ for the solutions with one degree of overconstraint and $r_f=6$ for the non overconstrained solutions. These solutions can be obtained from the solution in Fig. 2 by introducing idle mobilities in the closed loop (*PPPP*) – see Tables 5-7. We note that the total number of the joint parameters that lose their independence in a closed loop coincides with the connectivity between the distal links of the associated open kinematic chain obtained by splitting up the fixed base of the closed loop [6].

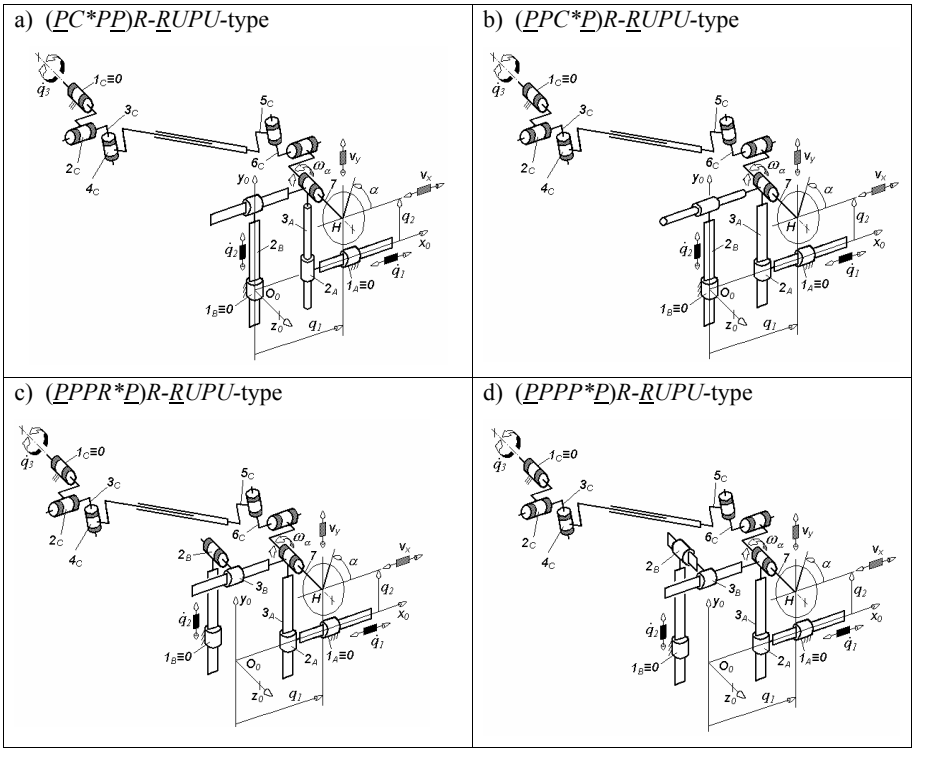

Table 5: Derived kinematic structures of maximally regular PMs with planar motion of the moving platform and three degrees of overconstraint.

a) (<u>P</u>C*C*<u>P</u>)R-<u>R</u>UPU-type

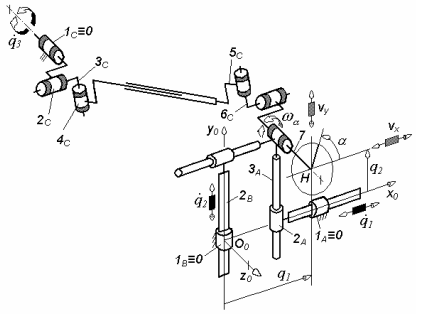

b) (<u>P</u>C*PR*<u>P</u>)R-<u>R</u>UPU-type

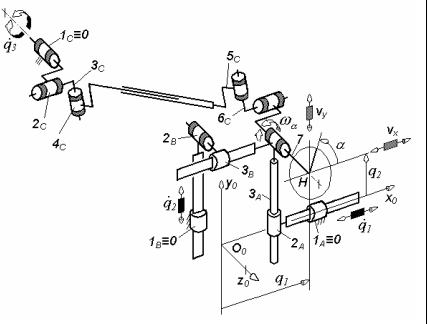

c) (<u>P</u>C*PP*<u>P</u>)R-<u>R</u>UPU-type

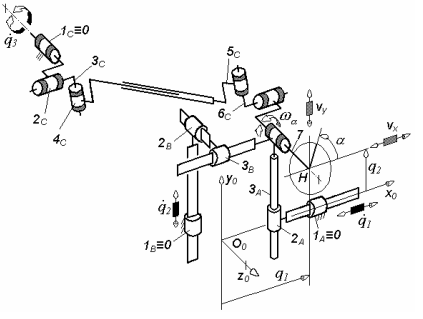

d) (<u>P</u>PC*R*<u>P</u>)R-<u>R</u>UPU-type

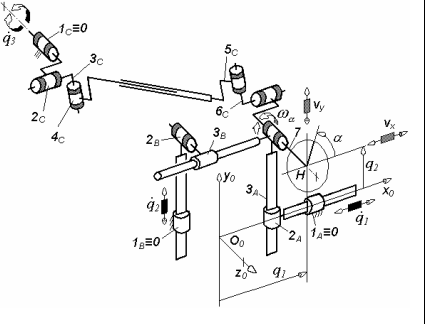

e) (<u>P</u>PC*P*<u>P</u>)R-<u>R</u>UPU-type

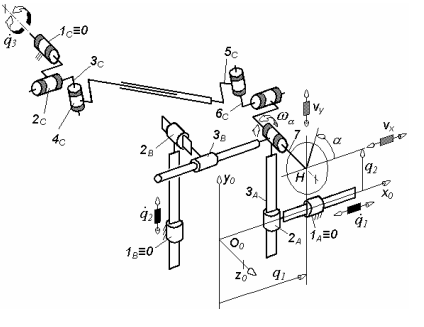

Table 6: Derived kinematic structures of maximally regular PMs with planar motion of the moving platform and two degrees of overconstraint.

a) (*PC*C*RP*)*R*-*RUPU*-type

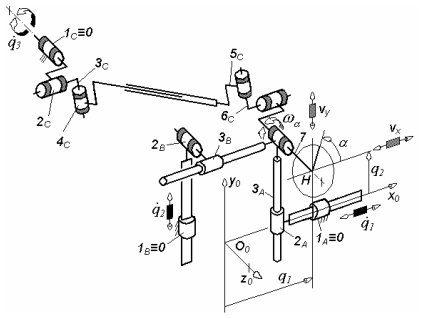

b) (*PC*C*P*P*)*R*-*RUPU*-type

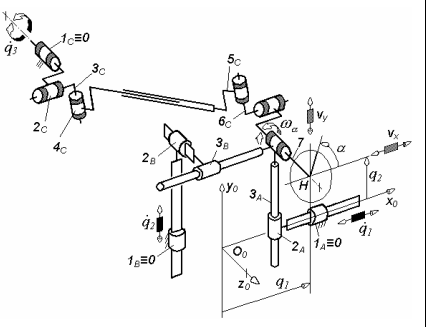

c) (*PC*C*C*P*)*R*-*RUPU*-type

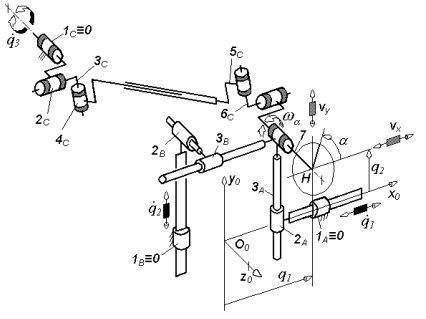

Table 7: Derived kinematic structures of maximally regular PMs with planar motion of the moving platform: solutions with one degree of overconstraint (**a** and **b**) and non overconstrained solutions (**c**)

4 CONCLUSIONS

Mobility, connectivity, redundancy and overconstraint represent the main kinematic criteria for structural synthesis of parallel robots. An approach has been proposed for structural synthesis of overconstrained and non overconstrained maximally regular parallel robots with planar motion of the moving platform. The Jacobian matrix mapping the articulated and the operational vector spaces of the maximally regular parallel robotic manipulators proposed in this paper is the 3×3 identity matrix throughout the entire workspace. Basic and derived solutions with various degrees of overconstraint are presented for the first time. These solutions are obtained by a systematic approach of structural synthesis founded on the theory of linear transformations and an evolutionary morphology. The approach integrates the new formulae for mobility, connectivity, redundancy and overconstraint of parallel manipulators recently proposed by the author. The method proposed in this paper can be easily extrapolated to structural synthesis of other types of parallel robot with various combinations of translational and rotational motions of the moving platform.

REFERENCES

[1] J. K. Salsbury, J. J. Craig. Articulated hands: force and kinematic issues. *International Journal of Robotics Research*, **1**, 1-17, 1982.

[2] J. Angeles. *Fundamentals of robotic mechanical systems*: *Theory, methods, and algorithms*. Springer, New York, 1997.

[3] A. Fattah, A. M. Hasan Ghasemi. Isotropic design of spatial parallel manipulators. *International Journal of Robotics Research*, **21**, 811-824, 2002.

[4] K. E. Zanganeh, J. Angeles. Kinematic isotropy and the optimum design of parallel manipulators. *International Journal of Robotics Research*, **16**, 185-197, 1997.

[5] K. Y. Tsai, D. Huang. The design of isotropic 6-DOF parallel manipulators using isotropy generators. *Mechanism and Machine Theory*, **38**, 1199-1214, 2003.

[6] G. Gogu. *Structural synthesis of parallel robots*. Springer, Dordrecht, 2008.

[7] J. P. Merlet. *Parallel robots*, 2nd edn, Springer, Dordrecht, 2006.

[8] M. Carricato, V. Parenti-Castelli. Singularity-free fully-isotropic translational parallel mechanisms. *International Journal of Robotics Research*, **22**, 161-174, 2002.

[9] H. S. Kim, L-W. Tsai. Evaluation of a Cartesian parallel manipulator. In Advances in robot kinematics, J. Lenarčič and F. Thomas, eds. Kluwer Academic Publishers, 21-28, 2002.

[10] X. Kong, C. M. Gosselin. Type synthesis of linear translational parallel manipulators. In Advances in robot kinematics, J. Lenarčič and F. Thomas, eds. Kluwer, pp. 453-462, 2002.

[11] G. Gogu. Structural synthesis of fully-isotropic translational parallel robots via theory of linear transformations. *European Journal of Mechanics– A/Solids*, **23**, 1021-1039, 2004.

[12] G. Gogu. Fully-isotropic T3R1-type parallel manipulators. In: On advances in robot kinematics, Lenarčič, J., Galletti, C. (eds). Kluwer Academic Publishers, Dordrecht, 265-272, 2004.

[13] G. Gogu. Fully-isotropic over-constrained planar parallel manipulators. Proceedings of IEEE/RSJ International Conference on Intelligent Robots and Systems, Sendai, pp 3519-3524, 2004.

[14] G. Gogu. Fully-isotropic hexapods. In: Advances in robot kinematics: Mechanisms and motion, J. Lenarčič, B. Roth, eds. Springer, Dordrecht, pp 323-330, 2006

[15] G. Gogu. Structural synthesis of fully-isotropic parallel robots with Schönflies motions via theory of linear transformations and evolutionary morphology. *European Journal of Mechanics– A/Solids*, **26**,:242-269, 2007.

[16] M.J.D. Hayes, P.J. Zsombor-Murray, C. Chen. Unified kinematic analysis of general planar parallel manipulators. *ASME Journal of Mechanical Design*, **126**:866-874, 2004.

[17] K.H. Hunt. Geometry of robotic devices. *Mechanical Engineering Transactions*, **7**, 213-220, 1982.

[18] J. Rooney, C. F. Earle. Manipulator postures and kinematics assembly configurations. Proceedings of the 6th World Congress on the Theory of Machines and Mechanisms, pp. 1014-1020, 1983.

[19] K.H. Hunt. Structural kinematics of in parallel actuated robot arms. *Journal of Mechanisms, Transmissions and Automation in Design*, **105**, 705-712, 1983.

[20] B. Sumpter, A. H. Soni. Simulation algorithm of Oklahoma Crawdad robot. Proceedings of the 9th Applied Mechanisms Conference, 1985.

[21] A.H. Shirkhodaie, A.H. Soni. Forward and inverse synthesis for a robot with three degrees of freedom. Proceedings of the 19th Summer Computation Simulation Conference, 851-856, 1987.

[22] C. M. Gosselin, J. Angeles. The optimum kinematic design of a planar three-degree-of-freedom parallel manipulator. *ASME Journal of Mechanisms, Trans., and Automation in Design*, **110**, 35-41, 1988.

[23] C. M. Gosselin, J. Sefrioui, M. J. Richard. Solution polynomiale au problème de la cinématique directe des manipulateurs parallèles plans à 3 degrés de liberté. *Mechanism and Machine Theory*, **27**, 107-119, 1992.

[24] H.R.M. Daniali, P-J. Zsombor-Murray, J. Angeles. The kinematics of a 3 dof planar and spherical double-triangle parallel manipulator. Computational Kinematics, J. Angeles, P. Kovacs and G. Hommel, eds. Kluwer, 153-164, 1993.

[25] C. M. Gosselin, J-P. Merlet. On the direct kinematics of planar parallel manipulators: special architectures and number of solutions. *Mechanism and Machine Theory*, **29**, 1083-1097, 1994.

[26] C. M. Gosselin, J. Wang. Singularity loci of planar parallel manipulator. Proceedings of the 9th World Congress on the Theory of Machines and Mechanisms, 1982-1986, 1995.

[27] H.R.M. Daniali, P-J. Zsombor-Murray, J. Angeles. Singularity analysis of planar parallel manipulators. *Mechanism and Machine Theory*, **30**, 665-678, 1995.

[28] C. M. Gosselin, S. Lemieux, J-P. Merlet. A new architecture of planar three-degree-of freedom parallel manipulator. Proceedings of IEEE Int. Conf. on Robotics and Automation, 3738-3743, 1996.

[29] J-P. Merlet. Direct kinematics of planar parallel manipulators. Proceedings of IEEE International Conference on Robotics and Automation, pp. 3744-3749, 1996.

[30] R.L. Williams II, A.R. Joshi. Planar parallel 3-RPR manipulator. Proceedings of the 6th Conference on Applied Mechanisms and Robotics, pp. 1-8, 1999.

[31] S. Caro, D. Chablat, P. Wenger, J. Angeles. The isoconditioning loci of planar three-dof parallel manipulators. In: Recent Advances in Integrated Design and Manufacturing in Mechanical Engineering, G. Gogu, D. Coutellier, P. Chedmail and P. Ray, eds. Kluwer Academic Publishers, 129-138, 2003.

[32] I. A. Bonev, D. Zlatanov, G. M. Gosselin. Singularity analysis of 3-DOF planar parallel mechanisms via screw theory. *ASME Journal of Mechanical Design*, **125**:573-581, 2003.

[33] J. M. Hervé, F. Sparacino. Structural synthesis of parallel robots generating spatial translation. Proceedings of the 5th IEEE International Conference on Advanced Robotics, 2079-2082, 1991.

[34] J. M. Hervé, "Design of parallel manipulators via the displacement group," Proceedings of the 9th World Congress on the Theory of Machines and Mechanisms, pp. 2079-2082, 1995.

[35] A. Frisoli, D. Checcacci, F. Salsedo, M. Bergamasco. Synthesis by screw algebra of translating in-parallel actuated mechanisms. In: Advances in robot kinematics, J. Lenarčič and M. M. Stanišić, eds. Kluwer Academic Publishers, 433-440, 2000.

[36] X. Kong, C. M. Gosselin. Generation of parallel manipulators with three translational degrees of freedom based on screw theory. Proceedings of CCToMM Symposium on Mechanisms, Machines and Mechatronics, Montreal, 2001.

[37] Y. Fang, L-W. Tsai. Structural synthesis of a class of 4-dof and 5-dof parallel manipulators with identical limb structures. *International Journal of Robotics Research*, **21**, 799-810, 2002.

[38] Z. Huang, Q.C. Li. Type synthesis of symmetrical lower-mobility paralle mechanisms using the constraint-synthesis method. *International Journal of Robotics Research*, **22**, 59-79, 2003.

[39] G. Gogu. Mobility of mechanisms: a critical review. *Mechanism and Machine Theory*, **40**, 1068-1097, 2005.

[40] G. Gogu. Chebychev-Grubler-Kutzbach's criterion for mobility calculation of multi-loop mechanisms revisited via theory of linear transformations. *European Journal of Mechanics– A/Solids*, **24**, 427-441, 2005.

[41] G. Gogu. Mobility and spatiality of parallel robots revisited via theory of linear transformations. *European Journal of Mechanics– A/Solids*, **24**, 690-711.

[42] G. Gogu. Mobility criterion and overconstraints of parallel manipulators. Proceedings of International Workshop on Computational Kinematics Cassino, 2005.

[43] T. G. Ionescu. Terminology for mechanisms and machine science. *Mechanism and Machine Theory*, **38**, 597-901, 2003

IAK 2008
Conference on Interdisciplinary Applications of Kinematics
A. Kecskeméthy, V. Potkonjak and A. Muller (eds.)
Lima, Peru, 9–11 January 2008

A DESIGN-TO-TASK APPROACH FOR WIRE ROBOTS

Tobias Bruckmann*, Lars Mikelsons*, and Manfred Hiller*

*Chair for Mechatronics
University of Duisburg-Essen, Campus Duisburg, Lotharstrasse 1, 47057 Duisburg, Germany
e-mail: {bruckmann,mikelsons,hiller}@imech.de,
web page: http://www.imech.de

Keywords: Parallel Kinematics, Synthesis, Design-to-Task, Optimization, Interval Analysis, Wire Robot

Abstract. *Wire robots consist of a moveable end-effector which is connected to the machine frame by motor driven wires. Since wires can transmit only tension forces, at least $m = n + 1$ wires are needed to tense a system having n degrees-of-freedom. This leads to a kinematical redundancy and a $m-n$ dimensional solution space for the wire force distribution. For their calculation, sophisticated mathematical methods are required. Nevertheless workspace analysis is an important task in applications. Discrete methods do not produce satisfying results, since intermediate points on the discrete calculation grids are neglected. To overcome this problem, intervals instead of points can be used. On the one hand, this leads to reliable results, on the other hand, the approach can be extended to solve synthesis tasks, which is even more important in practical applications. In this paper, a Design-to-Workspace approach using interval analysis is presented, i.e. calculation of an optimal robot layout for a given workspace. Furthermore, a first extension of this approach to a Design-to-Task approach is presented. Design-to-Task denotes the problem of calculating the optimal robot for a specific task.*

1 INTRODUCTION

At the Chair for Mechatronics, a testbed for tendon-based Steward-platforms (SEGESTA Seilgetriebene Stewart-Plattformen in Theorie und Anwendung) has been developed during the past few years (Fig. (1)). Presently, the SEGESTA teststand has $n = 6$ d.o.f. and uses $m = 8$ wires to move the platform along desired trajectories [12]. Wires can transmit only tension forces, thus at least $m = n+1$ wires are needed to tense a system having n degrees-of-freedom. This results in a kinematical redundancy. Therefore, the solution space of the wire force distribution has dimension $m - n$. For this reason, the workspace analysis requires sophisticated mathematical methods. Discrete methods, which are widely used as in [6] and [21], suffer from the fact that only a finite number of points is examined. Thus, properties of the examined points are accredited to the points in between though they might differ, i.e. points outside the real workspace may appear as part of the calculated workspace. In [3] an analytical approach for the workspace-boundary computation of wire-based systems is shown. Since only the workspace boundary is computed, properties of inner points like stiffness can not be considered. In [20] a method for the calculation of the workspace of an underconstrained wire robot is presented. An approach to calculate the workspace boundaries is also shown in [8] while an approach for continuous workspace analysis of wire robots is presented in [9] and [5]. The latter presents also an Design-to-Workspace approach, which even maybe of greater practical relevance than workspace analysis for application. In literature, usually optimization is performed with respect to the size (or volume) of the workspace or workspace indices, e.g. [11] and [19]. Again, discrete methods are widely used as in [22]. An approach for planar systems is shown in [7]. In [15] an algorithm to verify given trajectories is presented. Here the Design-to-Workspace concept is extended by trajectory generation and verification, resulting in a Design-to-Task approach which guarantees globally optimal trajectories as well as globally optimal geometrical parameters at the same time. Note that the used approach allows to combine different workspace criteria. Within this paper, the usable workspace is defined by a force equilibrium which is later on coupled with a stiffness requirement. The force equilibrium can be described as ([17],[21])

$$\begin{bmatrix} \boldsymbol{\nu}_1 & \cdots & \boldsymbol{\nu}_m \\ \boldsymbol{p}_1 \times \boldsymbol{\nu}_1 & \cdots & \boldsymbol{p}_m \times \boldsymbol{\nu}_m \end{bmatrix} \begin{bmatrix} f_1 \\ \vdots \\ f_m \end{bmatrix} + \begin{bmatrix} \boldsymbol{f}_p \\ \boldsymbol{\tau}_p \end{bmatrix} = 0 \tag{1}$$

with $\boldsymbol{\nu} = \frac{\boldsymbol{l}_\mu}{|\boldsymbol{l}_\mu|}, \quad \mu = 1, \ldots, m$ and $\boldsymbol{f} > 0$ or in a more compact form as

$$\boldsymbol{A}^{\mathrm{T}} \boldsymbol{f} + \boldsymbol{w} = \boldsymbol{0}, \quad \boldsymbol{f} > 0. \tag{2}$$

where there following symbols are used:

- The coordinate frame C_B is the base frame, while C_P is connected to the platform (Fig. 2).
- The vectors $\boldsymbol{b}_\mu$ denote the positions of the winch points, represented by the points where tendons are led through small ceramic eyes which are fixed.
- $\boldsymbol{p}_\mu$ are the platform-fixed vectors to the connecting points
- $\boldsymbol{l}_\mu$ denote the tendon vectors from the platform to the winches.
- The forces in the tendons are described by f_μ, where $\boldsymbol{f}_P$ and $\boldsymbol{\tau}_P$ denote all other applied forces and torques acting on the platform.

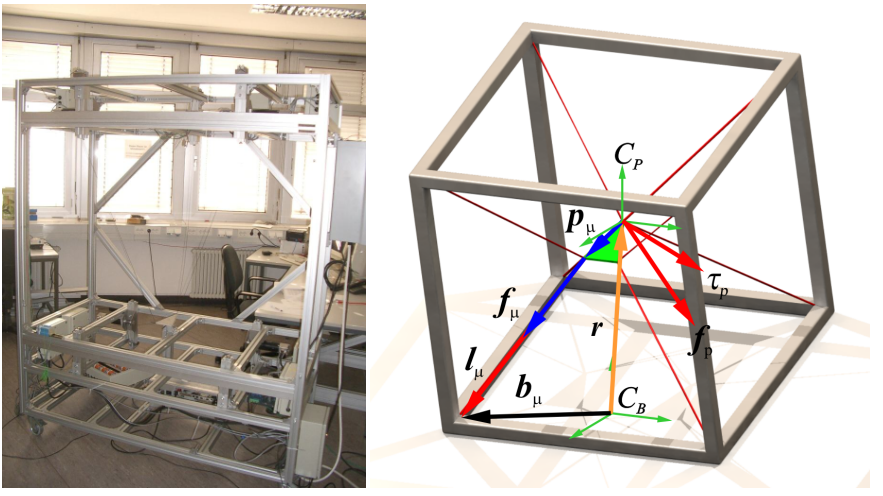

Figure 1: SEGESTA Testbed and Symbol Definitions for a General Tendon-Based Stewart-Platform

Using this formula as a criterion for workspace calculation, the problem can be described as a *Constraint Satisfaction Problem (CSP)*. There exist various methods for solving CSPs. Within this paper a method based on interval analysis is used [18].

2 CONSTRAINT SATISFACTION PROBLEM

A CSP is the problem of determining all $\underline{c} \in \mathcal{X}_c$ such that

$$\begin{aligned} \boldsymbol{\Phi}(\boldsymbol{c}, \boldsymbol{v}) &> 0 \\ \forall\, \boldsymbol{v} &\in \mathcal{X}_v \end{aligned} \tag{3}$$

where $\boldsymbol{\Phi}$ is a system of real functions defined on a real domain representing the constraints. It will be shown later that for a description of the workspace, this problem has to be extended to

$$\begin{aligned} \boldsymbol{\Phi}(\boldsymbol{c}, \boldsymbol{v}, \boldsymbol{e}) &> 0 \\ \forall\, \boldsymbol{v} &\in \mathcal{X}_v \\ \exists\, \boldsymbol{e} &\in \mathcal{X}_e. \end{aligned} \tag{4}$$

Within this definition

- $\boldsymbol{c}$ is the vector of the *calculation variables*,
- $\boldsymbol{v}$ is the vector of the *verification* and,
- $\boldsymbol{e}$ is the vector of the *existence variables*.

The solution set for *calculation variables* of a CSP is called $\mathcal{X}_S$ i.e.

$$\begin{aligned} \boldsymbol{\Phi}(\boldsymbol{c}, \boldsymbol{v}, \boldsymbol{e}) &> 0 \\ \forall\, \boldsymbol{c} &\in \mathcal{X}_S \subset \mathcal{X}_c \\ \forall\, \boldsymbol{v} &\in \mathcal{X}_v \\ \exists\, \boldsymbol{e} &\in \mathcal{X}_e \end{aligned} \tag{5}$$

where $\mathcal{X}_c$ is the so-called search domain, i.e. the range of the calculation variables in which is searched for solutions. Within the used solver framework, CSPs are implemented independently as so-called requirements and can be arbitrary combined.

3 CONTINUOUS WORKSPACE ANALYSIS

Examining Eq. (2), the structure matrix $\boldsymbol{A}^{\mathrm{T}}$ needs to be inverted to calculate the tendon forces $\boldsymbol{f}$ from a given platform pose and given external forces $\boldsymbol{w}$. Since $\boldsymbol{A}^{\mathrm{T}}$ has a non-squared shape, this is usually done using the Moore-Penrose pseudo inverse. Thus, the calculated forces will be a least squares solution. In fact, not a least squares result but a force distribution within predefined tensions is demanded. To overcome this problem, the structure matrix is divided into a squared $n \times n$ matrix $\boldsymbol{A}_{pri}^T$ and a second matrix $\boldsymbol{A}_{sec}^T$ with $r = m - n$ columns. Now, the resulting force distribution can be calculated as

$$\boldsymbol{f}_{pri} = -{\boldsymbol{A}_{pri}^T}^{-1}(\boldsymbol{w} + \boldsymbol{A}_{sec}^T \boldsymbol{f}_{sec}). \tag{6}$$

In this equation, $\boldsymbol{f}_{sec}$ is unknown. Every point and wrench satisfying

$$\boldsymbol{f}_{\min} \leq \boldsymbol{f}_{sec} \leq f_{\max} \tag{7}$$

and leading to primary tendon forces

$$\boldsymbol{f}_{\min} \leq \boldsymbol{f}_{pri} \leq f_{\max} \tag{8}$$

belongs to the workspace. Hence Eqs. (7) and (8) represent a CSP of the form of Eq. (4) with $\boldsymbol{f}_{sec}$ as existence variable. To calculate a workspace for a specific robot, the following variable set for the CSP is used:

- The platform coordinates are the *calculation variables*.
- The tendon forces $\boldsymbol{f}_{sec}$ are the *existence variables*.
- Optionally, the exerted external wrench $\boldsymbol{w}$ and desired platform orientations can be set as *verification variables*. The workspace for a fix orientation of the platform is called *constant orientation workspace* according to [14]. On the other hand, sometimes free orientation of the platform within given ranges must be possible within the whole workspace. The resulting workspace is called the *total orientation workspace*. In Fig. 3, the workspace of a simple plain manipulator is shown, based on the force equilibrium condition. In Fig. 4, the workspace under a possible external load range is shown.

3.1 Stiffness

Besides the force equilibrium, additional workspace conditions can be applied. Due to the high elasticity of the tendons (using plastic material, e.g. polyethylene), the stiffness may be low in parts of the workspace. Thus, for practical applications, especially if a predefined precision is required, it may be necessary to guarantee a given stiffness for the whole workspace. Otherwise, the compensation of elasticity effects by control may be required. Generally, this should be avoided as far as possible by an appropriate design. As shown in [21], the so-called passive stiffness can be described as the reaction of a mechanical system onto a small pertubation, described by a linear equation:

$$\delta \boldsymbol{w} = \boldsymbol{K}(\boldsymbol{x}) \delta \boldsymbol{x} \tag{9}$$

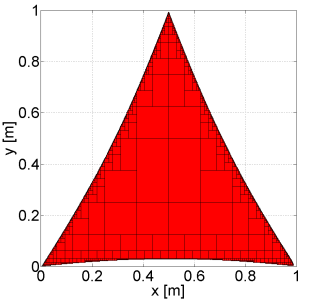

Figure 2: Force equilibrium workspace of plain manipulator, 2 translational d.o.f., $\boldsymbol{w}^T = (0,0)N, f_{\text{min}} = 10N, f_{\text{max}} = 90N$

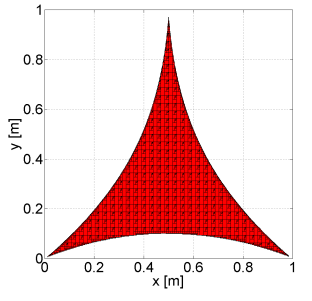

Figure 3: Force equilibrium workspace of plain manipulator, 2 translational d.o.f., $\boldsymbol{w}^T = ([-20,20]N, [-20,20]N), f_{\text{min}} = 10N, f_{\text{max}} = 90N$

where

$$\boldsymbol{K}(\boldsymbol{x}) = k' \boldsymbol{A}^T(\boldsymbol{x}) \boldsymbol{L}^{-1}(\boldsymbol{x}) \boldsymbol{A}(\boldsymbol{x}). \tag{10}$$

Here, $\boldsymbol{L}$ is the diagonal matrix of the tendon lengths and k' is the proportionality factor (force per relative elongation), treating the tendons as linear springs. For the calculation, the inverse problem

$$\delta \boldsymbol{x} = \boldsymbol{K}(\boldsymbol{x})^{-1} \delta \boldsymbol{w} \tag{11}$$

is solved and evaluated where only domains having a position pertubation within the predefined limits δx_{min} and δx_{max} under predefined loads between δw_{min} and δw_{max} are considered as workspace. This equation can again be treated as a CSP. The stiffness workspace for a simple plain manipulator is shown in Fig. 5 while the combined stiffness and force equilibrium workspace is shown in Fig. 6.

4 CONTINUOUS WORKSPACE SYNTHESIS

Workspace Synthesis describes the process of obtaining the geometrical parameters for a set $\mathcal{M} := \{m_\alpha\}, \alpha \in \mathcal{I}$ of manipulators providing a predefined workspace. This predefined workspace $\mathcal{W}_p$ is guaranteed to be a subset of each obtained manipulator's workspace $\mathcal{W}_\alpha$, i.e.

$$\mathcal{W}_p \subset \mathcal{W}_\alpha. \tag{12}$$

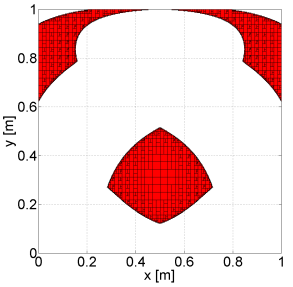

Figure 4: Stiffness workspace of plain manipulator, 2 translational d.o.f., $k' = 1000N, \delta\boldsymbol{x} = ([-0.015, 0.015]N, [-0.015, 0.015]N), \delta\boldsymbol{w} = ([-20, 20]N, [-20, 20]N)$

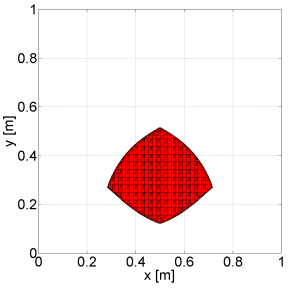

Figure 5: Combined force equilibrium and stiffness workspace of plain manipulator, 2 translational d.o.f., $\boldsymbol{w}^T = ([-20, 20]N, [-20, 20]N), \delta\boldsymbol{w} = ([-20, 20]N, [-20, 20]N), f_{\text{min}} = 10N, f_{\text{max}} = 90N, k' = 1000N, \delta\boldsymbol{x} = ([-0.015, 0.015]N, [-0.015, 0.015]N)$

In order to formulate the synthesis problem as a CSP of the form of Eq. (4), Eqs. (7) and (8) are considered again. This time the roles of the variables have to be interchanged:

- The workspace coordinates are the *verification variables*, i.e. all found parameter sets m_α describe manipulator configurations having at least the demanded workspace $\mathcal{W}_p$. Again, optionally the exerted external wrench $\boldsymbol{w}$ and a platform orientation can be given as *verification variables*.
- The tendon forces $\boldsymbol{f}_{sec}$ are the *existence variables*
- The geometrical parameters are the *calculation variables*, i.e. $\mathcal{M} = \mathcal{X}_S$.

4.1 Design-to-Workspace

Optimization is always performed with respect to a cost function. This cost function is in general arbitrary. In industrial application usually the term ”optimal” is used with respect to economic aspects, i.e. costs. In the case of wire robots, the most cost-driving factor are the wire winch units. Thus, every optimization method should reduce the number of winches as far as possible. Subsequently, within the set of all suitable robots with a minimum number of winches, a further optimization criterion can be employed. A reasonable choice is the volume

expansion. On one hand, reducing the expansion of the robot saves space within a production facility which reduces costs, on the other hand, the required wire lengths are minimized. In literature, usually the optimization is performed with respect to the size (or volume) of the workspace or workspace indices. Here, another approach is used [18]: Not a maximum size of the workspace is demanded, but the guaranteed covering of a predefined domain taking the above mentioned economic aspects into account at the same time. The following algorithm performs the required steps:

Algorithm *Design Optimization*

1. Set the number of tendons m = 3
2. Perform a Workspace Synthesis
3. If the Synthesis delivers no solution, $m = m + 1$ and go to 2
4. Perform a Global Optimization on the solution set regarding a cost function $C(\boldsymbol{c})$

Note that the initial number of wires was chosen with respect to practical aspects, i.e. d.o.f. = 2. The global optimization can be performed using interval analysis and is described in detail in [10].

4.2 Design-to-Task

The Design-to-Workspace method results in manipulators, guaranteed to have a desired workspace. Thus, the manipulator is able to perform every task within this workspace. Nevertheless, from the economic point of view, there is a need for manipulators which perform a specific task in minimum time, with minimum energy consumption or with lowest possible power. A typical industrial application is e.g. the pick-and-place task, moving a load from one point to another. Usually, this task is performed within series production, i.e. it is repeated many times. In such an application the optimal manipulator for sure finishes the job in minimal time with respect to the technical constraints (here, the term optimal is used with respect to minimal time without loss of generality). Thus, the set-up of a specialized (i.e. task-optimized) manipulator can be profitable. When using classical industrial robots, the freedom to modify the mechanical setup of the robot is very limited. Thus, only the trajectories can be modified and optimized with respect to the task. Due to the modular design of a wire robot, the task-specific optimization can be seperated into two tasks:

- Optimization of the robot: within all suitable designs, the robot which performs the task in shortest time is chosen
- Optimization of the trajectory: within all possible trajectories, the trajectory which connects the points in shortest time is chosen. The concepts needed for this step are partly explained in [2],[1] and [13].

By treating this task as a CSP, both claims can be optimized at the same time. Therefore, the trajectory is described as a spline. The spline is defined by the boundary conditions for the poses (and their derivations with respect to time) at the connection points. Therefore these quantities are the calculation variables. Formulation of the constraint to be fulfilled works straight forward. At first the trajectory between the connection points is computed. Then it is checked if the complete trajectory belongs to the workspace. Hence, the CSP looks the

same as in Eq. (7) and (8) except the trajectory generation. Afterwards an optimization on all possible trajectories is performed. For reasons of performance the optimization should be done at runtime. For integrated optimization, the variables are assigned as follows. Note, that also a separate optimization of robot and trajectory is possible:

- Robot optimization
  - The robot base is described by the positions of the winches. To optimize the robot, the winches can be moved. Therefore, $\boldsymbol{b}_i$ are *calculation variables*
  - The end effector is described by the positions of the platform anchor points $\boldsymbol{p}_i$. To optimize the robot, these points can be moved on the platform. Therefore, $\boldsymbol{p}_i$ are *calculation variables*
- Trajectory optimization
  - For every spline segment i, a travel time $T_i, i = 1, \ldots, s$ is needed where s is the number of trajectory segments. To calculate the minimum time, T_i is a *calculation variable*
  - Every connection point can be crossed at an arbitrary pose with arbitrary velocity, acceleration and jerk within predefined boundaries. Since the travel times depend on these assignments, they are *calculation variables*
  - For the whole trajectory, a path parameter t is assigned. Usually, it is normalized between zero and one. Since the whole trajectory shall be traced for validity, t is a *verification variable*

Optionally, the exerted external wrenches $\boldsymbol{w}$ can be set as *verification variables*. First, depending on the segment times T_i and the connection point pose, velocity, acceleration and jerk, the coefficients of the trajectory polynomials are calculated [6]. The polynomials describing the splines result in a description of the cartesian coordinates along the trajectory. With the knowledge of these coordinates, the regular workspace analysis can be employed. Note, that inertia loads resulting from the calculated accelerations are added to the platform loads w. If stiffness plays a role for the specific task, it can be checked additionally by the already introduced CSP. Note, that by this approach only the optimal trajectory which can be described by splines of the used order is generated. The example in Fig. (7) shows the result of an optimization for the manipulator structure shown in Fig. (6). Note that due to performance reasons and restricted time here the spline parameters are fixed. A $n = 3$ d.o.f. wire robot with $m = 4$ wires is considered. It consists of a bar-shaped platform connected by four winches. For simplicity in this example only one intermediate point is used. Hence, to guarantee continuity in terms of position, velocity, acceleration and jerk, at least one polynomial of 5th order and one polynomial of 6th order are required.

5 INTERVAL ANALYSIS

Interval Analysis is a powerful tool to solve CSPs. Therefore a short introduction is given in the following section. For two real numbers a, b an interval $I = [a, b]$ is defined as follows

$$[a, b] := \{r \mid a \leq r \leq b\}\,, \tag{13}$$

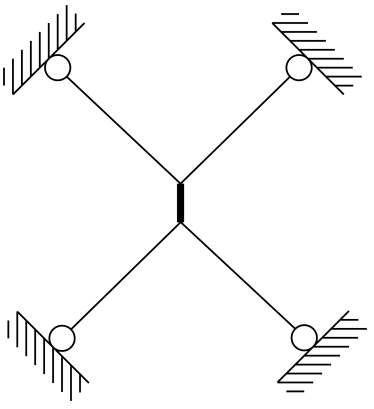

Figure 6: Example Manipulator with bar-shaped Platform

where

$$a \leq b. \tag{14}$$

Then b is called the supremum and a the infimum of I. A n-tupel of intervals is called box or interval vector. It is possible to define every operation $\circ$ on $\mathbb{R}$ on the set of intervals $\mathbb{I} = \{[a, b] \mid a, b \in \mathbb{R}, a \leq b\}$, such that the following holds:
Let $I_0, I_1 \in \mathbb{I}$ be two intervals. Then

$$\forall u \in I_0,\ \forall v \in I_1\ \exists z \in I_0 \circ I_1 \tag{15}$$

where

$$z = u \circ v. \tag{16}$$

Hence

$$\max_{u \in I_0, v \in I_1} u \circ v \leq \mathrm{Sup}(I_0 \circ I_1), \tag{17}$$

where $<$ is not unusual. This phenomenon is called overestimation and causes additional numerical effort to get sharp boundaries. For sure the same holds for $\min$ and Inf. Thus for input intervals $I_0, \ldots, I_n$ interval analysis delivers evaluations for the domain $I_0 \times I_1 \times \ldots \times I_n$. This evaluation is guaranteed to include all possible solutions, e.g.

$$[1, 3] + [2, 4] = [3, 7]\,. \tag{18}$$

In some cases overestimation can be eliminated, e.g.

$$[1, 3] + [1, 3] \cdot [-2, 1] = [-5, 6] \tag{19}$$

while

$$[1, 3] \cdot (1 + [-2, 1]) = [-3, 6]\,. \tag{20}$$

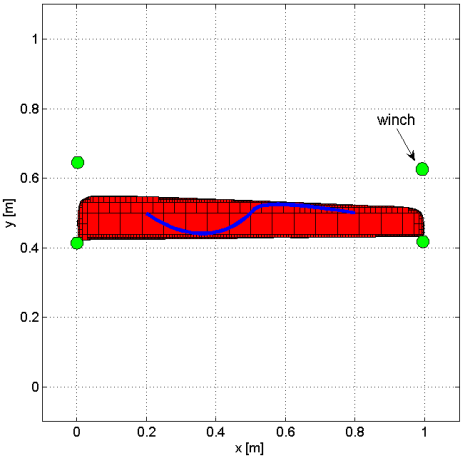

Figure 7: Manipulator optimized for shown path. Winch y-positions are the free optimization parameters.

5.1 Solving CSPs using Interval Analysis

As shown in detail in [18], the CSP can be solved using interval analysis which guarantees reliable solutions [10],[16],[15]. Solving the CSP with interval analysis delivers a list of boxes $\mathcal{L}_S$ representing an inner approximation of $\mathcal{X}_S$. According to Eq. (5), the solutions in $\mathcal{L}_S$ hold for total $\mathcal{X}_v$ and a subset of $\mathcal{X}_e$. Additionally, available implementations for interval analysis computations are robust against rounding effects. The following CSP solving algorithms have been proposed in [18]. To use it for the special problem of analyzing parallel tendon robots, they have been extended. Details are described in the next sections.

5.1.1 Algorithm Verify

Verify is called with a box $\underline{\hat{c}}$ and checks whether

$$\begin{aligned} &\underline{\Phi}(\underline{\hat{c}}, \underline{v}, \underline{e}) > 0 \\ &\forall\, \underline{v} \in \mathcal{X}_v \\ &\exists\, \underline{e} \in \mathcal{X}_e \end{aligned} \tag{21}$$

is valid for the given box $\underline{\hat{c}}$. Here the domain $\mathcal{X}_v$ is represented by the list of boxes $\mathcal{L}_T^v$. Thus, the result can be *valid*, *invalid*, *undefined* or *finite*. If at least one box is invalid, the whole search domain does not fulfill the required properties and is therefore invalid.

Algorithm *Verify*

1. Define a search domain in the list $\mathcal{L}_T^v$. In the simplest case, $\mathcal{L}_T^v$ contains one search box.
2. If $\mathcal{L}_T^v$ is empty, the algorithm is finished with *valid*.
3. Take the next box $\underline{\hat{v}}$ from the list $\mathcal{L}_T^v$.

4. If the diameter of the box$\underline{\hat{v}}$ is smaller than a predefined value ϵ_v return with *finite*.
5. If existence variables are present, call *Existence* with $\underline{\hat{c}}$ and $\underline{\hat{v}}$. If the result is *valid*, goto (2). If the box is invalid, return with *invalid*. If the box is *finite*, goto (10).
6. Evaluate $\underline{\hat{h}} = \underline{\Phi}(\underline{\hat{c}}, \underline{\hat{v}})$
7. If Inf $\underline{\hat{h}} > \underline{0}$, the infimum of $\underline{\hat{h}}$ is greater than 0 in all its components. Thus, the box is valid . Goto (2).
8. If Sup $\underline{\hat{h}} < \underline{0}$, the supremum of $\underline{\hat{h}}$ is smaller than 0 in at least one component. Thus, the box is invalid. Return with *invalid*.
9. If Inf $\underline{\hat{h}} < \underline{0} <$ Sup $\underline{\hat{h}}$, $\underline{\hat{h}}$ is rated as *undefined*.
10. Divide the box on a verification variable and add the parts to $\mathcal{L}_T^v$. Goto (2).

5.1.2 Algorithm Existence

Existence is a modification of *Verify*. It is called with the boxes $\underline{\hat{c}}, \underline{\hat{v}}$ and checks whether

$$\begin{aligned} &\underline{\Phi}(\underline{\hat{c}}, \underline{\hat{v}}, \underline{e}) > 0 \\ &\exists\, \underline{e} \in X_e \end{aligned} \tag{22}$$

is valid. Here the domain $\mathcal{X}_e$ is represented by the list of boxes $\mathcal{L}_T^e$ The result can be *valid*, *invalid* or *finite*. If at least one box is valid, the whole search domain fulfills the required properties and is therefore valid.

Algorithm *Existence*

1. Define a search domain in the list $\mathcal{L}_T^e$. In the simplest case, $\mathcal{L}_T^e$ contains one search box.
2. If $\mathcal{L}_T^e$ is empty, the algorithm is finished with *invalid*.
3. Take the next box $\underline{\hat{e}}$ from the list $\mathcal{L}_T^e$.
4. If the diameter of the box $\underline{\hat{e}}$ is smaller than a predefined value ϵ_e, return with *finite*.
5. Evaluate $\underline{\hat{h}} = \underline{\Phi}(\underline{\hat{c}}, \underline{\hat{v}}, \underline{\hat{e}})$
6. If Inf $\underline{\hat{h}} > \underline{0}$, the infimum of $\underline{\hat{h}}$ greater than 0 in all its components. Thus, the box is valid . Return with *valid*.
7. If Sup $\underline{\hat{h}} < \underline{0}$, the supremum of $\underline{\hat{h}}$ smaller than 0 in at least one component. Goto (2).
8. If Inf $\underline{\hat{h}} < \underline{0} <$ Sup $\underline{\hat{h}}$, $\underline{\hat{h}}$ is rated as *undefined*. Divide the box on an existence variable and add the parts to $\mathcal{L}_T^e$. Goto (2).

5.1.3 Algorithm Calculate

Calculate is called with a search domain for $\underline{c}$ represented by a list of boxes $\mathcal{L}_T^c$. It uses *Existence* or *Verify* to identify valid boxes within the search domain. Thus, the result is a list $\mathcal{L}_S$ of valid boxes (and optionally the lists $\mathcal{L}_I$ for invalid boxes and $\mathcal{L}_F$ for finite boxes, respectively).

Algorithm *Calculate*

1. Define a search domain in the list $\mathcal{L}_T^c$. In the simplest case, $\mathcal{L}_T^c$ contains one search box.
2. Create the lists
   (a) $\mathcal{L}_S$ for solution boxes,
   (b) $\mathcal{L}_I$ for invalid boxes,
   (c) $\mathcal{L}_F$ for finite boxes.
3. If $\mathcal{L}_T^c$ is empty, the algorithm is finished.
4. Take the next box $\hat{\underline{c}}$ from the list $\mathcal{L}_T^c$.
5. If the diameter of the box $\hat{\underline{c}}$ is smaller than a predefined value ϵ_c the box is treated as *finite* and thus moved to the list $\mathcal{L}_F$. Goto (3).
6. If verification variables are present, call *Verify* with $\hat{c}$. Otherwise call *Existence* with $\hat{c}$ and an empty box for $\hat{v}$.
7. If the result of *Verify* is *valid*, move the box to the solution list $\mathcal{L}_S$. Goto (3).
8. If the result of *Verify* is *invalid*, move the box to the invalid list $\mathcal{L}_I$. Goto (3).
9. If the result of *Verify* is *finite*, move the box to the finite list $\mathcal{L}_F$. Goto (3).

5.1.4 Calling Sequence

Let $\mathcal{X}_c, \mathcal{X}_v \neq \emptyset, \mathcal{X}_e \neq \emptyset$ be given and represented as lists of boxes $\mathcal{L}_T^c, \mathcal{L}_T^v, \mathcal{L}_T^e$. In order to determine $\mathcal{L}_S$, *Calculate* is called with the search domain $\mathcal{L}_T^c$. Within *Calculate*, *Verify* is called. Since existence variables are present, *Existence* is called in order to validate the current calculation box (Otherwise in *Verify* the CSP would be directly evaluated). In the *Existence* algorithm the CSP is evaluated and the result is rated. In case that the result is *undefined*, the current box is divided on an existence variable. In case that the *Existence* algorithm returns with *finite*, the calling algorithm divides on its own variables and calls *Existence* again. If the result is *valid* or *invalid*, the result is directly returned to the calling algorithm. If *valid* is returned, the result is valid for all values within $\hat{\underline{c}}$ and $\hat{\underline{v}}$. It is noteworthy that the calculation time increases considerably with the number of variables and decreasing $\epsilon_i, i \in \{c, v, e\}$. The same calling sequence and return behavior is used in *Calculate* calling *Verify*.

5.1.5 Additional Requirements

Again, solving the force equilibrium is a computationally expensive task, so it is desired to find and evaluate computationally cheaper requirements in advance to save computation time. These requirements exclude parameter sets from the solution $\mathcal{L}_T^c$, i.e. they result in an overestimation which is then processed by the force equilibrium requirement. In case of a plain manipulator, generally it makes no sense to put winches inside the desired workspace (there may be special applications which use such a setup, but in this case the user should decide this explicitly), thus a parameter set containing a winch position within the workspace can be refused. Additionally, when defining the search domain for the winch positions, normally all winches are free to move within this area. This will result in redundant parameter set solutions where equivalent setups with permutated winches appear, i.e. taken a plain manipulator with a point-shaped platform with 2 translational d.o.f. and 3 tendons, a winch position set $(x_1 = 0, y_1 = 0), (x_2 = 0.5, y_2 = 1), (x_3 = 0, y_3 = 1)$ has the same properties as set $(x_1 = 0, y_1 = 0), (x_2 = 0, y_2 = 1), (x_3 = 0.5, y_3 = 1)$. Thus, it makes sense to check if a new winch parameter set is equivalent to an already checked one. In simple cases, an order for the winches can be set, e.g. by logical trees, which allows an effective precheck.

6 CONCLUSIONS AND FUTURE WORK

In this paper, an extension of the methods described in [4] and [15] is presented. It offers powerful methods for the design of a wire robot in terms of optimal and verified results using automated synthesis, Design-to-Workspace and Design-to-Task. By formulating these tasks as CSPs, the step from workspace analysis to synthesis and design is straight forward. Due to the formulation as CSPs, the different requirements can be reused and combined. Even inverse tasks (i.e. analysis and synthesis) can be handled by the same requirement implementation, just by interchanging variable roles [18]. In this paper, interval analysis is focused to solve the CSPs. It delivers reliable results (e.g. it is robust against rounding effects), but the calculation is computationally expensive. Therefore, other CSP solving strategies maybe advantageous. Due to the superiority of interval analysis in terms of robustness and reliability one can even think of hybrid solvers. The combination of interval analysis and genetic algorithms is part of our current work. In case of a Design-to-Workspace challenge the winch positions can be discretized and optimized by an genetic algorithm, while the desired workspace is still guaranteed by embedded interval based analysis. Furthermore runtime optimization is a main topic of the current research.

ACKNOWLEDGEMENTS

This work is supported by the German Research Council (Deutsche Forschungsgemeinschaft) under HI370/24-1 and SCHR1176/1-2.

REFERENCES

[1] Corrado Guarino Lo Bianco and Aurelio Piazzi. A hybrid algorithm for infinitely constrained optimization. *International Journal of Systems Science*, 32(1):91–102, 2001.

[2] Corrado Guarino Lo Bianco and Aurelio Piazzi. A semi-infinite optimization approach to optimal spline trajectory planning of mechanical manipulators. In M. A. Goberna and

M. A. Lopez, editors, *Semi-Infinite Programming: Recent Advances*, chapter 13, pages 271–297. Kluwer Academic Publisher, 2001.

[3] Paul Bosscher, Andrew T. Riechel, and Imme Ebert-Uphoff. Wrench-feasible workspace generation for cable-driven robots. *IEEE TRANSACTIONS ON ROBOTICS*, 22:890–902, 2006.

[4] T. Bruckmann, L. Mikelsons, M. Hiller, and D. Schramm. 6th polish german workshop 2007: System integration; proceedings. In Eberhard Kallenbach, Tom Ströhla, and Nadine Brauer, editors, *Analysis and Synthesis of Parallel Tendon-based Manipulators*, pages 74–80, Illmenau, Germany, 5.7.-8.7. 2007. Wissenschaftsverlag Thüringen. ISBN 978-3-936404-19-7.

[5] Tobias Bruckmann, Lars Mikelsons, Dieter Schramm, and Manfred Hiller. Continuous workspace analysis for parallel cable-driven stewart-gough platforms. *to appear in Proceedings in Applied Mathematics and Mechanics*, 2007.

[6] S. Fang. *Design, Modeling and Motion Control of Tendon-based Parallel Manipulators*. Ph. D. dissertation, Gerhard-Mercator-University, Duisburg, Germany, 2005. Fortschritt-Berichte VDI, Reihe 8, Nr. 1076, Düsseldorf.

[7] A. Fattah and S. K. Agrawal. On the design of cable-suspended planar parallel robots. *ASME Transactions, Journal of Mechanical Design*, 127(5):1021–1028, 2005.

[8] M. Gouttefarde, J.-P. Merlet, and D. Daney. Determination of the wrench-closure workspace of 6-dof parallel cable-driven mechanisms. In *Advances in Robot Kinematics*, pages 315–322, Ljubljana, June 26-29 2006.

[9] Marc Gouttefarde, Jean-Pierre Merlet, and David Daney. Wrench-feasible workspace of parallel cable-driven mechanisms. *2007 IEEE International Conference on Robotics and Automation, ICRA 2007, 10-14 April 2007, Roma, Italy*, pages 1492–1497, 2007.

[10] Eldon Hansen. *Global Optimization using Interval Analysis*. Marcal Dekker, Inc., 1992.

[11] A.M. Hay and J.A. Snyman. The optimal synthesis of parallel manipulators for desired workspace. In *Advances in Robot Kinematics*, pages 337–346, Caldes de Malavalla, 2002.

[12] M. Hiller, S. Fang, S. Mielczarek, R. Verhoeven, and D. Franitza. Design, analysis and realization of tendon-based parallel manipulators. *Mechanism and Machine Theory*, 40, 2005.

[13] Jean-Pierre Merlet. Trajectory verification in the workspace for parallel manipulators. *The International Journal of Robotics Research*, 13(4):326–333, 1994.

[14] Jean-Pierre Merlet. *Parallel Robots*. Kluwer Academic Publishers, Norwell, MA, USA, 2000.

[15] Jean-Pierre Merlet. A generic trajectory verifier for the motion planning of parallel robots. *Journal of Mechanical Design*, 123:510–515, 2001.

[16] Jean-Pierre Merlet. Solving the forward kinematics of a gough-type parallel manipulator with interval analysis. *Int. J. of Robotics Research*, 23(3):221–236, 2004.

[17] A. Ming and T. Higuchi. Study on multiple degree of freedom positioning mechanisms using wires, part 1 - concept, design and control. *International Journal of the Japan Society for Precision Engineering*, 28:131–138, 1994.

[18] A. Pott. *Analyse und Synthese von Parallelkinematik-Werkzeugmaschinen*. Ph. D. dissertation, Gerhard-Mercator-University, Duisburg, Germany, 2007. Fortschritt-Berichte VDI, Reihe 20, Nr. 409, Düsseldorf.

[19] J. Pusey, A. Fattah, S. K. Agrawal, and E. Messina. Design and workspace analysis of a 6-6 cable-suspended parallel robot. *Mechanism and Machine Theory*, 2004. Vol. 39, No.7, pp.761-778.

[20] A.T. Riechel and I. Ebert-Uphoff. Force-feasible workspace analysis for underconstrained, point-mass cable robots. In *IEEE International Conference on Robotics and Automation*, volume 5, pages 4956– 4962, 26 April-1 May 2004.

[21] Richard Verhoeven. *Analysis of the Workspace of Tendon-based Stewart Platforms*. PhD thesis, University of Duisburg-Essen, 2004.

[22] Guilin Yang, Cong Bang Pham, and Song Huat Yeo. Workspace performance optimization of fully restrained cable-driven parallel manipulators. *International Conference on Intelligent Robots and Systems*, 2006.

IAK 2008
Conference on Interdisciplinary Applications of Kinematics
A. Kecskeméthy, V. Potkonjak and A. Müller (eds.)
Lima, Peru, 9–11 January 2008

GAIT SIMULATOR BASED ON THE PARALLEL STEWART-GOUGH PLATFORM

Gonzalo Sevillano[*], Dante Elías[*], Rocio Callupe[†], Ricardo Marcacuzco[†], Benjamín Barriga[*]

[*]Sección de Ingeniería Mecánica-Departamento de Ingniería
Pontificia Univesidad Católica del Perú, Lima, Perú
e-mail: delias@pucp.edu.pe, web page: http://www.pucp.edu.pe/facultad/ingenieria/

[†] Biomedical Laboratory -Sección de Electricidad y Electrónica-Departamento de Ingeniería
Pontificia Univesidad Católica del Perú, Lima, Perú
e-mails: rcallup@pucp.edu.pe

Keywords: Stewart-Gough platform, gait simulator, parallel mechanism.

Abstract. *This paper shows a solution used to obtain a normal human gait simulator based on the Stewart-Gough platform parallel mechanism. This simulator, a precise and objective tool, makes it possible to better study the ways humans gait, thus aiding in the diagnosis and rehabilitation treatment of patients with motor injuries, 18 years and over. It is estimated that, in Peru, 37.3% of all handicapped patients who need specialized treatment present motor injuries. The prototype designed in this first stage consists of a fixed base connected to a mobile platform by means of six parallel hydraulic linear actuators (hydraulic cylinders). Additionally, the principal pieces of equipment include position sensors (linear potentiometers) for each actuator, control valves, and a hydraulic unit. Different design programs were used for the analysis and design of the prototype. A preliminary 2D analysis (AutoCAD) of the maximum displacement to be generated made it possible to determine the distances and critical angles of the mechanism. Moreover, Matlab was used to analyze the workspace for normal gait as well as the trajectory of the mobile platform through the application of inverse kinematics. SolidWork was used to model the geometry of the components of the prototype in order to evaluate the shape interference while CosmosWork and Cosmos M, using the finite element method, were used to analyze the forces and critical elements. This simulator will make it possible to research the kinematics and dynamics of a Stewart-Gough platform reproducing repetitions of one movement with a small error margin on position, force, and torque. This will be useful in the design and construction of the simulator*

1 INTRODUCTION

The Pan American health Organization has estimated that, in Peru, with a total national population of 27.148.101 people in 2003, there are 8.491.926 handicapped people, **1.019.032 of whom (target population) need specialized treatment**.

Human gait, which is closely associated with locomotion, is difficult to evaluate due to the complexity of its execution. Its analysis is, therefore, usually subjective, that is, qualitative. The difficulty of the description of movement and of the interpretation of the data obtained is due to the various degrees of freedom present, the comparison between subjects, and the pre and post treatment situations, among others [2], [3], [4], [5]. For this reason, doctors need objective criteria for the analysis of problems in locomotion in order to be able to make a rational decision regarding the prescription of surgical procedures, orthesis, physiotherapy, and medication. Thus, the analysis of human gait became the object of within the area of research on the rehabilitation of handicapped people [2].

An important factor in the rehabilitation of lower limbs of post-trauma patients is being able to reproduce repetitions of a movement –of an ankle, for instance, or of any foot movement that is to be evaluated. These repetitions can be developed in position, force, or torque by a simulator with a very small error margin. Therefore, these simulators are of interest to researchers, for interaction with a virtual environment expands the range of applications for rehabilitation and training of patients with walking dysfunctions. Maintaining a controlled environment, away from the risks and troubles of a real environment, makes these simulators into a viable option for medical, sports, and military applications.

Gait simulators are being developed through the use of manipulators based on Stewart-Gough platform parallel mechanisms. This mechanism consists of a fixed base (non-moving platform) connected to a mobile platform by means of six linear actuators. The position of the fixed platform, relative to the fixed base, is modified thanks to the six actuators, which are controlled coordinately and independently, thus generating the desired displacement. Currently, Rutgers University and the University of Medicine and Dental Surgery, both located in New Jersey, USA, are developing a mobility simulator. This simulator uses two Stewart-Gough platforms that can control positions and forces for each foot in six degrees of freedom (DOF) [6]. Moreover, Tsukuba University in Japan has developed a gait simulator based on a parallel mechanism with three degrees of freedom [7].

It is important to highlight the fact that nowadays parallel mechanisms are being widely studied due to their mechanical advantages over serial mechanisms. Among these advantages we find their high load capacity and rigidity with low structural weight, improved precision in the position of the final effector, increased operation speeds when compared to another type of robotic structure, and great capacity to modify the form of their structure. These advantages have made it possible for parallel mechanisms, especially those with 6 DOFs, to be used in diverse technological applications such as numeric control tool machines, assembly line robots, stabilizing platforms for antennas and solar collectors, pilot training simulators (airplanes, helicopters, trucks, etc.), simulators used to evaluate automobile performance, manipulators for remote surgical interventions, rehabilitation platforms for patients with locomotive dysfunction, human gait simulators, etc. Therefore, the analysis and modeling of a parallel mechanism, depending on the application for which it is intended, is very important for the design, construction, and evaluation of the system into which it is to be integrated.

This paper intends to aid in the development of a human gait simulator of the Stewart-Gough platform type, applied to the rehabilitation of patients with locomotive dysfunction. It specifically presents the kinematic and load analysis that facilitated the design of the 6-DOF Stewart-Gough parallel platform mechanism for the simulation of normal human gait.

2 DESIGN REQUIREMENTS

In order to establish the design of a simulator, one must first determine the requirements that must be fulfilled by the 6 DOF Stewart-Gough platform parallel mechanism. The design requirements are reach, speed, and force, all of which must be based on parameters of the analysis of human gait. Hence, it was decided to use the charts of dimensions and values of human gait by Zinkovsky et al [2] and Whittle [4]. These charts provide, for the gait period, the variations in angles of the lower limbs while walking, the reaction forces on the ground, and the angular velocity of the ankle. The data obtained, and an analytical analysis according to Whittle [4] allowed the development, using Autocad, of a geometrical model of the trajectory required in order to reproduce normal human gait with the simulator (Fig. (1)).

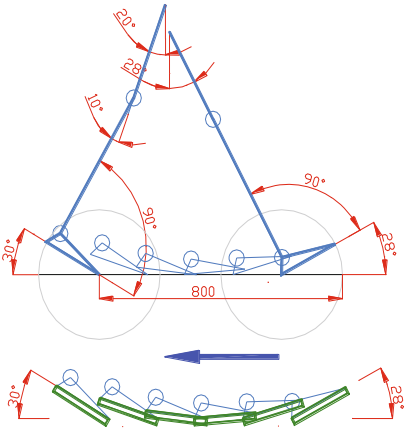

Figure 1: Model of the stance phase of a normal gait period

The gait simulator consists of two parallel Stewart-Gough platform mechanisms (one for each of the user's feet). It is therefore fundamental to consider the position restriction (separation) of the platform for an adequate simultaneous operation. This position restriction, for an adequate normal gait, is related to the width of the step, which fluctuates between 50 an 100 mm [4].

Fig. (2) shows the analysis of the swing phase of the gait period. In this phase, which lasts approximately 40% of the gait period (estimated time: 0,356 s), we find the critical values of displacement, velocity, and orientation of the platform.

Based on this analysis, it was possible to define the preliminary geometry, which is of utmost importance for the kinematics analysis. With the information on the position and velocity that must be attained by the mobile platform, it is possible to analyze the inverse kinematics of the mechanism in order to find the longitudes, velocities, and forces on the actuators and joints.

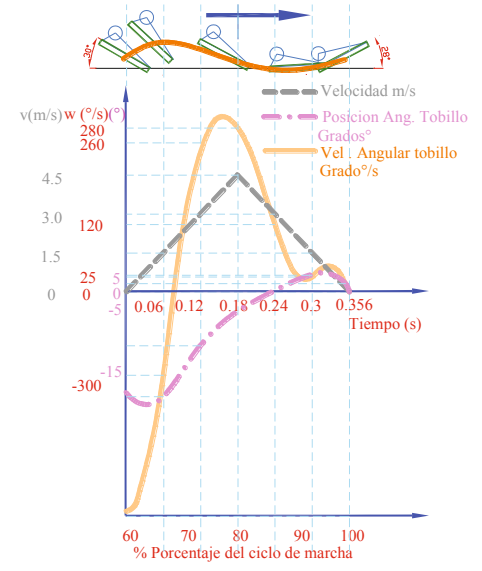

Figure 2: Position, velocity, and orientation during the swing phase of human gait

3 KINEMATIC ANALYSIS AND WORKSPACE

3.1 Inverse Kinematics

In Fig. (3), which shows a basic outline of the Stewart-Gough platform, we find the fixed reference system (FRS), located in point O [X_f, Y_f, Z_f] of the fixed base. However, in order to more easily describe the orientation of a mobile object with respect to the FRS, the mobile object was assigned a new system of coordinates [X_m, Y_m, Z_m], which was then called mobile reference system (MRS), with O_m, as its point of origin, in order to study the spatial relationship between these two systems [8], [9].

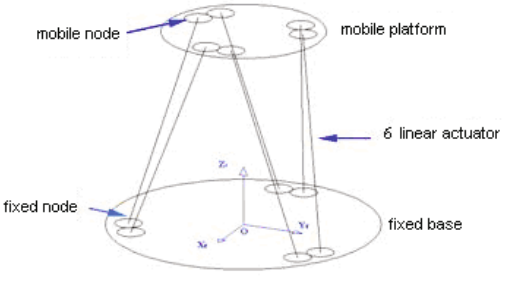

Figure 3: 3D scheme of the platform

The inverse kinematics analysis was based on a previous study carried out by Guo and Li [10], which used a rotation matrix with Euler angles to define the orientation of the mobile platform. First, a rotation sequence is described in order to define the matrix. Then one does a vectorial analysis among the points that connect the actuators to the mobile platform and the fixed base. This makes it possible to define the position vectors for each one of the actuators. Finally, one defines the length of each actuator for specific positions of the mobile platform.

The speeds of the actuators are determined from the speed of the points that connect the mobile platform to the actuators. We will call these points *mobile nodes*. Through the kinematics of rigid solids in space, the speeds of the mobile nodes are related to the previously estimated speeds of translation and rotation of the center of the mobile platform. By projecting the speed of each mobile node over the unitary vector of its corresponding actuator, the linear speed of each actuator is calculated.

3.2 Constant orientation workspace (COW)

The constant orientation workspace is defined by all the possible locations of the center of the mobile platform with a previously defined constant orientation. Since a 6 DOF parallel mechanism has, therefore, six generalized coordinates, it is necessary that at least three of them stay constant in order to obtain a tridimensional representation in space. In the COW, the coordinates that remain constant are the rotation angles. In order for the mechanism of the gait simulator meet the reach requirements (gait analysis), it is crucial that the workspace cover all the translations and orientation established. Since most of the movement in human gait takes place in the sagittal plane, it was decided to make it coincide with the X-Z plane of the mechanism. This facilitates the comparison of the COW to the trajectory of human gait as shown in Fig. (4).

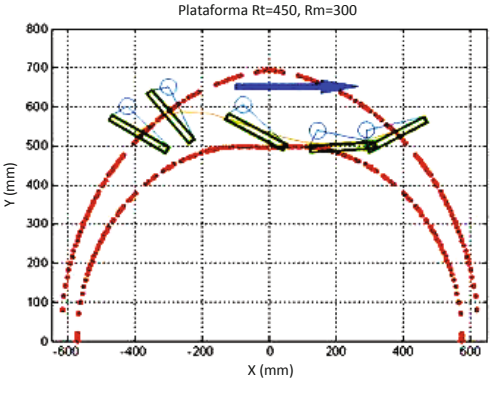

Figure 4: Comparison of the COW and the trajectory of the swing phase

The COW is based on the inverse kinematics of the mechanism, which permitted the calculation of the optimal geometry using an interactive program developed in Matlab.

In the design of these parallel mechanisms it is necessary to establish at least one parameter that serves as a base to determine the dimensions of the other parameters [11]. In this case, since we had a set of six hydraulic cylinders, the parameter that was established was the length of the actuators (hydraulic cylinders 500 mm in length with an additional extension of

200 mm. Using the program developed in Matlab, the two most important characteristics for the design were defined: i) geometrical dimensions of the mobile platform and the fixed base, ii) location of the actuators on the mobile platform and the fixed base (distance between the mobile nodes and the fixed nodes). The latter was achieved by determining the COWs for different configurations of the position of the mobile nodes and the fixed nodes. Once the geometry had been defined, the degrees of freedom of the mechanism were analyzed in order to determine the type of joints to implement [13]. This analysis was carried out in two stages. A) considering the actuators as two separate elements, which determines that the mobile platform has 6 DOFs, b) considering the actuators as one element, which determines that the mobile platform lacks movement (static equilibrium condition). This analysis made it possible to establish that two different types of joins are needed: one that offers 3 DOFs and another that has 2 DOFs.

4 ANALYSIS OF LOADS AND JOINT DESIGN

4.1 Load analysis

The analysis done in this study has focused preliminarily on a static analysis, with some dynamic considerations to be able to approximate the reaction forces. Therefore, the reaction forces on the joints and the actuators have been analyzed for different loads according to the trajectory [4]. It was assumed that the mechanism was in static equilibrium for each position in the trajectory.

The external forces that act on the mechanism are: the interaction forces between the foot and the floor during normal gait [4] and the forces caused by the approximate weight of the components. Besides, an additional inertial force was added due to the movement of the mechanism. The value of this inertial force was estimated in 3000 N in the horizontal direction (axis X). For this estimate, we considered: i) the almost linear trajectory, ii) change of orientation of the extremes of the trajectory, iii) zero velocity of the extremes, iv) acceleration and deceleration phases, as shown in Fig. (2), v) approximate weight of 70 kg for an average person [4].

The static analysis was resolved using the finite element method through the Cosmos M software, where the structure was modeled with all the restrictions and loads for different working positions.

Unlike the static analysis, parallel mechanisms, especially those with multiple bodies in closed loops with kinematics restrictions, dynamic models are difficult to obtain analytically. Owing to the inherent complexity of these mechanisms, the solution to dynamic models can only be obtained using numerical methods. Among the various methods that can be used to obtain these dynamic models we can mention: Newton-Euler, Lagrange, virtual work principle, Kane method, etc. [10].

The most widely recommended formulation is the one obtained through the use of the Newton-Euler equations imposing restrictions by means of Lagrange's multipliers and the application of the virtual work principle [14]. The Lagrange-Euler formulation, which in spite of having a high computational cost, has the advantage of automatically eliminating the restriction forces [9]. Recently, Guo and Li [10] have carried out a detailed analysis of the inverse kinematics and dynamics of a parallel manipulator with six DOF. The analysis has been derived for a parallel mechanism with six kinematics chains and one linear actuator in each chain.

The dynamic analysis is usually used to do system simulations in order to optimize control strategies. However, unlike parallel mechanisms, dynamic models have not been widely developed. The limited development of dynamic models thus prevents the statement of general

control algorithms. Arancil et al mentions that current control system are of the uncoupled type, conformed by a kinematics model that generates differenced for the articulations and their actuators [14]. Also, due to the intense computational tasks that limit a real-time scheme, it is recommended to plan the trajectory in the Cartesian space and use redundant control systems. Indeed, parallel mechanism control is still an open field and the works done so far are not quite rigorous [14].

In the case of the parallel mechanism designed, the dynamic analysis for the implementation of the control system is currently in process.

4.2 Joint design

The importance of joint design resides on the fact that they limit the workspace of the mechanism due to their own physical limits. These limitations occur because of the geometrical restrictions in the design of the joints of the actuators and the mobile platform and the fixed base. One way to describe these limitations is defining the workspace generated by these joints. This space, depending on the type of joint (ball or universal), can approximate an inverted pyramid with its lower vertex placed in the center of each joint. Consequently, the movement of each actuator must be within the limit established by the workspace generated by its corresponding joints (to the mobile platform and the fixed base) [11], [12].

Considering the DOF analysis of the mechanism presented, it was decided to use universal joints between the actuators and the fixed base. The forces found in the static analysis and the working configuration were taken into account for this design.

The design of the joints between the actuators and the mobile platform was more complex since the use of a ball joint was limited by the extreme positions that must be accomplished by the mobile platform. This joint must cover a limit angle of 170º, which means that a special design must be used. Therefore, using the 2DOF offered by the universal union, a double-row angular contact bearing was used to provide a 3DOF on its axis. Besides, taking into consideration that there must be no relative spinning between the cylinder and the rod of the actuator because a displacement sensor will be installed on each actuator (Celesco linear potentiometer & signal adapter designed in this work), an additional bearing was added, which would absorb any relative spin.

Fig. (5) shows the joints designed, which are used to assemble the actuators onto the fixed base and the mobile platform.

Figure 5: a- fixed base universal joint, b- mobile platform universal joint

Two methods were used to verify the design of the joints:

- Geometrical modeling and design using SolidWork (3D Cad software): The assembly of the whole platform was done and the different critical positions were simulated. The interferences were determined verify whether the components of the mechanism were superimposed.

- Determinations of the COW with restrictions: using the program developed in Matlab to find the COW, and adding the geometrical restrictions to make the joints, it was possible to determine the working space within which the mobile platform can be displaced.

5 RESULTS

While implementing the analysis of the inverse kinematics on Matlab, and based on the results obtained, it was possible to find an optimal geometrical design for this mechanism, which fulfills the reach requirements to simulate normal human gait. The program implemented in Matlab facilitates a more detailed analysis of the workspace, which makes it possible to evaluate the performance of any configuration for these parallel mechanisms, as shown in Fig. (6).

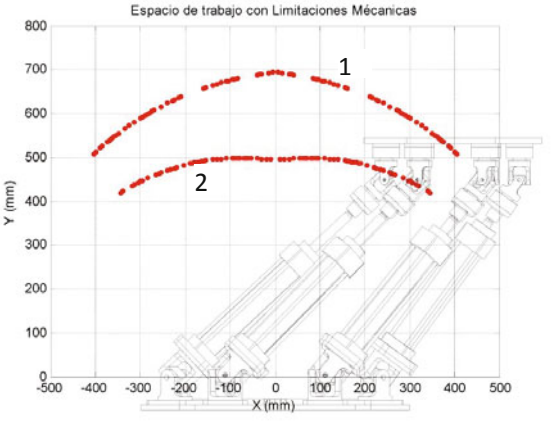

Figure 6: Constant orientation working spaces, X-Z plane, 1-upper limit curve, 2-lower limit curve, orientation (0,0,0)

Through the application of our knowledge of machine element calculus and materials resistance, it was possible to complete the mechanical design of the gait simulator for each of its main components (fixed base, mobile platform, upper joints, lower joints, etc.). This allowed us to finish the assembly and production plans. Fig. (7) shows a 3D projection of the mechanical design of the normal gait simulator based on the Stewart-Gough platform. This figure shows two platforms, one for each foot.

The force and speed results determined in this study, according to the parameters required for the mobile platform, makes it possible to select each of the components that complement the mechanical design of the normal gait simulator. For this first prototype of gait simulator, the following has been contemplated: i) six hydraulic cylinders with 200 mm stroke (40 mm and 20 mm bore and shaft diameter respectively), ii) hydraulic unit consisting of a gauge pump (11 cm^3/turn), a 5 HP electric motor at 1.800 rpm, proportional valves for the control of the simulator as well as other components needed for the adequate operation of the unit, iii) six position sensors for each actuator.

Figure 7: 3D projection of the mechanical design of the normal gait simulator based on the Stewart-Gough platform

6 CONCLUSIONS

- This research constitutes one of the first efforts in Peru, with a sound scientific and technological base, to develop gait simulators aimed at the treatment and rehabilitation of patients with motor injuries in their lower limbs. The development of this equipment will enable doctors to make use of objective criteria for the analysis and diagnosis of locomotive problems in order to make better decisions regarding the medical treatment and the rehabilitation process or a surgery.
- Regarding the design of parallel mechanisms, and concretely the design of the normal gait simulator for this project, we identified difficulties concerning the use of only one type of software. Therefore, we can conclude that having access to different commercial programs makes it possible to integrate the advantages that each of them has. In our case, we required AutoCAd for 2D geometric modeling (preliminary gait analysis, assembly and production plans), SolidWork for 3D geometric modeling (identification of interferences, assembly of components), Matlab for kinematics and workspace analysis, Cosmos M and Cosmos Work for load analysis using finite elements, MS Excel for processing the results, among others.
- The available kinematics model can be implemented in the gait simulator based on the Stewart-Gough platform. Moreover, this model is being used for the development of a platform for stabilizing equipment installed on marine ships.
- The modeling dynamics must be developed taking into account the geometrical and structural configuration of the parallel mechanism designed. This is due to the fact that dynamic modeling is the base for the implementation of the control system. Moreover, the control system must ensure that the gait simulator responds a swift and smooth response to load variations. This is important because the gait simulator will be used by a patient with lower-limb motor injuries.

ACKNOWLEDGEMENTS

The authors wish to thank the Dirección Académica de Investigación (DAI) and Sección de Mecánica of Pontificia Universidad Católica del Perú for their sponsorship of this work.

REFERENCES

[1] J. Arroyo. *El derecho a la salud de las personas con discapacidad*. Fondo Editorial del Congreso del Perú, 2006.

[2] L. Andrade, Análise De Marcha: Protocolo Experimental A Partir De Variáveis Cinemáticas E Antropométricas. Tesis de Maestria en Universidade Estadual de Campinas, Faculdade de Educação Física, Brasil, 2002.

[3] V. Zinkovsky, V. Sholuha and A. Ivanov. *Mathematical modelling and computer simulation of biomechanical systems*. World Scientific Publishing Company, 1996.

[4] M. Whittle. *Gait analysis: An introduction*. Butterworth-Heinemann, 1996.

[5] Hreljac, R. Imamura, R. Escamilla and W. Edwards. When does a gait transition occur during human locomotion?. *Journal of Sports Science and Medicine*, **6**, 36-43, 2007.

[6] R. Boian, M. Bouzit, G. Burdea and J. Deutsch. Dual Stewart platform mobility simulator". Proceedings 9th International Conference on Rehabilitation Robotics, USA, Jun 28 - Jul 1, 2005.

[7] H. Yano, H. Noma, H. Iwata and T. Miyasato. Shared Walk Wnvironment Using Locomotion Interface. Proceedings of the ACM 2000 Conference on Computer Supported Cooperative Work, ACM Press, Philadelphia, Pennsylvania, Dec., 2000.

[8] A. Barrientos, L. Peñin, C. Balaguer, R. Araci. *Fundamentos de Robótica*. McGraw Hill, Interamericana de España, 1997.

[9] F. Yanes, Modelación y simulación de un manipulador basado en un mecanismo paralelo tipo plataforma Stewart. Tesis Magíster en Ingeniería, Pontificia Universidad Católica de Chile, 1997.

[10] H. Guo and H. Li. Dynamic analysis and simulation of a six degree of freedom Stewart platform manipulator. Proceedings of the Institution of Mechanical Engineers. *J. of Mechanical Engineering Science*, **220**, 61-72, 2006.

[11] J. Merlet, INRIA Sophia-Antipolis. Determination of 6D-workspaces of gough-type parallel manipulator and comparison between different geometries. *Int. J. of Robotics Research*, **18**, 902-916, 1999.

[12] J. Merlet. Determination of orientation workspace of a parallel manipulators. *J. of Intelligent and Robotic Systems*, **13**, 143-160, 1995.

[13] G. Baránov. *Curso de la teoría de mecanismos y máquinas,* MIR –Moscú, 1979.

[14] R. Aracil, R. Saltaren, J. Sabater y O. Reinoso. Robots paralelos: máquinas con un pasado para una robótica del futuro. *Revista Iberoamericana de Automática e Informática Industrial*, **3**, 16-28, 2006

IAK 2008
Conference on Interdisciplinary Applications of Kinematics
A. Kecskeméthy, V. Potkonjak and A. Muller (eds.)
Lima, Peru, 9–11 January 2008

A PROPOSAL FOR A NEW DEFINITION OF THE DEGREE OF FREEDOM OF A MECHANISM

Manfred L. Husty, Hans-Peter Schröcker

Unit Geometry and CAD, Institute of Basic Sciences in Engineering
University Innsbruck, Technikerstraße 13, A6020 Innsbruck, Austria
e-mail: manfred.husty@uibk.ac.at, hans-peter.schroecker@uibk.ac.at
web page: http://geometrie.uibk.ac.at

Keywords: Degree of freedom, kinematic mapping, Hilbert dimension.

Abstract. Using the algebraic representation of mechanisms via kinematic mapping we give a new definition of the degree of freedom of a mechanism. This definition takes into account the design of the mechanism and will yield the correct results for mechanisms with special dimensions, when classical formulas like e.g. the Grübler-Kutzbach-Tschebysheff formula fail.

1 INTRODUCTION

There is a long history in defining and computing the degree of freedom (DoF) of a mechanical system. It starts with a classical paper of Euler and continues until today. An overview of most of the classical concepts starting with Euler's formula up to the most recent developments can be found in a paper by Alizade et. al. [1]. Virtually all of the developed concepts use topological information to determine the DoF. The number of links, joints, loops, number of screw pairs, simple structural groups, number of kinematic pairs, number of links with variable length, just to enumerate some of them.

It is not surprising that all of these concepts fail whenever the mechanisms has "special dimensions". We do not elaborate at the moment what special dimensions mean. Concepts of overconstrained, exceptional and pathological mechanisms have been introduced.

It has to be emphasized that exceptional or pathological behavior of a mechanisms is always linked to special design parameters. Therefore one has to take into account the geometry of the mechanism to define the degree of freedom. Recent developments in the algebraic description of mechanisms using kinematic mapping give the motivation to come up with a natural definition of DoF. To do this we will use the natural invariants of the algebraic varieties associated to the mechanisms.

In Section 2 we recall basic concepts of kinematic mapping and introduce the algorithms that translate the motion behavior of a mechanisms into algebraic equations. Section 3 introduces the new definition of DoF after providing necessary basic results from algebraic geometry. In Section 4 we show how the concept of constraint equations can be used to compute the Jacobian matrix of a manipulator.

2 KINEMATIC MAPPING

The fundamental concept of relating mechanical structures with algebraic varieties is Study's kinematic mapping [10, 11]. It associates to every Euclidean displacement α a point $\mathbf{x}$ in real projective space P^7 of dimension seven or, more precisely, a point on the Study quadric $S \subset P^7$. There exist other kinematic mappings besides Study's but these topics are beyond the scope of the present text. A formal definition of Study's kinematic mapping is given below in Subsection 2.1.

Our description is based on the original works of Study [10, 11]. These are comprehensive and deep but not always easily readable texts and, unfortunately, only available in German. Modern references on the same topic include [6] or [9].

2.1 Study's kinematic mapping

Euclidean three space is the three dimensional real vector space $\mathbb{R}^3$ together with the usual scalar product $\mathbf{x}^T\mathbf{y} = \sum_{i=1}^{3} x_i y_i$. A Euclidean displacement is a mapping

$$\gamma\colon \mathbb{R}^3 \to \mathbb{R}^3, \quad \mathbf{x} \mapsto \mathbf{A}\mathbf{x} + \mathbf{a} \tag{1}$$

where $\mathbf{A}$ is a proper orthogonal three by three matrix and $\mathbf{a} \in \mathbb{R}^3$ is a vector. The entries of $\mathbf{A}$ fulfill the well-known orthogonality condition $\mathbf{A}^T \cdot \mathbf{A} = \mathbf{I}_3$, where $\mathbf{I}_3$ is the three by three identity matrix.

The group of all Euclidean displacements is denoted by $\mathrm{SE}(3)$. It is a convenient convention to write Equation (1) as product of a four by four matrix and a four dimensional vector according

to

$$\begin{bmatrix}1\\ \mathbf{x}\end{bmatrix} \mapsto \begin{bmatrix}1 & \mathbf{o}^T\\ \mathbf{a} & \mathbf{A}\end{bmatrix} \cdot \begin{bmatrix}1\\ \mathbf{x}\end{bmatrix}. \tag{2}$$

Study's kinematic mapping $\varkappa$ maps an element α of $\mathrm{SE}(3)$ to a point $\mathbf{x} \in P^7$. If the homogeneous coordinate vector of $\mathbf{x}$ is $[x_0 : x_1 : x_2 : x_3 : y_0 : y_1 : y_2 : y_3]^T$, the kinematic pre-image of $\mathbf{x}$ is the displacement α described by the transformation matrix

$$\frac{1}{\Delta}\begin{bmatrix}\Delta & 0 & 0 & 0\\ p & x_0^2+x_1^2-x_2^2-x_3^2 & 2(x_1x_2-x_0x_3) & 2(x_1x_3+x_0x_2)\\ q & 2(x_1x_2+x_0x_3) & x_0^2-x_1^2+x_2^2-x_3^2 & 2(x_2x_3-x_0x_1)\\ r & 2(x_1x_3-x_0x_2) & 2(x_2x_3+x_0x_1) & x_0^2-x_1^2-x_2^2+x_3^2\end{bmatrix} \tag{3}$$

where

$$\begin{aligned} p &= 2(-x_0y_1+x_1y_0-x_2y_3+x_3y_2),\\ q &= 2(-x_0y_2+x_1y_3+x_2y_0-x_3y_1),\\ r &= 2(-x_0y_3-x_1y_2+x_2y_1+x_3y_0), \end{aligned} \tag{4}$$

and $\Delta = x_0^2+x_1^2+x_2^2+x_3^2$. The lower three by three sub-matrix is a proper orthogonal matrix if

$$x_0y_0+x_1y_1+x_2y_2+x_3y_3 = 0 \tag{5}$$

and not all x_i are zero. If these conditions are fulfilled we call $[x_0 : \cdots : y_3]^T$ the *Study parameters* of the displacement α.

The important relation (5) defines a quadric $S \subset P^7$ and the $\varkappa$-image of $\mathrm{SE}(3)$ is this quadric minus the three dimensional subspace defined by

$$E\colon x_0 = x_1 = x_2 = x_3 = 0. \tag{6}$$

We call S the *Study quadric* and E the *exceptional* or *absolute generator*.

The parameterization (3) of $\mathrm{SE}(3)$ may look rather artificial and complicated but it has an important feature: *The composition of displacements in Study parameters is bilinear* (see [7]). In [10] Study shows that

- this requirement cannot be fulfilled with a smaller number of parameters and
- the representation of Euclidean displacements is unique, up to linear parameter transformations and transformations via identically fulfilled relations between the parameters.

Moreover, the Study parameters are closely related to the ring of *biquaternions* or *dual quaternions* as we shall rather say.

For the description of a mechanical device in P^7 we usually need the inverse of the map given by Equations (3) and (4), that is, we need to know how to compute the Study parameters from the entries of the matrix $\mathbf{A} = [a_{ij}]_{i,j=1,\ldots,3}$ and the vector $\mathbf{a} = [a_1, a_2, a_3]^T$. Until recently, kinematics literature used a rather complicated and not singularity-free procedure, based on the Cayley transform of a skew symmetric matrix into an orthogonal matrix (see [3]). The best way of doing this was, however, already known to Study himself. He showed that the homogeneous quadruple $x_0 : x_1 : x_2 : x_3$ can be obtained from at least one of the following proportions:

$$\begin{aligned} x_0 : x_1 : x_2 : x_3 &= 1+a_{11}+a_{22}+a_{33} : a_{32}-a_{23} : a_{13}-a_{31} : a_{21}-a_{12}\\ &= a_{32}-a_{23} : 1+a_{11}-a_{22}-a_{33} : a_{12}+a_{21} : a_{31}+a_{13}\\ &= a_{13}-a_{31} : a_{12}+a_{21} : 1-a_{11}+a_{22}-a_{33} : a_{23}+a_{32}\\ &= a_{21}-a_{12} : a_{31}+a_{13} : a_{23}-a_{32} : 1-a_{11}-a_{22}+a_{33}. \end{aligned} \tag{7}$$

In general, all four proportions of (7) yield the same result. If, however, $1+a_{11}+a_{22}+a_{33}=0$ the first proportion yields $0:0:0:0$ and is invalid. We can use the second proportion instead as long as $a_{22}+a_{33}$ is different from zero. If this happens we can use the third proportion unless $a_{11}+a_{33}=0$. In this last case we resort to the last proportion which yields $0:0:0:1$. Having computed the first four Study parameters the remaining four parameters $y_0:y_1:y_2:y_3$ can be computed from

$$\begin{aligned} 2y_0 &= a_1x_1+a_2x_2+a_3x_3,\\ 2y_1 &= -a_1x_0+a_3x_2-a_2x_3,\\ 2y_2 &= -a_2x_0-a_3x_1+a_1x_3,\\ 2y_3 &= -a_3x_0+a_2x_1-a_1x_2. \end{aligned} \tag{8}$$

2.2 Constraint varieties

In this part we demonstrate how kinematic mapping can be used to translate mechanisms to algebraic varieties in P^7. These varieties describe the possible configurations of the mechanism and are called *constraint varieties*. This approach has been used in various papers to discuss the direct kinematics of Stewart-Gough platforms [4], singularities and self motions of platform mechanisms [5] or the inverse kinematics of serial robots [8].

There are two fundamental operations how the algebraic varieties describing a mechanism can be obtained. Most of the time we will have a parametric representation of the motion capabilities of a mechanism. Then we obtain the constraint equations by implicitization. Sometimes the constraint equations are obtained by transforming a Cartesian constraint into the kinematic image space. This is done for example when we know that a point of the moving system (e.g. the coupler) is bound to move on a geometric object (e.g. a curve or a surface). It is important to note that one can derive the algebraic equations for a normal form of the linkage and transform the equations in the kinematic image space to obtain general positions. Geometrically, this means that one uses the most appropriate (best adjusted) coordinate system to describe the mechanism, or parts of it. The operation to put the mechanism and the end-effector into general position is performed in the image space. The most important reason to do this, is that in the image space this operation is linear, i.e. it does not increase the degree of the involved equations.

A parameterized representation of the kinematic image of a revolute joint can be derived in such a normal form by taking a rotation about the z-axis with an angle φ, which is described by the matrix

$$\mathbf{A}=\begin{bmatrix} 1 & 0 & 0 & 0\\ 0 & \cos\varphi & -\sin\varphi & 0\\ 0 & \sin\varphi & \cos\varphi & 0\\ 0 & 0 & 0 & 1 \end{bmatrix}. \tag{9}$$

Its kinematic image, computed via (7) and (8) is

$$\mathbf{r}=[1+\cos\varphi:0:0:\sin\varphi:0:0:0:0]^T. \tag{10}$$

As φ varies in $[0,2\pi)$, $\mathbf{r}$ describes a straight line on the Study quadric which reads after algebraization

$$\overline{\mathbf{r}}=[1:0:0:u:0:0:0:0]^T. \tag{11}$$

It is a straight line and computing its algebraic equations is elementary. Still, we will show how to carry out these computations explicitly because this demonstrates a general procedure for

obtaining constraint varieties. Consider the kinematic image (10). It is given in a normal form and we see that it is described by six linear equations

$$\begin{aligned} &H_1(\mathbf{x})\colon x_1 = 0,\ H_2(\mathbf{x})\colon x_2 = 0,\ K_0(\mathbf{x})\colon y_0 = 0,\\ &K_1(\mathbf{x})\colon y_1 = 0,\ K_2(\mathbf{x})\colon y_2 = 0,\ K_3(\mathbf{x})\colon y_3 = 0. \end{aligned} \tag{12}$$

These equations describe six hyperplanes in the kinematic image space and the line is the intersection of these six linear spaces. In order to obtain the constraint variety of a revolute joint in general position we have to transform the hyperplanes $H_i(\mathbf{x})$, $K_j(\mathbf{x})$ via the projective transformations using the operators $\mathbf{T}_f$ and $\mathbf{T}_m$:

$$\mathbf{y} = \mathbf{T}_f\mathbf{T}_m\mathbf{x}, \quad \mathbf{T}_m = \begin{bmatrix} \mathbf{A} & \mathbf{O} \\ \mathbf{B} & \mathbf{A} \end{bmatrix}, \quad \mathbf{T}_f = \begin{bmatrix} \mathbf{C} & \mathbf{O} \\ \mathbf{D} & \mathbf{C} \end{bmatrix}, \tag{13}$$

where

$$\begin{aligned} \mathbf{A} &= \begin{bmatrix} m_0 & -m_1 & -m_2 & -m_3 \\ m_1 & m_0 & m_3 & -m_2 \\ m_2 & -m_3 & m_0 & m_1 \\ m_3 & m_2 & -m_1 & m_0 \end{bmatrix}, \quad \mathbf{B} = \begin{bmatrix} m_4 & -m_5 & -m_6 & -m_7 \\ m_5 & m_4 & m_7 & -m_6 \\ m_6 & -m_7 & m_4 & m_5 \\ m_7 & m_6 & -m_5 & m_4 \end{bmatrix} \\ \mathbf{C} &= \begin{bmatrix} f_0 & -f_1 & -f_2 & -f_3 \\ f_1 & f_0 & -f_3 & f_2 \\ f_2 & f_3 & f_0 & -f_1 \\ f_3 & -f_2 & f_1 & f_0 \end{bmatrix}, \qquad \mathbf{D} = \begin{bmatrix} f_4 & -f_5 & -f_6 & -f_7 \\ f_5 & f_4 & -f_7 & f_6 \\ f_6 & f_7 & f_4 & -f_5 \\ f_7 & -f_6 & f_5 & f_4 \end{bmatrix}, \end{aligned} \tag{14}$$

and $\mathbf{O}$ is the four by four zero matrix.

The matrices $\mathbf{T}_m$ and $\mathbf{T}_f$ commute and they induce transformations of P^7 that leave fixed the Study quadric S, the exceptional generator E, and the *exceptional quadric* $F \subset E$, defined by the equations

$$F\colon x_0 = x_1 = x_2 = x_3 = 0, \quad y_0^2 + y_1^2 + y_2^2 + y_3^2 = 0. \tag{15}$$

The entries of the matrices $\mathbf{T}_m$ and $\mathbf{T}_f$ are the Study parameters of the transformations, that bring the fixed and the moving coordinate systems into general positions. The quadrics S and F and the three space E are special objects in the geometry of the kinematic image space. A more elaborate discussion on the transformations $\mathbf{T}_m$ and $\mathbf{T}_f$ and their properties can be found in [7] and [8]. A mechanism is described by a subvariety V of P^7 representing the constraints or the motion capabilities of the mechanism. A non-generic position of V with respect to S, E and F distinguishes its kinematic properties from a projectively equivalent subvariety W.

The procedure described above does not only work for linear equations but also for algebraic equations of arbitrary degree. It is emphasized once more that projective transformations are linear and therefore do not alter the degree of the transformed equations.

3 ALGEBRAIC DEFINITION OF DEGREES OF FREEDOM

Historically most of the developed formulas to determine the DoF of a mechanism use the topological structure and fail whenever special design parameters cause anomalies. Exceptional, pathological or over-constrained mechanisms need special treatment. An overview of most of the classical concepts starting with Euler's formula up to the most recent developments can be found in [1].

Within the setting of algebraic geometry and the theory developed in above it is natural to define the degree of freedom of a mechanism as the *Hilbert dimension of the algebraic variety associated with the mechanical device.*

To obtain a more formal definition of the above statement we have to provide some standard definitions from algebraic geometry. They are taken from [2], a reference which also treats some problems in robotics. The set of polynomials in $x_0, \ldots, x_k$ forms a ring which is denoted by $k[x_0, \ldots x_n]$. If k is a field and $f_1, \ldots, f_s$ are polynomials in $k[x_0, \ldots, x_n]$, and if

$$\mathbf{V}(f_1, \ldots, f_s) = \{(a_1, \ldots, a_n) \in k^n \colon f_i(a_1, \ldots, a_n) = 0, \quad \text{for all} \quad 1 \leq i \leq s\}$$

then $\mathbf{V}(f_1, \ldots, f_s)$ is called an affine variety defined by the polynomials f_i. The definition says essentially that the affine variety is the zero set of the defining polynomials. In case of homogeneous polynomials the variety is called a projective variety. The most important object in algebraic geometry is an ideal I, which is a subset of $k[x_0, \ldots, x_n]$ that satisfies the following properties (see [2]):

(i) $0 \in I$.
(ii) If $f, g \in I$, then $f + g \in I$.
(iii) If $f \in I$ and $g \in k[x_0, \ldots, x_n]$ then $f \cdot g \in I$.

To come to the formal definition of the Hilbert dimension we need one more ingredient. The set of leading terms $LT(I)$ of an ideal is defined by

$$LT(I) = \{cx^\alpha \colon \text{there exists } f \in I \text{ with } LT(f) = cx^\alpha\}$$

The ideal generated by the set $LT(I)$ is called leading term ideal and denoted by $\langle LT(I)\rangle$. Now the dimension can be computed using the dimension theorem ([2]), which states:

Theorem. *Let $V = \mathbf{V}(I)$ be an affine variety, where $I \subset k[x_1, \ldots, x_n]$ is an ideal. If k is algebraically closed, then*

$$\dim V = \textit{ maximum dimension of a coordinate subspace in } \mathbf{V}(\langle LT(I)\rangle).$$

Symbolic computation software like Maple, Mathematica or Singular have direct commands to perform the necessary computations. The algorithms behind the commands use Gröbner bases, compute the ideal $\mathbf{V}(\langle LT(I)\rangle)$ and the maximal coordinate subspace in this ideal. Another possibility is to compute the Hilbert polynomial. Its degree also gives the dimension of the ideal.

In kinematics caution has to be taken with respect to reality of the variety and its intersection with the exceptional generator E. The direct kinematics of the Stewart-Gough platform can provide an example to show the procedure. We use the algorithm provided in [4] to obtain the algebraic description of the device. Six sphere constraint equations yield six quadratic polynomials in the image space coordinates. When we add the Study quadric equation and compute the Hilbert dimension we obtain $\dim = 2$. The reason for this result is the intersection of the constraint equations with the exceptional generator E. Every sphere constraint variety contains the exceptional quadric F. This problem can be overcome easily by adding a normalizing condition ($x_0^2 + x_1^2 + x_2^2 + x_3^2 = 1$) which removes the exceptional generator from the ideal. Then we obtain a zero dimensional component which determines the 40 discrete solutions. That is, for fixed leg lengths the degree of freedom is, in general, zero. For an actual example we take a hexagonal Stewart Gough platform which can be represented by the following set of polynomial

equations that generates the ideal describing the direct kinematics of this manipulator. Using the following commands:

```
> with(Groebner):
> F:=[U4,U2,U3,U8,U10,U7,h1,x_0^2+x1^2+x2^2+x3^2-1];
```

$$F := [244x_1y_0 - 792x_3y_2 - 244x_0y_1 + 1370y_3x_1 - 1370x_3y_1 + 422x_0y_2 + 439323x_2^2 + 1465x_3^2 + 999x_0^2 - 436859x_1^2 + 792x_2y_3 - 422x_2y_0 - 544796x_0x_3 + 505072x_2x_1, -101x_1y_0 - 156x_3y_2 + 101x_0y_1 + 156x_2y_3 + 68081x_0x_3 - 101796x_2x_1 - \tfrac{4401}{4}x_1^2 - \tfrac{4401}{4}x_3^2 - \tfrac{4401}{4}x_2^2 - \tfrac{4401}{4}x_0^2, -61x_1y_0 + 198x_3y_2 + 61x_0y_1 - 198x_2y_3 - 68203x_0x_3 - 126565x_2x_1 - \tfrac{6713}{2}x_1^2 - \tfrac{6713}{2}x_3^2 - \tfrac{6713}{2}x_2^2 - \tfrac{6713}{2}x_0^2, -204402x_0x_3 - 297x_2x_1 - \tfrac{3749}{2}x_1^2 - \tfrac{3749}{2}x_3^2 - \tfrac{3749}{2}x_2^2 - \tfrac{3749}{2}x_0^2, -404x_1y_0 - 624x_3y_2 + 404x_0y_1 + 1082y_3x_1 - 1082x_3y_1 - 700x_0y_2 - 375644x_2^2 - 22627x_3^2 - 22712x_0^2 + 330305x_1^2 + 624x_2y_3 + 700x_2y_0 - 545284x_0x_3 - 408372x_2x_1, x_0y_0 + x_1y_1 + x_2y_2 + x_3y_3, -640x_1y_0 - 5664x_3y_2 + 640x_0y_1 + 384y_3x_1 - 384x_3y_1 + 1496x_0y_2 + 4y_0^2 + 4y_3^2 + 4y_2^2 + 4y_1^2 + 1891923x_2^2 + 1761263x_3^2 - 87533x_0^2 - 218193x_1^2 + 5664x_2y_3 - 1496x_2y_0 - 1089888x_0x_3 + 391552x_2x_1, x_0^2 + x_1^2 + x_2^2 + x_3^2 - 1]$$

```
> HilbertDimension(F,tdeg(x_0,x_1,x_2,x_3,y0,y1,y2,y3));
```

$$0$$

Maple computes the correct dimension 0 which states algebraically that the zero set of the ideal generated by the equations above consists of a set of discrete points. Kinematically it means that the mechanism with the given set of input parameters (coordinates of the anchor points and length of the legs) will have a discrete set of assembly modes. Note that the actual degree of freedom of a Stewart-Gough platform with fixed leg lengths can be greater than zero. To show this we let Maple compute the Hilbert dimension of another set of constraint equations. This time we have only seven equations because one of the variables (x_0) had been set to zero. This set of equations belongs to the Griffis-Duffy type of 6-SPS platform mechanisms [5].

```
> with(Groebner):
> G:=[U2,U3,U4,U5,h1,U7,x0^2+x1^2+x2^2+x3^2-1];
```

$$G := [-4x_2y_3 + 12x_1y_0 + 4y_2x_3 + 4\sqrt{3}x_1x_2, 8\sqrt{3}x_2y_0, -4x_2y_3 - 12x_1y_0 + 4y_2x_3 + 4\sqrt{3}x_1x_2, -\tfrac{2}{3}\sqrt{3}(\sqrt{3}x_2y_3 - 3\sqrt{3}x_1y_0 - \sqrt{3}y_2x_3 + \sqrt{3}x_2^2 + \sqrt{3}x_3^2 - 3x_1x_2 + 3x_2y_0 - 3y_3x_1 + 3x_3y_1), 4\sqrt{3}y_0(\sqrt{3}x_1 + x_2), 4y_0^2 + 4y_1^2 + 4y_3^2 + 4y_2^2 + x_3^2(2 - R) + x_1^2(2 - R) + x_2^2(2 - R) + 2\sqrt{3}x_3y_1 + 6x_1y_0 + 2y_2x_3 + 2\sqrt{3}x_2y_0 - 2x_2y_3 - 2\sqrt{3}y_3x_1 + x_1^2 - x_3^2 + 2\sqrt{3}x_1x_2 - x_2^2, x_1y_1 + x_2y_2 + x_3y_3, -1 + x_1^2 + x_2^2 + x_3^2]$$

```
> HilbertDimension(F,tdeg(x1,x2,x3,y0,y1,y2,y3));
```

$$1$$

The computation of the Hilbert dimension yields 1 although the topology of this mechanism is exactly the same as the topology of the mechanism before. It has the same number of links, joints and loops. All the known formulas to compute the degree of freedom will tell that both devices will have the same degree of freedom. Algebraically the result above means that the ideal generated by the set of G is one dimensional, the algebraic variety generated by the zero set of these equations is one dimensional and consists therefore of a curve. Kinematically this means that the mechanism has one degree of freedom. It has a self motion (see [5]).

The most important finding is therefore, that the geometry (the dimensions, the design) of a mechanism is taken into account when the Hilbert dimension is used to compute the degree of freedom, not only the topology.

4 MECHANISM SINGULARITIES

The singular configurations of a mechanism are an important topic in mechanism analysis. The precise definition and classification of mechanism singularities is far beyond the scope of this article (compare [12] and the references therein). In particular, singular configurations of a mechanism do not necessarily correspond to singularities of the mechanism's constraint varieties. To obtain a formal definition of singularity in kinematics within the algebraic setting provided in this paper we can follow the exposition in [2] and apply the results therein to the constraint varieties of the mechanism. Let $V \in k^n$ be a constraint variety and let $p = [p_0, \ldots, p_7]^T$ be a point on V. The *tangent space* of V at p, denoted $T_p(V)$, is the variety

$$T_p(V) = \mathbf{V}(d_p(f)\colon f \subset \mathbf{I}(\mathbf{V})) \tag{16}$$

of linear forms of all polynomials contained in the ideal $\mathbf{I}(\mathbf{V})$ in point p (see [2], page 486). With this definition we can immediately link the tangent space to the local degree of freedom of the mechanism: The local degree of freedom is defined as $\dim T_p(V)$. Computationally the differentials are to be taken with respect to the Study parameters x_i, y_i. In kinematics these differentials are collected in the *Jacobian matrix* of the manipulator

$$\mathbf{J}(f_j) = \left(\frac{\partial f_j}{x_i}, \frac{\partial f_j}{y_i}\right), \tag{17}$$

where f_j are polynomials describing the constraints, the Study condition, and a normalizing condition (e.g. $x_0^2 + x_1^2 + x_2^2 + x_3^2 - 1 = 0$). The normalizing condition has to be added to avoid dimensional problems coming from the exceptional generator E. In a nonsingular position of the mechanism the Jacobian $\mathbf{J}$ will have maximal rank. A singular position is characterized by rank deficiency of $\mathbf{J}$ and the defect is directly related to the local degree of freedom. It has to be noted that this definition of the Jacobian of a mechanism yields exactly the same results as the classical definitions.

5 CONCLUSION

In this paper a new definition of the degree of freedom of a mechanical device is given. It takes into account the dimensions of the mechanism. It is believed that this definition will help to overcome difficulties that appear when the device has a special geometry. Furthermore a new algorithm to compute the local degree of freedom is given. This algorithm uses the dimensions of the local tangent spaces of the algebraic varieties to compute the local degree of freedom of the mechanism. There are still a lot of open problems linked to the algebraic description of mechanical devices. But there are results and algorithms that allow the transformation of mechanical devices into the language of algebraic geometry.

REFERENCES

[1] R. Alizade, C. Bayram, and E. Gezgin, Structural synthesis of serial platform manipulators. *Mechanism and Machine Theory*, **42**(5), 580–599, 2007.

[2] D. A. Cox, J. B. Little, and D. O'Shea, *Ideals, Varieties and Algorithms*. Springer, 3 edition, 2007.

[3] G. H. Golub and C. F. Van Loan, *Matrix Computations*. Baltimore: John Hopkins University Press, 3 edition, 1996, ISBN 978-0-8018-5414-9.

[4] M. L. Husty, An algorithm for solving the direct kinematics of general Stewart-Gough platforms. *Mechanism and Machine Theory*, **31**(4), 365–380, 1996.

[5] M. L. Husty and A. Karger, Self motions of Stewart-Gough platforms, an overview. In *Proceedings of the workshop on fundamental issues and future research directions for parallel mechanisms and manipulators*, pages 131–141, Quebec City, Canada, 10 2002.

[6] M. L. Husty, A. Karger, H. Sachs, and W. Steinhilper, *Kinematik und Robotik*. Springer, Berlin, Heidelberg, New York, 1997.

[7] M. L. Husty and H. P. Schröcker, Algebraic geometry and kinematics. To be published in IMA volume "Nonlinear Computational Geometry" (edited by I. Emiris, F. Sottile, and T. Theobald), 2008.

[8] M. Pfurner, *Analysis of spatial serial manipulators using kinematic mapping*. Ph.D. thesis, University Innsbruck, 2006.

[9] J. M. Selig, *Geometric Fundamentals of Robotics*. Monographs in Computer Science, Springer, New York, 2005.

[10] E. Study, Von den Bewegungen und Umlegungen. *Math. Ann.*, **39**, 441–566, 1891.

[11] E. Study, *Geometrie der Dynamen*. B. G. Teubner, Leipzig, 1903.

[12] D. Zlatanov, R. G. Fenton, and B. Benhabib, Identification and classification of the singular configurations of mechanisms. *Mechanism and Machine Theory*, **33**(6), 743–760, 1998.

IAK 2008
Conference on Interdisciplinary Applications of Kinematics
A. Kecskeméthy, V. Potkonjak and A. Muller (eds.)
Lima, Peru, 9–11 January 2008

MODELLING OF MECHANISMS IN CONTAINER GLASS FORMING MACHINES

Burkhard Corves*

* Institut für Getriebetechnik und Maschinendynamik

RWTH Aachen University, 52056 Aachen, Germany
e-mail: corves@igm.rwth-aachen.de,
web page: http://www.igm.rwth-aachen.de/

Keywords: glass forming machines, linkages, modelling, design, simulation, test, verification, virtual machine.

Abstract. *Machines for container glass forming are in themselves multi-axis machines with a lot of different coordinated mechanisms. In order to come up with a fast and reliable glass forming process a proper layout and design of the different mechanisms involved is of utmost importance. Therefore the focus of this paper is on the systematic, mechatronic approach for the layout and design of mechanisms where in most cases planar and spatial mechanisms with non-uniform transfer characteristics are used. One of the most important steps within the design of the mechanisms inside a virtual design process is the proper modelling and simulation of the mechanism which includes both the kinematic and the dynamic modelling. Furthermore it is necessary to take care of a proper dynamic model of the actuation system involved. In this paper a model for pneumatic actuation and for servo electric actuation will be presented.*

1 INTRODUCTION

Considering that the forming of a glass container starting from the forming of a drop of molten glass with a honey-like viscosity at a temperature of approximately 1150°C until the push-out of the glass container onto the conveyor belt at approximately 450°C takes only about ten to twenty seconds depending on the size of the container, which can either be a small perfume flacon of less than 50g or a large champagne bottle of almost 1kg, then a glass forming machine can mainly be seen as a heat extraction machine. This already characterizes the harsh environment under which the mechanisms, that ensure a fast and precise motion, have to perform [1].

A considerable number of different motion devices are used within glass forming machines. They can be subdivided into passive and active systems. A passive motion system is e.g. the delivery system, which guides the glass gob from the gob distributor into the blank side mould. More interesting with regards to the topics of this paper are active motion devices. Therefore in this paper the focus will be on the systematic, mechatronic approach for the lay-out and design of mechanisms, i.e. planar and spatial mechanisms with non-uniform transfer characteristics.

Due to the non-uniform motions of the active motion devices, time variant inertia forces and inertia torques together with the non-linear dynamic behaviour of the drive system, the complete system model becomes rather complex. In order to properly predict the system behaviour, it is necessary to model the complete mechatronic system as exactly as possible in a multidisciplinary approach. This means that the modelling must include the dynamic behaviour of the drive system and the nonlinear mechanism behaviour.

Additionally it will also be shown, that by means of lab and field measurements a validation of the system model can be made. After such a validation the system model can be used as a basis for selecting suitable control algorithms. Furthermore different concepts for drive systems, e.g. pneumatic or electric can be compared.

2 FROM GOB TO BOTTLE: THE IS GLASS FORMING PROCESS

The most common version of container glass forming machines in use today is based on a parallel layout of the machine. Since its invention more than 80 years ago the Individual Section (IS)-Machine as shown in Fig. (1) has been the accepted industry standard for glass container production world-wide [1].

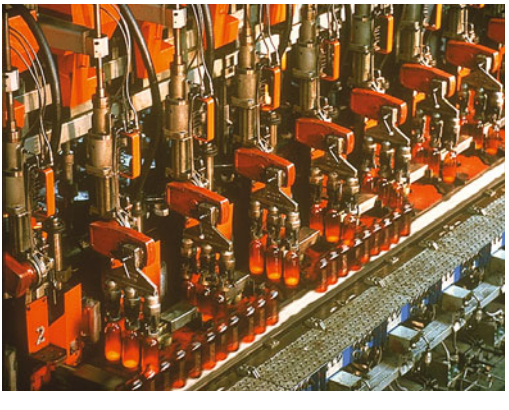

Figure 1: Blank side of an IS machine

This quite outstanding success over such a long period of time is mainly based on an initial design that allowed continuous further development in order to increase production performance. Several similar sections are arranged such, that the glass forming process takes place at the same time on all sections with a time delay governed by the firing order of the gob distributor, which delivers the gob to the delivery system of each section.

Today generally three different glass forming processes can be performed on an IS Machine [2]: The traditional Blow&Blow process, the common Press&Blow process and the advanced Narrow Neck Press&Blow process (NNPB). All processes are based on a two-step forming process with a parison formed in the blank side mould as an intermediate product which after passive reheating and inverting to the blow mould is blown up to the final container shape. This two step process is necessary in order to homogenize the temperature state of the prison whose inner and outer surface due to the contact with the mould material has cooled down considerably. Otherwise deteriorations of the glass surface with negative effect with regard to the strength of the final container could occur.

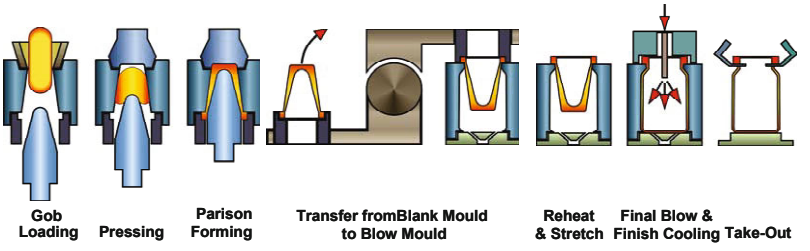

Figure 2: Press & Blow Process

Fig. (2) shows as an example the Press & Blow process. After the gob has been loaded via gob distributor and deflector system through the funnel into the blank mould, the parison is pressed and formed upside down by placing the baffle on top of the blank moulds and moving the plunger from its loading position upwards until the glass volume completely fills the blank mould. After the plunger and baffle have been removed and the mould halves have been opened, the parison is inverted from blank to blow side for parison reheat and final blow. After closing the blow moulds and parison reheat the container is finally formed by applying final blow with optional vacuum assist and finish cooling. At the end of the process the container is picked up by the take out and placed on the dead plate for additional cooling and final delivery into the lehr.

3 TUNED PRECISION: THE IS SECTION AND ITS MECHANISMS

The short description of the glass forming process on an IS section already shows, that precision and repeatability of the section mechanisms is of vital importance for a precise container forming process [3]. In order to properly realize the above described forming process on blank side, it is necessary to synchronise the motion of all mould parts such as blank side moulds, funnel, baffle, plunger and neckring in a coordinated and precise manner. Fig. (3) shows the blank side mould open & close mechanism, baffle mechanism and funnel mechanism as the major mechanisms on blank side.

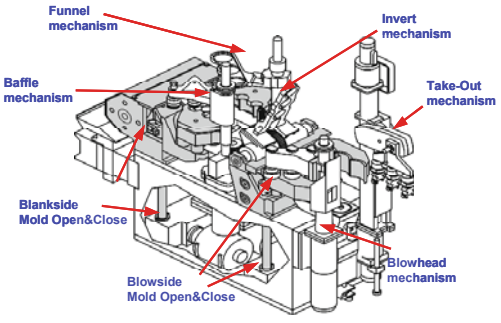

Figure 3: Section mechanisms

On the blow side the same applies to the mould parts that form the blow side cavity, where the parison as a result of the blank side process is blown up to the final container shape. Bottom plate, blow head and take-out have to be coordinated for this process step. Time wise the two forming processes on blank and blow side are connected by the invert mechanism, which inverts the parison from blank to blow side. This inverting must be done as swift as possible without damaging the soft parison due to excessive inertia forces. On blank side the next forming cycle can only start once the invert mechanism has been reverted to blank side. Similarly the forming process on blow side must wait until the finished container has been taken out of the blank mould by the take out mechanism. It is obvious that a stable and repetitive glass forming process is the key to a high quality glass container. This process stability and precision has a lot to do with the section mechanisms, whose motion under high cycle rate and high precision must be optimally coordinated.

3.1 Motion Generation: Twist Mechanisms

Most of the mechanisms used today and in the past for generating the necessary motion sequences are pneumatically driven. Very typical mechanisms are the so called twist mechanisms. These mechanisms are spatial cam mechanisms with linear actuation through a pneumatic cylinder and a combined translational and rotational output motion. All twist mechanisms start from an out-of-way position with a combined translational and rotational motion of the twist arm which at the end of motion is restricted to a purely translational motion as shown in Fig. (4).

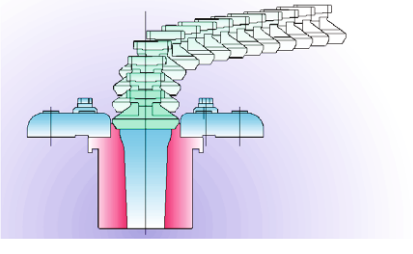

Figure 4: Typical twist motion

Fig. (5) shows a schematic sketch of the baffle mechanism together with the fixed cylindrical cam and the pneumatic cylinder. Besides this baffle mechanism also the funnel mechanism and the blow head mechanism are of the same kinematic design.

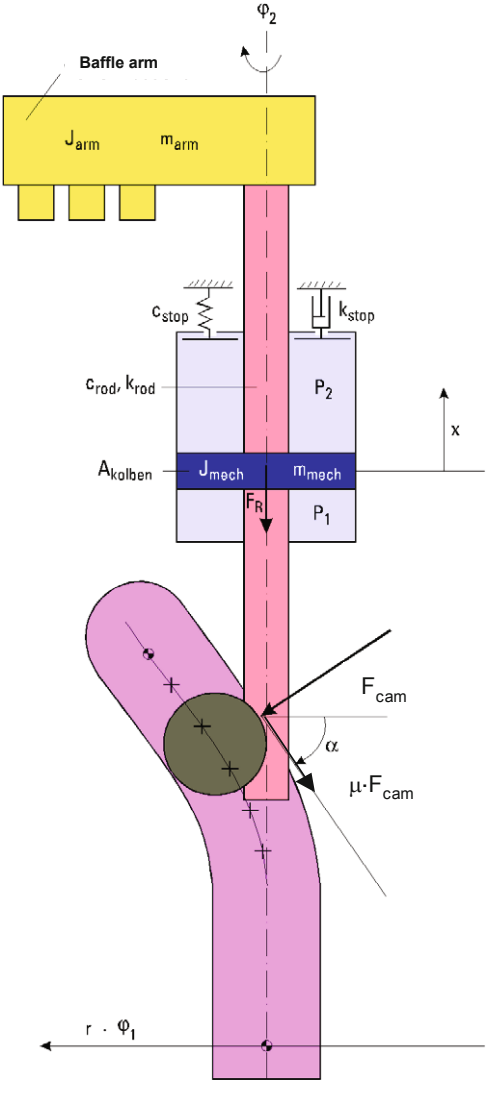

Figure 5: Physical model of the baffle mechanism

By taking the baffle mechanism as an example it will be shown in the following, how a simulation model can be derived, which allows to describe the dynamic behavior of spatial cam mechanisms with pneumatic drives.

The physical model of the baffle mechanism shown in Fig. (5) contains all parameters such as masses, inertias, spring rates, damping and forces which influence the kinematic and dynamic behavior of the mechanism. This model especially also considers the torsional elasticity of the piston rod in order to model the resulting torsional vibration of rod and arm. Furthermore the transfer function between the translational input motion x of the pneumatic cylinder and the rotational motion φ_1 of the baffle arm plays an important role. This transfer function is governed by the cylindrical cam which is displayed in Fig. (5) in a flat projection. The above described physical model is a multi body system with a degree of freedom equal to 2. Using the Newton/Euler formalism for the two independent coordinates x and φ_2 the following differential equations can be derived:

$$\ddot{\varphi}_2 = \frac{-c_{rod}\cdot(\varphi_2-\varphi_1)-k_{rod}\cdot(\dot{\varphi}_2-\dot{\varphi}_1)}{J_{arm}} \tag{1}$$

$$\ddot{x} = \frac{1}{m_{ges}+C_1\cdot J_{mech}\cdot\varphi_1'^2}\cdot\begin{pmatrix} A_{Kolben}\cdot(p_1-p_2)-m_{ges}\cdot g-F_R \\ -c_{stop}\cdot\Delta x-k_{stop}\cdot\Delta\dot{x}+F_{spring}+F_{clamp} \\ -C_1\cdot\left(-c_{rod}\cdot(\varphi_2-\varphi_1)-k_{rod}\cdot(\dot{\varphi}_2-\dot{\varphi}_1)\right) \\ -C_1\cdot\left(k_{Kolben}\cdot\left(\frac{D_{Kolben}}{2}\right)^2\cdot\dot{\varphi}_2+J_{mech}\cdot\varphi_1''\cdot\dot{x}^2\right) \end{pmatrix} \tag{2}$$

It should be noted, that the coordinate φ_1 which appears in both equations is not an independent co-ordinate but rather expresses the transfer function of the rotational motion $\varphi_1=\varphi_1(x)$. The terms $c_{stop}\cdot\Delta x$ and $k_{stop}\cdot\Delta\dot{x}$ describe the forces that result from the piston reaching its end stop at either end which means that Δx and $\Delta\dot{x}$ must be computed separately for both situations. The spring force F_{spring} must be considered only if an additional spring is used in order to speed up the upward motion. The clamping force F_{clamp} describes the force that appears when the baffle arm is pressed onto the blank molds. This force is ruled by the bending elasticity of both arm and rod. The torsional elasticity and material damping of the piston rod is described by the parameters c_{rod} and k_{rod}. Additionally Eq. (2) shows that friction caused by the rotational and translational motion of the piston has been considered. The rotational friction has been assumed as being velocity proportional and the translational friction which describes the friction of the rod against its bearings together with the friction between the piston and the inside of the pneumatic cylinder, can be modeled as stick-slip friction (stiction). It should be noted that the pressures p_1 and p_2 are additional independent variables that are ruled by additional differential equations which can be derived for the dynamic behavior of the pneumatic cylinder as shown in the following section.

Special interest should be given to the abbreviation C_1 in Eq. (2). As shown in Fig. (5), the contact force between fixed cam and cam roller is the vector sum of the normal force F_{cam} and the tangential friction force $\mu\cdot F_{cam}$. Thus the constraint between cam and cam roller is non-holonomic with

$$C_1 = \frac{1}{r_{cam}}\cdot\frac{r_{cam}\cdot\varphi_2'+\text{sign}(\dot{x}_2)\cdot\text{sign}(F_{cam})\cdot\mu_{cam}}{1-\text{sign}(\dot{x}_2)\cdot\text{sign}(F_{cam})\cdot\mu_{cam}\cdot r_{cam}\cdot\varphi_2'} \tag{3}$$

Eq. (3) contains the unknown constraint force F_{cam}. Within the design procedure for the spatial cam contour this force is of great importance [4]. The non-holonomic constraint expressed by Eq. (3) means, that the differential equation system cannot be directly solved. On the other hand the solution of the non-linear differential equation system in any case requires

the use of a numerical differential equation solver. This allows to use the solution for the unknown force F_{cam} of the previous integration step. Detailed analysis and tests which have been made within Matlab/Simulink© have proven the validity of this approach.

3.2 Motion Actuation: Pneumatic Cylinder

The physical model of the pneumatic cylinder, which is the basis for the simulation of the dynamic behavior of the pneumatic cylinder is displayed in Fig. (6). It shows all important parameters which influence the dynamic behaviour of the pressure inside both cylinder chambers. This model not only considers the flow characteristics for inlet and outlet but also the leakage of both cylinder chambers. Also pneumatic end position damping can be simulated by means of piston position dependant inlet and outlet cross sections. As an alternative, also hydraulic end position damping with stepped hydraulic constraints has been modelled too.

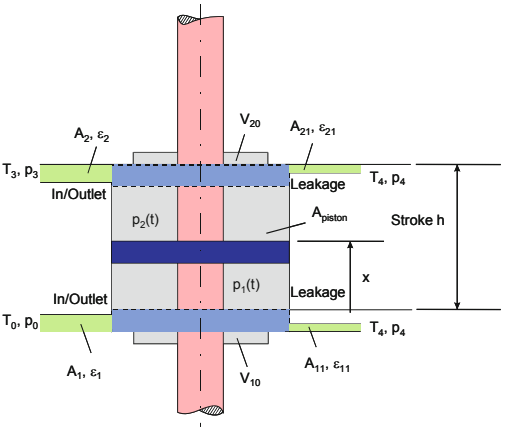

Figure 6: Pneumatic cylinder model

Starting from the first fundamental equation for stationary flow processes under consideration of time dependant mass flow the dynamic behavior of the pressure inside the cylinder chambers can be expressed by the following non linear first order differential equations [5]:

$$\frac{dp_1}{dt} = \frac{n}{V_{10} + x \cdot A_{Kolben}} \left[\begin{array}{l} \varepsilon_1 \cdot A_1 \cdot p_0 \cdot \sqrt{2 \cdot R \cdot T_0} \cdot \left(\frac{p_1}{p_0} \right)^{\frac{\kappa-1}{\kappa}} \cdot \psi_{10} \\ - \varepsilon_{11} \cdot A_{11} \cdot p_4 \cdot \sqrt{2 \cdot R \cdot T_4} \cdot \left(\frac{p_1}{p_4} \right)^{\frac{3\kappa-1}{2\kappa}} \cdot \psi_{41} \\ - \dot{x} \cdot A_{Kolben} \cdot p_1 \end{array} \right] \quad (4)$$

$$\frac{dp_2}{dt} = \frac{n}{V_{20} + (h - x) \cdot A_{Kolben}} \left[\begin{array}{l} -\varepsilon_2 \cdot A_2 \cdot p_3 \cdot \sqrt{2 \cdot R \cdot T_3} \cdot \left(\frac{p_2}{p_3} \right)^{\frac{3\kappa-1}{2\kappa}} \cdot \psi_{32} \\ -\varepsilon_{21} \cdot A_{21} \cdot p_4 \cdot \sqrt{2 \cdot R \cdot T_4} \cdot \left(\frac{p_2}{p_4} \right)^{\frac{3\kappa-1}{2\kappa}} \cdot \psi_{42} \\ +\dot{x} \cdot A_{Kolben} \cdot p_2 \end{array} \right] \quad (5)$$

The dimensionless function $\psi_{i,j}$ describes the flow through an ideal nozzle dependant from the pressure ratio p_i/p_j, where a distinction must be made between subcritical und supercritical flow. Of course for a practical application inlet and outlet flow of a pneumatic cylinder very seldom can be modeled as an ideal nozzle. This effect is covered through a certain penalty function. Also it should be noted that the pressures p_0, p_3 and p_4 are considered constant supply or ambient exhaust pressure. Also temperatures T_0, T_3 and T_4 are considered constant.

3.3 Twist Mechanism Model: Simulation and Verification

The differential equations presented in the previous section already show that a lot of parameters have to be ascertained in order to properly model the behavior of mechanisms with pneumatic drive. Among these parameters are such that can be collected rather easily such as kinematic dimensions, spring rates and inertias. But especially the determination of friction parameters is difficult. Therefore measurements have been made, where not only the pressure inside both cylinder chambers has been monitored, but also the translational and rotational motion of the baffle arm. Based on these measurements calculations have been made with a simulation model that based on the above differential equations has been programmed within Matlab/Simulink©. In an iterative process starting with exact or assumed values for all parameters a very good conformity between measured and calculated pressure for the lower and upper cylinder chamber of the baffle mechanism could be proven as shown in Fig. (7).

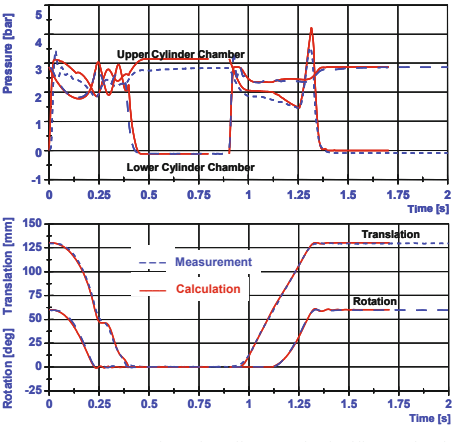

Figure 7: Pressure and motion diagram for baffle mechanism

The pressure curve and even the pressure peaks caused by the end stroke damping during upward motion show good accordance between measurement and simulation. This is also true for the pressure fluctuations that appear during downward motion. Also the motion diagrams displayed in Fig. (7) show good correlation. It should be noted that not only the deceleration phase during the downward motion but also the torsional vibration of the baffle arm during the end of the upward motion have been simulated properly. Of course the verification of the simulation model and its parameters has not been based purely on the comparison shown in Fig. (7). In fact several measurements of the real system with different parameters such as supply pressures, flow restrictions and inertias have been made and compared with simulations.

The simulations described above are not just of pure scientific interest but should especially serve towards getting a better understanding of the mechanism behavior and also to trigger design changes in order to optimize the mechanism. In this context it is important to realize, that the simulation allows to determine values of forces, pressures or motions which are hardly possible to measure at the real object. This is especially true for the contact force between cam roller and cam contour as shown in Fig. (8).

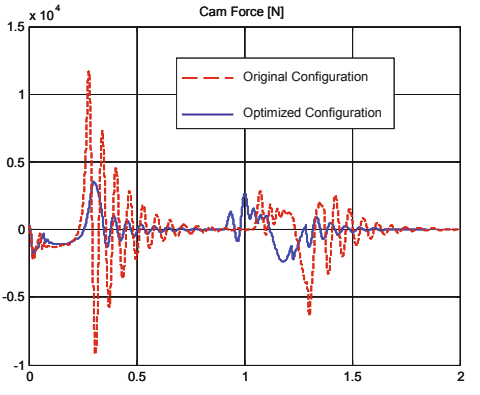

Figure 8: Calculated cam force for different settings

From the design point of view this force should be as low as possible. By changing the motion profile generated by the cam or by changing the control of the pneumatic cylinder the cam force can be reduced considerably.

3.4 Force Generation: Mould Open & Close Mechanism

Additionally to the twist mechanism described in the previous sections also the mould open and close mechanism that is used in slightly different kinematic configurations both on blank and blow side of the IS section has been modeled. It consists of two coupled four-bar linkages operated by an eccentric slider-crank mechanism located inside the section box [6] and two symmetrical four-bar linkages supporting the moulds on top of the section frame.

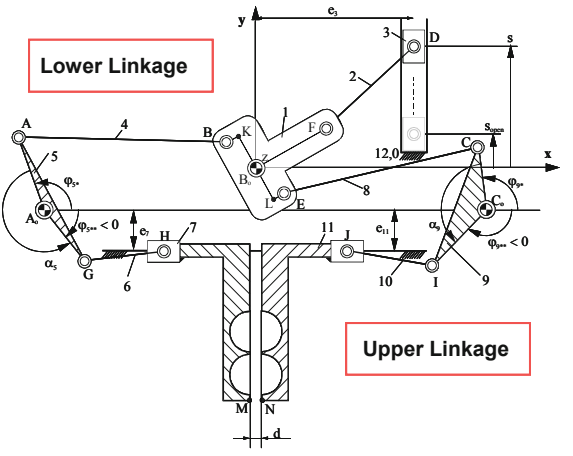

Figure 9: Kinematic schematic of mould open & close mechanism

The kinematic model of the mechanism in Fig. (9) reflects the non-linear transfer function between translational input motion of the pneumatic cylinder and rotational output motion of the mould holder arms. Lower and upper linkage are interconnected in A_0 and C_0 by mold shafts. Their torsional elasticity must be taken into account when modeling the motion behavior of the mechanism.

By applying a certain pressure in the pneumatic cylinder, the piston 3 will be driven from its starting position such that the two mold holder arms 7 and 11 will be closed. The applied pressure together with the piston diameter and the transfer characteristic of the linkage system also determines the closing force.

For the model of the pneumatic cylinder that is used to actuate the mould open & close mechanism the same model can be used as described in section 3.2.

3.5 Mould Open & Close Mechanism Model: Simulation and Verification

For a verification of the complete model containing the model of the mould open & close mechanism and the pneumatic cylinder model, measurements of the pressure in the two cylinder chambers, the motion of the mould holder arm and the closing force between the mould holder arms have been made for different configurations. As for the validation for the model of the twist mechanism these measurements were taken as a basis for simulation runs. Again using an iterative process uncertain parameters as friction, damping etc. could be identified by comparing measurement and simulation. This process based on a larger set of measurements under different conditions finally led to very good coherence between model and reality as shown in Fig. (10).

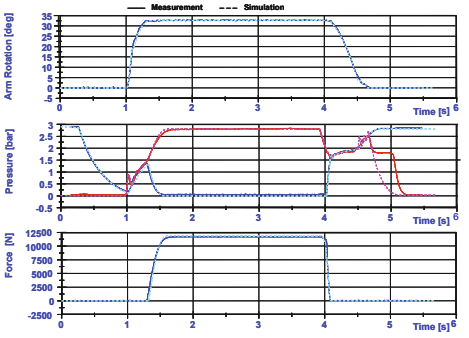

Figure 10: Measurement and Simulation for mould open & close

It is virtually impossible to distinguish the measured and simulated graphs for the motion of the mould holder arm, the lower and upper cylinder pressure and the mould closing force.

3.6 Alternative Motion Actuation: Servo Electric Motor

As an alternative for the pneumatic drive generally used today for IS-section mechanisms, also a servo electric drive has been considered and modeled. Both for the twist mechanism and for the mould open & close mechanism a configuration with a rotational servo electric motor that drives a screw through an elastic coupling and a nut which is connected to the translationally moving rod can be realized. After setting up a dynamic model of the servo electric motor together with the screw and nut combination, this model can simply replace the model of the pneumatic drive in order to have a complete model of servo electric drive and mechanism and thus be able to compare the two drive concepts.

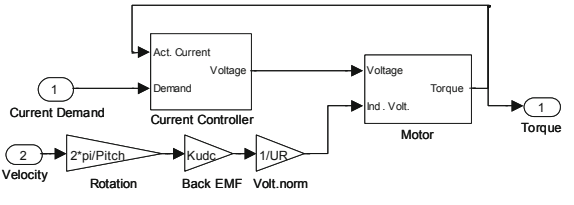

Figure 11: Servo electric drive model

Fig. 11 shows the Simulink© representation of the simulation model used for the servo electric drive. The dynamic behavior of the motor has been modelled as a DC-motor with the parameters coil resistance R and the inductivity L. Furthermore the self-induction of the motor has also been considered through the electro magnet flux constant K_{EMF}. This leads to the following differential equation:

$$\frac{dI}{dt} = -\frac{R}{L} \cdot I + \frac{1}{L} \cdot \left(U - U_{EMF}\right) \text{ with } U_{EMF} = K_{EMF} \cdot n \tag{6}$$

The model of the current controller shown in Fig. (12) is based on an analog PI-controller, described by the parameters K_p and T_I. Additionally a current saturation with an anti-wind-up loop has been modeled.

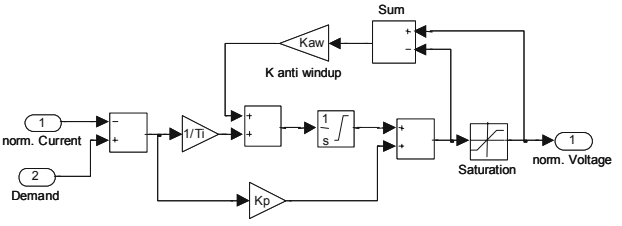

Figure 12: Servo electric drive model

The top layer of the cascaded control approach is a digital position controller shown in Fig. (13). In a certain analogy to classical cam mechanisms, the profile of the position demand is very important. The motion profile should be properly adapted to the velocity and acceleration limits of the system.

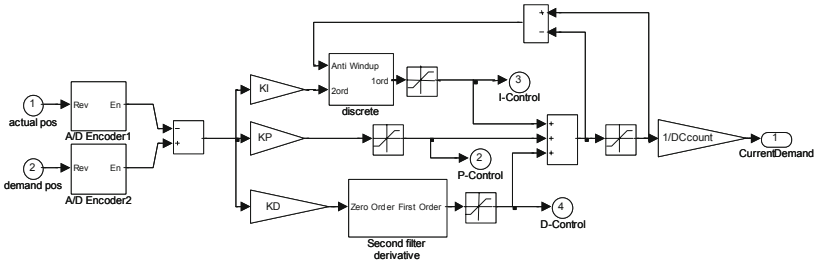

Figure 13: Model of the digital position controller

The motion profile that was used contains a constant velocity phase and trapezoidal acceleration and deceleration phases at the beginning and the end of the complete profile. This represents a good compromise between the dynamic requirements and the functionalities of commercial control systems that can be found on the market.

3.7 Precision and Speed: Servo Electric Twist Mechanisms

Fig. (14) shows the physical model that was used to model the servo electric twist mechanism with servo electric drive and screw & nut combination. Not only the contact force between cylindrical cam and roller but also the contact force between spindle and nut is modeled by taking friction effects into account.

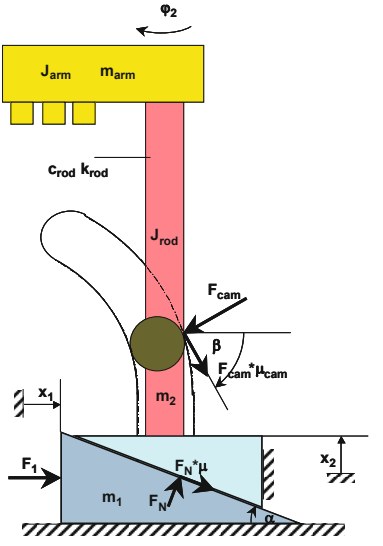

Figure 14: Model of the servo electric twist mechanism with screw & nut combination

Spindle and nut are depicted in a flat projection as an inclined plane with friction, where the force F_1 can be determined from the torque on the screw and its effective diameter.

Similar to the equations derived in section 3.1 the dry friction within the contact between spindle and nut is a non holonomic constraint leading to a differential equation system, which cannot be solved directly. The strategy used to overcome this problem by using a simulation model within Matlab/Simulink© is principally similar to the strategy described in section 3.1.

Starting from experience gathered from the simulation of the pneumatically actuated baffle mechanism, most of the parameters for the servo electric twist mechanism could be taken from the original pneumatic model. But also additional parameters, i.e. data necessary for the models shown in Figs. (12) and (13) as well as inertia and stiffness data for motor and elastic coupling between motor and spindle must be considered. As already explained in section 3.6, the motion profile contains a constant velocity phase and trapezoidal acceleration and deceleration phases at the beginning and the end of the complete profile. This usually symmetric profile can be made asymmetric using the algorithm described in [7].

Fig. (15) shows that choosing a proper motion profile leads to a considerable reduction of the cam contact force even when comparing to the already optimized pneumatic actuation.

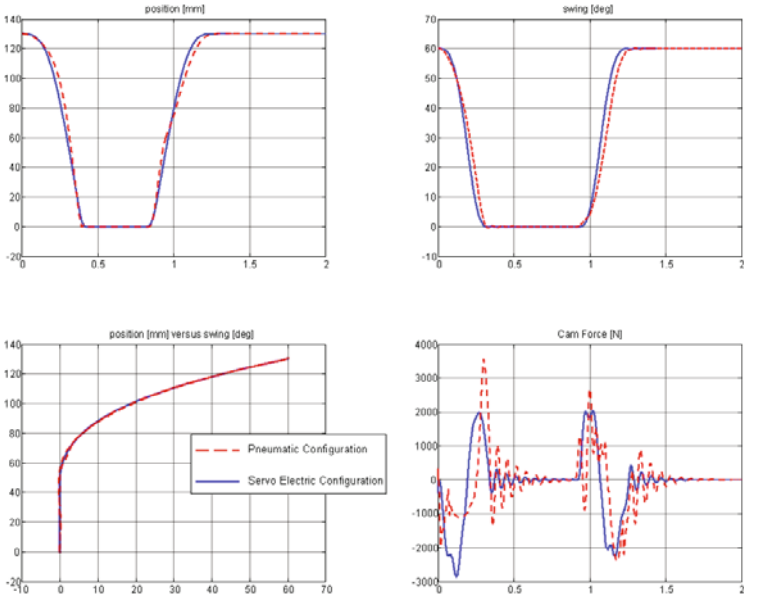

Figure 15: Comparison of optimized pneumatic and servo electric baffle mechanism

4 SUMMARY

In this paper methods for the simulation of mechanisms with non linear transfer function have been presented. These methods not only consider the mechanism itself but also the dynamics of the actuation device, such as pneumatic or servo electric actuation. Especially in the area of container glass forming machines, where precise and repeatable motion is required, such simulation techniques are helpful in order to optimize the glass forming process.

By using simulation methods both for pneumatic and electric drive systems not only the dynamic behavior of the mechanical mechanism but also the nonlinear dynamic behavior of the pneumatic drive or the influence of position and current control of the electric drive system can be considered. Comparisons between measurement and simulation prove the reliability of the simulation model. Finally a tool is available that allows to optimize an existing system or to design a new pneumatic or electric drive concept.

REFERENCES

[1] Grüninger, W.: IS-Section Performance: A strong base for innovation. *International Glass Review*, **Spring/Summer 1997**, 87-89, 1997.

[2] Corves, B.: *Formgebung bei Hohlglas – Forming of Hollow Ware*. In: VDMA und Messe Düsseldorf GmbH (Hrsg.): *Glass (Editon II): Glasherstellung – Glasveredlung Prozesse und Technologien, Glass Production – Glass Refinement Processes and Technologies*. Düsseldorf, 80-91, 2002.

[3] Corves, B.: IS-Machine Performance - Requirements and Developments. Parma: XII Convegno A.T.I.V 1996. *International Glass Journal,* **91**, 37-42, 1997.

[4] Corves, B.; Niggemann, H.: CAD-based, graphical dimension synthesis of spherical and spatial cam transmissions with the programme CADiS. Proceedings of EuCoMeS, the rst European Conference on Mechanism Science; Obergurgl, Austria, February 21–26 2006.

[5] Corves, B.: Mechatronic in Container Glass Forming. Proceedings of Mechatronic 2006, 4th IFAC-Symposium on Mechatronic Systems in Eng., Heidelberg, Germany, September 12–14, 2006.

[6] Houben H.: Parison and Container Forming. *Glass Production Technology International*, 94-101, 1995.

[7] VDI 2143 Bl. 1: *Bewegungsgesetze für Kurvengetriebe: Theoretische Grundlagen*.

IAK 2008
Conference on Interdisciplinary Applications of Kinematics
A. Kecskeméthy, V. Potkonjak and A. Müller (eds.)
Lima, Peru, 9–11 January 2008

PREDICTING PROTEIN CONFORMATIONAL TRANSITIONS BY TRAJECTORY PLANNING THROUGH TORSION ANGLE PROPENSITY MAPS

Christopher Madden, Peter Bohnenkamp, Kazem Kazerounian, and Horea T. Ilieş

Department of Mechanical Engineering
University of Connecticut
e-mails: cpm04002,peytah@gmail.com, kazem,ilies@engr.uconn.edu

Keywords: Protein, Kinematic Pathway, Conformation, Transition, Energy Landscape

Abstract. *The function of a protein macromolecule often requires conformational transitions between two native conGgurations. Understanding these transitions is essential to the understanding of how proteins function, as well as to the ability to design and manipulate protein-based nano-mechanical systems. It is widely accepted that the pathway connecting two native protein conformations in nature should satisfy a minimum energy criterion. The premise of this paper is that such a pathway can be found by using dihedral angle combinations that have been shown to have a high probability of occurrence in naturally observed proteins. In order to quantify this probability, we are proposing statistical propensity torque maps for tuples of dihedral angles. These maps are constructed in the angle space, similar to the Ramachandran Charts, but are based on data obtained from more than 38,600 proteins from Protein Data Bank (PDB) so that each map contains the experimentally observed pairs of dihedral angles* (φ_i, ψ_i)*,* (φ_i, ψ_{i+1})*,* $(\varphi_i, \varphi_{i+1})$ *and* (ψ_i, ψ_{i+1})*.*

1 INTRODUCTION

Proteins are nature's nano kinematic devices. At the macroscale, kinematic devices follow a constrained motion between two or more configurations in order to perform their functions. Similarly, the function of protein macromolecules often requires conformational transitions between two native configurations that are made possible by the intrinsic mobility of the protein. Understanding these transitions is essential to the understanding of how proteins function, as well as to the ability to design and manipulate protein-based nano-mechanical systems [3].

Macroscopic kinematic devices have relatively few components and, therefore, a rather small number of variables defining their spatial configurations. Broadly, these macroscopic devices move in a relatively uncluttered environment even when obstacles are present. On the other hand, the transitional pathway of a protein moving between two native configurations is significantly more complex due to the very large number of "design variables" and is therefore a computationally enormous task. Moreover, the external stimuli that cause these conformational changes are not completely understood. Computational models of proteins based on first principles can be both practical and valuable in understanding transition pathways of the proteins.

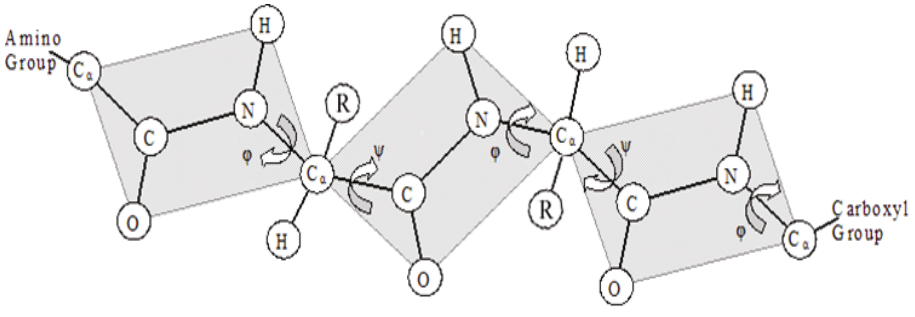

Figure 1: Amino Acid Chain with dihedral angles as generalized coordinates.

It is generally agreed upon that functional proteins have two or more native structures that are relatively close in terms of the corresponding potential energy values [13, 5, 8, 15]. Furthermore, it takes a relatively small amount of energy to trigger the transition from one conformation to another. Thus, it is common to assume that the pathway between the native conformations is a "valley" in the potential energy landscape. To understand such pathways, a detailed description of the kinematic motion of the molecule as well as the energy landscape corresponding to the kinematic structure is needed. Numerous methods have been developed to describe the conformational transition of the proteins along preferred energy pathways. A straight forward attempt is linear interpolation of the end point native conformations [4]. Such methods can also be improved by additional energy minimization [12]. While these methods are useful in visualization of the conformational transition, they do not necessarily represent the physical motion of the protein. More complex approaches include introduction of artificial potential forces in conjunction with Molecular Dynamics Simulation to force the protein motion from one conformation to another [16, 7]. However, the enormous computational requirement of the MDS severely limits the applicability of these methods. Furthermore, the accuracy of assuming large potential forces for guiding the conformation has not been quantified.

Traditional engineering based methods have proven very useful in studying the conforma-

tional pathways. One such method is normal modal analysis of the protein structures [6, 22, 23]. While effective, due to the linear nature of modal analysis, such methods are, at best, local in time domain. By developing elastic models of the protein as a network of mass and springs, the efficacy of normal modal analysis is expanded globally throughout the conformational transition [11, 17]. One other class of approaches searching for the protein conformational pathways, which are deeply rooted in engineering applications, are based on robot motion planning algorithms [1, 24]. Such approaches have been remarkably successful in navigating the environment surrounding a robot, partly because that environment is assumed to be known. In the context of protein motion, the challenges faced by these approaches stem from the facts that the energy landscape is essentially unknown, and is defined in a high dimensional space whose dimension is much larger than the dimension of the spaces encountered in the typical robot motion planning problems.

In this work, we propose a new method for interactive planning of transitional pathways of a given protein. It is widely accepted that the pathway connecting two native protein conformations in nature should satisfy a minimum energy criterion. The premise of this paper is that such a pathway can be found by using dihedral angle combinations that have been shown to have a high probability of occurrence in naturally observed proteins. We propose the statistical propensity torque maps[1] for tuples of dihedral angles that capture the probability of occurrence of specific dihedral angle combinations in nature. This is so because our maps are constructed in the angle space, similar to the Ramachandran charts, but are based on data obtained from more than 38,600 proteins from Protein Data Bank (PDB) so that each map corresponds to pairs of dihedral angles (φ_i, ψ_i), (φ_i, ψ_{i+1}), $(\varphi_i, \varphi_{i+1})$ and (ψ_i, ψ_{i+1}). These maps are explained in more detail in Section 3.

2 OUR PROTEIN MODEL

We model the protein molecule as a kinematic chain of rigid bodies connected by revolute joints [9, 10, 2, 19, 20, 21]. In our novel approach, known as the Successive Kineto-Static Fold Compliance Method, the conformational changes of the peptide chain are driven by an inter-atomic force field without the need for Molecular Dynamic Simulation. Instead, the chain complies under the Kineto-Static effect of the force field in such a manner that each rotatable joint changes by an amount proportional to the effective torque on that joint. This process successively iterates until all of the joint torques have converged to zero. The resulting conformation is in a minimum potential energy state. This methodology has been used to develop the PROTOFOLD protein simulation software, and has been shown to be orders of magnitude more efficient and robust than traditional Molecular Dynamics Simulation [18].

3 DIHEDRAL ANGLE PROPENSITY MAPS

Protein backbone structure in the serial chain kinematic model is uniquely defined by the set of dihedral angles φ (the amino angle) and ψ (the carboxyl angle) for each amino acid (residue). The set of these angles for all residues in the chain constitute the generalized coordinates of the backbone. In this work, we have modeled 20 of the 22 amino acids known to exist in the nature (the discovery of the last two has only been announced recently). In our model, the conformational transitions of the proteins are the result of the changes in the main chain dihedral angles and side rotamer angles.

[1] In the robotics literature, a concept similar to our propensity maps is known as the dihedral work envelopes.

3.1 Steric Interaction and the Dihedral Angle-Space Propensity Maps

The driving forces behind protein folding are the interactions between the atoms that form the protein. As the joint angles change, the relative positions (distance) of atoms as well as the inter-atomic forces change as well. The inter-atomic forces and, thus, the potential energy of the protein increase very quickly as the distance between two atoms approaches the diameter of the van der Waals spheres. The set of corresponding dihedral angles can be computed for any such distance. On the other hand, the natural tendency of protein structures (and essentially of any physical system) is to move towards states having lower potential energy. Therefore the angle combinations that create high potential energy states can be considered to be prohibited zones. The corresponding configurations are the "sterically disallowed" configurations. In an analogous robotic system, a set of joint angles defining a sterically disallowed configuration would produce joint angles that would correspond to self collision of the robot.

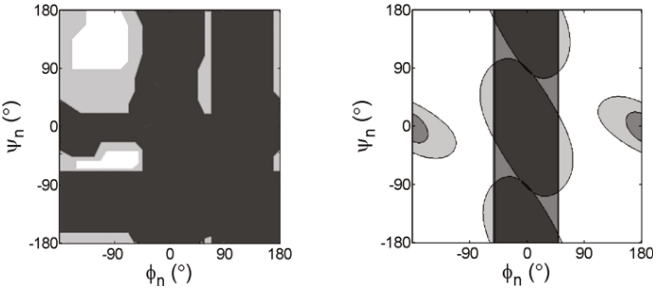

Figure 2: (a) Ramachandran Chart; (b) Glycine Self Collision Chart

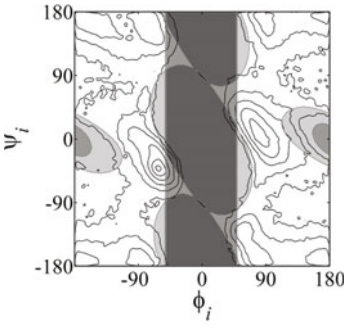

Figure 3: Outline of sterically prohibited angle space for Glycine overlaid onto dihedral angle population density from PDB.

In 1963, [14] used both experimental and analytical methods to develop a set of inter-atomic minimum distances in amino acids. Their results are included in Table 1, where the left column corresponds to atoms in the two peptide planes connected by an α-C.

Note that there are two limits listed in the table: a normal limit, and an extreme limit. At the atomic level there can be no interference between particles in the structure which is physically prevented by a steady increase in the repulsive force between two potentially interfering atoms. The conventional Ramachandran Map is a projection of the domain of the function (the torus) onto the plane and shows the fully allowed, partially allowed, and disallowed regions for a dihedral angle tuple. These regions are constructed based on geometric derivations of the inter-atomic distances for various non-bonded atoms of the polypeptide, and by comparing these analytically obtained distances with those shown in Table 1.

Type of Contact	Normal Limit (Å)	Extreme Limit (Å)
H to H	2	1.9
H to O	2.4	2.2
H to N	2.4	2.2
H to C	2.4	2.2
O to O	2.7	2.6
O to N	2.7	2.6
O to C	2.8	2.7
N to N	2.7	2.6
N to C	2.9	2.8
C to C	3	2.9

Table 1: Inter-atomic limiting distances [14]

The kinematic chain model of a polypeptide (for example, as we implemented in PROTOFOLD) can also be used to detect sterically disallowed angle combinations. The minimum distances shown in Table 1 can be coupled with a rigid sphere collision model set up in the kinematic chain model. The dihedral angles are varied between $0^o < \varphi < 360^o$, and $0^o < \psi < 360^o$, while monitoring the inter-atomic distances, which will result in the set of $\varphi - \psi$ pairs that cause unstable structures. This set will be different for each amino acid. [14] performed such an analysis for each amino acid, and combined the results in one chart that entails the ranges of $\varphi - \psi$ values that are sterically disallowed. This chart known as the "Ramachandran" chart or map (Fig. (2a)), and has been traditionally shown over the ranges $-180^o <= \varphi <= 180^o$, and $-180^o <= \psi <= 180^o$ in the Cartesian plane. The darkest regions indicate dihedral angle combinations that are strictly sterically disallowed. Grey regions indicate sterically "strained" combinations, or, in other words, higher energy states that are still possible. White regions denote sterically allowed angle combinations. Figure (2b) is the map generated from a rigid sphere collision test implemented for only one amino acid structure, i.e., the Glycine. Note that many more angle combinations are considered sterically allowed for Glycine than for all amino acids, and that the Glycine map is a subset of the Ramachandran map.

In nature, dihedral angle combinations sometimes occur inside sterically disallowed regions. This happens when a disallowed angle combination results in an overall decrease in the potential energy of the structure. This phenomenon is relatively rare.

3.2 Generating Dihedral Angle Propensity Maps

The $\varphi - \psi$ propensity maps can be generated by using the rigid sphere model. Alternatively, such maps encoding the statistical distribution of angle combinations observed in nature could be generated from the experimentally observed data found in the Protein Data Bank, which contains information on more than 40,000 proteins. While both techniques result in analogous map contours, PDB based maps contain details of the population propensity. This is illustrated in Fig. 3 where we superimpose the maps obtained via the two methods mentioned above for a Glycine residue: the shaded areas are obtained from the collision model, and the contour curves (isocurves) have been computed based on PDB data. Furthermore, observe that the difference between the charts, as illustrated in Figs. (2a) and (2b), clearly indicates that the typical Ramachandran chart (Fig. (2a)) is inadequate for computing propensity regions for all the dihedral angles in all amino acid sequences. Therefore, we have developed torque charts

for the dihedral angle sets (φ_i, ψ_i) as well as (φ_i, ψ_{i+1}), $(\varphi_i, \varphi_{i+1})$ and (ψ_i, ψ_{i+1}). Since we modeled 20 (of the 22) amino acids known to exist in nature, 400 possible sequences exists for a pair of residues. Therefore the total number of maps in our master collection is 1220 $(20 + 400 + 400 + 400)$ maps, which were developed based on 38,642 proteins from PDB. Figure 4 illustrates four such maps (one corresponding to each angle set).

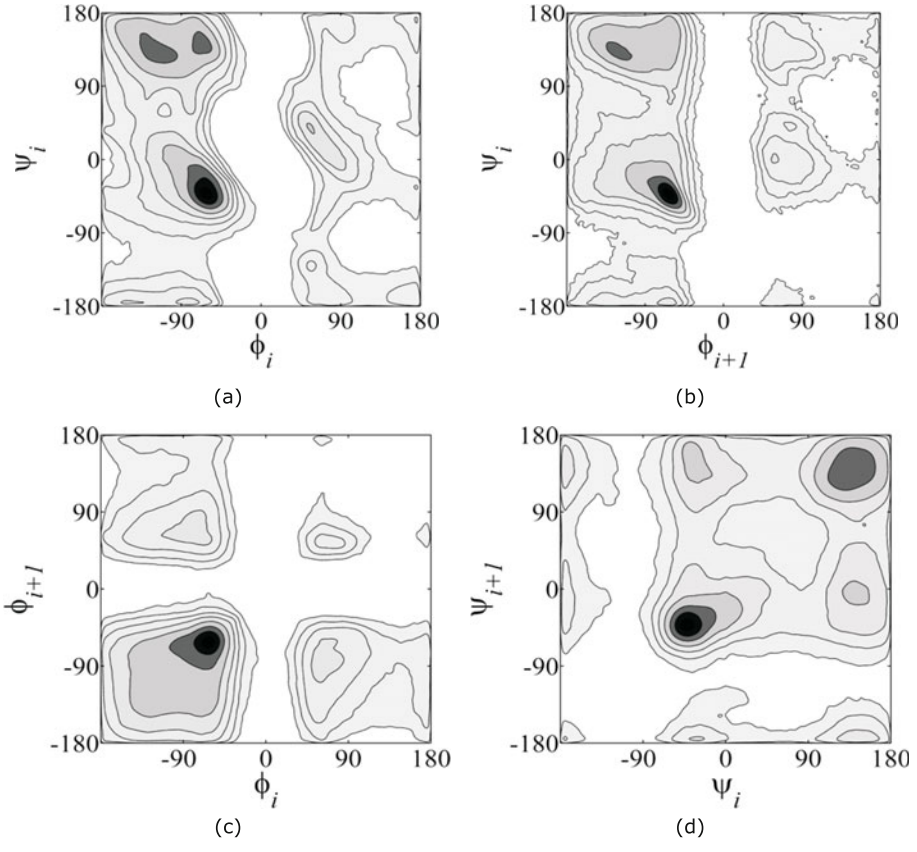

Figure 4: Four sample combination of dihedral angle work envelopes.

Darker regions indicate higher population density observed in nature and hence more favorable energy configurations.

4 DIHEDRAL ANGLE-SPACE PROPENSITY MAPS AS NAVIGATION GUIDES

In our numerical experiments we focused on the protein 1FOX, whose two known native conformations are shown in Fig. 5. These two native conformations, known as 1FOX and 2FOW, have been computed based on data obtained from PDB.

Observe that PDB contains a set of dihedral angles for the backbone for each of the two native conformations. However, our dihedral angles are slightly different than those found in PDB due

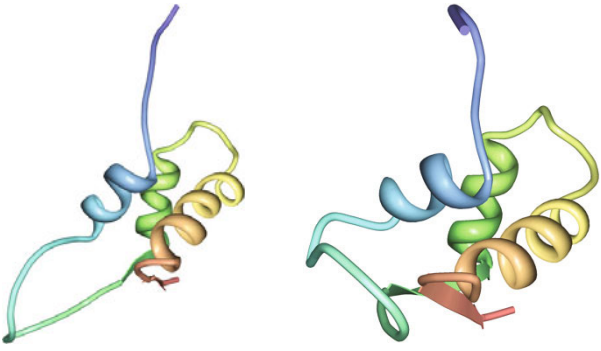

(a) (b)

Figure 5: (a) 1FOX ribbon plot (b) 2FOW ribbon plot.

to both our serial kinematic chain model of connected rigid bodies as well as to the improved numerical model of the peptide planes [19], but the differences are negligible for the purpose of this work. There are 76 residues in this protein molecule, which result in 152 dihedral angles for the back bone. Consequently there are a total number of 213 torsion propensity maps.

A point in each of these maps corresponds to a specific set of values for the corresponding angles. Therefore, each of the two native conformations 1FOX and 2FOW are represented in each of our maps by one point in the torsion angle work space. Each curve connecting these two points (for a given map), represents a pathway for that particular set of dihedral angles. Then the pathway taking the protein from one native configuration to the other will be obtained by combining all these angle level pathways.

4.1 Shortest Distance Linear Pathways

Clearly, the simplest way to connect two points is by straight line, which is the basis of most of the existing visualization techniques for conformational transitions. Figure 6 shows four of these maps with the linear pathway in angle space for conformational transition. The larger circle at one end of the path in each chart indicates the initial conformation (i.e. 1FOX). The lines shown are the shortest distance between the two end conformations. The darker regions in the chart indicate lower energy conformations and, therefore, naturally higher population density in PDB. Moreover, Figs. (6a) through (d) show the linear pathways with color-coded lines (coded on a gray scale) that correspond to the potential energy of the protein. Figure 7 shows the same map as Fig. (6c) but with the color-coded pathway (RGB scale) as a function of the same potential energy of the molecule along the path. It can be clearly seen that the portions of the path on higher energy domains (lighter, or less populated regions) indicate higher total potential energy for the transitional conformation at that point on the pathway.

4.2 Selected Direction Linear Pathways

The first step in adjusting the pathway to obtain a transition whose trajectory is more energy favorable was to select the direction of the linear paths in the angle space. To change each angle from an initial to a final value, two rotational directions can be selected (cw or ccw about the joint axis). Therefore four distinct linear paths are possible between the two end points in each

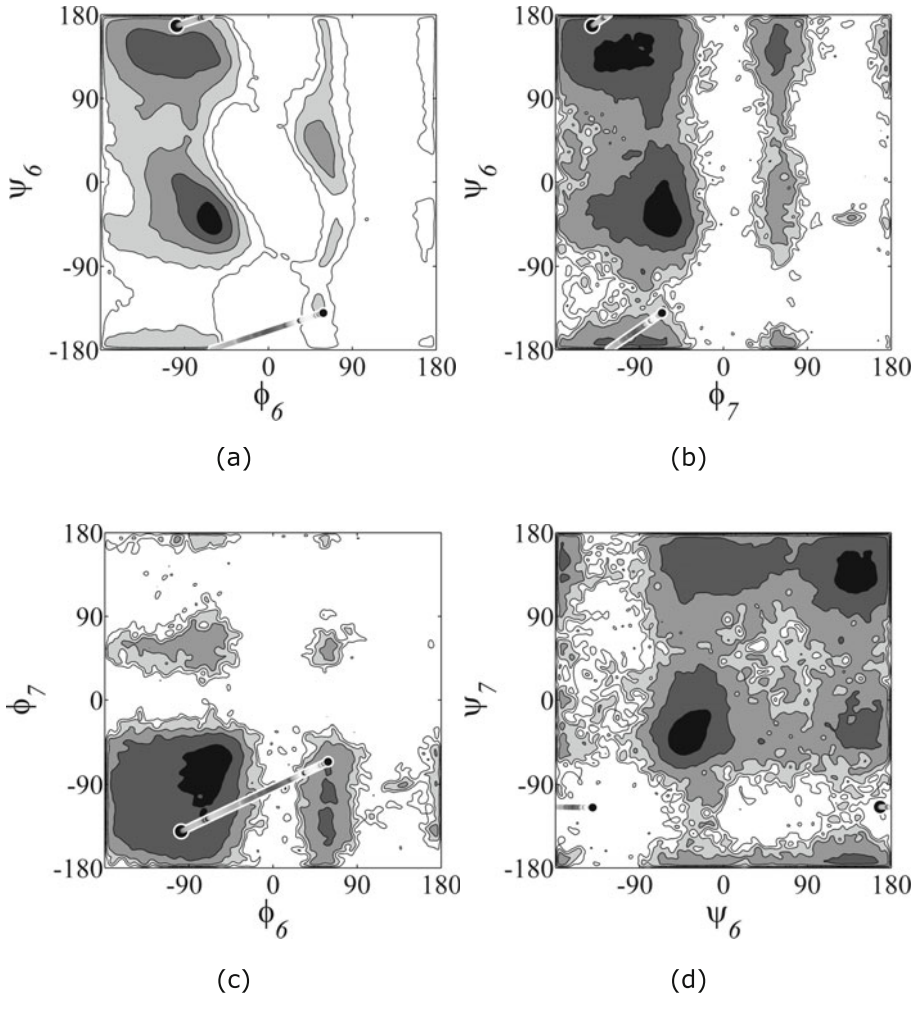

Figure 6: Conformational transition pathway of the dihedral angles along shortest distance linear paths in the third and forth residues (LYS-THR) of the protein molecule (1FOX to 2FOW).

chart. In our computer implementation each one of the four directions are evaluated for the sum of the molecule's potential energy along the path. The output of this evaluation is interactively used to select one of the four paths. Figure 8 shows sample selected paths.

4.3 Improved Energy Pathways

Through visual inspection of the charts (see sample charts in Fig. 8), the user can interactively force the paths to go through lower energy conformations as indicated by higher population intensity (darker regions). In our computer implementation, the trajectory modification

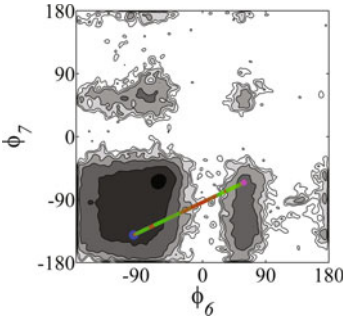

Figure 7: The chart of Fig. (6c) with the color-coded path to indicate total potential energy of the molecule throughout the conformational transition.

is possible through introduction of additional trajectory points, or dragging existing trajectory points to new locations. Figure 9 shown sample charts where the selected linear pathways are modified visually by the user.

4.4 Minimum Energy Pathways

To fulfill the objective of obtaining a path of minimal energy between two low energy end conformations, the interactively designed pathways described above need to be further optimized. The kineto-static compliance method implemented in PROTOFOLD [10, 9] is applied to the curvilinear angle space pathways. PROTOFOLD can perform additional fine tuning of the pathways by rotating the joint angles that will relieve the highest remaining joint torques. Figure 10 illustrates the relationship between the linearly interpolated, planned and optimized paths in angle space. The contours shown are very simple representations of the complex energy landscape between the start and end conformations. If the end goal is to minimize the overall energy rise over the entire conformational motion, then the path should follow an isoenergy contour.

Given a pathway planned in angle space, energies are calculated for a set of intermediate conformations between the known end configurations using the AMBER force field applied to the kinematic model. Successive Kineto-Static Fold Compliance method in PROTOFOLD is used to move the kinematic model at each given intermediate conformation to one of lower energy. This process is repeated for all intermediate conformations, under the restriction of minimal joint rotation to keep continuity between adjacent intermediates. If this were not in place, two adjacent conformations could diverge in angle space and the resulting pathway would be discontinuous. The energy minimized pathway very closely follows the planned input pathway in angle space, but is able to traverse a much lower energy profile.

This method is especially effective at relieving local areas of intense atomic interaction that cause high energy, but are not detected through angle space planning alone. Running this optimization procedure for the sections of the pathway that contain large jumps in energy is both computationally effective, since it does not have to run for all intermediate conformations, and effective at removing the largest energy barriers. Figure 11 shows how one can avoid large energy barriers with minimal changes in angle space of intermediate conformations by running this optimization procedure.

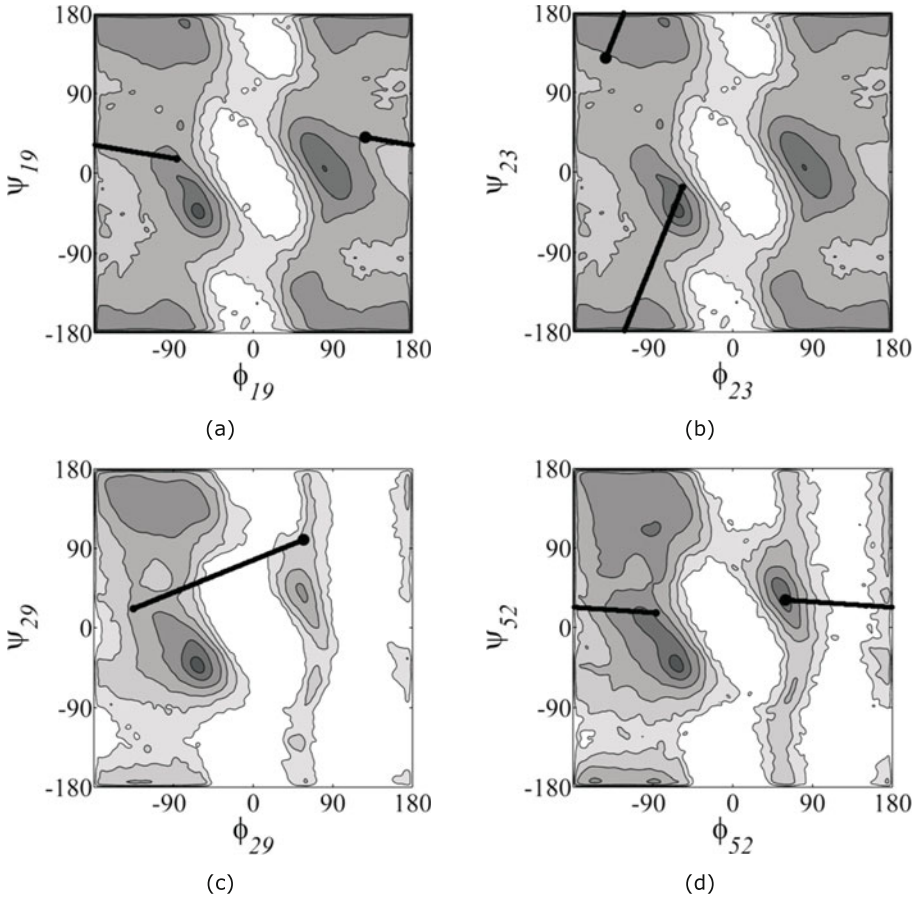

Figure 8: Sample conformational transition pathway of the dihedral angles along energy favorable linear paths in protein molecule (1FOX to 2FOW).

4.5 Simulation Results

Figure 12 shows the energy profile of the various pathways that we have simulated in this work. The potential energy is directly related to the equivalent joint torques calculated in PROTOFOLD. In Fig. 12, the Euclidean norm of the torque vector (summation of the square of all joint torques) is evaluated at discrete points along the pathway. As seen in Fig. 12, the best direction linear paths show some improvements over the shortest linear paths in some segments of the pathway, but not everywhere.

From these plots it is evident that the designed path which is interactively designed by the user based on chart navigation leads to significantly more favorable energy profiles than the linear pathways in the torsion angle space. Furthermore, using these paths as the initial guess in the energy minimization performed by the PROTOFOLD further improves the energy profile of the pathways. Samples of the final energy optimum pathways are illustrated in Fig. 13.

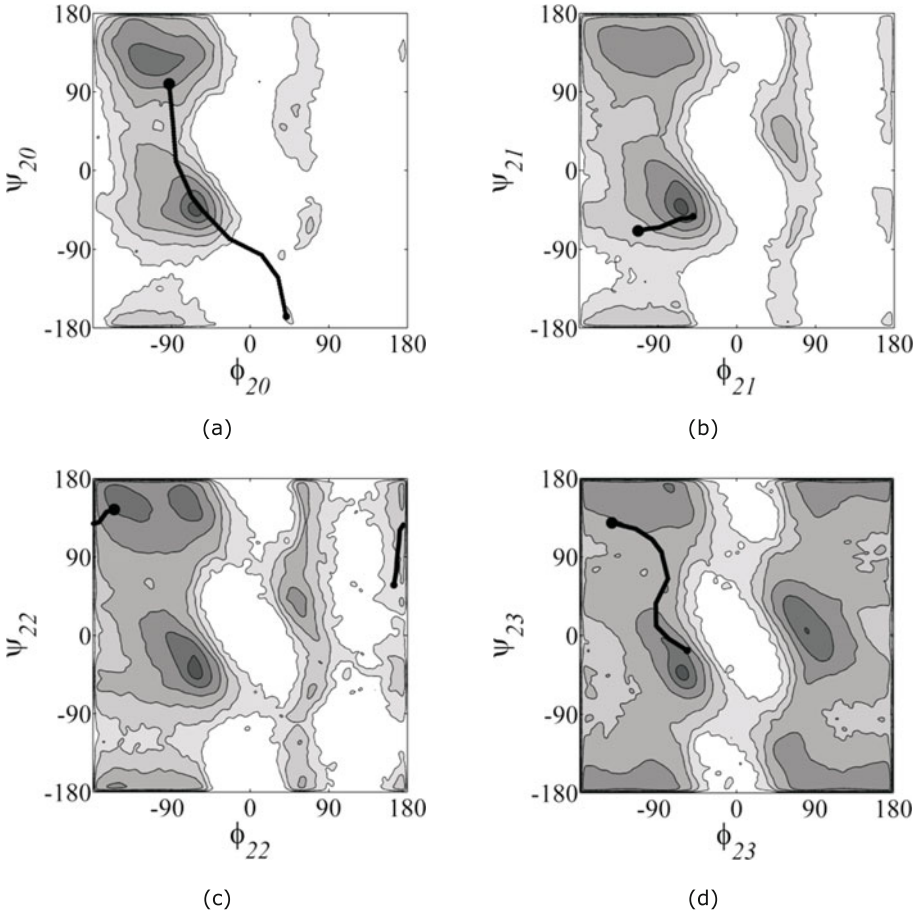

Figure 9: Sample conformational transition pathway of the dihedral angles modified interactively by the user to result in more energy favorable trajectories (1FOX to 2FOW).

5 CONCLUSIONS

In this paper we have developed a systematic methodology for developing pathways for the conformational transition of the functional protein molecules. The pathways are developed based on torsion angle propensity maps obtained from the data available on more than 38,000 protein chains in the Protein Data Bank (PDB). Our numerical simulations indicate that these charts provide an very effective strategy for charting minimum energy profile pathways.

REFERENCES

[1] N. M. Amato and G. Song. Using motion planning to study protein folding pathways. *Journal of Computational Biology*, 9(2):149–168, 2002.

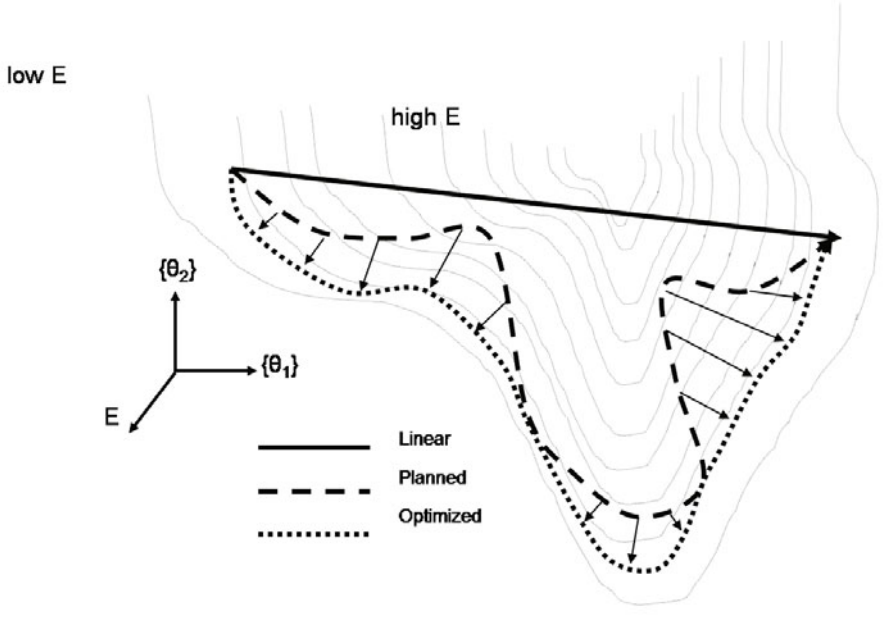

Figure 10: Three dimensional contour representation of energy landscape with various angle space paths..

[2] P. Bohnenkamp, K. Kazerounian, and H.T. Ilies. Strategies to avoid energy barriers in ab initio protein folding. In *12th IFToMM (International Federation of the Theory of Mechasims and Machines) World Congress*, Besanon, France, 2007.

[3] G. S. Chirikjian, K. Kazerounian, and C. Mavroidis. Analysis and design of protein based nanodevices: Challenges and opportunities in mechanical design. *Journal of Mechanical Design*, 127(4):695–698, 2005.

[4] M. Gerstein and W. Krebs. A database of macromolecular motions. *Nucleic Acids Research*, 26(18):4280–4290, 1998.

[5] N. Gibbs, A. R. Clarke, and R. B. Sessions. Ab initio protein structure prediction using physicochemical potentials and a simplified off-lattice model. *Proteins-Structure Function and Genetics*, 43(2):186–202, 2001.

[6] C. Guilbert, F. Pecorari, D. Perahia, and L. Mouawad. Low frequency motions in phosphoglycerate kinase. a normal mode analysis. *Chemical Physics*, 204(2-3):327–336, 1996.

[7] C. Guilbert, D. Perahia, and L. Mouawad. A method to explore transition paths in macromolecules - applications to hemoglobin and phosphoglycerate kinase. *Computer Physics Communications*, 91(1-3):263–273, 1995.

[8] K. Itoh and M. Sasai. Coupling of functioning and folding: photoactive yellow protein as an example system. *Chemical Physics*, 307(2-3):121–127, 2004.

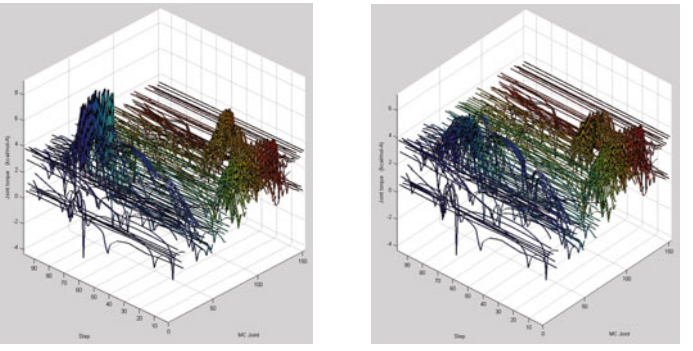

(a) (b)

Figure 11: Plot of torques on every main chain joint during 1FOX-2FOW transition following (a) planned angle space pathway and (b) energy optimized angle space pathway. Note the local, large magnitude reduction in energy accomplished through the optimization.

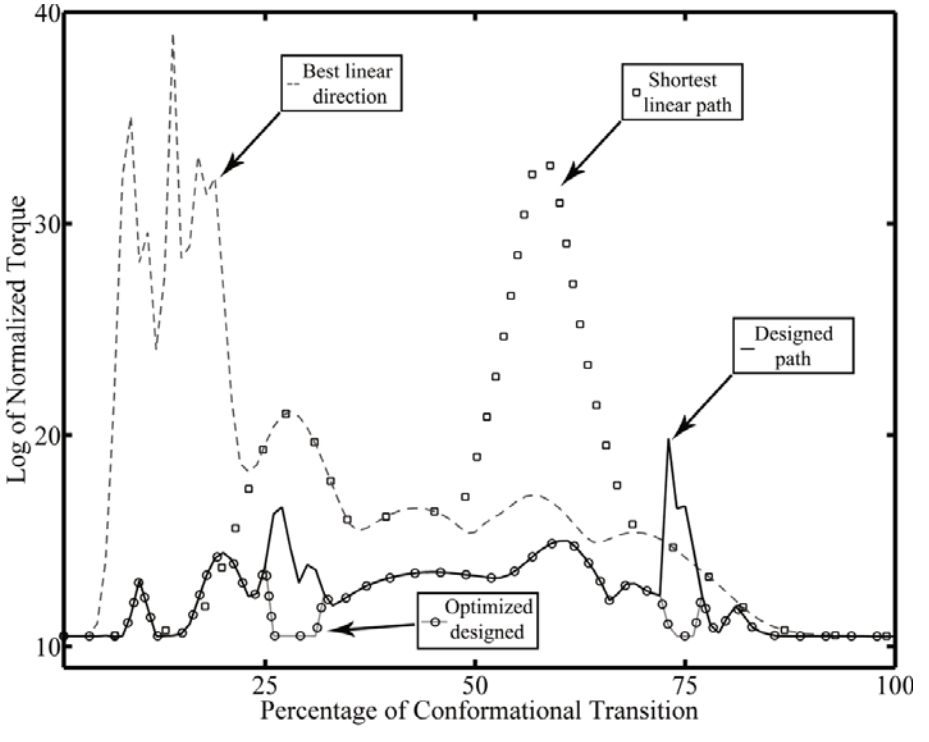

Figure 12: Simulated Pathways.

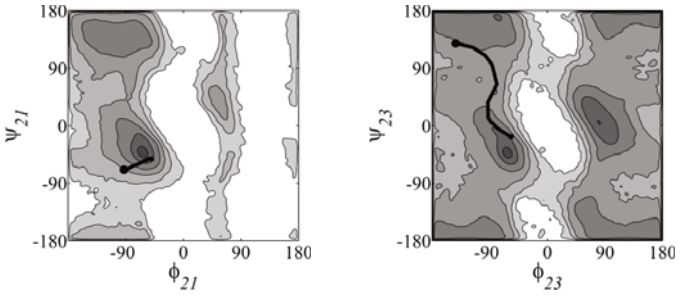

(a) (b)

Figure 13: Sample conformational transition pathway of the dihedral angles along the energy optimized pathways obtained by PROTOFOLD (1FOX to 2FOW).

[9] K. Kazerounian, K. Latif, and C. Alvarado. Protofold: A successive kinetostatic compliance method for protein conformation prediction. *Journal of Mechanical Design*, 127(4):712–717, 2005.

[10] K. Kazerounian, K. Latif, K. Rodriguez, and C. Alvarado. Nano-kinematics for analysis of protein molecules. *Journal of Mechanical Design*, 127(4):699–711, 2005.

[11] M. K. Kim, R. L. Jernigan, and G. S. Chirikjian. An elastic network model of HK97 capsid maturation. *Journal of Structural Biology*, 143(2):107–117, 2003.

[12] W. G. Krebs, J. Tsai, V. Alexandrov, J. Junker, R. Jansen, and M. Gerstein. Tools and databases to analyze protein flexibility; approaches to mapping implied features onto sequences. *Macromolecular Crystallography, Pt D*, 374:544–+, 2003.

[13] O. Miyashita, P. G. Wolynes, and J. N. Onuchic. Simple energy landscape model for the kinetics of functional transitions in proteins. *Journal of Physical Chemistry B*, 109(5):1959–1969, 2005.

[14] G.N. Ramachandran, C. Ramakrishnan, and V.J. Sasisekharan. Stereochemistry of polypeptide chain configurations. *Journal of Molec. Biology*, 7:95–99, 1963.

[15] H. A. Scheraga, A. Liwo, S. Oldziej, C. Czaplewski, J. Pillardy, D. R. Ripoll, J. A. Vila, R. Kazmierkiewicz, J. A. Saunders, Y. A. Arnautova, A. Jagielska, M. Chinchio, and M. Nanias. The protein folding problem: Global optimization of force fields. *Frontiers in Bioscience*, 9:3296–3323, 2004.

[16] J. Schlitter, M. Engels, and P. Kruger. Targeted molecular-dynamics - a new approach for searching pathways of conformational transitions. *Journal of Molecular Graphics*, 12(2):84–89, 1994.

[17] A. D. Schuyler and G. S. Chirikjian. Efficient determination of low-frequency normal modes of large protein structures by cluster-NMA. *Journal of Molecular Graphics & Modelling*, 24(1):46–58, 2005.

[18] HJ. Su, J Parker, K Kazerounian, and H.T. Ilies. A comparison of kinetostatic and multibody dynamics models for simulating protein structures. In *Mechanisms and Robotics Conference, ASME IDETC*, September 2007, Las Vegas, 2007.

[19] R. Subramanian and K. Kazerounian. Improved molecular model of a peptide unit for proteins. In *ASME 2006 International Design Engineering Technical Conferences & Computers and Information in Engineering Conference*, volume DETC 2006 - 99315, Philadelphia, Pennsylvania, USA, 2006.

[20] R. Subramanian and K. Kazerounian. Kinematic mobility analysis of peptide based nanolinkages. *Mechanism and Machine Theory*, 42(8):903–918, 2007.

[21] R. Subramanian and K. Kazerounian. Residue level inverse kinematics of peptide chains in the presence of observation inaccuracies and bond length changes. *Journal of Mechanical Design*, 129(3):312–319, 2007.

[22] F. Tama and Y. H. Sanejouand. Conformational change of proteins arising from normal mode calculations. *Protein Engineering*, 14(1):1–6, 2001.

[23] F. Tama, W. Wriggers, and C. L. Brooks. Exploring global distortions of biological macromolecules and assemblies from low-resolution structural information and elastic network theory. *Journal of Molecular Biology*, 321(2):297–305, 2002.

[24] L. Tapia, X. Y. Tang, S. Thomas, and N. M. Amato. Kinetics analysis methods for approximate folding landscapes. *Bioinformatics*, 23(13):I539–I548, 2007.

IAK 2008
Conference on Interdisciplinary Applications of Kinematics
A. Kecskeméthy, V. Potkonjak and A. Müller (eds.)
Lima, Peru, 9–11 January 2008

POTENTIAL APPLICATIONS OF HYBRID SYSTEMS IN BIOMECHANICS

Wojciech Kowalczyk

Chair for Mechanics and Robotics
University of Duisburg-Essen, Campus Duisburg, Lotharstrasse 1, 47057 Duisburg, Germany
e-mail: wojciech.kowalczyk@uni-due.de, web page: http://www.uni-due.de/lmr

Keywords: biomechanics, biofluid mechanics, hybrid systems, artificial neural network, fuzzy logic

Abstract. *Research activities in live sciences like biomechanics and biofluid mechanics based solely on established experimental and numerical methods come very often across their limits. However, many of biological circumstances in the nature are difficult to quantify using standard procedures. As an example the sensory sensations of patients during the biomechanical investigations or the sensory sensations in mouth during the food consumption can be given. In order to overcome these limitations and include such interesting and from many points of view important research fields the application of systems that consist of some combined methods – hybrid systems – is proposed. In the current paper the use of experiments, numerical methods, artificial neural network and fuzzy logic as a part of hybrid systems is discussed. Additionally, two potential applications of hybrid systems in biomechanics are drafted.*

1 INTRODUCTION

Many of circumstances in the research fields like biomechanics and biofluid mechanics consist of phenomena with different characteristics. First of all, systems are defined by geometry parameters, velocity, acceleration, force, stress and can be described by mathematical and mechanical laws. The second type of information about considered systems can be given in the form of fuzzy parameters. These parameters are defined firstly as linguistic variables. At this stage the investigation of the systems including such variables becomes impossible by the solely application of mathematical relationships. The solution of this problem is delivered by fuzzy logic. It enables the description and the control of observed phenomena using linguistic variables.

Another example where the coupling of two different methods becomes interesting is extraction of the knowledge about the system from experimental and/or numerical data by means of artificial neural network (ANN). Furthermore, ANN enables the investigation of phenomena that have no mathematical formulation.

The current paper aims at the brief demonstration of abilities of coupled methods and the presentation of possible applications of such hybrids in biomechanics.

2 METHODS

The most common research methods used in the biofluidmechanis and biomechanics are since many years established experimental and numerical approaches. For example in the biofluid mechanics such experimental methods like Laser Doppler Anemometry LDA and Particle Image Velocimetry PIV can be named. In biomechanics very popular systems for the investigation of the human's gait consist of Electromyography EMG, treadmills and gait laboratory which enable the collection of information according to the kinematics and dynamics of the investigated object. From the theoretical point of view there are some numerical methods like Finite Element Method FEM for the structure mechanics and Finite Volume Method FVM for the fluid mechanics to name two. Due to the increasing efficiency of numerical algorithms and the dynamical development in the range of High Performance Computing HPC also the parallel application of both numerical methods for the calculation of problems with Fluid Structure Interaction FSI becomes more and more importance.

Nevertheless, in the follow the experimental and numerical approaches mentioned above are not regarded. Instead of that, further methods, i.e. ANN and fuzzy logic as well as their combinations are addressed.

2.1 Artificial neural network

Artificial neural networks are often applied if the observed phenomena have no mathematical description or if the classification and extraction of information from data flood is necessary. Additionally, one of the most important advantages of neural network is the ability to learn about considered circumstances and the prediction of new states.

Neurons of an ANN are distributed into some layers. The input and output layers are coupled with the hidden layer by connections of different weight. Fig. 1 illustrates the general form of the feedforward neural network. The hidden layers are build of one row/column or a matrix. They aim at the generation of a relationship between the input and the output layer. ANNs learn by being trained. This means that they change their internal structure adaptively by modifying the weights of the hidden artificial neurons based on the provided information. After being trained ANN are able to find specific patterns, for example in the data pool arising from several numerical simulations. The theory of ANN is described in details by Zell [1].

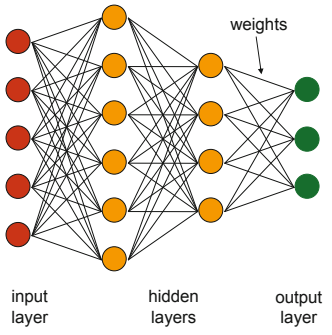

Fig. 1 Artificial neural network (feedforward).

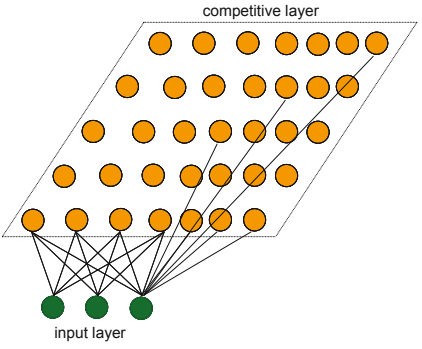

Fig. 2 Self-organizing map.

Besides of this "classical" type of neural network (s. Fig. 1) the Self-Organizing Map (SOM) is very often used in the range of pattern identification. In comparison to supervised feedforward network the unsupervised SOM contains only of two layers, namely the input and the competitive layer [2, 3] (s. Fig 2).

The artificial neural networks find wide application in biomechanics. The main investigation fields with ANN focus on the classification of gait and EMG data as well as on the biomechanical modeling considering the definition of relationships between EMG and the kinetics of human gait. An extensive survey of ANN applications in the clinical biomechanics finds in Schöllhorn [4]. Hereby, an advice on the review literature relating to the use of ANN in physical medicine and rehabilitation [5], analytical techniques for gait data [6, 7], biomedical engineering [8], classification and pattern recognition of biological systems [9] and medical imaging and signal processing [10] is attached.

2.2 Fuzzy logic

Such linguistic definition of a system like "young", "old", "middle old", "warm", "less warm" or the expression of sensory sensations like pain, to name a few, can not be described by means of analytical or numerical methods. In order to involve such process parameters into the biomechanical analysis, the use of fuzzy logic algorithms [11] has to be taken into account. The difference between binary and fuzzy description of a variable shows Fig. 3.

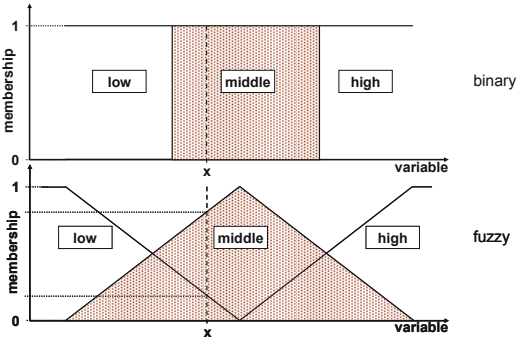

Fig. 3 Comparison between binary and fuzzy approach.

In contrary to the classical set theory of crisp sets fuzzy logic delivers the opportunity to define a membership of a set element to an attribute gradually in the range between 0 and 1 Therefore, the membership functions are overlapping. The input sets can be related to the occurring dynamical parameters of human gait, to linguistic statements of patients, and to the parameters like time and temperature in the biomechanical study. Rules which are implemented in the fuzzy system reflect the expert knowledge of the developer of the system. The rules follow the structure "IF input variable IS fuzzy set THEN output variable IS degree of fuzzy set". AND- and OR-junctions as well as negations are valid in order to define the conditions. An example in biomechanics can be defined as follows: "IF gait velocity IS low AND time after surgery IS long THEN pain IS middle to 0.7 and low to 0.3".

3 HYBRID SYSTEMS

In order to increase the capability and the efficiency of several approaches or open new research possibilities in the biofluid mechanics and biomechanics, hybrid systems that joint some methods are developed. Below some examples showing a successful application of hybrid systems in the biofluid mechanics are presented.

3.1 Hybrid system: experiment and numerical simulation

The Granular Activated Sludge (GAS), used in wastewater treatment, presents several advantages in comparison with the Conventional Activated Sludge, e.g. good settling ability [12] due to higher density, compact shape with up to 5 mm diameter and higher capacity of biomass retention. In order to investigate in details the influence of mechanical forces on the formation and properties of the granules as well as settling abilities in the both experimental and numerical investigations are carried out [13, 14]. The laboratory SBR in this study consists of 1 m long Plexigas tube with an internal diameter of 9 cm, see Fig. 1

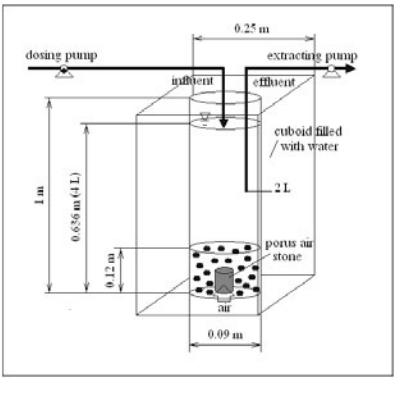

Fig. 4. The laboratory SBR [13].

The SBR has a cyclic character with following five steps per cycle granula formation i.e. fill, react, settle, draw and idle. The longest and the most important cycle for experimental investigations is the react phase, which is the object of our investigation in the experimental and the numerical analysis. In this step, air bubbles cross the synthetic waste water causing fluid and granula motion.

The experimental measurements of velocity distribution for the liquid phase are carried out with an optical in-situ Particle Image Velocimetry PIV technique. In the 3D numerical approach a multiphase control volume, composed of one continuous (wastewater) and two dispersed phases (air bubbles and granules), is analysed with the Eulerian-Eulerian model.

Nevertheless, both methods show their limitations during the investigation of such complex problems. In the experiment it is not possible to investigate the velocity distribution in the distance from the wall higher as 3 cm due to the density of granula. From the numerical point of view the simulations of 3D multiphase flow is connected with a significant computational cost.

In order to eliminate these restrictions, the experimental results are used as initial conditions in the numerical simulation. Hereby, different configurations of the planes with the experimental velocity distribution are analyzed (s. Fig. 5).

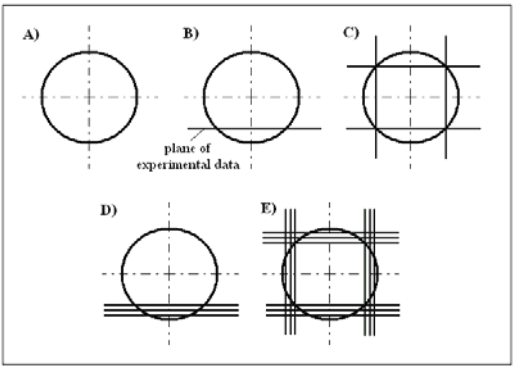

Fig. 5 The distribution of planes with experimental data [14].

The results of all five cases (A-E) confirm beneficial effect of coupled methods. In comparison to the standard case A, where no experimental data were implemented and the initial velocity of all three phases equals to zero, significant acceleration in the calculation time (s. Fig. 6) and much better convergence is reached. Additionally, because of the boundary conditions from the experiment the velocity field calculated numerically agrees much better the experimental observations.

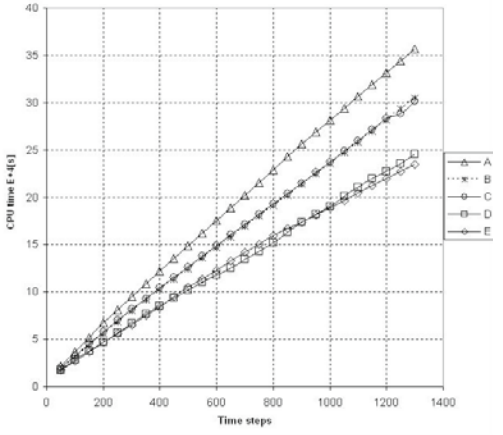

Fig. 6 The time needed for the numerical simulation of the cases A-E [14].

3.2 Hybrid system: artificial neural network and numerical simulation

In the next example the application of ANN to predict main attributes of the fluid flow in the bioreactor (s. Fig. 4) is presented. If the knowledge about detailed flow in the bioreactor is not necessary, the information in form of characteristic parameters as the height of the vortexes, the centre of the vortexes, maximal velocity can be predicted by ANN (s. Fig. 7). The process parameters like the volume fraction of air and granula, the diameter of granula and the geometry of the bioreactor are used as input variables in the neural network. In this case the ANN was able to predict the main attributes of the flow within some milliseconds. The comparison of these results with numerical simulations shows an average error of approx. 5 %.

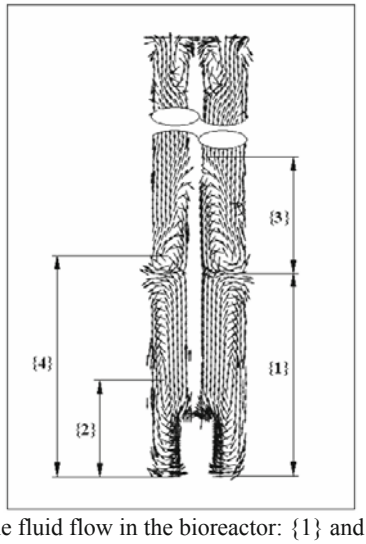

Fig. 7 Main attributes of the fluid flow in the bioreactor: {1} and {3} describe the height of the vortexes; {2} and {4} describe the center of the vortexes [14].

3.3 Hybrid system: experiment, artificial neural network and *a priori* knowledge

Hybrid systems can be also completed using more than two methods. As an example the smoothing of experimental results from PIV measurements by the use of ANN is shown. In order to guarantee "physical knowledge" about a flow during the smoothing process, an additional functional node (s. Fig. 8 and Fig. 9) with the Taylor hypothesis is applied [15]. The Taylor hypothesis enables the description of the creeping flow induced by microorganisms. The exigency of such smoothing procedure is caused by the biocompatibility of the measurement system. Since reliable investigations of a fluid flow induced by microorganisms are possible only in their natural environment low concentration of yeast cells in the fluid is applied as PIV tracers. The application of higher concentration of yeast cells changed the fluid flow and the use of artificial tracer particles is not possible due to reaction (chemotaxis) of microorganisms that influences their behavior. The small number of tracers causes image artifacts, which can be removed by the proposed hybrid system.

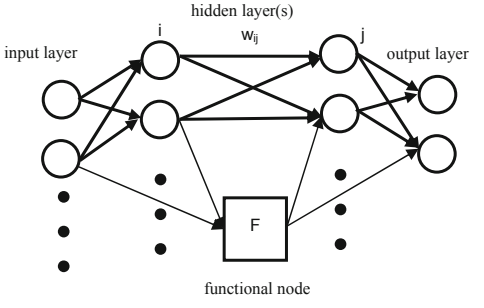

Fig. 8 Feedforward artificial neural network with functional node [15].

The Taylor hypothesis is implemented within the ANN as shown in Fig. 9. The initial pattern of the flow field is iteratively altered by change of the velocity components u and v. These changes are carried out up to the moment in which Ta (value of the Taylor function) equals approx. zero (i.e. convergence criterion of 10^{-6} is considered). Thus, the neuronumerical hybrid has been proven to detect reliably the spurious velocity vectors provoked by, both, image artifacts and moving boundaries like the contraction of the zooid.

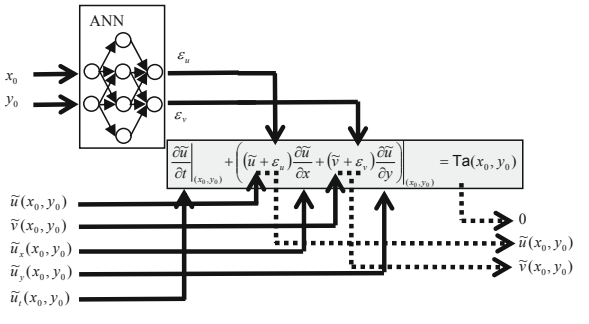

Fig. 9 Implementation of the Taylor hypothesis in the ANN [15].

3.4 Hybrid system: experiment, numerical simulation, artificial neural network and fuzzy logic.

As last example for the application of a hybrid system to enhance the research abilities in the range of biofluid mechanics the joint of experiment, numerical simulation, ANN and fuzzy logic is introduced. Here, the influence of fluid mechanics in mouth on the sensory sensations of subjects during the consumption of full fat and low fat dairy products is investigated [16]. The hybrid system consists of following steps: i) in the experiments the rheological behavior of a liquid food is measured, ii) the rhological curves are implemented into the CFD (computational fluid dynamics) code, where the calculation of the fluid flow in the model mouth is carried out, iii) using the ANN the extraction of the data from the numerical results is undertaken and iv) by means of fuzzy logic the correlation between "the physics" of the flow and by subjects linguistically formulated attributes like creaminess or smoothness is realized.

4 POTENTIAL APPLICATIONS OF HYBRID SYSTEMS IN BIOMECHANICS

Having some different examples of beneficial influence of coupled methods on the enhancement of research abilities, two potential applications of hybrid systems in biomechanics are drafted below.

4.1 Reduction of skin motion artifacts

The artifacts induced by skin motion during the biomechanical investigations of human gait are a very common problem. Because of the dynamical behaviour of the subject during biomechanical measurements location of markers change their position with respect to the bone or joint axis. Hereby both translational and rotational displacements in the range of some millimetres are possible. Since early eighties literature documents significant effort of many research groups working on this topic based particularly on the rigid body models [17]. One of the newest algorithms named local motion estimation (LME) proposed in [18] use virtual humans and extended Kalman filters estimating the kinematical variables directly from 2D data. Despite of many interesting research activities focusing on the reduction of the influence of skin movement on the biomechanical measurements, the results contain significant errors of the marker location relative to bone or joint centre.

In this approach a hybrid system consisting of superquadric algorithms [19] and artificial neural networks is proposed for minimizing of skin movement artifacts. The reduction of skin movement artifacts is carried out by artificial neural network. For example, self organizing maps (SOM) [2] are able to reveal continuous displacement fields. The ANN is trained with data containing position of markers, assumed position of virtual bone or joint centers and assumed kinematical variables like velocity and angles. Detailed geometrical correlation of markers with implicit surfaces of superquadrics enables precise localization of their original and new position. The identification and correction of artifacts induced by skin movement is carried out by trained ANN within a very short time ($t << 1s$). In order to enhance the abilities of the hybrid system further activities to involve non-linear material behavior of skin in the error reduction are planed in ongoing investigations.

4.2 Involving of pain in biomechanics

According to the example where the sensory sensations of subjects with respect to the rheological fluid dynamical behavior of food in mouth is investigated, further possible application of a hybrid system in biomechanics can be taken into account. An observation of re-

search activities in biomechanics reveals that the pain, for example after a surgery, significantly influences the dynamical parameters of a human gait [20, 21, 22]. Additionally, data obtained by means of electromyography EMG and electroencephalography EEG acquire the characteristic muscle activities and electrical activities of the brain for different types of disorder. Thus, an enormous information flood during such complex interdisciplinary investigations is to be expected. In this situation a hybrid system that on the one hand extracts information properly describing the human gait from the physical point of view and on the other hand accepts connection with the linguistic formulation of the pain and the orthopedic knowledge is needed. As a solution a hybrid that consists of an experimental analysis in the biomechanical laboratory, EMG, EEG, ANN and fuzzy logic is proposed.

5 CONCLUSIONS

The combination of some methods for the solution of problems in biomechanics can enhance the research abilities and complete the knowledge about many interesting phenomena. In the current paper the significant role of the ANN and fuzzy logic in biomechanics is presented. Additionally, the successful applications of the hybrid systems to increase the computational efficiency, the extraction of data and the coupling of numerical and linguistic variables are confirmed by presented examples. Furthermore, two possible applications of hybrid systems in biomechanics, where the kinematical and dynamical information from the gait laboratory can be coupled with the pattern recognition realized by ANN as well as linguistic variables describing sensory sensation of pain are drafted. Concluding it can be stated that the hybrid systems as a research method in biomechanics have a great potential to be accessed.

REFERENCES

[1] A. Zell. *Simulation Neuronaler Netze*, Addison-Wesley, 1996.

[2] T. Kohonen. *Self-Organizing Maps*, Springer, Berlin, 2001.

[3] M. Takatsuka, R.A. Jarvis. Encoding 3D structural information using multiple self-organizing feature maps, *Image and Vision Computing*, 19, 99-118, 2001.

[4] W.I. Schöllhorn. Applications of artificial neural nets in clinical biomechanics. *Clinical Biomechanics*, 19, 2004.

[5] L. Ohno-Machado, T. Rowland. Neural network applications in physical medicine and rehabilitation, *American Journal of Physical Medicine and Rehabilitation*, 78, 392-398, 1999.

[6] T. Chau. A review of analytical techniques for gait data. Part 1: fuzzy, statistical and fractal methods, *Gait & Posture*, 13, 49-66, 2001.

[7] T. Chau. A review of analytical techniques for gait data. Part 2: neural network and wavelet methods, *Gait & Posture*, 13, 102-120, 2001.

[8] R. Nayak, L.C. Jain, B.K.H. Ting. Artificial neural networks in biomedical engineering: a review, Sydney, Australia, *http://sky.fit.qut.edu.au/~nayak/Papers/apcom.pdf*, 2001.

[9] R.M.F. Sabbatini. Neural networks for classification and pattern recognition of biological signals. *In: Proceedings of the Annual International IEEE Conference on the*

Engineering in Medicine and Biology Society, Los Alamitos, IEEE Press, San Diego, CA, 1993.

[10] A.S. Miller, B.H. Blott, T.K. Hames. Review of neural network applications in medical imaging and signal processing, *Medical and Biological Engineering and Computing*, 30, 449-464, 1992.

[11] W.M. Lippe. *Soft-Computing mit neuronalen Netzen, Fuzzy-Logic und Evolutionären Algorithmen*, Springer, Berlin, 2006.

[12] T. Etterer, P.A. Wilderer. Generation and properties of aerobic granular sludge. *Water Science Technology*, 43, 19-26, 2001.

[13] B.E. Zima, L. Diez, W. Kowalczyk, C. Hartmann, A. Delgado. Biofluid mechanical investigations in Sequencing Batch Reactor (SBR), *Chemical Engineering Science*, 63, 599-608, 2007.

[14] L.Díez, B.E. Zima, W. Kowalczyk, A. Delgado. Investigation of multiphase flow in Sequencing Batch Reactor (SBR) by means of hybrid methods, *Chemical Engineering Science*, 62, 1803-1813, 2007.

[15] H.Petermeier, W.Kowalczyk, A.Delgado, C. Denz, F. Holtmann. Detection of microorganismic flows by linear and nonlinear optical methods and automatic correction of erroneous images artefacts and moving boundaries in image generating methods by a neuronumerical hybrid implementing the Taylor's hypothesis as a priori knowledge, *Experiments in Fluids*, 42, 611-623, 2007.

[16] K. Mathmann, W. Kowalczyk, A. Delgado. Development of a Hybrid Model Predicting the Mouthfeel of Yogurt, *Food Quality and Preferences*, submitted, 2007

[17] C.W. Spoor, F.E. Veldpaus. Rigid body motion calculated from spatial coordinates of markers, *Journal of Biomechanics*, 13, 391-393, 1980.

[18] P. Cerveri, A. Pedotti, G. Ferrigno. Kinematical model sto reduce the effect of skin artifacts on marker-based human motion estimation, *Journal of Biomechanics*, 8, 2228-2236, 2005.

[19] L. Chevalier, F. Jaillet, A. Baskurt. Segmentation and superquadric modeling of 3D objects, *In Proceedings of WSCG 2003*, 2003.

[20] A. McHardy, H. Pollard. Lower back pain in golfers: a review of the literature, *Journal of Chiropractic Medicine*, 4, 135-143, 2005

[21] M. Henriksen, E.B. Simonsen, T. Alkjær, H. Lund, T. Graven-Nielsen, B. Danneskiold-Samsøe, H. Bliddal. Increased joint loads during walking – A consequence of pain relief in knee osteoarthritis, *The Knee*, 13, 445-450, 2006

[22] A.Karahan, N. Bayraktar. Determination of the usage of body mechanics in clinical settings and the occurrence of low back pain in nurses, *International Journal of Nursing Studies*, 41, 67-75, 2004.

IAK 2008
Conference on Interdisciplinary Applications of Kinematics
A. Kecskeméthy, V. Potkonjak and A. Muller (eds.)
Lima, Peru, 9–11 January 2008

AN ALTERNATIVE FOR HUMAN GAIT MODELLING USING THE BONDGRAPH TECHNIQUE

Roberto Hernani*, Gregorio Romero† and Ramsi Jazmati**

* Departamento de Ingeniería Mecánico-Eléctrica
Universidad de Piura, Perú
Email: rhernani@udep.edu.pe

† Departamento de Ingeniería Mecánica y Fabricación
Universidad Politécnica de Madrid, España
Email: gromero@etsii.upm.es

** Departamento de Rehabilitación
Universidad de Navarra, España
Email: rjazmati@unav.es

Keywords: Human gait, Bond Graph, Inverse kinematics, Skeletal muscle systems.

Abstract: *The systematic analysis of the human gait with a skeletal or neuromuscular disorder is a valuable clinical instrument to determine the nature and severity of the disease. At present, there are many institutions that have developed a series of numerical models that simulate and analyze biomechanics systems such as the human gait.*
Many of these models require diverse and segmented programming to incorporate various effects of the dynamics of the body such as the performance of the muscles and tendons, the passive and active resistance to movement, and other physiological effects. One of the alternatives to simulate biomechanical systems is the use of the Bond Graph modeling technique. The modular modeling with multi-domains, a feature of the Bond Graph technique, is one of its potential advantages compare to other methods. The equations generated with the use of this technique are equivalent to those techniques developed with more traditional methods, but the modules can be easier and more comfortable to use in conjunction with models of neuromuscular control functions, models that incorporate the elasticity properties in the bones and tendons, etc. The proposed model, comprised of seven segments, is developed to estimate the torque and the power in the joints. This model is simulated and validated using the processed experimental data of a normal gait in GCD (Gait Cycle Data) format file.

1 INTRODUCTION

Nowadays, the field of simulation covers fields as diverse as the calculation of mechanisms, the solution of electrical circuits or hydraulic circuits or the heat transfer within an air conditioning installation. These simulations are reflected in graphs that give an idea of how a certain system would work in reality, but also to optimize its functioning and get certain concrete results.

Lately, one of the areas of computer simulation is of the skeletal-muscular system of the human body which can resemble a mechanism that is complemented with the torques in the joints caused by the action of muscles and tendons, either for the purpose of surgery training or to understand their behavior among others things.

In this paper a model of the human gait is developed using the techniques of Bond Graph. The elements used in it, called "doors", focus on the transfer of energy through "*flows*" and "*efforts*" (for example, velocities and forces in the field of linear mechanics). The "*graphs*" combined suitably allow to incorporate effects such as mechanical, electrical, thermodynamic, elastic, etc. into the dynamic system.

The developed model corresponds to the human gait in the sagittal plane and contains 7 segments. Six of the segments represent the feet, shanks and thighs. The remaining segment is for the upper body –head, arms and trunk (HAT)– rigidly joined to the rest through the pelvis. Each segment is regarded as a rigid solid and therefore, the mechanism can be represented as 7 links united by simple joints. The model using this technique of Bond Graph has been designed and simulated using the software *Bondin ©,* developed by Dr. G. Romero of the Polytechnics University of Madrid, Spain (Grupo de Ingeniería Gráfica y Simulación, Departamento de Ingeniería Mecánica y Fabricación).

For the simulation and validation of the model, data was used from a normal gait cycle supplied in GCD (Gait Cycle Data) format [1], obtained in a *Hospital of Austria* using the systems of motion-capture from *Vicon Motion Systems*.

2 THE HUMAN GAIT USING THE BOND GRAPH MODELING

As mentioned by Pop [2] the application of Bond Graph to human gait modelling was first proposed by Matthijsse et al. [3] , [4]. Two 13-segment models were described with which the single and double support phases could be individually simulated. Foot elevation was used to switch between models. However, no inverse or direct dynamic simulation or experimental results were reported.

Validation is an important aspect of model development. Pezzack et al. [5] used Newtonian mechanics to develop a model which was then validated in three steps: first, computational accuracy was checked against hand calculations; next, ground reaction forces (GRFs) predicted by the model were checked against forceplate measurements; and finally, the accuracy with which the model predicted zero GRF at the distal end of the swing limb during the single support phase was verified. The results reported were accurate to within 15%, and the errors were attributed to errors in the body segment accelerations. Kingma et al. [6] validated their 3D model in two steps: first, by comparing the GRFs computed by the model with those from forceplate data, and then by comparing the torques at the hip joint resulting from bottom-up and top-down mechanical analysis. They concluded that the most rigorous method of validating the model is by comparison with forceplate measurements. However, it was shown by McCaw and DeVita [7] that errors in spatial alignment of the COP can introduce considerable errors in the lower extremity torques when forceplate readings are used in kinetic calculations.

Pop [8] developed a human gait Bond Graph 8-segment model using the kinetic method. Contreras et al. [9] developed a Bond Graph 7-segment model using both the kinetic and the multiport method proposed by Karnopp y Rosemberg [10]. In this paper, a Bond Graph 7-segment model is developed using the kinematic method, proposed by Vera [11] for rigid body beams.

2.1 Bond Graph of a rigid solid using the global coordinate system

Fig. 1 shows the spatial motion of a rigid solid. In a global coordinate system, the speeds of displacement and of rotation of the mass-center are independent one to the other respectively.

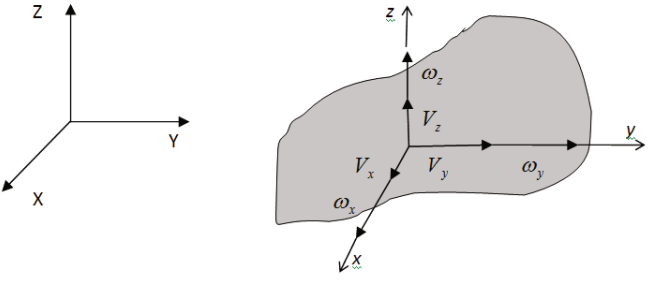

Figure 1: Reference system of a solid.

The 2D analysis of the velocities at the ends of the beam in a global coordinate system will be given by:

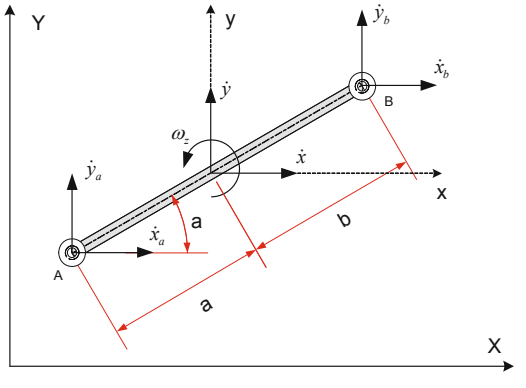

Figure 2: Planar 2D rigid beam in global coordinates.

The equations related to the speeds at the ends will be:

$$\begin{aligned} \dot{x}_a &= \dot{x} + \omega_z \cdot a \cdot \sin\alpha \\ \dot{y}_a &= \dot{y} - \omega_z \cdot a \cdot \cos\alpha \\ \dot{x}_b &= \dot{x} - \omega_z \cdot b \cdot \sin\alpha \\ \dot{y}_b &= \dot{y} + \omega_z \cdot b \cdot \cos\alpha \end{aligned} \tag{1}$$

The diagram of graphs of the beam will be defined as:

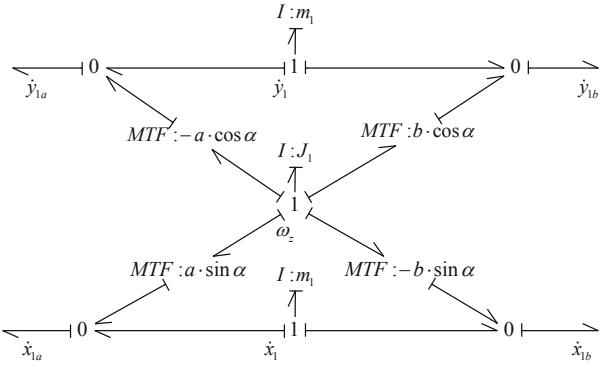

Figure 3: Bond Graph of the 2D rigid beam with movement in the plane *xy* using global coordinates.

In a global coordinate system, the union between two beams is very simple to achieve since the speeds of these two beams are exactly the same at the joint point. For the two beams articulated as shown in fig. 4, the diagram of graphs is defined in fig. 5.

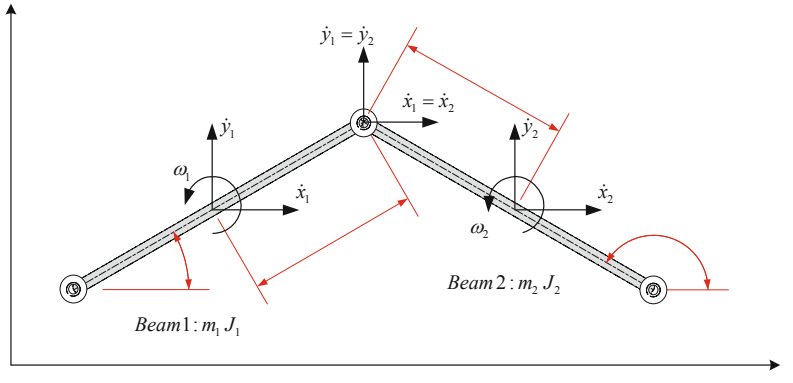

Figure 4: Two 2D rigid beams articulated in global coordinates.

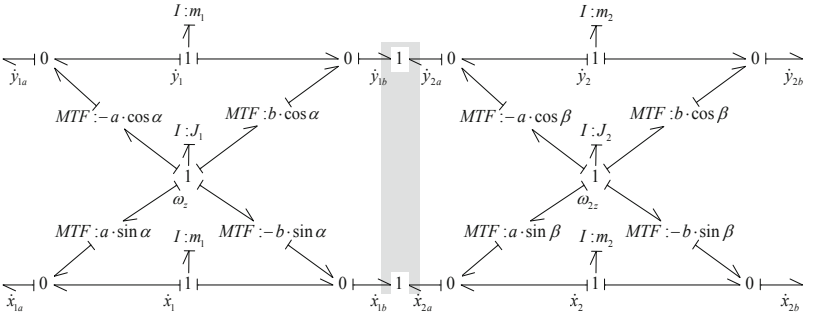

Figure 5: Bond graph of the articulation of two 2D rigid beams with movement in the plane *xy* using global coordinates.

In the Bond Graph modelling it is important to eliminate the differential causalities of the inertia elements (inductive) i.e. there are dependent variables that in certain programs of Bond Graph modelling do not allow developing the proposed models. Normally this disadvantage can be surpassed by adding capacitive and resistive elements in the joints. Using the *Bondin* software, it is not necessary to add these elements because it solves the causality problems or conflicts and calculates all the differential and algebraic equations. By this reason, the program has the capacity to solve models with both integral and differential causalities according to the needs, Romero et al. [12].

2.2 The Bond Graph 7-segment model of the human gait

There are two approaches to solving the model: direct and inverse dynamic models. A direct dynamic model is one that expresses the temporary evolution of joint coordinates in function of the forces and torques involved. An inverse dynamic model on the other hand is one that expresses the forces and torques that intervene in the function of the evolution of joint coordinates and its derivatives.

The model to follow is the inverse dynamic problem where the input values will be the displacement of the mass-center of the pelvis and the flexure/extension angles of the hip, knee and ankle.

4-segment model is considered for the kinematic analysis, the pelvis rigidly coupled to the head, arms and trunk (HAT) and the lower limb consisting of the right thigh, shank and foot united through a simple articulation (see fig. 6).

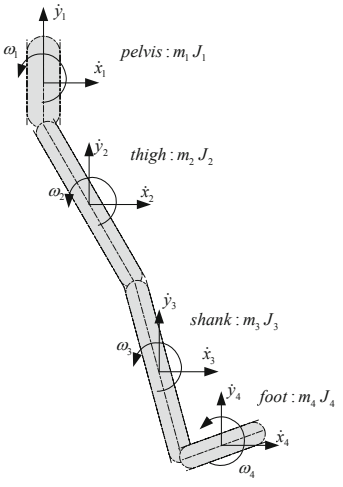

Figure 6: Scheme of the right leg for a 4-segment model.

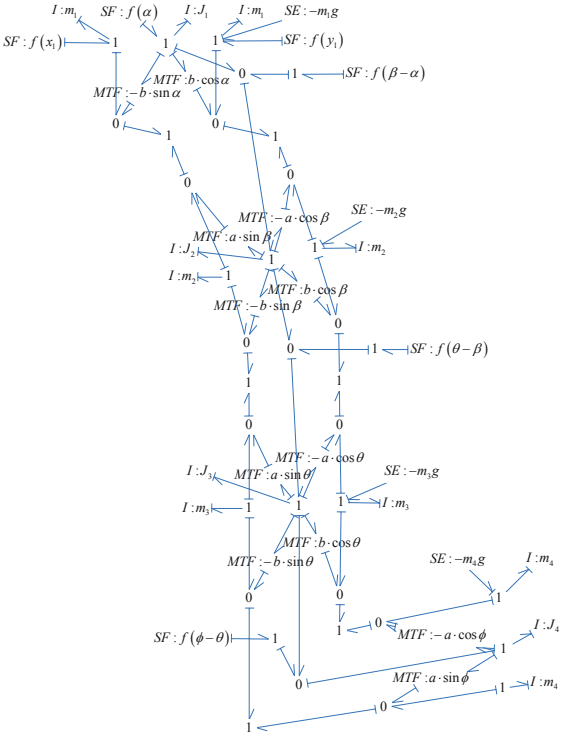

Figure 7: Detailed Bond Graph diagram of the right leg for a 4-segment model.

The data introduce in the model are the *RightPelvicOrigen* displacement and the *RightHipFlexExt*, *RightKneeFlexExt* and *RightDorsiPlanFlex* angles obtained from the GCD file. This data has been adapted using *Maple* (a mathematical software from MapleSoft ™) to be applied in the Bond Graph model using the *Bondin* software.

The kinematic results of the simulation are shown in the following graphics of fig. 8, 9 and 10. These figures show the 2D displacement of the joints using the *GDC* file (left side) and the results using the *Bondin* software (right side). The model uses the *CAMARC II* standard AVR (Anterior, Vertical and Right) right-handed Cartesian axes. On the sagittal plane is the *x* axis for the anterior direction and *z* axis for the vertical one.

Kinematically, the results are optimum, showing the standard trajectories of the hip, knee and ankle joints for a normal gait.

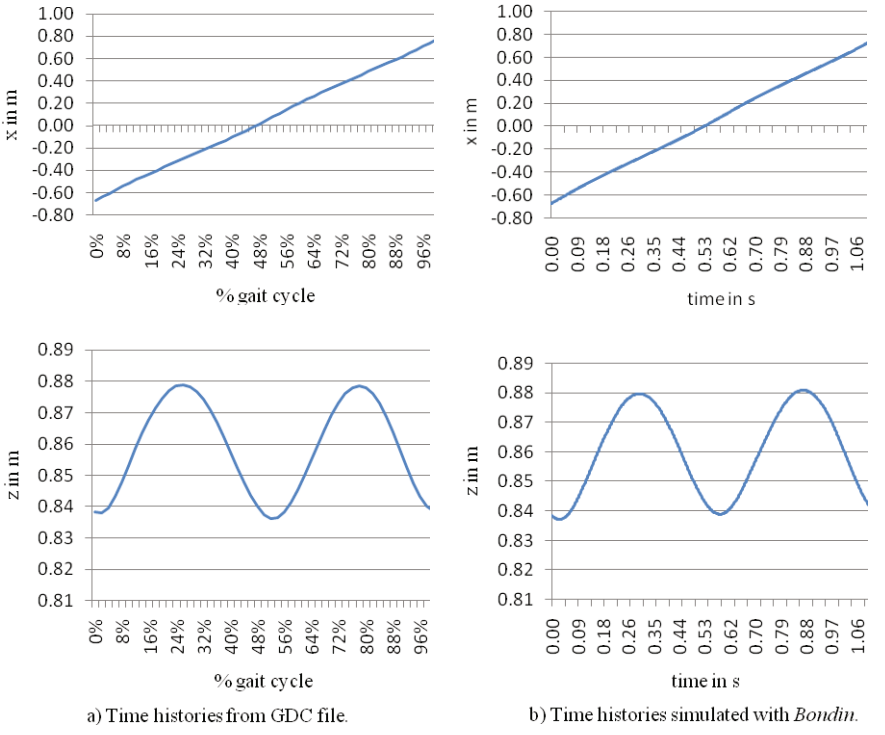

a) Time histories from GDC file. b) Time histories simulated with *Bondin*.

Figure 8: *RightHipJointCentre* displacement.

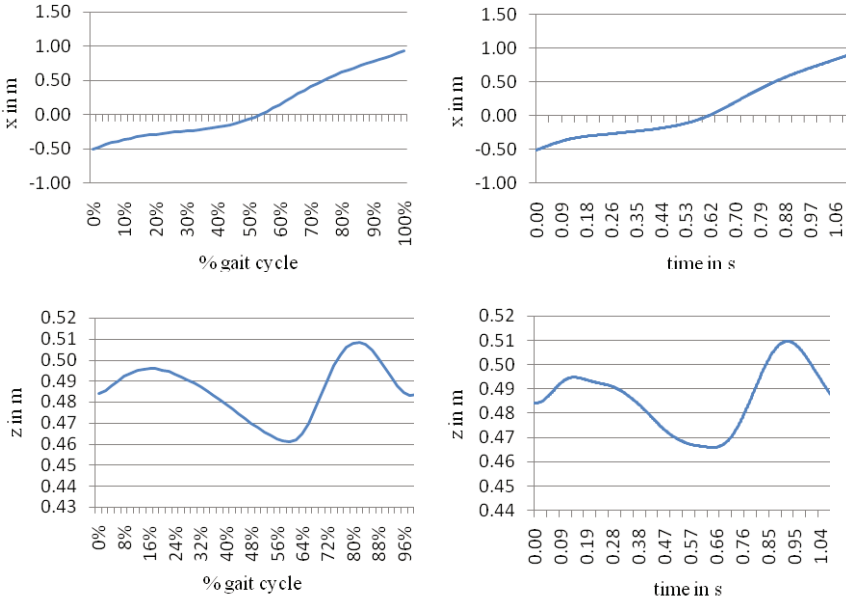

a) Time histories from GDC file. b) Time histories simulated with *Bondin*.

Figure 9: *RightKneeJointCentre* displacement.

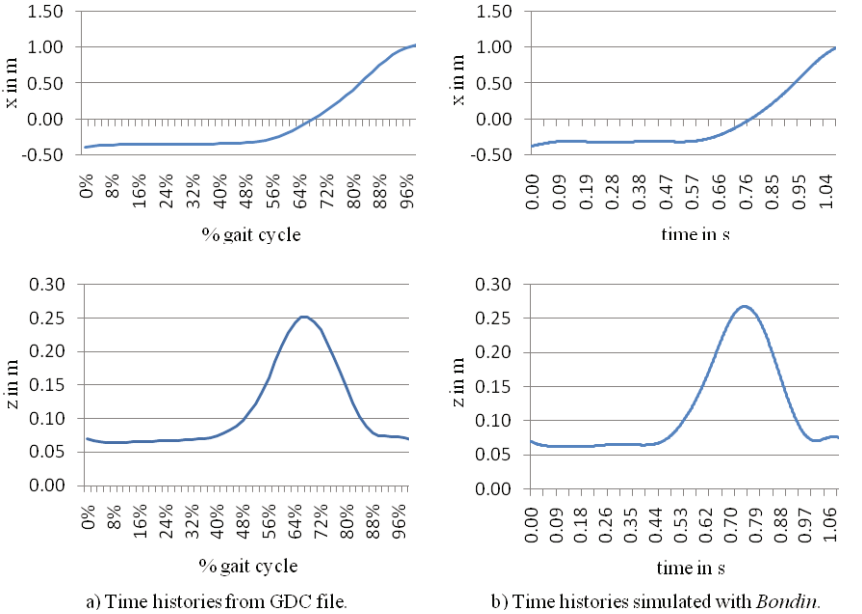

a) Time histories from GDC file. b) Time histories simulated with *Bondin*.

Figure 10: *RightAnkleJointCentre* displacement.

To make the dynamic analysis, it is necessary to work with the complete 7-segment model. There are two options for the validation of the model. The first option is to add –in the contact between the feet and the ground– spring-damper elements to simulate the ground reaction forces (GRFs) in order to calculate these forces and to compare them with the forceplate measurements. This way is relevant for direct dynamics. The second option is to input the forceplate measurements as external forces on each foot (see fig. 11) and then to compare the calculated torques in the joints with the values of the normal human gait contained on the GCD file. This is an inverse dynamics method and this is the option used to validate the 2D model simulated in this paper.

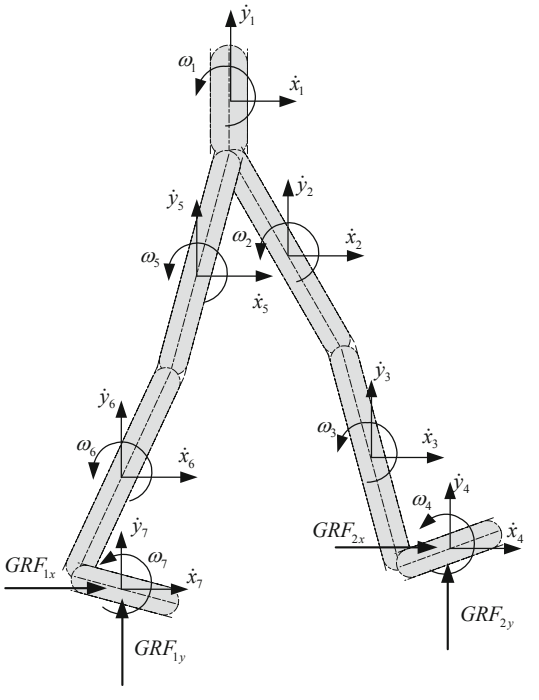

Figure 11: Scheme with reaction forces for a 7-segment model.

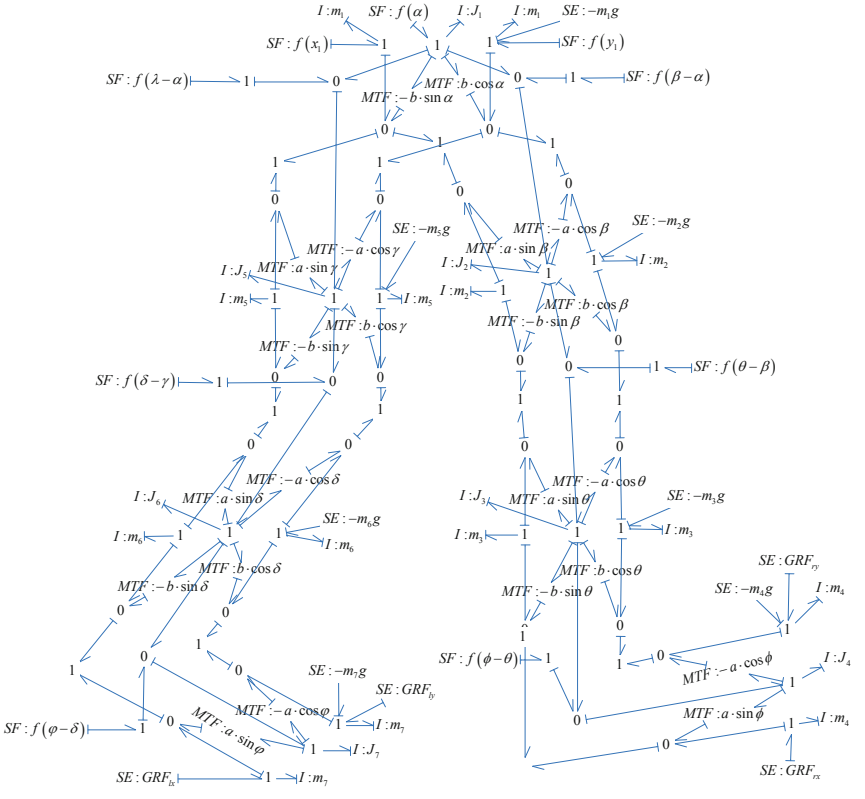

Figure 12: Detailed Bond Graph diagram for with reaction forces for a 7-segment model.

From the simulation of the inverse dynamics, the time histories of torques in the joints of the right leg in fig. 13, 14 and 15 are obtained. The left leg, not shown in this paper, has corresponding properties. In addition, it is possible to obtain the joint powers as shown in Figure 16.

Generally, torques and powers are plotted graphically as a function of the gait cycle. In this case, they are plotted graphically as a function of the time in order to facilitate the matching of the experimental data. The time base default used on the GCD format file is 51 samples of 2% through the gait cycle. For the model of this paper, 100% of the gait cycle corresponds to 1.129 seconds.

It can also be observed in fig. 13, 14 and 15 that there are few variations in relation to the torques read from the GCD file for a normal human gait compared with the results achieved in the 7-segment model using the Bond Graph technique.

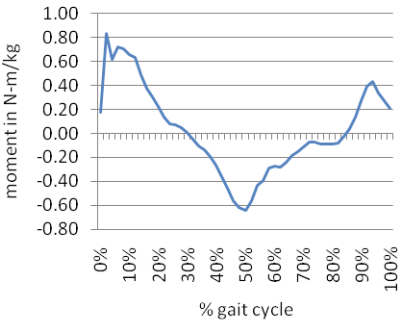

a) Time histories from GDC file.

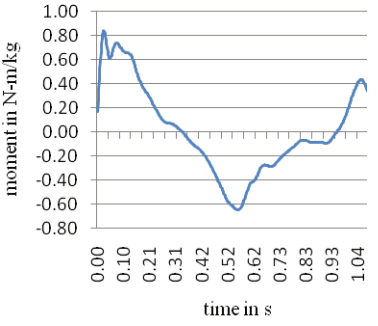

b) Time histories simulated with *Bondin*.

Figure 13: Right hip flexion/extension moment results.

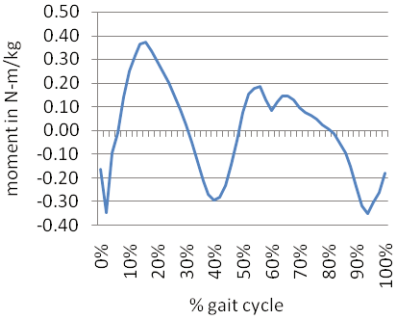

a) Time histories from GDC file.

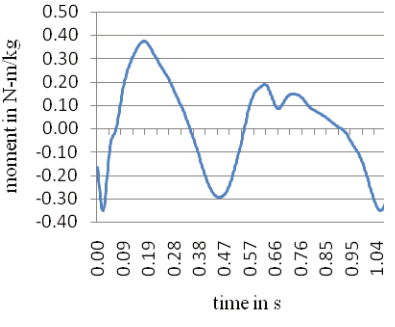

b) Time histories simulated with *Bondin*.

Figure 14: Right knee flexion/extension moment results.

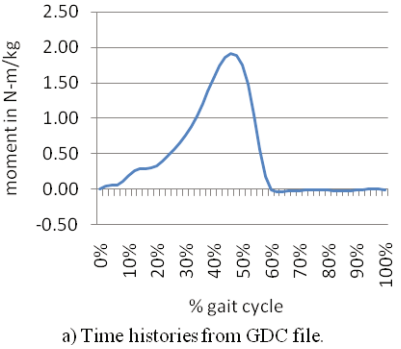

a) Time histories from GDC file.

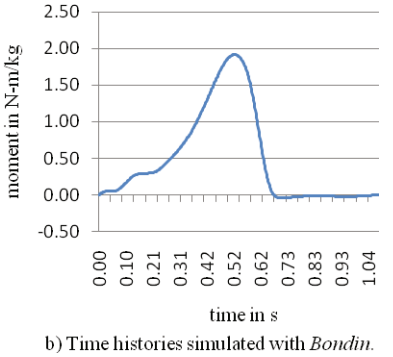

b) Time histories simulated with *Bondin*.

Figure 15: Right dorsi/plantar flexion joint moment results.

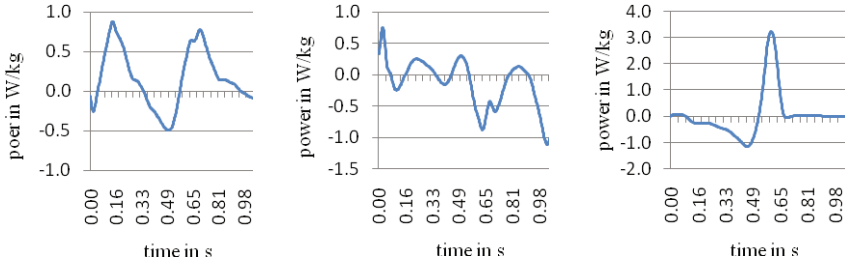

Figure 16: Right hip, knee and ankle joint powers results using *Bondin*.

The variations that appear in the results are due to the fact that the model has been developed at the sagittal plane, which does not consider the amplitude of movement of the front and vertical planes. Also, the knee and ankle joints have been considered as simple articulations, where sliding displacements have been despised. However, the model serves as a first major approximation to simulate the human gait in the sagittal plane using the Bond Graph technique.

3 CONCLUSIONS

As per the obtained results, we conclude that the Bond Graph technique using the kinematic method is valid for the modeling approach of the human gait. The next step is to work the model in three dimensions.

The modular and multi-domain characteristics of the Bond Graph technique allow one to add or to remove components very easily. This, in addition to improve the model, has a valuable teaching component that is manifested in the gradual development of the model. In future simulations, the knee and ankle articulations would be considered as sliding joints by inserting a four-link model. Moreover, the forces in the joints would be replaced by the muscular models also developed using the Bond Graph technique. On this last one, a modification of the model proposed by Wojcik [13] would be used.

REFERENCES

[1] Michael Stolz. Modellbildung, Simulation und Analyse der menschlichen Beinbewegung zur Vorbereitung chirurgischer Eingriffe. Master's thesis, Graz University of Technology, 2002.

[2] C. Pop. Bondgraphs Modeling and Model Evaluation of Human Locomotion Using Experimental Data. *University Of Waterloo*. Extracted from World Wide Web: http://mme.uwaterloo.ca/~jph/pubs/bondgraph.pdf

[3] P. C. Matthijsse and P. C. Breedveld. Modelling and simulation of human gait in three dimensions using multibond graphs and implicit integration routines. In *Congress Proceedings*, pages 477-480. 7-th Congress of the International Society of Electrophysiological Kinesiology, 1988.

[4] P. C. Matthijsse and P. C. Breedveld. Modelling and simulation of human gait in three dimensions with multibond graphs. In *Congress Proceedings*, pages 208-209. XII International Congress of Biomechanics, Los Angeles, California, 1989.

[5] J. C. Pezzack and R. W. Norman. A validation of the joint reaction force and resultant moment output of an "n" link plane motion model of the human. In Anonymous.

[6] I. Kingma, M. P. de Looze, H. M. Toussaint, H. G. Klijnsma, and T. B. M. Bruijnen. Validation of a full body 3-d dynamic linked segment model. *Human Movement Science*, 15: 833 - 860, 1996.

[7] S. T. McCaw and P. DeVita. Errors in alignment of center of pressure and foot coordinates affect predicted lower extremity torques. *Journal of Biomechanics*, 28:985 - 988, 1995.

[8] C. Pop, A. Khajepour, J. P. Huissoon, and A. E. Patla. Application of Bondgraphs to Human Locomotion Modeling", *Proceeding of the HKK Conference and Symposium,* University of Waterloo, Canada June 13-16: 85-90, 1999.

[9] L. Contreras and Maximo R. Modelammiento de la Marcha Humana por medio de gráficos de unión. *Tecnura*, 16: 26-42, 2005.

[10] D. C. Karnopp, D. L. Margolis, and R. C. Rosenberg. *System Dynamics: a Unified Approach,* 2nd ed., John Wiley & Sons, Inc., New York, NY. 1975.

[11] C. Vera. Simulación de sistemas dinámicos mediante la técnica del BOND-GRAPH**.** *Madrid: ETSI Industriales*, 1993.

[12] G. Romero et al. Optimized procedures for obtaining the symbolic equations of a dynamic system by using the Bond-Graph technique. *International Conference on Bond Graph Modeling and Simulation ICBGM'05*. New Orleans. SCS Publishing, Simulation Series. Vol.37, No.1, 51 – 58, 2005.

[13] L. Wojcik. Modeling of musculoskeletal structure and function using a modular bond graph approach. *Journal of the Franklin Institute*, 340: 63–76, 2003.

IAK 2008
Conference on Interdisciplinary Applications of Kinematics
A. Kecskeméthy, V. Potkonjak and A. Müller (eds.)
Lima, Peru, 9–11 January 2008

OPTIMIZED KINEMATICAL POSITIONING AND GUIDANCE OF A SERIAL ROBOT FOR MOTION SIMULATION

Matthias Marx[⋆], Michele Conconi[†], Martin Tändl[⋆] and Andrés Kecskeméthy[⋆]

[⋆]Chair for Mechanics and Robotics
University of Duisburg-Essen, Campus Duisburg, Lotharstrasse 1, 47057 Duisburg, Germany
e-mail: matthias.marx@uni-due.de, martin.taendl@uni-due.de and
andres.kecskemethy@uni-due.de
web page: http://www.uni-due.de/lmr

[†]Department of Mechanical, Nuclear, Aviation and Metallurgical Engineering, University of Bologna,
Viale del Risorgimento, 2, Bologna, Italy
e-mail: michele.conconi@mail.ing.unibo.it

Keywords: Motion simulation, robot control, trajectory design, inverse kinematics.

Abstract. *Described in this paper is an approach for generating control inputs for a serial robot motion simulator such that prescribed linear acceleration at the end-effector are accomplished as close as possible. The method takes into account the workspace limits, and uses the internal interpolation cycle of the robot controller to generate the corresponding trajectories. The PI parameters of the internal interpolation are identified from test measurements. The path planning algorithm uses the damped least squares method together with a refinement based on optimization for navigating the robot along the user-prescribed accelerations under avoidance of singularities. The approach is demonstrated for the Kuka robot roboCoaster. It is shown that the desired accelerations can be generated accurately and with high repeatability, making the approach suitable for generic simulation tasks.*

1 Introduction

In most applications of industrial robots, the goal is to generate optimal end-effector motion so that a prescribed trajectory is followed accurately and smoothly in terms of position and velocity (feed rate). In special applications, such as physical motion simulators or when handling sensitive goods, precise interpolation of a trajectory is not required, but accelerations are prescribed as functions of time or by given limits. One application of acceleration control is generic motion simulation with the Kuka KR 500 TÜV robot. Currently, three such generic-motion Kuka simulators are operated in Germany: one by the DLR ([1]), one by the Max Planck Institute for Biological Cybernetics in Tübingen ([2]) and one in the Chair for Mechanics and Robotics of the University Duisburg-Essen. The present work addresses the problem of input generation for such a robot such that acceleration prescription is fulfilled as close as possible and no workspace limits are violated. The simulator setup used for the current work is shown

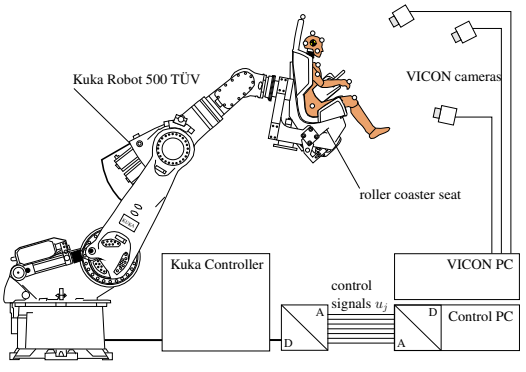

Figure 1: Schematic representation of robot, controller and motion capturing system

in fig. 1. It consists of the robot and a roller-coaster seat fixed at the robot flange. The motion is generated via six analog input signals u_j, which are produced by an external PC in feed-forward control mode. The system is monitored by Vicon motion capture system for probing the motion of robot and test person in the seat.

2 Model description

Fig. 2 a) shows a lateral view of the KR 500 TÜV robot with six axes and seat mounted on the robot flange. The pose of the end-effector frame $\mathcal{K}_{\mathrm{EE}}$ with respect to the base frame $\mathcal{K}_0$ is described by the position vector $\underline{r}_{\mathrm{EE}}$ and the rotation matrix ${}^0\mathbf{R}_{\mathrm{EE}}$ as a function of the axis angles $\underline{q} = [\,\varphi_1\,,\,\varphi_2\,,\,\varphi_3\,,\,\varphi_4\,,\,\varphi_5\,,\,\varphi_6\,]^{\mathrm{T}}$. The z-axis of $\mathcal{K}_{\mathrm{EE}}$ points in cranial, the x-axis points in view direction (from posterior to anterior) and the y-axis points to the left of the test person. In the following, it is assumed that all vectors are decomposed in the end-effector frame. The velocity and acceleration of the end-effector are computed by

$$\underline{\mathrm{t}}_{\mathrm{EE}} = \mathbf{J}\,\dot{\underline{q}} \quad \text{and} \tag{1}$$

$$\dot{\underline{\mathrm{t}}}_{\mathrm{EE}} = \mathbf{J}\,\ddot{\underline{q}} + \dot{\mathbf{J}}\,\dot{\underline{q}} + \underline{e}_z\,g. \tag{2}$$

In these equations, $\underline{\mathrm{t}}_{\mathrm{EE}} = [\,\underline{\omega}_{\mathrm{EE}},\,\underline{v}_{\mathrm{EE}}\,]^{\mathrm{T}}$ is the twist of the end-effector combining the angular velocity $\underline{\omega}_{\mathrm{EE}}$ and linear velocity $\underline{v}_{\mathrm{EE}}$; $\mathbf{J}$ is the Jacobian of the manipulator, mapping joint rates

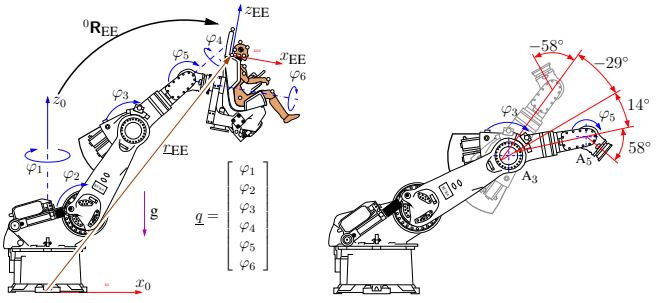

a) kinematic structure b) allowed ranges for φ_3 and φ_5

Figure 2: Kinematical model of the Kuka KR 500 TÜV

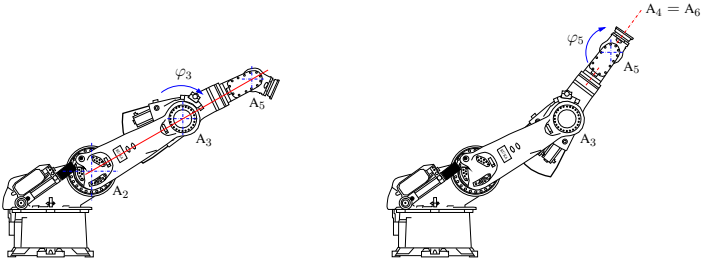

a) straight-arm degeneracy b) hand singularity

Figure 3: Singular configurations related to axes three and five

$\underline{\dot{q}}$ to the end-effector twist. In the expression for the end-effector acceleration $\underline{\dot{t}}_{EE}$, $\underline{e}_z\, g$ is the acceleration of gravity acting along the z-axis of the fixed frame $\mathcal{K}_0$. Due to safety restrictions, the joint angles of axes three and five are limited by physical stops to the intervals [-29°, +14°] and [-58°, +58°] (fig. 2 b). Moreover, the straight-arm degeneracy ($\varphi_3 = 3°$), shown in fig. 3 a) and the hand singularity ($\varphi_5 = 0°$, fig. 3 b) lie in these narrow intervals. The robot is controlled via analog set-point angle signals sent to analog input ports of the robot. Due to a low-pass input filter and controller components, there is time delay and other distortion between the set-point angle signal and the actual robot axis angle trajectory (see fig. 5 a)). In order to avoid this lag behavior, the controller parameters need to be identified, as described next.

3 Identification of controller parameters

The robot controller is a time-discrete controller with 0.012 s sample time for trajectory interpolation (IPO) and Kuka's Robot Sensor Interface ([3]) respectively. The current control of the servo motor has a sample time of 0.0005 s. During operation, the moment of inertia with respect to any axis is not constant. In the light of the high contribution of constant gear inertias, the model was simplified to diagonal mass matrix with constant diagonal components. Thus for each axis j the time-continuous model shown in fig. 4 is used. Here, u_j is the input signal, P_j and T_j are constants of the low-pass filter for the input signal, $P_{\text{vel},j}$, $P_{\text{field},j}$ and K_j are the coefficients of the simplified velocity- and field controllers of the servo motor, M_j is the motor

moment, $M_{0,j}$ a constant additional moment and Θ_j is the moment of inertia of the robot arm. The state space model is

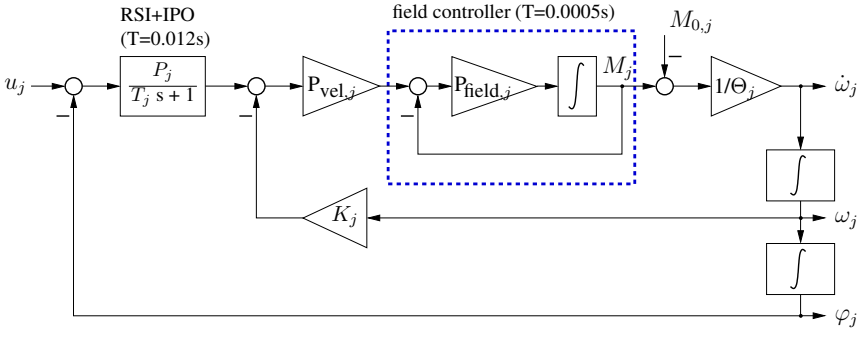

Figure 4: Block-diagram of the controller model

$$\begin{aligned} \dot{\underline{x}}_j &= \mathbf{A}_j\,\underline{x}_j + \mathbf{B}_j \begin{bmatrix} u_j(t) \\ M_{0,j} \end{bmatrix} \\ \underline{y}_j &= \mathbf{C}_j\,\underline{x}_j \end{aligned}$$

where

$$\underline{x}_j = \begin{bmatrix} M_j \\ \omega_j \\ \varphi_j \\ h_j \end{bmatrix},\ \mathbf{A}_j = \begin{bmatrix} -P_{\text{field},j} & -K_j\,P_{\text{field},j}\,P_{\text{vel},j} & 0 & P_{\text{field},j}\,P_{\text{vel},j} \\ 1/\Theta_j & 0 & 0 & 0 \\ 0 & 1 & 0 & 0 \\ 0 & 0 & -P_j/T_j & -1/T_j \end{bmatrix},$$

$$\underline{y}_j = \begin{bmatrix} \dot{\omega}_j \\ \omega_j \\ \varphi_j \end{bmatrix},\ \mathbf{B}_j = \begin{bmatrix} 0 & 0 \\ 0 & -1/\Theta_j \\ 0 & 0 \\ P_j/T_j & 0 \end{bmatrix} \quad \text{and} \quad \mathbf{C}_j = \begin{bmatrix} 1/\Theta_j & 0 & 0 & 0 \\ 0 & 1 & 0 & 0 \\ 0 & 0 & 1 & 0 \end{bmatrix}$$

with controller matrices $\mathbf{A}_j$, $\mathbf{B}_j$ and $\mathbf{C}_j$, state variables $\underline{x}_j$ and output-variable vector $\underline{y}_j = [\,\dot{\omega}_j\,,\omega_j\,,\,\varphi_j\,]^{\mathrm{T}}$, $j = 1,\ldots,6$, with $\omega_j = \dot{\varphi}_j$.

The parameters $\underline{p} = \left[\,P_{\text{field},j}\,,\,P_{\text{vel},j}\,,\,K_j\,,\,M_{0,j}\,,\,\Theta_j\,\right]$ are unknown and need to be identified from measurements. In the present case, sinusoidal input $u(t)$ was employed (fig. 5 a)). The identification was performed separately for each axis j, performing a standard least squares fitting

$$\text{minimize}\ \frac{1}{2}\sum_i (\hat{\varphi}_{j,i} - \varphi_j(\underline{p}, t_i))^2$$

between real axis angles $\hat{\varphi}_{j,i}$ measured at time t_i and the simulated axis angle $\varphi_j(t_i)$. Fig. 5 shows measured and simulated trajectories of the second robot axis angle for an initial guess $\underline{p}_0$ and the optimized model parameters $\underline{p}^\star$.

Controller parameters that have been identified with simple test signals also lead to a good fit between simulation and measurement for general input signals. This is shown in fig. 6, where the noise in the measurement results from artifacts of the measurement procedure which could not be avoided completely.

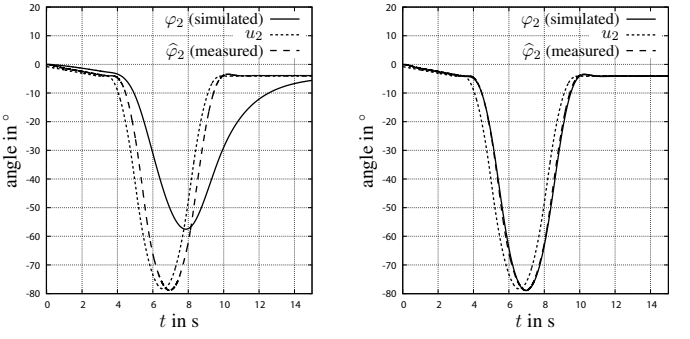

a) with initial guess $\underline{p}_0$ b) with final controller model parameters $\underline{p}^\star$

Figure 5: Measured and simulated angles of second robot axis

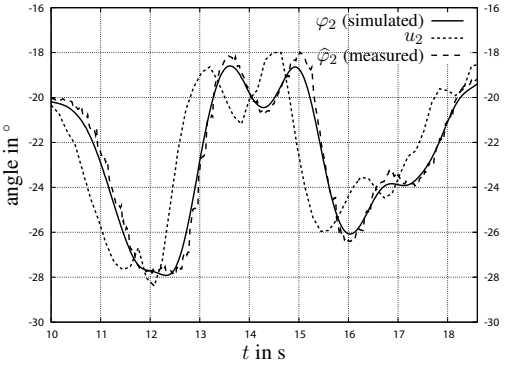

Figure 6: Fit between simulated and measured angles for general input signal

4 Generation of input signals

Let the acceleration at the end-effector be prescribed at r sampling points t_i as $\hat{\underline{\dot{t}}}_{\mathrm{EE,i}}$, and let the unknown input signals $u_j(t)$ be linear interpolations between r vertices $(t_i,\ u_{i,j})$ at the same sampling points (assumed here to be equal due to the constant input/output sampling rate of the robot controller). The signal vertices $u_{i,j}$ are collected in the design vector $\underline{x}_u$. The optimization problem is formulated as

$$\begin{aligned}
\text{minimize} \quad & \mathrm{F}(\underline{x}_u) = \frac{1}{2}\sum_{i=1}^{r}\left(\hat{\underline{\dot{t}}}_{\mathrm{EE,i}} - \underline{\dot{t}}_{\mathrm{EE}}(\underline{x}_u, t_i)\right)^2 \qquad (3)\\
\text{subject to} \quad & \underline{\ell}_{\underline{x}} \le \underline{x}_u \le \underline{u}_{\underline{x}}\\
& \underline{q}_{\min} \le \underline{q}_i \le \underline{q}_{\max} \forall i \in [1,\ldots,r]\\
& \underline{\dot{q}}_{\min} \le \underline{\dot{q}}_i \le \underline{\dot{q}}_{\max} \forall i \in [1,\ldots,r]\\
& \underline{\ddot{q}}_{\min} \le \underline{\ddot{q}}_i \le \underline{\ddot{q}}_{\max} \forall i \in [1,\ldots,r],
\end{aligned}$$

where for every evaluation of F, the dynamic equations of the controller model are integrated using the input functions $\underline{u}(t) = [\, u_1(t), \ldots, u_6(t) \,]$, leading to axis angle trajectories $\underline{q}(t)$, angle rates $\underline{\dot{q}}(t)$ and joint accelerations $\underline{\ddot{q}}(t)$. With these quantities, $\underline{\dot{t}}_{\mathrm{EE}}(\underline{x}_u, t_i)$ is computed using eqn. 2. In addition, limits on the axis angles, angle rates and accelerations are described as unilateral constraints.

While the optimization problem looks quite simple, in practice, the system will fail to converge due to poor initial value guesses. This makes the approach useless if no method for obtaining "good" initial guesses $\underline{x}_{u,0}$ is found. Three approaches for accomplishing this are presented next.

4.1 Inverse kinematics

A plausible initial guess for $\underline{x}_u$ can be immediately obtained from the inverse kinematics relationship

$$\underline{\ddot{q}} = \mathbf{J}^{-1}(\hat{\underline{\dot{t}}}_{\mathrm{EE}} - \dot{\mathbf{J}}\, \underline{\dot{q}} - \underline{e}_z\, g). \tag{4}$$

By integrating eqn. 4 twice, the joint angle trajectories $\tilde{\underline{q}}(t)$ are obtained. These can be used as an initial guess for the optimization by setting $\underline{u}(t_i) := \tilde{\underline{q}}(t_i)$. In this work, the initial value $\tilde{\underline{q}}_0 = [\, -45°, -41°, 13°, 0°, 28°, 0° \,]^{\mathrm{T}}$, $\tilde{\underline{\dot{q}}}_0 = \underline{0}$ was used for the integration. Although the initial value has a sufficient distance from any singularity, integration runs into a singularity of the Jacobian $\mathbf{J}$ and fails shortly before $t = 2s$ as shown in fig. 7 a).

4.2 Fixation of three axes and inverse kinematics in the remaining subspace

To avoid singularities of the Jacobian, some axes (for example A2, A3 and A5) of the robot can be fixed, leading to a simpler manipulator with regular Jacobian. The remaining axis angle accelerations $\underline{\ddot{q}}_{1,4,6} = [\, \dot{\omega}_1,\, \dot{\omega}_4,\, \dot{\omega}_6 \,]^{\mathrm{T}}$ are computed by

$$\underline{\ddot{q}}_{1,4,6} = \mathbf{J}^{+}_{1,4,6}(\hat{\underline{\dot{t}}}_{\mathrm{EE}} - \dot{\mathbf{J}}\, \underline{\dot{q}} - \underline{e}_z\, g). \tag{5}$$

Here, $\mathbf{J}^{+}_{1,4,6}$ is the generalized inverse of $\mathbf{J}_{1,4,6}$, consisting of the first, fourth and sixth column of $\mathbf{J}$.

Fig. 7 b) shows the axis angle accelerations computed with this approach using the same initial value as in section 4.1. Integration is possible throughout the complete domain, but the accelerations are too high to be performed by the real robot and become very large at $t = 6s$.

4.3 Inverse kinematics with damped least squares method

To avoid the aforementioned singularities, adjusted joint accelerations $\underline{\ddot{q}}^{\star}$ are computed using the damped least squares solution of [4]

$$\text{minimize} \;\; \| \; - \hat{\underline{\dot{t}}}_{\mathrm{EE}} + \mathbf{J}\, \underline{\ddot{q}} + \dot{\mathbf{J}}\, \underline{\dot{q}} + \underline{e}_z\, g \, \|^2 + \lambda^2 \, \| \, \underline{\ddot{q}} \, \|^2, \tag{6}$$

where the first term corresponds to the difference between prescribed and computed end-effector accelerations, $\lambda^2 \, \| \, \underline{\ddot{q}} \, \|^2$ is a penalty term that punishes high joint accelerations in the vicinity of singularities and λ is a damping factor for controlling the trade-off between fit and singularity avoidance. The solution of eqn. 6 becomes

$$\underline{\ddot{q}}^{\star} = \mathbf{J}^{\mathrm{T}}(\mathbf{J}\, \mathbf{J}^{\mathrm{T}} + \lambda^2 \mathbf{I})^{-1}(\hat{\underline{\dot{t}}}_{\mathrm{EE}} - \dot{\mathbf{J}}\, \underline{\dot{q}} - \underline{e}_z\, g). \tag{7}$$

By integrating eqn. 7 twice, the joint angle trajectories $\tilde{\underline{q}}(t)$ are obtained. Integration leads to reasonable joint angle accelerations near the start of the trajectory (fig. 7 c), but due to the

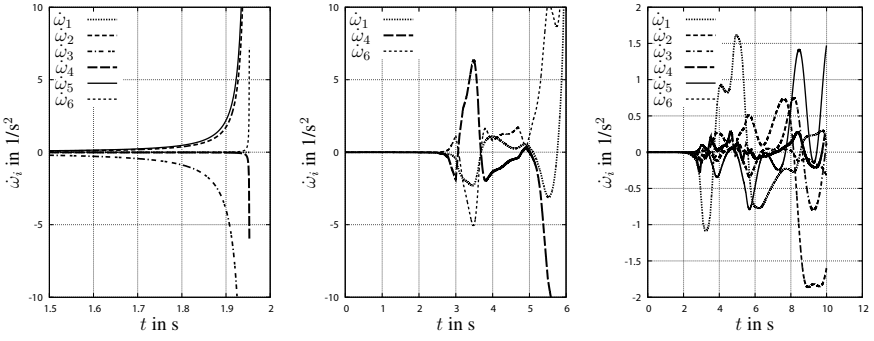

a) direct inverse kinematics b) inverse kinematics in subspace c) damped least squares approach

Figure 7: Joint angle accelerations for different inverse dynamics approaches

penalty term the first term in eqn. 6 is not forced exactly to zero by the optimizer and thus kinematical errors occur which in practical cases lead to a drift after a finite time (see fig. 8a). This is circumvented by the optimization procedure eqn. 3.

5 Experiment

The aforementioned algorithms were tested for the example of the simulation of a passenger car lane change maneuver. Shown in figures fig. 8 a) and b) are the results for application of damped least squares with $\lambda = 1.5$ and the optimization procedure of eqn. 3. It is clearly seen that with the optimization procedure the robot can track user-prescribed accelerations quite well, while for the damped least squares method the achieved trajectories drift apart from the target trajectories after approximately 4 seconds.

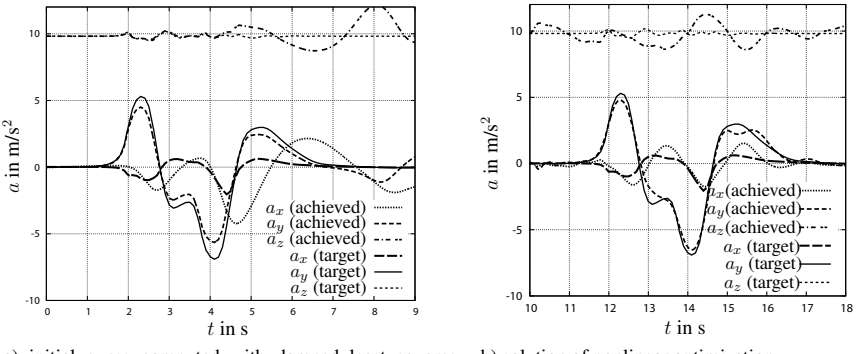

a) initial guess computed with damped least squares method b) solution of nonlinear optimization

Figure 8: Initial guess joint angle trajectory computed with the damped least squares method

6 Conclusions

In conclusion, the present paper shows that by a two-stage procedure it is possible to generate control inputs for a robot leading to a good matching with prescribed accelerations. First, an initial guess for the input signals is computed using the singularity-free damped least squares method. Then, these signals are used as an initial guess for a nonlinear optimization, taking into account workspace limits and actuator dynamics. The approach was tested for the linear accelerations acting on the driver of a car performing a lane change maneuver. Measurements with our KR 500 Motion simulator "Moving Dome" showed a good accordance between desired and measured accelerations.

REFERENCES

[1] J. Heindl, M. Otter, H. Hirschmüller, M. Frommberger, N. Sporer, F. Siegert, and H. Heinrich. The robocoaster as simulation platform - experiences from the first authentic mars flight simulation. In *Proceedings of the Motion Simulator Conference*, Braunschweig, Germany, September 21 2005.

[2] K. Beykirch, F. M. Nieuwenhuizen, H. J. Teufel, H.-G. Nusseck, J. S. Butler, and H. H. Bülthoff. Control of a Lateral Helicopter Side-step Maneuver on an Anthropomorphic Robot. In *Proceedings of the AIAA Modeling and Simulation Technologies Conference and Exhibit*, Hilton Head, South Carolina, August 20–23 2007.

[3] KUKA Roboter GmbH. *Robot Sensor Interface (RSI) Release 2.0.* KUKA Roboter GmbH, 2001.

[4] Y. Nakamura and H. Hanafusa. Inverse kinematics solutions with singularity robustness for robot manipulator control. *Journal of Dynamic Systems, Measurement and Control*, 108(3):163 – 171, 1986.

IAK 2008
Conference on Interdisciplinary Applications of Kinematics
A. Kecskeméthy, V. Potkonjak and A. Muller (eds.)
Lima, Peru, 9–11 January 2008

A ONE-DEGREE-OF-FREEDOM SPHERICAL WRIST FOR THE MODELLING OF PASSIVE MOTION OF THE HUMAN ANKLE JOINT

Riccardo Franci* **and Vincenzo Parenti-Castelli†**

*PhD Student
University of Bologna, viale Risorgimento 2, 40136 Bologna, Italy
e-mail: riccardo.franci@mail.ing.unibo.it,
web page: www.eng.diem.unibo.it

†Professor
University of Bologna, viale Risorgimento 2, 40136 Bologna, Italy
e-mail: vincenzo.parenticastelli@mail.ing.unibo.it

Keywords: equivalent mechanisms, spherical wrist, ankle passive motion, ankle joint coordinate system.

Abstract. *The passive motion of the human ankle complex joint, i.e. the motion in virtually unloaded condition, has been recently modelled by means of a type 5-5 equivalent one-degree-of-freedom (DOF) fully parallel mechanism (FPM). The 5-5 FPM can replicate the complicated joint passive motion very well while at the same time it outlines the basic role of the main anatomical structures such as bones and ligaments. However, more simple mechanisms, although less accurate to simulate the passive motion, can be of great utility and of practical interest, in particular for the design of prostheses and orthoses. In this contest this paper shows that a one-DOF fully parallel spherical wrist mechanism (one-DOF SWM), which is more simple than the 5-5 FPM, can replicate the ankle passive motion fairly well. The one-DOF SWM mechanism still retains a strong connection with some of the main anatomical structures such as the bone shapes and the principal ligaments (TiCaL and CaFiL). With respect to previous papers still proposing a one-DOF SWM as an equivalent mechanism, this paper presents a novel iterative synthesis procedure which makes it possible to define an optimal geometry of the one-DOF SWM which replicates the experimental data much better.*

1 INTRODUCTION

The majority of human joints are the diarthrodial joints, also called synovial joints and allow the main movements of the human body. In particular, the knee and the ankle joints play a fundamental role in human locomotion.

A deeper understanding of the normal behaviour of these joints is still a crucial issue which must be further pursued in order to improve the treatment of joint degeneration, surgical planning and prosthetic design. In this last field, the study of the kinematic, static and dynamic behaviour of the articulation by means of mechanical models is fundamental to create new solutions and to optimize the existing ones.

Mechanisms (equivalent mechanisms) can be devised to emulate the relative motion of the main bones of the joint during passive motion. Many mechanical models of these joints have been proposed in the literature. A number of these models study the passive motion of the main bones of the human joints, that is the motion under virtually unloaded conditions, in order to clarify the role played by the principal anatomical structures of the articulation (such as articular surfaces and ligaments). The passive motion, frequently approximated with a planar motion, is indeed quite often a very complex spatial motion.

In particular, as a consequence of the high number of operations and prosthetic replacements, the knee is one of the most studied joints and there are several models of it, both bi-dimensional [1, 2, 3] and three-dimensional [4, 5, 6, 7], aimed at replicating the motion of this joint.

Based on a similar approach and by the same motivations, the ankle joint has been studied too. One of the first models of the ankle joint was the one-degree-of-freedom (DOF) planar four-bar linkage [3]. More recently, clinical evidence and experimental results showed that the passive relative motion of the tibia and the talus, which are the main bones of the ankle joint, is a complex spatial motion that can be replicated very well by one-DOF spatial equivalent mechanisms [8, 9]. These mechanisms are based on the geometry of the main anatomical structures of the ankle joint, namely on the shape of the talus and tibio/fibula bones at their interface and on two main ligaments.

In particular in [8] the relative motion of the talus/calcaneus, considered as a single bone, with respect to the tibia/fibula, also considered as a single bone, was modelled by two different equivalent mechanisms. The first one features three sphere-to-plane contact points between the talus and the tibia/fibula bones, while the second one models the tibiotalar interface by a single spherical pair.

Based on experimental evidence, a fibre of two ligaments (one fibre per ligament) was considered as isometric in each model, thus constraining the relative motion of the two main bones to a one-DOF motion.

In [9] three sphere-to-sphere contact points at the tibiotalar interface were identified and again two isometric fibres from the same ligaments were considered. As a result a type 5-5 spatial fully-parallel mechanism (FPM) with one-DOF was synthesized, which very accurately replicates the ankle joint passive motion.

The 5-5 FPM is an effective tool for the study of both the human ankle motion and the role of its main anatomical structures. However, the geometrical complexity of the mechanism does not allow for an easy implementation in a practicable prosthetic design. In fact, a prosthesis design must combine both accuracy, to well replicate the kinematics of the limb, and simplicity for an easy manufacturing. These features may be achieved by reducing the numbers of both links and kinematic pairs.

For this purpose, a one DOF spherical wrist mechanism (one-DOF SWM) is proposed in this

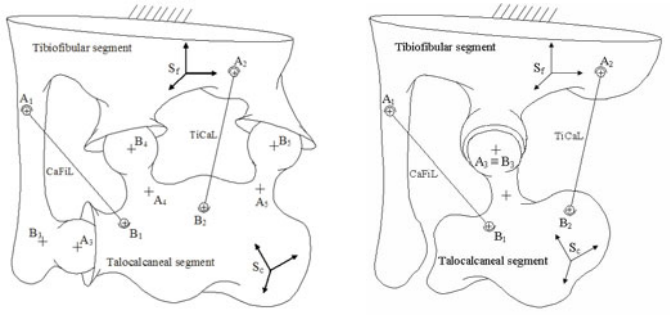

(a) (b)

Figure 1: Schematic representation of the two mechanisms with one-DOF: 5-5 fully-parallel mechanism (a) and spherical wrist mechanism (b).

paper as an equivalent mechanism. A one-DOF SWM was already presented in [8] but, probably due to the measurement techniques and to a not optimal procedure used for the geometrical dimension synthesis of the mechanism, the results were not completely satisfactory.

In this paper a new procedure to synthesize the optimal geometry of the one-DOF SWM will be presented and used in an iterative refinement process to provide the final geometry of the mechanism.

Simulation and experimental data will be compared to show the efficiency of the one-DOF SWM to replicate the ankle passive motion. Finally, the accuracy of the one-DOF SWM is compared to that obtained by the 5-5 FPM, previously presented in [9] which proved to be very effective, in order to show that although less accurate the one-DOF SWM can replicate the passive motion quite efficiently on one hand, while on the other it exhibits a much simpler geometrical structure.

2 KINEMATIC MODEL OF THE 5-5 PARALLEL MECHANISM

For clarity of presentation and to make the paper self-contained, a brief description of the 5-5 FPM presented in [9] as an equivalent mechanism for the ankle passive motion simulation is recalled in this section. The 5-5 mechanism showed the ability to simulate the ankle passive motion very efficiently, therefore it will be taken as a gold standard.

The 5-5 model relies upon the experimental observations that some fibres of the calcaneo-fibular ligament (CaFiL) and the tibiocalcaneal ligament (TiCaL) are nearly isometric during the ankle passive motion. Moreover, the tibia/fibula and the talus interface are considered in mutual contact at three points during flexion. The portion of each contact surface is modeled as a spherical surface.

According to these assumptions, with reference to Fig. 1a, the ligaments can be replaced with rigid binary links connected through spherical pairs centered at points $\mathbf{A}_i$, and $\mathbf{B}_i$, $i = 1, 2$, to the tibia/fibula and the talus respectively, while $\mathbf{A}_i$, and $\mathbf{B}_i$, $i = 3, 4, 5$, represent the centres of the talus/calcaneus and tibia/fibula spherical surfaces respectively. The resulting mechanism is thus a FPM of type 5-5 with one-DOF.

3 KINEMATIC MODEL OF THE EQUIVALENT ONE-DOF SPHERICAL WRIST

Based on a careful inspection of the shape of the articular surfaces of the tibia/talus pair on one hand and on the experimental observation that the two ligaments TiCaL and CaFiL exhibit some isometric fibres during the passive motion, a one-DOF spherical mechanism was considered for the ankle passive motion simulation. The model of the mechanism is schematically shown in Fig. 1b where the tibia and talus surfaces are modelled as spherical surfaces (centred at $\mathbf{A}_3$ and $\mathbf{B}_3$) interconnected to each other to form a spherical pair centred at point $\mathbf{A}_3 \equiv \mathbf{B}_3$; the two isometric fibres $\mathbf{A}_1\mathbf{B}_1$ and $\mathbf{A}_2\mathbf{B}_2$ of the CaFiL and TiCaL ligaments respectively are modelled as two binary rigid links, with constant length L_i, $i = 1, 2$, connected to the tibiofibular and to the talocalcaneal segments respectively by means of spherical pairs centered at points $\mathbf{A}_1$, $\mathbf{B}_1$ and $\mathbf{A}_2$, $\mathbf{B}_2$ respectively. A careful inspection reveals that the mechanism provides the talocalcaneal segment with one-DOF with respect to the tibiofibular segment. Indeed, Kutzbach's formula [10] foresees one-DOF considering that the rotations of the two ligaments about the respective axes $\mathbf{A}_1\mathbf{B}_1$ and $\mathbf{A}_2\mathbf{B}_2$ are inessential to the relative position of the two segments.

The closure equations of the spherical wrist can be found based on the consideration that each pair of points ($\mathbf{A}_i$, $\mathbf{B}_i$), $i = 1, 2$, is constrained to maintain a constant mutual distance L_i, during flexion motion while $\mathbf{A}_3$ and $\mathbf{B}_3$ must always be coincident. With these considerations, the model of the one-DOF spherical wrist can be expressed by:

$$\begin{aligned} &\|\mathbf{A}_i - R \cdot \mathbf{B}_i - \mathbf{P}\|^2 = L_i^2 \qquad (i = 1, 2) \\ &\mathbf{A}_3 - R \cdot \mathbf{B}_3 - \mathbf{P} = 0 \end{aligned} \tag{1}$$

where the points $\mathbf{A}_i$ and $\mathbf{B}_i$ are expressed in the Cartesian reference systems S_f and S_c respectively and the symbol $\|\cdot\|^2$ is the L^2-norm of the vector. The systems S_f and S_c are embedded in the tibiofibular segment and in the talocalcaneal segment respectively (see Fig.1) and their locations are arbitrarily chosen. The matrix R is the rotation matrix that transforms the components of a vector measured in S_c into the components of the same vector measured in the S_f and $\mathbf{P}$ is the position vector of the origin $\mathbf{O}_c$ of S_c with respect to the reference system S_f. The matrix R can be expressed as a function of three parameters: the angles α, β and γ (intra/extra rotation, pronation/supination and dorsi/plantar flexion of the foot with respect to the tiba) that represent the rotation angles of the human ankle, as defined by Grood and Suntay [11]. More detailed information on the coordinate reference systems is reported in Appendix A.

The equation system (1) represents the closure equation system of the one-DOF SWM. It is a system of five nonlinear equations in six variables: the three components of the position vector $\mathbf{P}$ and the three angles γ, α and β.

Therefore, for every given angle γ, the remaining five variables can be found by solving the equation system (1). System (1) is a nonlinear system which normally provides more than one solution for a given value of the input angle γ [12]. Specific procedures could be used to find all the possible solutions, however, in this context only one solution is of practical interest and can be easily found by a numerical method, for instance, by a quasi-Newton numerical procedure [13], as explained in Section 4.

4 PARAMETER OPTIMIZATION

The geometry of the equivalent spherical wrist is defined by 20 parameters: namely, the coordinates of points $\mathbf{O}_f$, $\mathbf{A}_1$, $\mathbf{A}_2$ in S_f and $\mathbf{O}_c$, $\mathbf{B}_1$, $\mathbf{B}_2$ in S_c and the 2 link lengths L_i, $i = 1, 2$.

The procedure to find the optimal set of the parameters is the same as described in [9], thus only the key aspects will be presented in this paper.

The experimental data provide both the geometric dimensions of the main anatomical structures, which are used as a first tentative geometry of the mechanism, and the pose (position and orientation) of the talus with respect to the tibia/fibula at a high number *n* of selected values of the flexion angle γ within a complete excursion.

At each step of the optimization iterative process, the closure equations (1) are solved for each measured flexion angle; thus the relative pose of the talocalcaneal segment with respect to the tibiofibular segment is iteratively compared with the pose obtained by measurement data by means of an error function *f* (objective function). The function is the sum of the squared and weighted errors of the experimental values with respect to the calculated ones, for all the *n* values of the flexion angle (γ). The function *f* is defined as follows:

$$f = \sum_{j=1}^{5} \sum_{i=1}^{n} \frac{\left(x_{ji} - x_{ji}^{*}\right)^2}{\left(x_{j_{max}} - x_{j_{min}}\right)^2} \tag{2}$$

where, x_{ji} is the actual value of the j-th dependent variable, $j = 1, 2, \ldots, 5$, of the five ones (the three coordinates of the origin of S_c and the two angles β and α) at the i-th pose, $i = 1, 2, \ldots, n$; x_{ji}^{*} is the corresponding experimental value of the variable x_{ji}; $x_{j_{max}}$ and $x_{j_{min}}$ are the maximum and minimum values of each of the dependent variables at the end of the process.

If equation system (1) does not provide a real solution then an arbitrarily high value is given to the objective function *f*. If the objective function reaches a minimum the process stops, otherwise a new geometry of the spherical wrist is defined and the iterative process is repeated. This particular objective function is proposed since it proved to be effective [7, 9, 14].

Moreover, since the function f is highly nonlinear and has discontinuities, the objective function is initially solved by means of a genetic algorithm or, alternatively, by means of the direct search method [15]. The obtained solution is then refined by means of a quasi-Newtonian algorithm [13].

It is worth noting that the introduction of lower and upper bounds to the values of the 20 parameters (points $\mathbf{A}_i$ and $\mathbf{B}_i$, $i = 1, 2, 3$ and lengths L_i, $i = 1, 2$), that define the geometry of the equivalent mechanism, provides a final geometry of the optimized equivalent mechanism which retains the anatomical feature of the ankle joint.

5 EXPERIMENTAL SESSION

An experimental session was conducted following the same procedure presented in [9], to collect experimental data, necessary for the synthesis of the equivalent mechanism.

In particular, a fresh-frozen amputated lower limb was analysed. The specimen included intact tibia, fibula, talus and calcaneus; capsula and ligaments were left intact, while the other human tissues were removed. A careful inspection of the specimens showed that they were not affected by abnormalities nor osteoarthritis.

The tibia was fixed to a horizontal workbench table with the toes upward while the other bones were free to move with respect to the tibia. A pin drilled along the calcaneus longitudinal axis and protruding from the posterior surface was in contact at a point with a rigid link, connected to the workbench by a revolute pair with axis parallel to the horizontal plane, which supports the pin and drives it to move with a five DOF relative motion with respect to the link itself.

Starting from a rest position in maximum plantarflexion, the joint was extended until maximum dorsiflexion, thus producing the desired motion of the talocalcaneal segment with respect to the tibiofibular segment. Since the weight of the talocalcaneal segment and the friction between the pin and the rigid link is negligible, then the motion of the talocalcaneal segment can be considered as obtained in a virtually unloaded condition.

The talus and the calcaneus on one hand and the tibia and fibula on the other hand were respectively considered as a single rigid body. Thus, only the relative movements of the ankle (or tibiotalar) joint were considered. This assumption was also confirmed by experimental results. Indeed, previous investigations [16] showed that the relative movements of the talus with respect to the calcaneus and the tibia with respect to fibula were negligible in passive flexion.

An opto-electronic system was used as an acquisition system for recording the pose of two trackers fixed to the tibia (Ti) and the talus (Ta) respectively, during a complete passive flexion-extension movement. A number of trials were performed but the experimental data were coherently recorded from one selected dorsi-plantar flexion trial.

A camera system can recognize the poses of the two trackers with respect to a Cartesian reference system fixed to the laboratory. Anatomical reference systems embedded in the tibia and talus respectively were defined by referring to anatomical landmarks, whose position was measured by a pointer.

In particular, the tibia anatomical coordinate system (S_f) was defined as follows:

- origin: located at the midpoint, IC, of the line joining the lower ends, LM and MM, of the tip of the lateral and medial malleolus respectively;
- y-axis: the line intersection between the quasi-frontal plane (defined by the malleoli and the head of the fibula landmarks) and the quasi-sagittal plane (orthogonal to the quasi-frontal and passing through the point IC and the tibial tuberosity landmarks);
- z-axis: the line connecting MM and LM, and pointing to the right hand side of the body.
- x-axis: as a consequence, according to the right hand rule.

Likewise, the talus anatomical reference system (S_c) was defined as follows:

- origin: coincident with the mid-point, IP, between the points AL and AM, respectively the tips of the lateral and medial anterior surface of the talus;
- y-axis: the line intersection between the quasi-frontal plane (defined by the points PL and PM, respectively the tips of the posterior lateral and medial surface of the talus, and the talus head landmark) and the quasi-sagittal plane (orthogonal to the quasi-frontal plane and passing through the point IP and the landmark of the talus head);
- z-axis: the line connecting the head of the talus and PM, and pointing to the right hand side of the body.
- x-axis: as a consequence, according to the right hand rule.

The specimens were then dissected and both the geometry of the articular surfaces and the insertion areas of the CaFiL and TiCaL ligaments were digitized by means of the same pointer. The coordinates of points measured by the pointer were given in the reference systems of the trackers.

The anatomical systems S_f and S_c were chosen so as to have their axes aligned with the anatomical axes, i.e. x-axis pointing forward, z-axis pointing to the right (LM for a right leg and MM for a left leg) and y-axis pointing proximally and orthogonal to the previous two.

The anatomical landmarks, that define the anatomical reference systems, were given in the reference systems of the trackers. The 4x4 transformation matrices ${}_{i,f}T$ (which transforms homogeneous coordinates from the tibial anatomical system to a reference systems of the tracker on the tibia) and ${}_{a,c}T$ (which transforms homogeneous coordinates from the talus anatomical system to a reference systems of the tracker on the talus) were evaluated. The transformation matrix ${}_{f,c}T$ from S_c to S_f, that describes the relative pose of talus to tibia, could then be easily computed by the simple transformation operator:

$$ {}_{f,c}T = ({}_{g,f}T)^{-1} \cdot {}_{g,c}T \tag{3} $$

where S_g is the reference system fixed to the camera and

$$ \begin{aligned} {}_{g,f}T &= {}_{g,i}T \cdot {}_{i,f}T \\ {}_{g,c}T &= {}_{g,a}T \cdot {}_{a,c}T \end{aligned} \tag{4} $$

In order to define the orientation of the talus with respect to the tibia, a sequence-independent joint coordinate system [11] was chosen. Three rotation axes that define the system were chosen as follows: the z-axis of S_f fixed to the tibia, the y-axis of S_c fixed to the talus, and an axis coincident with the shortest distance line of the other two axes to form a right hand reference system.

Three angles about these axes are defined: the ankle dorsiflexion(+)/plantarflexion(-) angle γ about the z-axis of S_c, the ankle internal(+)/external(-) rotation angle α about the y-axis of S_f, and the ankle pronation(+)/supination(-) angle β about a floating axis defined by the cross vector product of the unit vectors of the z-axis of S_f and the unit vector of the y-axis of S_c.

Based on these conventions the rotation matrix R can thus be computed, as described in Appendix A.

6 RESULTS

The poses of the talus with respect to the tibia obtained by the experimental sessions were compared with those obtained by both the SWM and the 5-5 equivalent FPM. Both experimental and simulation data are reported in Figures 2 and 3. In particular, the positions x, y, and z of the origin of the reference system S_c with respect to S_f and the angles α and β are reported in Fig. 2 and Fig. 3 respectively, as a functions of the ankle flexion angle γ.

The experimental results are identified by the symbol "Δ" and interpolated by a dash-dot line. The interpolation makes it possible to use a higher number of experimental data, which may be useful for the optimal synthesis of the geometry of both mechanisms (the 5-5 FPM and the SWM).

The results of the 5-5 mechanism replicate the passive motion of the human ankle joint slightly better than those obtained by the one-DOF spherical wrist mechanism.

This is an expected result since the synthesis of the 5-5 FPM can rely upon a greater number of parameters and can thus better fit a more complex motion. However, although simpler and less capable of simulating a complex motion, the SWM represents a more useful basis for a reliable prosthetic design.

Furthermore, the number of the SWM parameters being lower (fifteen) than those (twenty) of the 5-5 FPM, the computational time during the optimization process is significantly reduced.

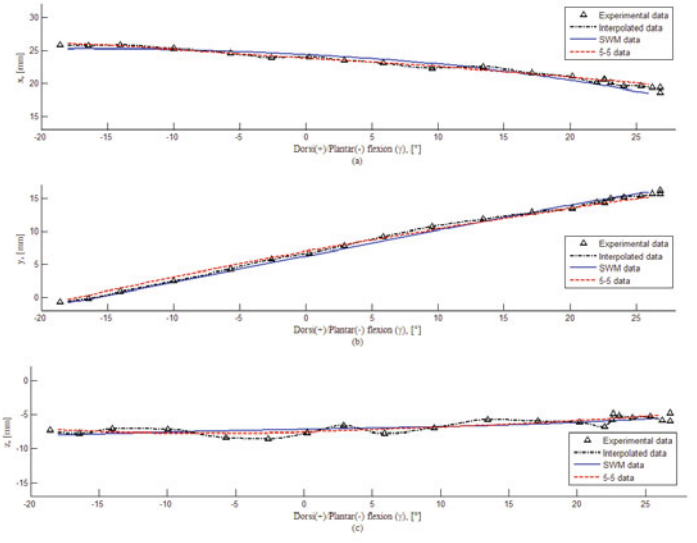

Figure 2: Passive motion simulation: x, (a), y, (b), and z, (c) versus ankle's flexion angle γ.

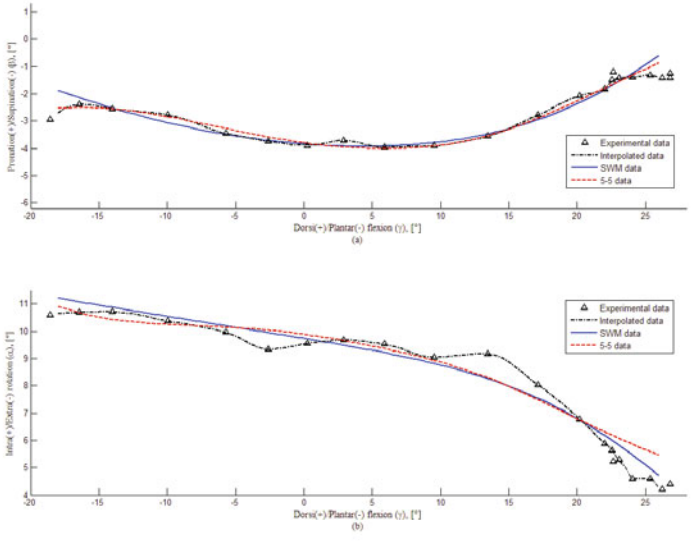

Figure 3: Passive motion simulation: angles β, (a), and α, (b), versus ankle's flexion angle γ.

It is worth noting that different geometries of the equivalent 5-5 parallel mechanism and the spherical wrist could have been synthesized, which might better fit the experimental data of the passive motion, but they might not better fit the anatomical structures of the natural ankle joint. The geometries synthesized in this paper are the best compromise that can well fit both the ankle passive motion and the ankle's main anatomical structures.

7 CONCLUSIONS

In this paper a one-DOF fully parallel spherical wrist mechanism (SWM) is presented for the simulation of the passive motion of the human ankle joint, that is the joint motion under virtually unloaded conditions.

The SWM is based on the main anatomical structures of the ankle joint, namely the talus and the tibio/fibula bones at their interface, and the TiCal and CaFil ligaments.

This mechanism was already presented in the literature [8] but the results were not completely satisfactory, probably due to the use of a non optimal synthesis procedure. In this paper, indeed, a new efficient iterative synthesis procedure was adopted which made it possible to synthesize an optimal geometry of the one-DOF SWM that allows a good replication of the experimental data collected on an in vivo specimen by a vision system.

The simulation results compared with those of a one-DOF 5-5 parallel mechanism, which proved [9] to simulate the ankle passive motion very well, exhibited a good degree of accuracy.

The purpose of the paper to find a mechanism simpler than the 5-5 FPM, but still capable of replicating the ankle passive motion with a good degree of accuracy, was successfully achieved. Indeed, the SWM is geometrically simpler, although still accurate enough, and computationally less expensive than the 5-5 FPM and may also represent a better basis for the design of prosthetic devices.

ACKNOWLEDGEMENT

This study was supported by MIUR and STARTER funds. The authors gratefully thank DPh. Alberto Leardini and his staff at the Istituti Ortopedici Rizzoli for the facilities and support provided for the collection of the experimental data.

REFERENCES

[1] J.D. Goodfellows and J.J. O'Connor. The mechanics of the knee and prosthesis design. *Journal of Bone Joint Surgery*, 60B:358–369, 1978.

[2] M.S. Hefzy and T.D.V. Cooke. Review of knee models: 1996 update. *Applied Mechanics Reviews*, 49(10 pt 2):187–193, 1996.

[3] A. Leardini, J.J. O'Connor, F. Catani, and S. Giannini. Kinematics of the human ankle complex in passive flexion: a single degree of freedom system. *Journal of Biomechanics*, 32(2):111–118, February 1999.

[4] D.R. Wilson and J.J. O'Connor. A three-dimensional geometric model of the knee for the study of joint forces in gait. *Gait and Posture*, 5:108–115, 1997.

[5] V. Parenti-Castelli and R. Di Gregorio. Parallel mechanisms applied to the human knee passive motion simulation. In J. Lenarcic and M. Stanisic Eds., editors, *Advances in Robot Kinematics*, pages 333–344. Kluwer Academic Publisher, 2000. ISBN 0-7923-6426-0.

[6] R. Di Gregorio and V. Parenti-Castelli. A spatial mechanism with higher pairs for modelling the human knee joint. *Journal of Biomechanical Engineering*, 125(2):232 – 237, 2003.

[7] N. Sancisi and V. Parenti-Castelli. A 1-dof parallel spherical wrist for the modelling of the knee passive motion. In *Proceedings of the 12th IFToMM World Congress in Mechanism and Machine Science*, pages 1–6, June 2007.

[8] R. Di Gregorio, V. Parenti-Castelli, J.J. O'Connor, and A. Leardini. Mathematical models of passive motion at the human ankle joint by equivalent spatial parallel mechanisms. *Medical & Biology Engineering & Computing*, 45(3):305–313, 2007.

[9] R. Franci and V. Parenti-Castelli. A 5-5 one degree of freedom fully-parallel mechanism for the modelling of passive motion at the human ankle joint. In *Proceedings of the ASME International Design Engineering Technical Conferences and Computers and Information in Engineering*, pages 1–8, September 2007.

[10] K. Kutzbach. Mechanische leitungsverzweigung; ihre gesetze und anwendungen. *Maschinbau der Betrieb*, 8(21):710–716, 1929.

[11] E.S. Grood and W.J. Suntay. A joint coordinate system for the clinical description of three-dimensional motions: application to the knee. *Journal of Biomechanical Engineering*, 105(2):136–144, May 1983.

[12] C. Innocenti and V. Parenti-Castelli. Echelon form solution of direct kinematics for the general fully-parallel spherical wrist. *Mechanism and Machine Theory*, 28(4):553–561, 1993.

[13] M.J.D. Powell. The convergence of variable metric methods for nonlinearly constrained optimization calculations. *Nonlinear Programming 3*, 3:27–63, 1978.

[14] A. Ottoboni, V. Parenti-Castelli, and A. Leardini. On the limits of the articular surface approximation of the human knee passive motion models. In *Proceedings of the 17th AIMeTA Congress of Theoretical and Applied Mechanics*, pages 1–11, September 2005.

[15] V. Torczon. On the convergence of pattern search algorithms. *SIAM Journal on Optimization*, 7(1):1–25, 1997.

[16] Alberto Leardini, Rita Stagni, and John J. OConnor. Mobility of the subtalar joint in the intact ankle complex. *Journal of Biomechanics*, 34:805–809., 2001.

Appendix A: Human Ankle Joint Coordinate System

This appendix provides the equations used to compute the rotation angles used in this paper and applied to the human ankle joint. The sequence-independent joint coordinate system is described in detail in [11].

As shown in Fig. 4, the Cartesian systems S_f and S_c are embedded in the tibia and talus respectively.

Unit vectors of the coordinate system which define the axes are denoted as $\mathbf{e}_1$, $\mathbf{e}_2$ and $\mathbf{e}_3$. The rotation axis $\mathbf{e}_1$, fixed to the tibia, is chosen coincident with the z_f-axis so that the rotation about it corresponds to the clinical motion of dorsi-plantar flexion. The rotation axis $\mathbf{e}_3$, fixed to the talus, is chosen coincident with the y_c-axis and the rotation about it corresponds to the clinical motion of internal-external rotation of the foot. The floating axis, defined by the unit vector $\mathbf{e}_2$, is the common perpendicular to the body fixed axes. Therefore, its orientation is given by the cross product of the unit vectors which define the orientation fixed axes:

$$\mathbf{e}_2 = \frac{\mathbf{e}_3 \times \mathbf{e}_1}{\|\mathbf{e}_3 \times \mathbf{e}_1\|} \tag{5}$$

The three angular rotations (γ, β, α) about $\mathbf{e}_1$, $\mathbf{e}_2$ and $\mathbf{e}_3$ respectively represent the clinical orientation of the foot with the convention described in Section 5.

The rotation matrix, that describes the orientation of S_c to S_f, is conveniently defined by thinking of the ankle joint in neutral position with the coordinate systems parallel to one another. In this configuration the direction of the unit vector $\mathbf{e}_2$ is coincident with the direction of the x-axis. If therefore, R_x, R_y and R_z described the rotation matrices about the axes $\mathbf{e}_2$, $\mathbf{e}_3$ and $\mathbf{e}_1$ respectively they can be expressed as follows:

$$R_{\mathbf{e}_1,\gamma} = \begin{bmatrix} c_\gamma & -s_\gamma & 0 \\ s_\gamma & c_\gamma & 0 \\ 0 & 0 & 1 \end{bmatrix} R_{\mathbf{e}_2,\beta} = \begin{bmatrix} 1 & 0 & 0 \\ 0 & c_\beta & -s_\beta \\ 0 & s_\beta & c_\beta \end{bmatrix} R_{\mathbf{e}_3,\alpha} = \begin{bmatrix} c_\alpha & 0 & s_\alpha \\ 0 & 1 & 0 \\ -s_\alpha & 0 & c_\alpha \end{bmatrix} \tag{6}$$

where c_x and s_x stand for $cos(x)$ and $sin(x)$ respectively.

If considering a right (Fig. 4a) and according to right hand rule, the rotation matrix that describes the orientation of S_c to S_f, is given as rotation about three axes:

$$R_{right} = R_{\mathbf{e}_1,\gamma} \cdot R_{\mathbf{e}_2,-\beta} \cdot R_{\mathbf{e}_3,\alpha} \tag{7}$$

$$R_{right} = \begin{bmatrix} c_\alpha c_\gamma + s_\alpha s_\beta s_\gamma & -s_\gamma c_\beta & s_\alpha c_\gamma - c_\alpha s_\beta s_\gamma \\ c_\alpha s_\gamma - s_\alpha s_\beta c_\gamma & c_\gamma c_\beta & s_\alpha s_\gamma + c_\alpha s_\beta c_\gamma \\ -c_\beta s_\alpha & -s_\beta & c_\alpha c_\beta \end{bmatrix} \tag{8}$$

In order to maintain the same clinical meaning for the rotations (α, β, γ) if considering a left leg, the sign of the angles α and β should be opposite to the right leg angles, as shown in Fig. 4b. Therefore, in this case the rotation matrix that describes the orientation of S_c to S_f, can be computed as:

$$R_{left} = R_{\mathbf{e}_1,\gamma} \cdot R_{\mathbf{e}_2,\beta} \cdot R_{\mathbf{e}_3,-\alpha} \tag{9}$$

$$R_{left} = \begin{bmatrix} c_\gamma c_\alpha + s_\gamma s_\beta s_\alpha & -s_\gamma c_\beta & -c_\gamma s_\alpha + s_\gamma s_\beta c_\alpha \\ s_\gamma c_\alpha - c_\gamma s_\beta s_\alpha & c_\gamma c_\beta & -s_\gamma s_\alpha - c_\gamma s_\beta c_\alpha \\ c_\beta s_\alpha & s_\beta & c_\beta c_\alpha \end{bmatrix} \tag{10}$$

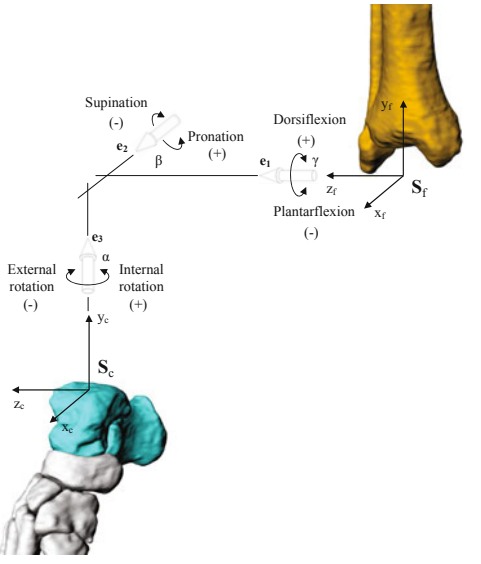

(a)

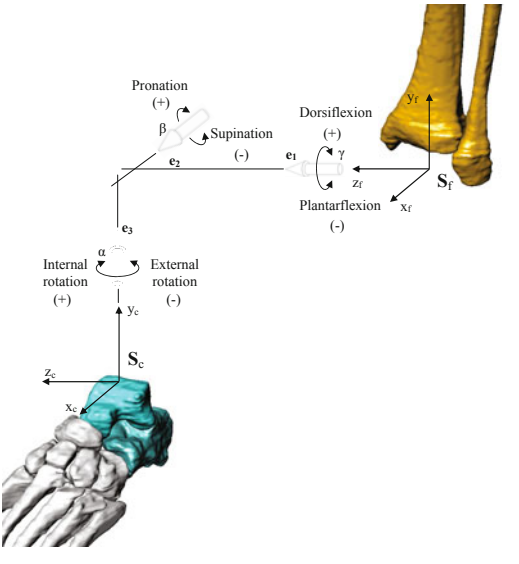

(b)

Figure 4: The Joint Coordinate System for the right leg (a) and the left leg (b).

If the rotation matrix R (R_{right} or R_{left} if the leg is right or left respectively) is known and given by

$$R = \begin{bmatrix} r_{11} & r_{12} & r_{13} \\ r_{21} & r_{22} & r_{23} \\ r_{31} & r_{32} & r_{33} \end{bmatrix} \tag{11}$$

the rotation angles (α, β, γ) can be computed as:

$$\begin{aligned} \beta &= atan2\left(r_{3,2}, \pm\sqrt{r_{3,1}^2 + r_{3,3}^2}\right) \\ \alpha &= atan2\left(\frac{-r_{3,1}}{c_\beta}, \frac{r_{3,3}}{c_\beta}\right) \\ \gamma &= atan2\left(\frac{-r_{1,2}}{c_\beta}, \frac{r_{2,2}}{c_\beta}\right) \end{aligned} \tag{12}$$

where $atan2(y, x) = arctan\left(\frac{y}{x}\right)$.

Author Index